



Thermo-hydraulic behaviour of dual channel superconducting Cable-In-Conduit Conductors for ITER

Bertrand Renard

► To cite this version:

Bertrand Renard. Thermo-hydraulic behaviour of dual channel superconducting Cable-In-Conduit Conductors for ITER. Reactive fluid environment. Université de provence; CEA Cadarache, 2006. English. NNT: . tel-01795347

HAL Id: tel-01795347

<https://theses.hal.science/tel-01795347>

Submitted on 18 May 2018

HAL is a multi-disciplinary open access archive for the deposit and dissemination of scientific research documents, whether they are published or not. The documents may come from teaching and research institutions in France or abroad, or from public or private research centers.

L'archive ouverte pluridisciplinaire **HAL**, est destinée au dépôt et à la diffusion de documents scientifiques de niveau recherche, publiés ou non, émanant des établissements d'enseignement et de recherche français ou étrangers, des laboratoires publics ou privés.

UNIVERSITE DE PROVENCE - AIX-MARSEILLE I
Ecole Doctorale Physique, Modélisation et Sciences pour l'Ingénieur
Association EURATOM-CEA
Département de Recherches sur la Fusion Contrôlée

THESE

pour obtenir le grade de
DOCTEUR de l'UNIVERSITE de PROVENCE
discipline : **MECANIQUE ENERGETIQUE**

présentée et soutenue publiquement par
Bertrand RENARD
le 18 septembre 2006

THERMO-HYDRAULIC BEHAVIOUR OF
DUAL CHANNEL SUPERCONDUCTING CABLE-IN-CONDUIT CONDUCTORS FOR ITER
COMPORTEMENT THERMO-HYDRAULIQUE DES SUPRACONDUCTEURS DE TYPE
CABLE-EN-CONDUIT À DOUBLE CANAL POUR ITER

JURY

| | | |
|------------------------|-----------------|--------------------|
| Pr. Roger MARTIN | IUSTI Marseille | Président du jury |
| Dr. Chantal MEURIS | CEA Saclay | Rapporteur |
| Pr. Michel FEIDT | UHP Nancy | Rapporteur |
| Pr. Lounès TADRIST | IUSTI Marseille | Directeur de thèse |
| Dr. Jean-Luc DUCHATEAU | CEA Cadarache | Responsable CEA |
| Dr. Luca BOTTURA | CERN Genève | Examinateur |
| Dr. Frédéric TOPIN | IUSTI Marseille | Examinateur |

Thermo-Hydraulic behaviour of dual-channel superconducting Cable-In-Conduit Conductors for ITER

Abstract

In an effort to optimise the cryogenics of large superconducting coils for fusion applications (ITER), dual channel Cable-In-Conduit Conductors (CICC) are designed with a central channel spiral to provide low hydraulic resistance and faster helium circulation. The qualitative and economic rationale of the conductor central channel is here justified to limit the superconductor temperature increase, but brings more complexity to the conductor cooling characteristics. The pressure drop of spirals is experimentally evaluated in nitrogen and water and an explicit hydraulic friction model is proposed. Temperatures in the cable must be quantified to guarantee superconductor margin during coil operation under heat disturbance and set adequate inlet temperature. Analytical one-dimensional thermal models, in steady state and in transient, allow to better understand the thermal coupling of CICC central and annular channels. The measurement of a heat transfer characteristic space and time constants provides cross-checking experimental estimations of the internal thermal homogenisation. A simple explicit model of global interchannel heat exchange coefficient is proposed. The risk of thermosiphon between the two channels is considered since vertical portions of fusion coils are subject to gravity. The new hydraulic model, heat exchange model and gravitational risk ratio allow the thermohydraulic improvement of CICC central spirals.

Keywords: cable-in-conduit conductors, superconducting magnets, fusion, forced flow, spiral, heat transfer coefficient, heat exchanger, ITER

Comportement thermo-hydraulique des supraconducteurs de type câble-en-conduit à double canal pour ITER

Résumé

Afin d'optimiser le contrôle cryogénique des aimants supraconducteurs pour la fusion (ITER), les conducteurs de type câble en conduit à double canal (CICC) comprennent un canal central qui assure une résistance hydraulique minimale et une circulation d'hélium rapide. Le canal central constitué d'une spirale limite la température des supraconducteurs, mais complique singulièrement le refroidissement du câble. Les pertes de charge de la spirale centrale sont évaluées en azote puis en eau pressurisée ; un modèle de frottement hydraulique est ainsi proposé. Les températures doivent être connues dans le câble, afin de garantir le fonctionnement des supraconducteurs sous charge thermique. Il est alors possible de définir les marges et de fixer la température d'entrée. Des modèles 1D analytiques en régime permanent et transitoire ont été développés afin de mieux comprendre le couplage thermique entre les canaux du CICC. La mesure des constantes caractéristiques d'espace et de temps fournit une évaluation expérimentale de l'homogénéisation thermique interne. Un modèle simple et explicite du coefficient d'échange intercanal est proposé. Le risque de thermosiphon existant entre les deux canaux dans les parties verticales des bobines de fusion est évalué grâce à un critère. Les nouveaux modèles hydrauliques, thermiques et le critère de risque de thermosiphon permettent l'amélioration thermo-hydraulique de la spirale centrale de CICC.

Mots-clefs : conducteurs de type cable-en-conduit, aimants supraconducteurs, fusion, circulation forcée, spirale, coefficient d'échange thermique, échangeur thermique, ITER

Thermohydraulisches Verhalten des Innengekühlten Zweikanalrohrsupleiterkabels für ITER

Kurzfassung

Um die Kryogen-Benutzung und -Kontrolle der Supraleitenden Großmagneten für die Kernfusion (ITER) zu optimieren, wurde der Zweikanalrohrsupleiterkabel (CICC) mit einer zentralen Spirale entworfen. Der Zentralkanal soll einen minimalen hydraulischen Widerstand und einen schnellen Heliumverkehr gewährleisten, führt jedoch zu einer schwierigeren Abkühlung des Kabels. Das qualitative und ökonomische Grundprinzip der Leiterspirale wird hier durch die Begrenzung der Supraleitertemperatur gerechtfertigt. Der Druckabfall der zentralen Spirale wird experimentell am Stickstoff und danach am Druckwasser ausgewertet und daraus ein hydraulisches Modell vorgeschlagen. Die Temperaturen im Kabel müssen quantitativ bekannt sein, um Hitzestörungen des Supraleiters während des Betriebes der Spule zu verhindern, sowie um ausreichende Spielräume mit entsprechend niedriger Eintrittstemperatur einzustellen. Es wurden analytische eindimensionale Modelle entwickelt, um die thermische Kopplung zwischen den Kanälen des CICC im Dauer- und Übergangszustand besser zu verstehen. Die Messung der Raum- und Zeit-Konstanten liefert eine Versuchsbewertung der internen thermischen Homogenisierung. Es wird ein einfaches und ausdrückliches Modell des globalen Zwischenkanal-Wärmeaustauschkoeffizienten vorgeschlagen. Das bestehende Thermosiphonrisiko zwischen den zwei Kanälen bei vertikaler Fusionsspulen verweist auf ein Kriterium. Das neue hydraulische Modell, das Wärmeaustauschmodell und das Kriterium des Thermosiphonrisikos erlauben schließlich die thermohydraulische Optimierung der Kabel-Zentralspirale.

Schlüsselwörter: Rohrsupraleiterkabel, Supraleitende Magneten, Kernfusion, gezwungenen Fluss, Spirale, Wärmeübertragungskoeffizient, Wärmeaustauscher, ITER

Association EURATOM-CEA
Département de Recherches sur la Fusion Contrôlée
Service Tokamak Exploitation et Pilotage
Groupe CRYomagnétisme
F-13108 Saint Paul-lez-Durance

Acknowledgements

I want to pay a special tribute to my real Boss in heaven and to my parents for the best gift of all: life.

I would like to thank master Philippe Bévillard for his invaluable art, humble pedagogy, altruistic endeavor and communicative confidence.

In this work my warmest gratitude goes to my CEA advisor Jean-Luc Duchateau who was always smiling and focused in teaching and guiding my work step by step. For his in-depth criticism and advice on my research I have the pleasure to thank my Ph.D. director Lounès Tadrist.

I am particularly grateful in experimental aspects of my thesis to H. Cloez, J-P. Serriès and P. Decool. A special mention goes to D. Ciazyński for his fantabulous criticism, leading me to adopt stringent scientific methods. This work would not have been successful without the contribution of M. Boehler, L. Bottura, P. Bruzzone, N. Commaux, D. Henry, J-Y. Journeaux, B. Lacroix, C. Le Niliot, P. Libeyre, A. Martinez, S. Nicollet, B. Rousset, B. Stepanov, M. Tena, F. Topin and B. Turck.

For their help and support: J. Alduini, N. Abid, N. Arnavielhe, D. Balaguer, M-C. Bertrand, J-P. Bonnet, H. Bottolier, P. Boubert, M-C. Brieu, Y. Corre, N. Dolgetta, J. Duplat, N. Ehret, S. Girard, B. Glas, I. Graour, D. Gravier, C. Grisolia, L. Larchevèque, C-A. Lebailly, M. Leboisne, P. Lepargneux, J-L. Maréchal, R. Martin, M. Nicolas, C. Itan, A. Pillon, P. Prochet, J. Pullino, P. Reynaud, F. Rigollet, S. Sanchez, C. Sierra, H. Slavik, N. Snacel, N. Thomas, D. Van Houtte, J-V. Vidal, L. Zani, and to many more people from GCRY, STEP, DRFC, IUSTI and Polytech' Marseille.

For their cheering support, my (choir) friends from Antequiem, Choeur Grégorien, Choeur ND de Joie, Choeur St Ephrem, ECP, Gaudete, Laudate Pueri, Offrandes Musicales, Pénitents gris, ICRSP Port-Marly, St Eugène-Ste Cécile.

This thesis was supported by CEA\INSTN. Experimental campaigns were funded by CEA/DSM/DRFC/STEP, CRPP/SULTAN, EFDA tasks M50 and CODES.

“Professeur agrégé” in Civil Engineering, option technical and energetical equipments, Bertrand Renard is an alumni of Ecole Normale Supérieure de Cachan and holds a Master of Science from the Massachusetts Institute of Technology.

Table of content

| | |
|--|-----------|
| Abstract | 3 |
| Résumé | 3 |
| Kurzfassung..... | 4 |
| Acknowledgements | 5 |
| Table of content..... | 6 |
| Introduction on thermonuclear fusion and tokamaks | 9 |
| 1 Dual channel Cable-In-Conduit Conductor | 13 |
| 1.1 Conductors for fusion..... | 13 |
| 1.1.1 Superconductivity..... | 13 |
| 1.1.2 Superconducting strands | 15 |
| 1.1.3 Superconducting conductors | 16 |
| 1.2 Cooling systems | 18 |
| 1.2.1 Heat loads and shields | 18 |
| 1.2.2 Forced flow cooling loop and refrigerator | 20 |
| 1.3 Dual Channel Cable-In-Conduit Conductors | 22 |
| 1.3.1 Dual channel concept | 22 |
| 1.3.2 Pressure drop reduction | 24 |
| 1.3.3 Thermal imbalance | 25 |
| 2 Pressure drop | 27 |
| 2.1 Bundle region pressure drop | 27 |
| 2.1.1 Existing models | 27 |
| 2.1.2 Katheder model limits and uncertainty | 28 |
| 2.1.3 Bundle pressure drop model improvement | 31 |
| 2.2 Experimental spiral friction in nitrogen | 33 |
| 2.2.1 Experimental campaign..... | 33 |
| 2.2.2 Compressibility | 35 |
| 2.2.3 Results and precision | 39 |
| 2.3 Experimental spiral friction in water [Ren06-3] | 41 |
| 2.3.1 Experimental campaign..... | 41 |
| 2.3.2 Results | 42 |
| 2.3.3 Precision | 43 |
| 2.4 Friction factor model | 45 |
| 2.4.1 Parameters driving turbulence..... | 45 |
| 2.4.2 Elaboration of the model | 52 |
| 2.4.3 Application | 55 |

| | |
|--|------------|
| 3 Interchannel heat exchange..... | 57 |
| 3.1 Steady state analysis [Ren06-1] | 57 |
| 3.1.1 Principle and hypothesis..... | 57 |
| 3.1.2 Heat equation solution..... | 58 |
| 3.1.3 Applications | 60 |
| 3.2 Assessment of the heat transfer coefficient in steady state | 61 |
| 3.2.1 Preliminary comments on experimental set-up | 61 |
| 3.2.2 Measure of the heat transfer coefficient in water | 64 |
| 3.2.3 Measure of the heat transfer coefficient H in cryogenic helium | 69 |
| 3.3 Transient analysis [Ren06-2] | 74 |
| 3.3.1 Principle and hypothesis..... | 74 |
| 3.3.2 Heat equation solution..... | 75 |
| 3.3.3 Application: Transition time τ | 76 |
| 3.4 Assessment of the heat transfer coefficient H in transient | 78 |
| 3.4.1 Transient experimental campaigns..... | 78 |
| 3.4.2 Water transient applicability | 79 |
| 3.4.3 Helium transient application | 80 |
| 3.5 Heat transfer model | 83 |
| 3.5.1 Unhomogeneous thermal resistances | 83 |
| 3.5.2 Convection coefficients..... | 85 |
| 4 Central channel spiral improvement..... | 89 |
| 4.1 Danger of thermosiphon..... | 89 |
| 4.1.1 The thermosiphon principle..... | 90 |
| 4.1.2 Evaluation of the risk | 92 |
| 4.1.3 Thermosiphon risk in ITER coils | 94 |
| 4.2 Design sensitivity to friction and heat transfer..... | 95 |
| 4.2.1 Friction sensitivity to spiral design | 96 |
| 4.2.2 Interchannel heat exchange sensitivity to spiral design | 98 |
| 4.2.3 Wrappings | 99 |
| 4.2.4 Central channel diameter and thickness | 101 |
| 4.3 Optimal central channel proposal..... | 102 |
| 4.3.1 Spiral improvement criteria..... | 102 |
| 4.3.2 Proposal of spiral design | 103 |
| 4.4 Other issues and alternative CICC design..... | 104 |
| 4.4.1 Strands compression..... | 104 |
| 4.4.2 Future investigations to optimise CICC thermohydraulics | 106 |
| Conclusions | 107 |
| Résumé détaillé :..... | 109 |
| 1. Conducteurs de type Câble-en-conduit à double canal | 110 |
| 2. Pertes de pression | 115 |
| 3. Echange thermique | 120 |
| 4. Dimensionnement de la spirale centrale..... | 129 |
| Appendix I: Test facility OTHELLO | 134 |
| Appendix II: Pressure drop measurements..... | 135 |
| Appendix III: Test facility HECOL | 140 |
| Appendix IV: Test facility SULTAN | 143 |
| Appendix V: Stationary thermal resolution | 146 |
| Appendix VI: Transient thermal resolution | 151 |
| Nomenclature and abbreviations | 154 |
| Bibliography | 157 |

Introduction on thermonuclear fusion and tokamaks

Since the industrial revolution in the XIXth century, the world population and the energy demand keep increasing. Today, the most important part of the power consumption comes from oil (~ 36%) but the world resources are limited and oil reserves exhaustion is predicted. Controlled fusion arises today as a solution which could supplant disappearing fossil energies (oil, coal). Research on fusion undertaken since nearly 50 years have led to the construction of large instruments intended to produce reactions of fusion, through the magnetic confinement of hot plasmas.

Since 1988, the Research Department of Controlled Fusion (or DRFC) ensures the operation of a Tokamak (Tore Supra) for scientific research. For this type of machine, the confinement of plasma is ensured by a magnetic field created by coils. Their design with coils using superconductivity reduces considerably the heat losses thus lowering the operating costs of the reactor.

Research on controlled fusion is presently dominated by the next establishment of the International Thermonuclear Experimental Reactor (ITER) in Cadarache. To design and build this machine, very specific research actions are carried out by CEA in DRFC. One of the major topics investigated for several years is related to the design of superconductor cables constituting the magnetic system of ITER.

Thermonuclear fusion

Two types of nuclear reactions make it possible to produce energy on a large scale:

- Fission, which consists in breaking a heavy nucleus by bombarding it with particles. A breaking nucleus produces energy and particles, which in turn travel and break other heavy nuclei, in a chain reaction. The atomic fission of uranium is used in the nuclear power plants.
- Fusion, which consists in combining two light nuclei to form a larger one and to release energy.

To fuse, the nuclei must overcome their natural repulsion. This is possible when the matter is brought up to very high temperatures (several tens of million degrees). The atoms are then separated in fundamental components: electrons and nuclei. They form a hot gas called plasma.

Although any random pair of light nuclei can fuse, the most accessible reaction is between deuterium and tritium (isotopes of hydrogen). Deuterium is very abundant and inexpensive. However tritium does not exist in nature. It is a strongly radioactive gas which can be produced from lithium.

To confine a plasma and obtain the level of density necessary to the reaction, either a magnetic or an inertial confinement is used.

Magnetic confinement

Plasma is confined in an immaterial box with a torus shape (Tokamak, Stellarator), created by magnetic fields. The density is low (10^{-5} times that of the air) but the plasma confinement time is “high” (a few seconds).

Tokamaks

Several types of magnetic boxes exist; the most powerful is called Tokamak, and was invented by the Russians in the fifties. It is the most studied and promising research path for fusion. In a tokamak, the confinement of the plasma is based on the property of charged particles to describe a helical trajectory around a line of magnetic field.

To trap the particle, the field line is closed on itself. The particle radius of gyration (Larmor radius) depends on the magnetic field intensity, on the mass and electric charge of the particle, and on its energy. The more powerful the magnetic field, the smaller the Larmor radius, the particle remaining in the vicinity of the field line. Electrons, much lighter than ions, have a smaller Larmor radius for the same energy. High energy particles have a larger Larmor radius than lower energy particles, and are thus more difficult to confine. The Larmor radius typically ranges from a few millimetres to a few centimetres.

In this basic configuration, the direction of the magnetic field is purely toroidal. Unfortunately, on a simple circular trajectory of this type, the particle undergoes a slow transverse drift, caused by the gradient of magnetic field and the centrifugal force, and whose direction depends on the electric charge sign. For example, ions will derive upwards (Figure 0-1).

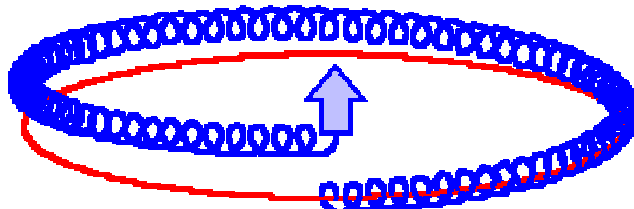


Figure 0-1: Ion drift in a tokamak, related to the magnetic field

To compensate for this undesirable effect, the configuration is stabilized by adding a poloidal component to the toroidal field. It is the magnetic configuration used in the tokamaks. The field lines become helices rolled up around torus surfaces encased in each other, called magnetic surfaces (Figure 0-2).

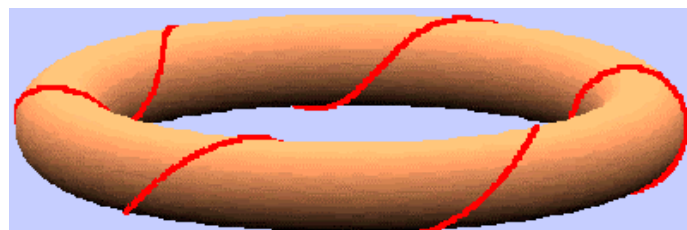


Figure 0-2: Trajectory resulting from the toroidal and poloidal magnetic field components

The particle passes half of its time “head up”, and the other half “head down” (Figure). The effect of the drift is compensated on average and particles remain confined close to their magnetic surface with a helicoid trajectory around the lines of already helical field.

In tokamaks, the toroidal magnetic field is generated by external coils, while the poloidal magnetic field is induced by a current circulating in the plasma. The plasma current is itself generated as the secondary of a transformer.

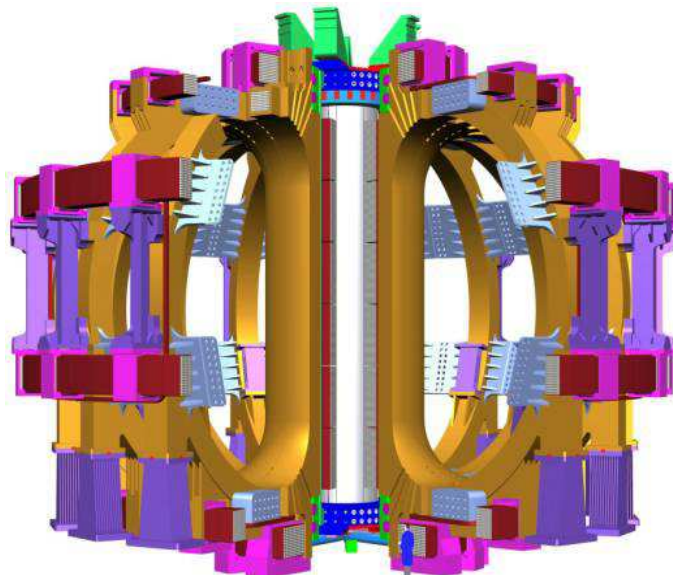


Figure 0-3: ITER magnetic configuration for plasma confinement (courtesy of ITER)

The ITER project

Thanks to remarkable results obtained these last years, the international research and engineering community is ready for further studies on magnetic controlled fusion. The next step is to demonstrate maintained combustion of a deuterium-tritium plasma over long times. It is the principal objective of the tokamak ITER, the next reactor to be built and operated in the framework of a world collaboration joining together countries which have been taking part for years in the fusion research program.

ITER (Figure 0-3) will be a superconducting tokamak of the largest size ever built. Tore Supra, a CEA superconducting tokamak has demonstrated on the long run since 1988, that superconductivity was not a technological obstacle for fusion. This technology gives access to long duration plasma discharges.

The principal objective of ITER is the study of plasmas in combustion, i.e. of plasmas where the proportion of self heating from fusion reactions exceeds 60%. The proportion of nuclear heating hardly ever reached 10% in the best discharges carried out in JET (Joint European Torus).

ITER will be the first machine integrating the majority of technologies necessary to the preparation of a sustainable fusion reactor: superconductivity, plasma-facing components, tritium layers, robotics and diagnostics (Figure 0-4).

ITER is a technological challenge in all fields, and particularly in the field of superconductivity. Its characteristics are rather impressive and prove the ambition of the project.

The major radius of the plasma will be 6.2 m and the minor radius of the plasma is 2 m. Confinement will be ensured by a toroidal field of 5.3 teslas, a plasma current of 15 MA. The current of the Toroidal Field (TF) system is 80 kA. Superconducting magnets and cryogenic facilities represent over a third of the construction investment cost of the machine.

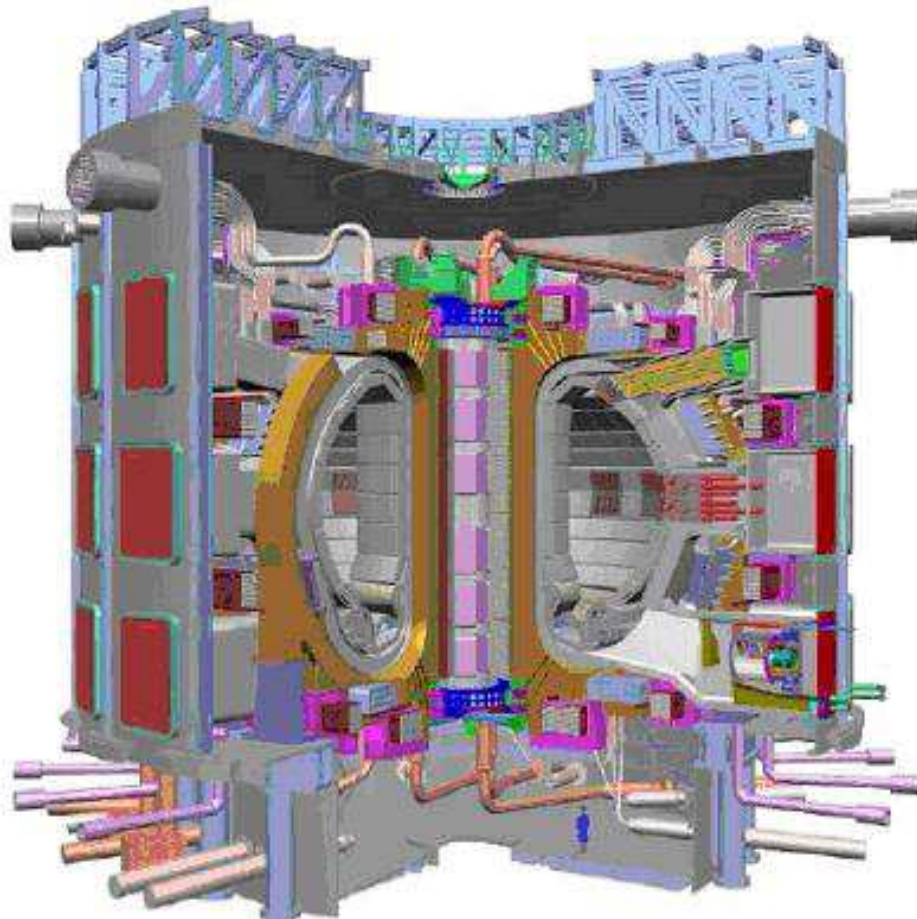


Figure 0-4: Diagram cut of ITER, with a man in blue at bottom, represented for scale
(courtesy of ITER)

Coils superconducting conductors require cryogenic cooling. The International Thermonuclear Experimental Reactor (ITER) project has triggered considerable work in the technologies of superconductor cryogenics, in the magnets themselves and in their supercritical helium supply networks. These conductor development programs are a source of input for a better understanding of CICC, applicable to any large magnet with high field (>5 T).

The aim of this thesis is to study and improve the thermohydraulic behaviour of the supercritical helium flow in the dual channel superconducting cable-in-conduit conductors constituting ITER coils.

1 Dual channel Cable-In-Conduit Conductor

1.1 Conductors for fusion

Since 15 years an important activity has been initiated in Cable-In-Conduit-Conductors (CICC). This activity is mainly related to fusion. In this domain, the sizes of the machines push to high current conductors, and high voltages during protection phases when the magnet must be rapidly deenergised [Weg02, Duc02].

The design of high current and high field conductors for fusion application has evolved to the present solution consisting in CICCs characterised by a steel jacket, an external electrical insulation, and forced flow cryogenic cooling.

The need of thermohydraulic design and optimisation of dual channel CICC has led to the construction of numerous full size cable samples, joint samples and prototypes called model coils. In the framework of the ITER preparation, a Poloidal Field Insert Coil is programmed for testing in Naka (Japan).

1.1.1 Superconductivity

History

In 1911, H. Kammmerling Onnes, which had successfully liquefied helium three years earlier, observed with G. Holst that the electrical resistance of mercury is null at very low temperature. This behaviour is contradictory with the Joule effect. Indeed when current circulates in a conducting material, losses cause heating of this conductor. These losses are proportional to the material resistance and to the square of the current. They become very important for high currents and thus large magnets.

In the case of superconductors, and even if it is impossible to assert that it is strictly null, resistivity becomes very weak (below $10^{-25} \Omega\text{m}$). This behaviour is the demonstration of a quantum effect. The resistivity being negligible, the losses by Joule effect are extremely weak. However these remarkable properties appear only for relatively low temperatures. The principal materials industrially available, like niobium-titanium and niobium-tin, must be cooled by liquid helium to 4.2 K to become superconducting.

Among superconductors, a singular class of materials was discovered in 1986 and is called “high critical temperature superconductors”. It gave birth to many hopes for a wider application of superconductivity. The weak current transport properties and extreme complexity and brittleness of these materials are still handicapping factors for short-term applications.

Critical parameters

- Critical field B_c

There is a critical magnetic field B_c above which the material is not superconducting.

- Critical temperature T_c

There is a critical temperature T_c above which the material loses the property of superconductivity. This temperature is very low, near the absolute zero. It is lower than 23 K for conventional materials and around 100 K for high critical temperature superconductors.

- Critical current density J_c

The current density circulating in a superconducting material has a defined value which is the critical current density J_c . J_c is a function of the field, of the temperature, and for some materials of the strain.

- Mechanical constraint

For some material, the critical parameters (B_c , T_c , J_c) are sensitive to the mechanical deformations (traction/compression). Mechanical constraints are not seen as a limit, but as a possible degradation of superconducting conductors performance.

Two types of superconductivity exist: type I and type II. Practically, only type II superconductors are used to produce magnetic fields in coils [Wilson]. A characteristic curve of type II superconductor can be well approximated in terms of electric field (E) and of current density (J) by:

$$E = E_c \left(\frac{J}{J_c} \right)^n \quad (1.1-1)$$

E_c et J_c are respectively the critical electric field and the current density. E_c is equal to 10^{-5} /m by convention.

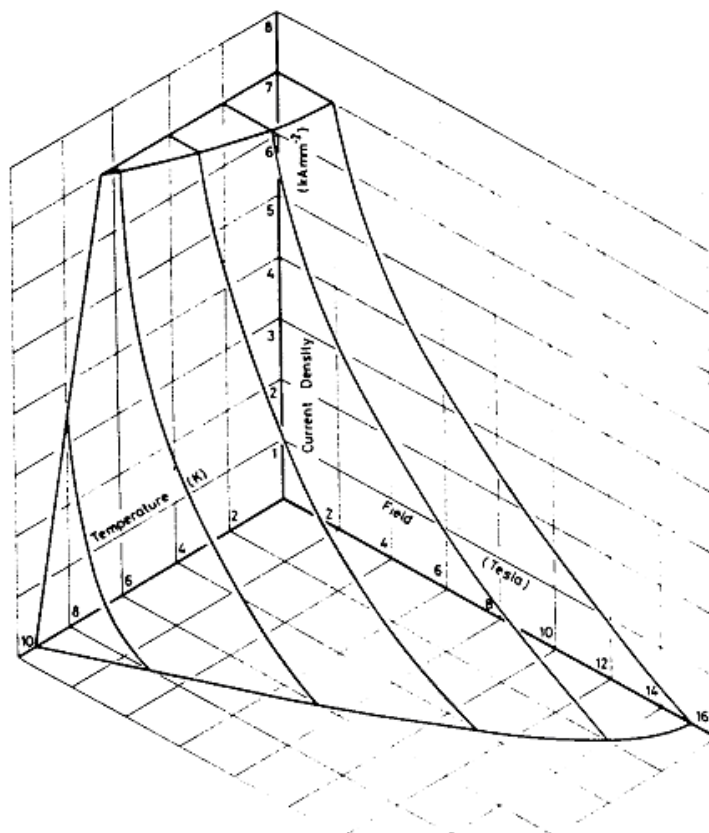


Figure 1-1: Niobium-Titanium critical surface
superconducting state under the surface $J_c = f(T, B)$

Critical surface

Critical field B_c , critical temperature T_c and critical current density J_c are thus the three parameters which limit the transport of current by superconductivity. These values are connected and define a critical surface (Figure 1-1) in the space (B , T , J). If one of these three parameters is exceeded, the material loses its superconducting state. It is therefore very important to control temperature through cryogenic cooling [Tix95].

1.1.2 Superconducting strands

Superconductors and strands: The materials most largely used for the manufacture of magnets are alloys containing niobium. Two main families exist:

- Alloys containing niobium and titanium
- Alloys containing niobium and tin

Niobium-titanium alloys

Niobium-titanium (NbTi) today is the most used and the least expensive among the superconducting materials. This material can be used for producing magnetic fields up to 11 T at 1.8 K. One of its greatest advantage is ductility. Niobium-titanium can thus be drawn into strands, twisted and cabled without degradation of the critical current due to mechanical constraints. Moreover, niobium-titanium strands do not require an elaborate heat treatment. A copper crown is always placed around the niobium-titanium strands.

The role of copper is to limit the heating in the event of a loss of superconductivity. In this case, the resistivity of the superconductor becomes very large and the current can temporarily redistribute into copper. It is also used to improve the thermal stability of the system thanks to a better thermal coupling of the superconducting strand heart with the coolant.

The magnets of TORE SUPRA use niobium-titanium cooled at 1.8 K. However for an operating temperature equal or higher to 4.2 K, the maximum field accepted with a sufficient safety margin cannot exceed 6 T [Lib05-1]. This is why this material is bound in ITER to the low field coils in the Poloidal Field (PF) system.

Niobium-tin alloys

Niobium-tin (Nb₃Sn) presents a critical field B_c higher than that of niobium-titanium: about 23 T at 4.2 K for pure niobium-tin and about 29 T for niobium-tin with titanium and tantalum additions.

This superconductor is fragile and a mechanical tension of more than 0.5% can irreversibly damage the strands. Strands manufacture (wire drawing, twisting, cabling and winding) must be carried out in strands in which the phase niobium-tin is not yet formed. A heat treatment is then carried out, the purpose of which is to carry out the diffusion of tin allowing the formation of the final superconducting compound. Heat treatment at temperatures of about 650°C lasts approximately three weeks, independently of the object size and mass.

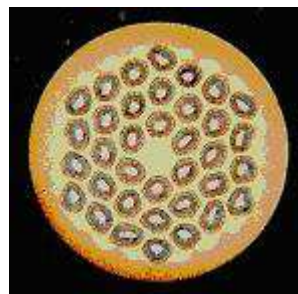


Figure 1-2: Section of an internal tin niobium-tin strand produced by Europa Metalli
(courtesy of Europa Metalli)

Two main different methods to manufacture these alloys are available. The first is known as “bronze method”. The elementary strand is composed of microscopic niobium filaments inserted in a bronze matrix. Tin confined in bronze diffuses in niobium during heat treatment. The second method is called “internal tin”. Niobium filaments are gathered in crown around a tin heart (Figure 1-2). The superconductor is produced during heat treatment.

This type of superconductor will be used for the high field coils of ITER (12-13 T). These coils are the toroidal field coils (TF) and the central solenoid (CS).

Copper is present for electrical and thermal stability in superconducting strands, but additional copper strands can be added to ensure protection in the event of transition to the normal state.

1.1.3 Superconducting conductors

Conductors used in fusion magnets

The Cable-In-Conduit-Conductors (CICC) of the project ITER are circular cables made up of a great number of superconducting strands ($\varnothing \sim 0.81$ mm) twisted in successive stages. The strands are drawn inside a jacket in which the supercritical helium coolant circulates [Tur93]. These cables have the following advantages:

- high transport current up to 70 kA
- circular symmetry favourable to even current distribution
- efficient local strands cooling by the helium circulation
- low magnetic losses in variable magnetic field
- easy external electric insulation (similar to that of a warm conductor)
- easy manufacture of the conductor by cable drawing through the stainless steel jacket

Forced flow conductors are well adapted to large fusion magnets. Indeed, their built-in steel jacket insulation installed around the conductor itself is better adapted to high voltage operations than the conventional bath cooled conductors [Rou97], more sensitive to short circuits [Lib05-1]. In addition, in operation these magnets are subject to heat deposition of different kinds which can be better removed by helium circulation. However, practically no magnets with use of CICC design is yet in operation today except the NbTi magnet of the Poloidal Field (PF) system of the LHD Torsatron in Japan [Sat00].

Nonetheless, the first plasmas of several machines equipped with magnets systems of this kind are shortly scheduled: SST1(India) and EAST (China) in 2005, KSTAR (Korea) in 2007, W7-X (Germany) in 2010, whose conductor cross-section is presented in Figure 1-3.

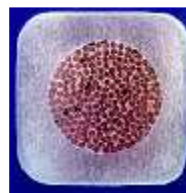


Figure 1-3: CICC cross-section of stellarator W7-X (courtesy of CEA/DAPNIA)

The trajectories followed by strands are helices rolled up around each other. The shape of the helical trajectories is controlled by two principal parameters: the twisting length L and the rolling radius R . There is a twisting length and rolling radius at each stage.

The structure of a cable in conduit can thus be described using the following parameters [Duc02, Bes98]:

- stages
- twisting length
- cable and strands diameters

Stages

The different levels of cable manufacture are called stages (see Figure 1-4). The first stage is obtained by twisting a defined number of strands. The second stage is obtained by twisting a defined number of units of the first stage and so on. For example, for a cable-in-conduit of the type [3 3 5 4 6], the first stage is made of three twisted strands: a triplet.

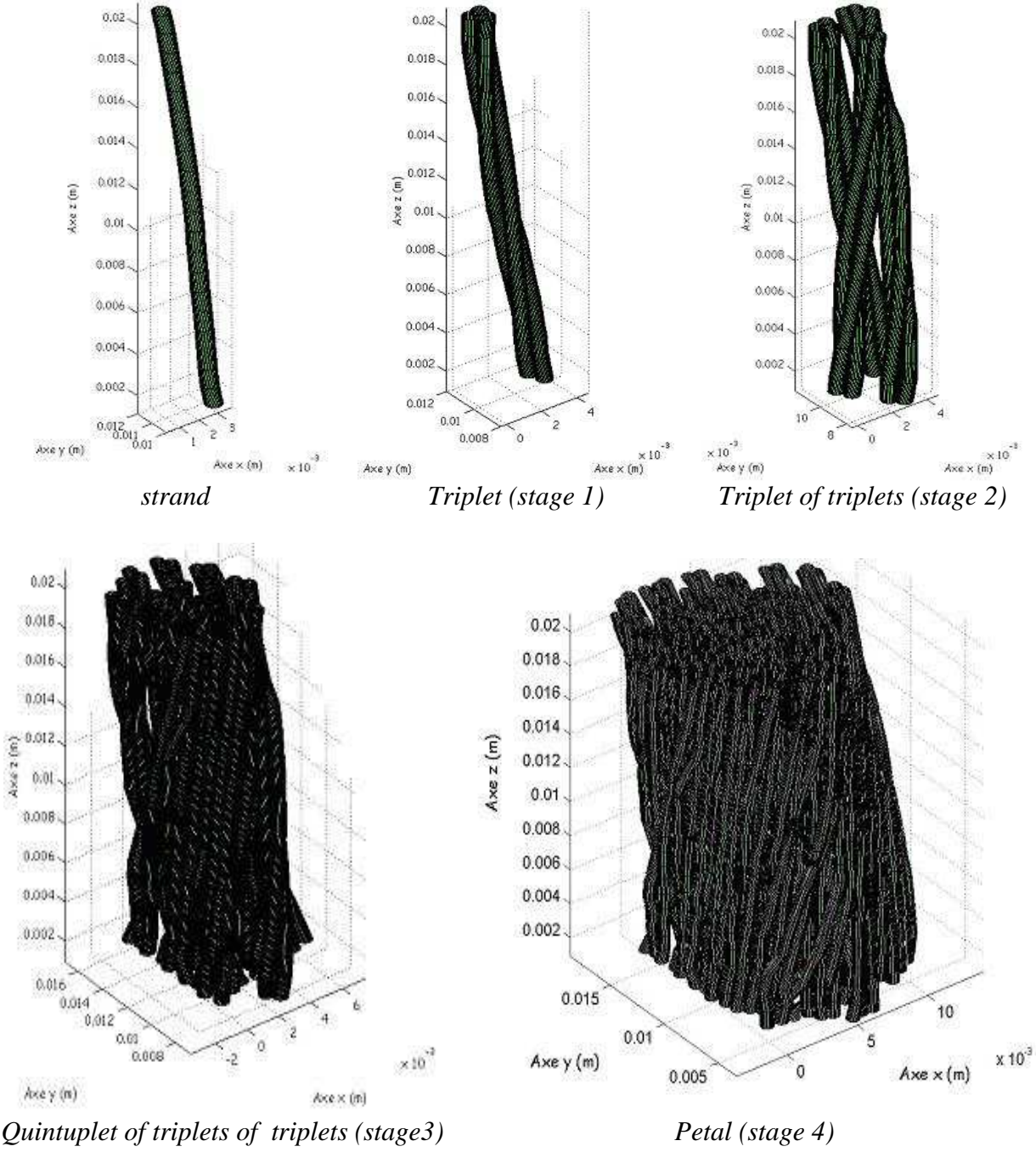


Figure 1-4: Manufacture of the different conductor stages of a superconducting petal

The second stage consists in the twisting of three triplets. The third stage is obtained by twisting five triplets of triplets. The last but one stage is called petal. It is insulated and protected by a stainless ribbon called wrapping.

1.2 Cooling systems

Because superconductors are sensitive to temperature [Zani04], the heat load falling on the magnets must be carefully evaluated in order to propose an effective cooling system.

1.2.1 Heat loads and shields

Heat load P_{hl} to the magnet system at 4.5 K

When the superconducting magnet system is at low temperature, heat coming from different sources is deposited. We will not enter into details about the different sources but classically one can identify in a fusion tokamak TF system (ITER):

- ac and eddy current losses in the winding, cases, and structures of the system (7.29 kW on average)
- heat loads due to current leads (~ 1 kW)
- residual nuclear heating escaping through the neutron shielding
- resistive joint losses in the magnets and static losses due to thermal radiation from thermal shields and thermal conduction through gravity supports and connections (11.9 kW)

The two first categories of heat sources are located in the metallic parts of the CICC (Figure 1-5). Nuclear radiation falls in all metallic volumes, preferentially on the row of conductors closest to the plasma. Static losses fall on the periphery of the magnet and can be partially removed by a helium circulation outside the magnetic system. These heat sources cannot be deflated: they constitute the imposed working conditions from the cryogenic viewpoint.

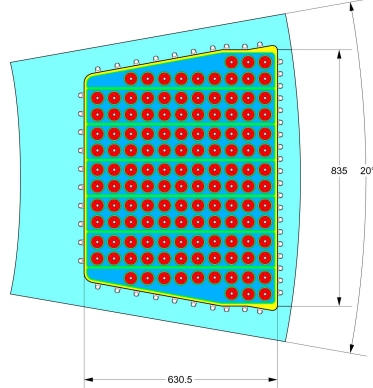


Figure 1-5: Cut of a TF coil inner leg; conductors are dark rings; thermal and neutronic shields are on the right, facing the plasma; the keystone shape allows to lean on other coils.

Mitigation of AC losses

0.055 mm thick stainless steel tape wrappings around the petals are meant to reduce the intensity of the eddy currents created by the AC field, and the generated heat. The Poloidal Field Insert Sample (PFIS) presented in upcoming section 1.3 is made of two asymmetric conductor legs, where the superconducting strand petals are wrapped in stainless steel with 80% coverage in the left leg, whereas on the right leg the subcable petals have been stripped of their wrappings before insertion in the jacket, itself compressed to reach a similar void fraction [Hur05]. The purpose of this asymmetry of the sample wrappings is to evaluate current recirculation minimization within the cable, and the thermohydraulic influence of wrappings.

Shielding of the neutronic radiation

In ITER the plasma neutronic fusion power (~500 MW) is shielded by shielding modules and the vacuum vessel, cooled by pressurised water, presented in Figure 1-6. Thus only the residual neutronic power reaches the TF coil system which surrounds the vacuum vessel (~10 kW instantaneous and 3 kW in average for a 500 s plasma discharge every 1800 s).

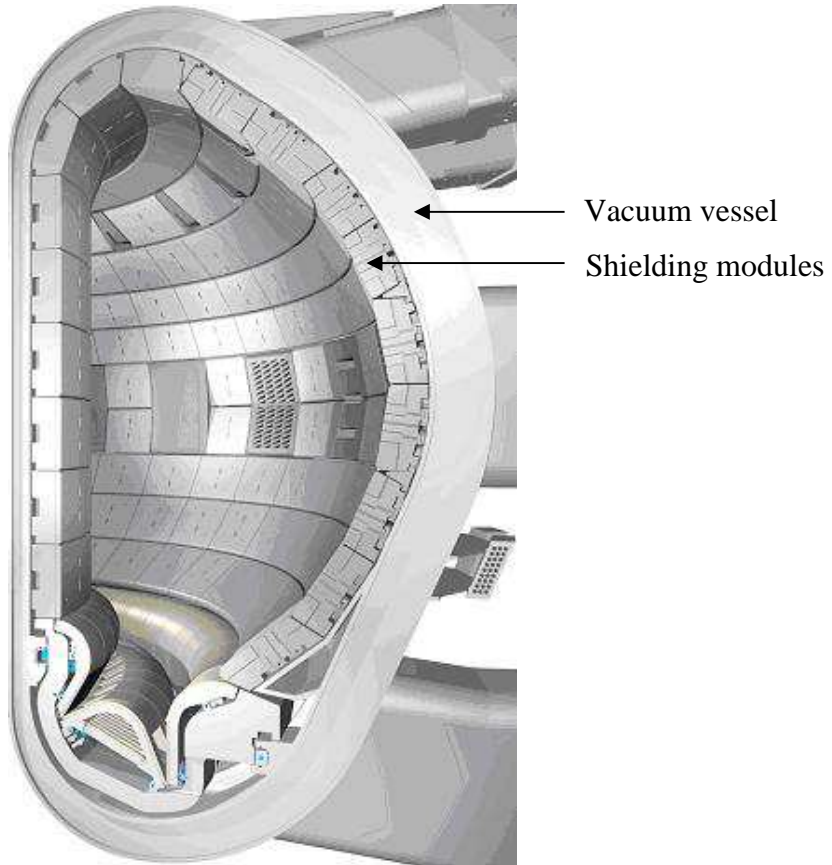


Figure 1-6: Cut view of the shields: plasma in the center; actively cooled plasma facing components and divertor (bottom); inside the vacuum vessel; coils outside (courtesy of ITER)

Thermal shield system

A complex system of thermal shields prevents heat radiation coming from the cryostat (upper CTS cylinder, central CTS etc.) and from the vacuum vessel (VVTS) from falling on the coils at 5 K (Figure 1-7). These thermal shields are cooled at 80 K. Heat radiation from 80 K to 5 K is evacuated by the circulating helium loop.

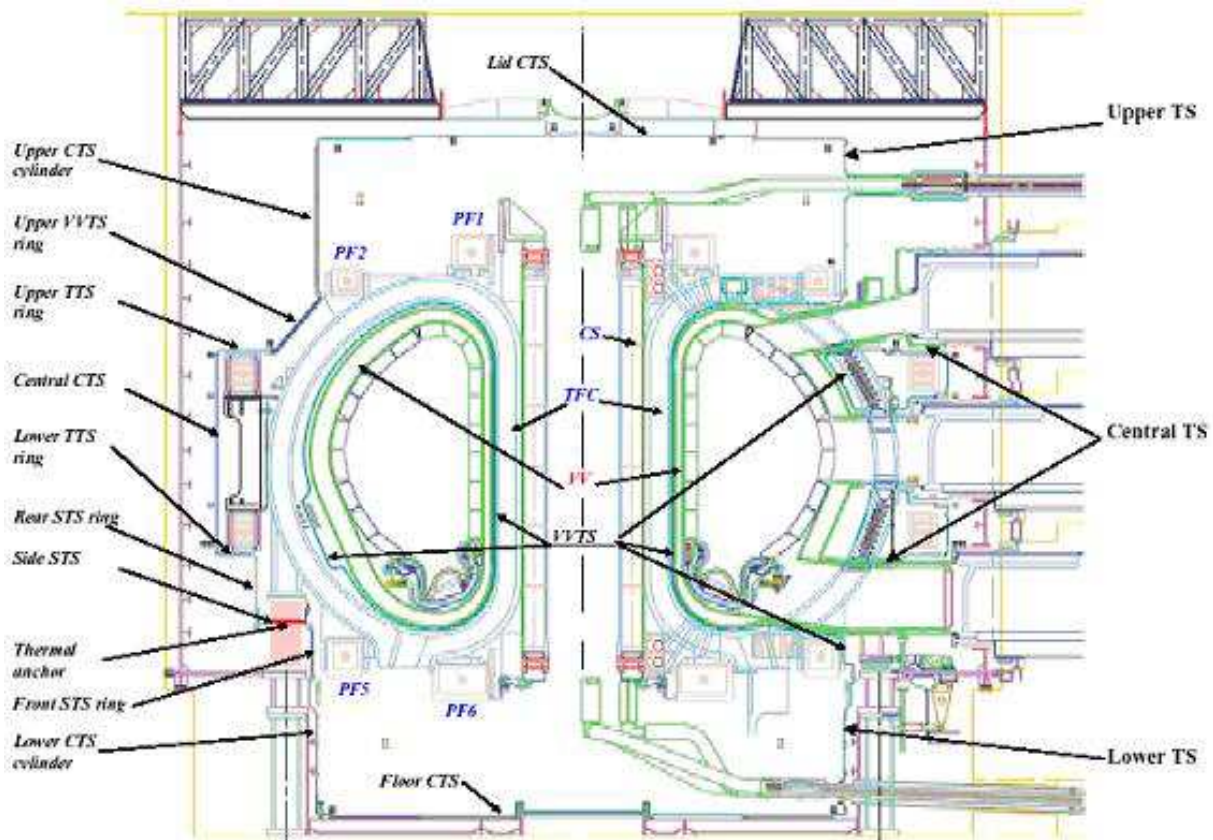


Figure 1-7: Thermal shields (TS) and coils position (TF, PF and CS) in ITER elevation view (courtesy of ITER)

1.2.2 Forced flow cooling loop and refrigerator

The heat load from all sources P_{hl} is removed from the coils to keep the temperature constant by circulating a mass flow through the conductor. This circulation requires a pump work to compensate the viscous pressure losses, and associated cryogenic power P_{circ} (11.4 kW). The electrical power associated with this cryogenic power is high: about 2.9 MW for the entire cryogenic circulation system of ITER (TF, PF and CS).

The aim of the thesis is to optimise the Cable-In-Conduit to reduce this power without affecting the superconducting strands temperature.

$$P_{circ} = \frac{m \cdot \Delta P_{circ}}{\rho \cdot \eta_{circ}} \quad (1.2-1)$$

m / ρ being the volumetric flow circulated in the conductors and ΔP_{circ} the pressure variation forced by the helium circulating pumps, affected by the efficiency η_{circ} .

The two main sources of heat loads on the 4.5 K refrigeration cold system are P_{hl} and P_{circ} , itself a direct function of P_{hl} because the mass flow rate m is chosen in proportion to the power to be removed, to keep superconductor temperature margins constant. P_{circ} is also related to the design of the magnet conductor and associated pressure drop characteristics (see Figure 1-8).

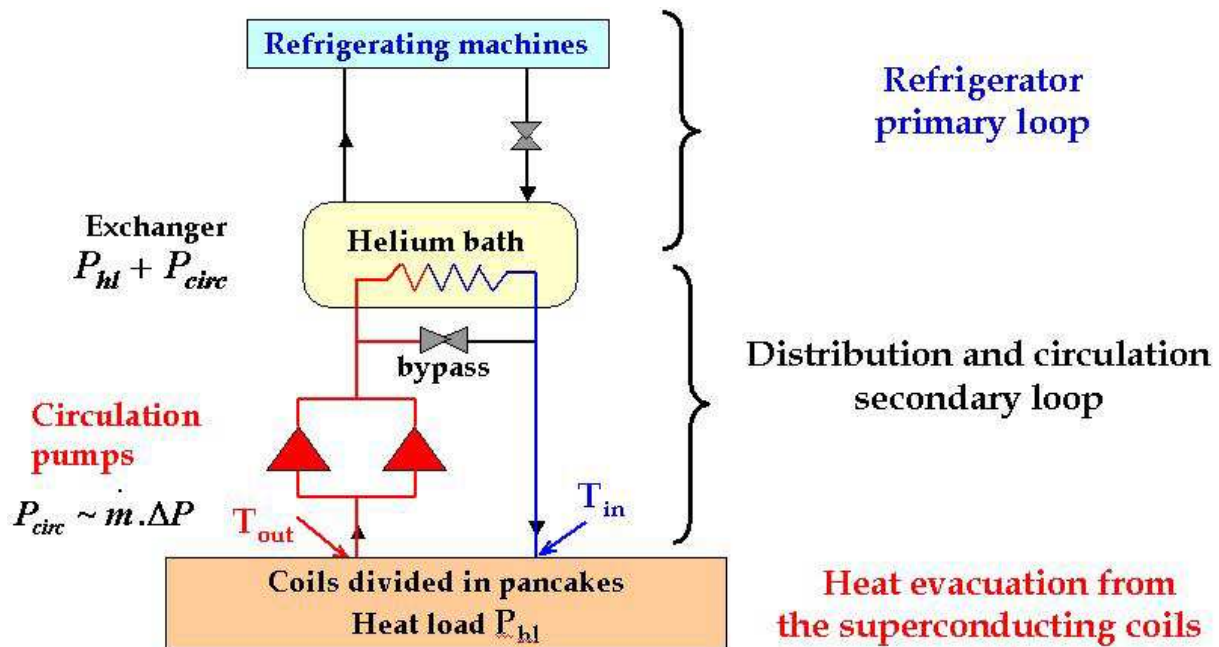


Figure 1-8: Cryogenic loops and circulation pressure drop in ITER expected design

A minimal mass flow rate is defined for each operation scenario to safely and actively evacuate heat load in the secondary loop. During plasma operation, the level of heat losses in the multi-strands ITER TF cable (1000-1500 strands) imposes a minimal mass flow of $8 \times 10^{-3} \text{ kg.s}^{-1}$ to safely remove the energy at the nominal temperature of 4.7 K and with a pressure drop of 0.06 to 0.1 MPa [ITER05].

Coils are divided into double-pancakes with conductors of ~ 700 m, the unit length of the conductor. To minimise the length of the channel used by the coolant, helium inlets are placed through the jacket, in the middle of the pancake conductor length. Helium flows in opposite directions from the middle to the electric joints at each end. The ITER TF system is constituted of 18 coils each made of 14 pancakes 380 m long.

The ideal place for the inlet of each pancake is in fact the hydraulic –not geometric– center of the conductor. This ideal positioning of helium inlets would require a hydraulic qualification of each pancake in both flow direction before the inlets are manufactured, in order to check that pressure drop is symmetrical, and to correct it if necessary.

Hydraulic acceptance tests performed on W7-X conductors unit lengths show discrepancies of up to $\pm 20\%$ in mass flow rate, with a normalised room temperature helium inlet pressure of 2 MPa and an outlet pressure of 0.1 MPa. It is likely that ITER pancakes will also have hydraulic resistance differences. It is expected that these hydraulic resistance differences could be lower than in W7-X due to the presence of a central channel (section 1.3).

For each helium distribution satellite, the most resistive pancake imposes the helium distribution pressure, to obtain the minimum nominal mass flow rate m_{min} . From this fixed pumping pressure, the various pancakes may have various mass flow rates $\geq m_{min}$. The pump work P_{circ} is proportional to total mass flow rate cumulating that of each pancake $m = \sum_{i=1}^n m_i \geq n \times m_{min}$. It is therefore mandatory to reduce excessive mass flow rates in the more favourable pancakes, using adjustable valves.

1.3 Dual Channel Cable-In-Conduit Conductors

In order to reduce conductor friction pressure drop, the strands are twisted around a spiral delimiting a low impedance central channel. The dual channel cable-in-conduit conductor (CICC) originally developed at CEA for high current superconducting magnets [Bes92] has now been selected for the International Thermonuclear Experimental Reactor (ITER) coils. The main advantage of this conductor is to provide a low hydraulic resistance as well as a temperature rise limitation [Duc02]. The low impedance central channel consisting of a stainless steel spiral pipe has a premium role in the distribution of mass flows and in the global pressure drop.

1.3.1 Dual channel concept

In certain cases, when the size of the system is very large, there is interest to use a special sort of cable in conduit: the so-called dual channel CICC, to minimize pressure drop and the associated cold power related to helium circulation. In this type of conductor, two channels are offered to helium transit: a central channel and the bundle region where strands are situated (see Figure 1-9). Two parallel hydraulic channels minimize the pressure drop for the necessary helium flow. Indeed a pressure drop at low temperature is highly expensive in terms of the cryogenic power consumed to recover the helium enthalpy change introduced by the loop circulating pumps. Heat loads are efficiently removed with a moderate pressure drop thanks to the central channel, which serves as an internal heat exchanger inside the conductor.

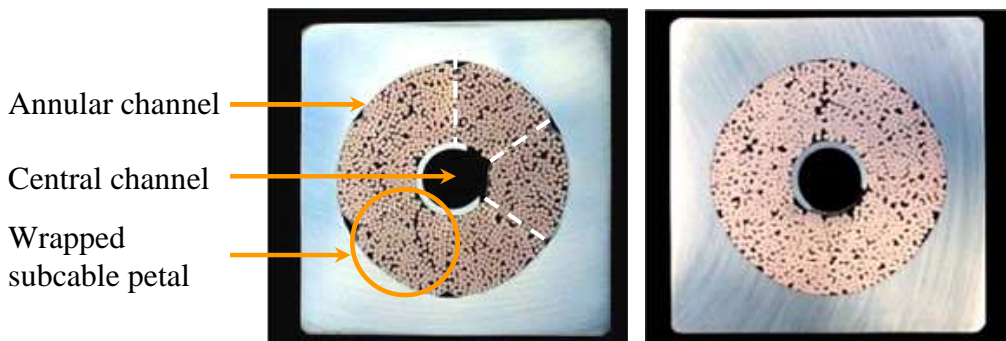


Figure 1-9: Cross-section of ITER Poloidal Field Insert Sample CICC with wrappings (W) left leg (L) and without wrappings (NW) right leg (R)

The design choices for this central channel have an important impact on the hydraulics, pressure drop and flow repartition, consequently influencing economical aspects of the project. Optimisation of forced flow conductor cooling [Raf03, Tad04] is best illustrated in the International Thermonuclear Experimental Reactor project (ITER). Experience about CICC electric and thermohydraulic behaviour has been accumulated but mainly in the tests of numerous prototypes called model coils. The conductor cross-sections of ITER PF insert samples are presented in Figure 1-9.



Figure 1-10: Burst representation of a cable in conduit with its six petals

The central channel is materialised by a spiral to maintain its diameter and guarantee that strands from the petals –even if cut– do not choke up the free-flow channel. The central spiral has a mechanical role when the conductor is under magnetic pressure forces.

Twisting the strands in six petals (Figure 1-10) around a low impedance central channel delimited by a loose spiral adds complexity to the geometry of strands and current redistribution in the conductor. Figure 1-11 illustrates the complexity of strands trajectories in a petal. The determination of these trajectories, associated to a local magnetic field calculation, makes it possible to evaluate in a realistic way the variation of the local electric field along the conductor. It is however not thoughtful to envision calculating the hydraulic resistance from detailed strands trajectories.

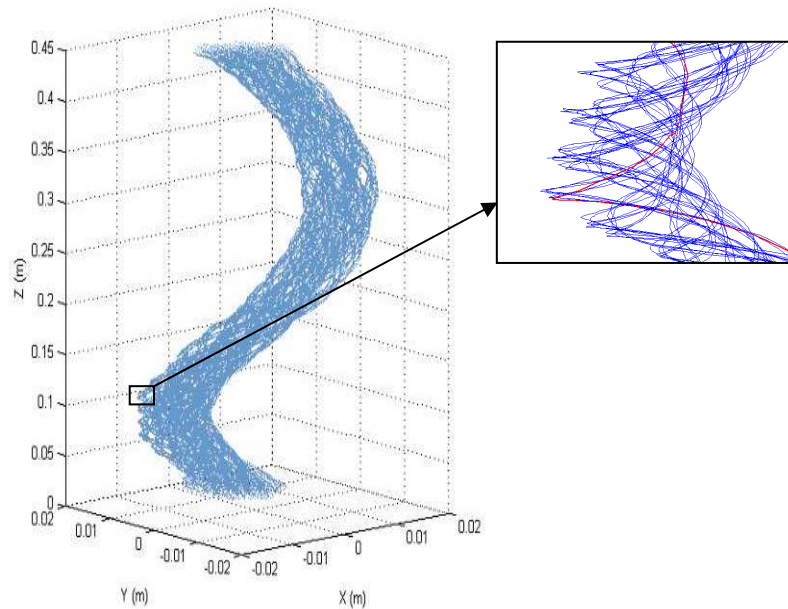


Figure 1-11: Strands Trajectories in a petal on a conductor PF twist length, with local zoom

The use of dual channel CICC is considered at present time in the case of the ITER project, but the possibility of application is interesting for any large magnet with high field. Its most critical use is illustrated on the Toroidal Field (TF) system of this machine, which is the largest magnet system of ITER.

1.3.2 Pressure drop reduction

The purpose of the central channel is to ease helium circulation by reducing pressure drop. The presence and geometry of a central channel strongly affects the global hydraulic pressure drop along the CICC unit length. The mass flow repartition is obtained with the hydraulic balance of pressure drop in both channels. A high variability was measured on strands bundle cable pressure drops; the central channel is expected to drive pressure drop and reduce cable hydraulic variability. The conductors studied are coil samples of ITER R&D programs prototypes.

Taking into account the level of TF coils heat loads, an isothermal helium mass flow rate of 8 g/s is a minimum needed to safely remove the energy from each individual pancake length. Comparisons of Table 1-1 are based on pressure drop measurements on spirals performed at CEA under a European contract [Nic02CODES], and on calculated projections. Based on these first results, it is possible to show that the impact of the central channel design is large on a project like ITER. Table 1-1 demonstrates that the optimisation of ITER CICCs has the potential to bring significant cryogenic cost reduction thanks to the central channel.

Table 1-1: Calculated comparison of conductors properties for different choices of central channel for the ITER TF system only.

| ITER TF conductor projections with various central channels | | | | |
|--|---|---------------------------------------|---------------------------------------|---|
| 0.6 MPa, 5 K, 8 g/s, 1400 strands, void = 0.332 | | | | |
| | Spiral 7/9 mm Perfor 50% ITER reference | Spiral 7/9 mm Perfor 28% | Smooth tube 7/9 mm | Smaller cable without central channel |
| Central channel friction coefficient | 0.12 | 0.057 | 0.017 | ∞ |
| Mass flow distribution | 5,1 g/s (annulus) 2,9 g/s (center) | 4,2 g/s (annulus) 3,8 g/s (center) | 3.5 g/s (annulus) 4.5 g/s (center) | 8 g/s (strands, homogeneous) |
| Pressure drop (380 m) | $0,9956 \times 10^5$ Pa | $0,77 \times 10^5$ Pa | $0,58 \times 10^5$ Pa | $1,9 \times 10^5$ Pa |
| Cryogenic power required for TF He recompression | 2,6 kW | 2.0 kW | 1.53 kW | 5.15 kW |
| Electric power of TF refrigerator | 650 kW | 500 kW | 382 kW | 1.288 MW |
| Refrigerator investment cost | 1.56 M€ | 1.2 M€ | 0.92 M€ | 3.1 M€ |
| Operating cost over 20 years; | 0.86 M€ | 0.67 M€ | 0.5 M€ | 1.7 M€ |

The pressure drop across a pancake is calculated neglecting singular pressure drops at inlet and outlet as well as mandatory design and manufacturing margins. An isentropic pump and an isobaric heat exchanger fight the isenthalpic pressure drop along the cable. The pump work is obtained from the fluid enthalpy variation with an efficiency of 0.6 (see equation (1.2-1)). In order to transform this work into cryogenic electrical consumption, the power is affected by the refrigerator global efficiency η_{cryo} :

$$\eta_{\text{cryo}} = f \cdot \eta_{\text{Carnot}} \approx \frac{1}{250} \quad (1.3-1)$$

with the Carnot efficiency $\eta_{Carnot} = \frac{T_2}{T_1 - T_2}$ and the quality factor $f = 0.25$ at 4.5 K

Finally, cost assumptions include 40 000 hours of operation at nominal power in a 20 years machine life-span, cryogenic power investment $600 \text{ k}\text{\euro}/\text{kW}_{\text{cryo}}$ (over 10 kW) and operating cost 33 \euro/MWh .

The worst situation is obtained when there is no central channel, where P_{circ} reaches the largest value of 5.15 kW. However, there would be a gain in the cable dimensions in this case, because the void in the superconducting strands must be kept constant for electrical and mechanical reasons.

Many concept and technology aspects of these forced flow cooling channels require deeper understanding, both in satisfactory levels of performance and in detailed physical processes. Spirals thermal properties including mass exchange between central and annular channels can only be assessed in a full CICC sample, where many parameters interfere.

1.3.3 Thermal imbalance

Though CICCs are meant to be as compact as possible, a central channel is self-justified as it reduces the circulation pressure drop, which therefore consumes less cryogenic power, hence reduces plant investment and operating costs. The design choices for this central channel have an important impact on the hydraulics –pressure drop and flow repartition– consequently influencing Reynolds, Prandtl, convection coefficients and thermal response of the cable. But the thermal inhomogeneity in the double helium flow within the cable brings complexity and a difference of temperature between central and annular channels under heat load. This leads to an increased temperature of the superconducting strands under heat load or unsteady cooling. An increased temperature in the heated strands reduces the superconductor temperature margin, as compared to an isothermal conductor with perfect transverse heat transfer.

Good thermal coupling allows helium circulating at higher velocity in the thermal exchanger central channel to efficiently extract power from the annular channel and keep the interchannel temperature difference low.

Assuming uniform central and annular CICC temperatures, a double channel conductor can be characterised by its annular (T_A) and central (T_C) temperatures only. This bithermal assumption allows to work with a 1D model of the CICCs. (Figure 1-12).

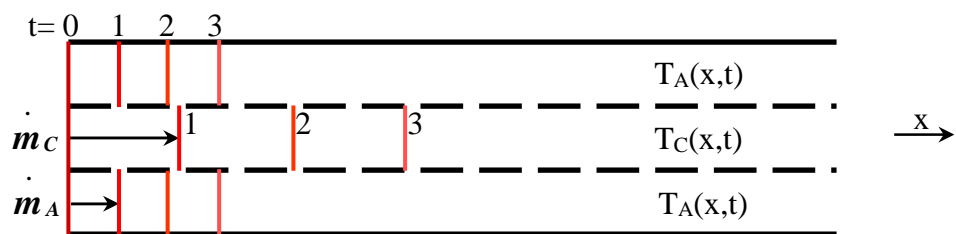


Figure 1-12: Propagation of a heat front: Longitudinal section of a double channel CICC, showing the annular and central temperatures T_A & T_C , the annular and central mass flow rates m_A & m_C .

Additionally to the temperature difference ($T_A - T_C$), the difference in velocity induces a temperature wave and spreading of any heat front along the cable. The heat homogenisation characteristics of the CICC must be understood in different thermal excitation configurations

(steady state and transient, for scenarii of heat depositions in the jacket and annular channel). The testing of CICC samples and model coils has brought evidence of a complex thermal behaviour.

The use of superconductivity for magnetic confinement fusion, as in the reactor ITER, requires a close evaluation, understanding and optimisation of thermal exchanges to maintain all superconducting strands under a sufficiently low temperature, especially during transients occurring for the reactor operation.

Literature thermohydraulic studies of rib-roughened high turbulence flows set aside work conducted in laminar, two-phase and phase change flows. Interesting studies include singular shape tubes [Cha00, Che01], square sections [Met90, Lio92], surfaces [Lew75, Han78, Tak96], internally finned tubes or inserts [Bos95, Man95, Liu01, Sar01], diaphragms in circular sections [Web71, Kim03] and rounded roughness in circular sections [Wei90, Pan93, Lon95, Vic04]. Spiral-like square roughness in circular section studies are applied to non-permeable heat exchangers where turbulence is promoted through added roughness with small turns and large gaps [Nun56, Gee80, Fir81]. On the contrary, CICC central channel spirals have a mechanical role hence large turns and smaller gaps.

Thesis content

Energetic studies about cryogenic fluid flow in a complex environment (porosity, turbulence), and thermal exchanges between coolant and superconducting strands (transfer and transport physics) are necessary to ensure a proper dimensioning of superconducting CICCs, of their dedicated cryogenic system, and to guarantee the nominal working properties of large-scale magnetic coils.

In this chapter, we have seen that the superconducting CICCs projected and developed in ITER possess two parallel channels: a low pressure-drop central channel delimited by a spiral, and an annular channel containing the superconducting strands. The dual channel conductor allows a more efficient cooling of the superconducting coils in a tokamak such as ITER. In order to further optimise the central channel spiral design, this thesis attempts to study in detail the thermo-hydraulic behaviour of spirals: the objectives are to better understand CICC thermo-hydraulics, to guarantee a correct cooling of the superconducting strands, and to provide dimensioning feed-in for the cryogenic systems and refrigerator.

In chapter 2 the central channel spiral pressure drop database is increased and in-depth friction study leads to a new pressure drop model, which was developed in the framework of this thesis [Ren06-3].

Two experimental methodologies of steady state [Ren06-1] and transient [Ren06-2] types for CICC thermal testing are developed in chapter 3, and lead to a thermal model for the heat transfer coefficient between the two channels.

Benefiting from the above original contributions, chapter 4 concludes by proposing an improvement of the ITER CICC design.

2 Pressure drop

Pressure drop, obeying a different law in each channel, equilibrates in these parallel channels. Spiral pressure drop is strongly dependant on geometric characteristics, because of their complex influence on turbulence.

Experimental pressure drop data are here studied and modelled in order to find a thermo-hydraulic optimum reduction of friction forces. Work first starts with friction because thermal properties are subordinate to hydraulics patterns.

In this chapter hydraulic models for the annular channel are first depicted (2.1), then experimental campaigns for investigation of pressure drop in the central channel spirals in pressurised nitrogen (2.2) and water (2.3) are detailed. Finally a pressure drop model is elaborated (2.4).

2.1 Bundle region pressure drop

Annular channel geometry –twisted strands, size of strands, void fraction– is dependant on electrical and mechanical constraints. The void fraction of superconducting strands petals is therefore considered fixed, and no thermohydraulic optimisation is sought on the annular channel geometry. Nonetheless, the annular channel geometry drives the pressure drop in the bundle. It is necessary to have a hydraulic model in the annular channel in order to solve the full CICC hydraulic law.

2.1.1 Existing models

Calculated central and annular pressure drops are balanced in order to obtain the mass flow repartition in the cable. An error on annular pressure drop automatically implies an error on the ratio $\alpha_A = \dot{m}_A / \dot{m}$ and introduces uncertainty on heat transfer and the whole thermohydraulic characteristics of the conductor. A study of CICC central channel cannot omit the understanding of annular hydraulics.

Porous medium model

The annular channel is an anisotropic permeable medium split into solid superconducting strands and pores, through which the fluid flows. Porous media have a fine structure, and the detailed flow around each element of the fine structure is typically not considered, but only mean flow properties are necessary. A porous medium can be described by a hydraulic law using a permeability, such as the Darcy law:

$$\Delta P = \frac{\mu \cdot L \cdot Q}{K \cdot S} = \frac{V \cdot \dot{m}}{\rho \cdot K \cdot S} = \frac{\mu \cdot L \cdot v}{K} \quad (2.1-1)$$

where μ is the dynamic viscosity, L the pipe length, S the pipe surface, V the volume ($S \times L$),

Q the volume flow rate, \dot{m} the mass flow rate, v the velocity, ρ the density and K the permeability. K quantifies the liquid flow path through the porous medium. This permeability is larger if the medium has less resistance to flow, (and if the void fraction is larger). As an example, it can be calculated using the relative roughness ϵ in the formula [Bre79]:

$$K = \frac{\epsilon \cdot D_h^2}{32} \quad (2.1-2)$$

The hydraulic diameter D_h has been derived for many common channel geometries in which the pore dimensions are known, and incorporated into an expression for permeability. However, except for known geometries, the capillary medium cannot be accurately characterised by a hydraulic diameter. Flow channels may deviate considerably from the ideal case assumed in these derivations, therefore an empirically determined permeability should be used whenever possible.

At higher superficial velocities v through the medium, the v^2 dependence of the pressure drop becomes significant and the Darcy law is replaced by the Forchheimer expression, to take into account non-linear inertia effects:

$$\Delta P = \frac{\mu L \cdot v}{K} + \beta_I \cdot \rho \cdot L \cdot v^2 \quad (2.1-3)$$

where β_I is the inertia (or non-Darcy flow) coefficient [Fou05]. Compressibility of the medium can cause the permeability to decrease with velocity. A permeability model is hence complicated and intrinsic. Permeameters are designed to evaluate the permeability of a piece of material, which is a difficult task [RenP97].

Porous medium model limit

The intrinsic difficulty with the porous medium model is the necessity to test the channel before a permeability K can be attributed. Indeed, while friction factors are defined for many microscopic and macroscopic types of roughness, permeability is not defined from the geometry but directly from a pressure drop measurement. Because no general law provides permeability constants for unknown samples, permeability is not a practical tool.

The porous medium model offers a linear law for low velocities ($Re \sim 1$), and a conjugated quadratic law for high velocities (useful above $Re > 10$). While the use of a porous medium law is efficient at very small Reynolds number, it comes close to a classical quadratic behaviour of hydraulic law for pipes when Re rises, hence loses its specific justification.

The Katheder model

In this model the annular channel is assimilated to a circular tube, with a hydraulic diameter D_h and a friction coefficient f . Based on a database of monochannel CICC experimental pressure drops, Katheder proposed a model (2.1-4) depending on the Reynolds number and void fraction only [Kat94].

$$f_A = \frac{(0.0231 + (19.6/Re^{0.7953}))}{void^{0.742}} \quad (2.1-4)$$

This validated model is advantageously simple. S. Fuchino also used a friction factor to model pressure drop of coolant in superconducting power transmission lines, but for a triplet of strands only [Fuc98], which cannot be extrapolated to the high number of strands used in the magnets of thermonuclear fusion reactors.

2.1.2 Katheder model limits and uncertainty

Since the database of available cabling patterns in monochannel and dual channel CICCs has been increased, it is possible to use these experimental results to validate the existing Katheder model. The difficulty to measure pressure drop in the superconducting strands bundle channel of dual channel CICCs should first be highlighted: tests are conducted on different geometries, in different fluids and with dubious methods to block the central

channel, or through calculations using an assumption on central channel pressure drop. It is much more difficult to draw conclusions from measurements of dual channel CICCs where uncertainty can indistinctly come from any of the parallel channels.

A state-of-the-art summary study [Zan05] could show a discrepancy up to (+/-) 40% between measured friction factors and the Katheder model. For an empirical law, this error margin is acceptable because it still provides a median predictive order of magnitude for bundle region pressure drop.

It should be noted that the Katheder explicit formula is to be used for a Reynolds validity domain above 1000. Latest developments with low pressure drop dual channel CICCs have strongly decreased mass flow rate through the annular channel, leading to Reynolds number values commonly between 700 and 1100. The use of the Katheder law out of its validity range is a source of additional imprecision.

Void fraction

While the void fraction obviously has a strong influence on the friction factor ($f_{A \text{ Katheder}} \propto \text{void}^{-\sqrt{2}/2}$), the Katheder model provides similar f values for different superconducting strands cabling twist choices. Different geometries with the same void fraction, hence indistinct for f_{Katheder} , lead to highly diverging pressure drops. The “zoology” of available conductors here demonstrates that additional parameters probably influence friction as well.

Even within the void fraction itself, the inhomogeneous repartition of the strands in the annular channel may be an important source of uncertainty in the Katheder formula: local minimal and maximal void fractions far from the mean value may drive the pressure drop. It is not possible to come up with a simple definition for a minimal and maximal void fraction, as these are deviations from an orderly twisting pattern, itself difficult to grasp in 3D. It is however interesting to compare extreme void fractions in Table 2-1.

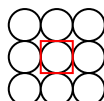
Commonly admitted void fractions for large magnets dual channel CICCs decrease from 36% to 32%, and are around 25% in the connections. Let's see how much room is left for twisting and moving:

- Straight pile void fraction: 21.5%

The void of an elemental volume around a strand of radius a is given by :

$$\text{void}_{\text{surface}} = (2a)^2 - \pi \cdot a^2 \quad (2.1-5)$$

$$\text{void \%} = \frac{4 - \pi}{4} = 21.5\% \quad (2.1-6)$$

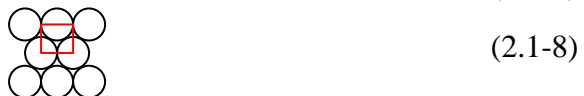


- Void fraction of an alternated pile: 9.3%

The elemental volume height is x: that of an isosceles triangle of basis length 2a for strands of radius a. The void fraction is calculated from:

$$\frac{x}{2a} = \cos(\pi/6) \quad (2.1-7)$$

hence: $x = a\sqrt{3}$ and



$$\text{void \%} = \frac{2\sqrt{3} - \pi}{2\sqrt{3}} = 9.3\% \quad (2.1-9)$$

These theoretical values can never be attained in practice, given the space required for strands twisting. In fact, it is only possible to diminish the void fraction and strands pinching by using compact rope twisting rationales. But a high strand density, which allows limited movements and pinching, would imply a reduced helium volume available for superconductor thermal stability.

Table 2-1: Typical variation range for void fraction in the ITER TFMC conductor

| | |
|--|------|
| global void fraction (%) | 33.2 |
| void fraction without dead corners (conductor with wrappings) | ~30 |
| joint void fraction | 25 |
| void fraction in perfectly piled cylinders | 9.3 |
| Void fraction in imperfectly piled cylinders | 21.5 |

Experimental uncertainty

An example of similar pressure drop measurements along pancake P1.1 & P1.2 and theoretical prediction curves is plotted (Figure 2-1) [Nic02] for the ITER TFMC model coil tested in TOSKA at FZK.

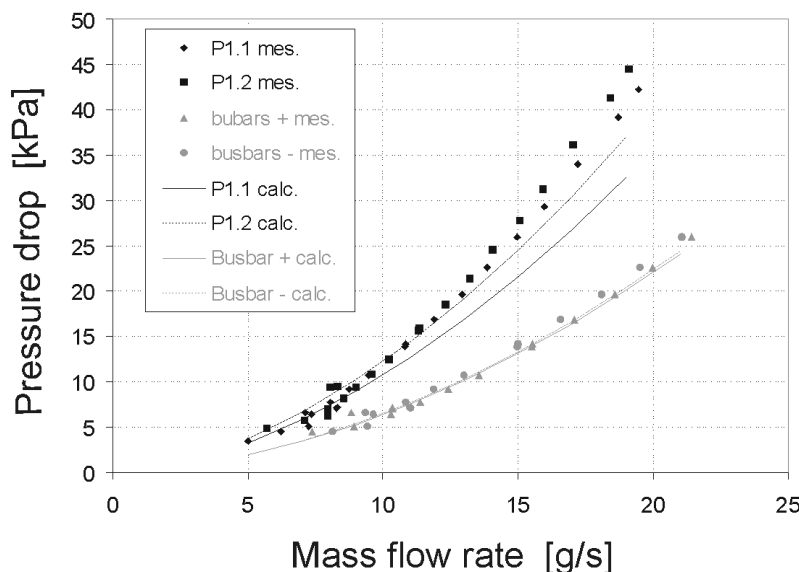


Figure 2-1: Theoretical and experimental pressure drop as a function of mass flow rate on the TFMC conductors tested in TOSKA (FZK) [Nic02]

Results of HECOL and TOSKA data are summarized in Table 2-2, where the pressure drop, proportional to the square of the mass flow, is described with a comparable coefficient k:

$$\Delta P = k L m^2 \quad (2.1-10)$$

Table 2-2: CICC pressure drops in water (HECOL, CEA) and helium (TOSKA, FZK), showing high deviation from calculated values

| Sample | TFMC P1.1 | TFMC P1.2 | TFMC | PFIS |
|---|--------------------|--------------------|--------------------|---------------------|
| Facility (research center) | TOSKA (FZK) | TOSKA (FZK) | HECOL (CEA) | water loop (PSI) |
| Fluid | He | He | H ₂ O | H ₂ O |
| Length L [m] | 72 | 82 | 8.15 | 4 |
| Mass flow rate used | $m - m_{C \ calc}$ | $m - m_{C \ calc}$ | $m - m_{C \ calc}$ | m_A |
| k calculated [kg⁻¹m⁻²] | 1.10×10^6 | 1.22×10^6 | 2.21×10^5 | |
| k measured [kg⁻¹m⁻²] | 1.52×10^6 | 1.46×10^6 | 1.72×10^5 | |
| Ratio theory/experience | 0.72 | 0.84 | 1.28 | 1.5 |

It should be noted that pressure drops measured in water (section 2.3) have always been slightly below theory, while previous measurements obtained in helium flow on a TFMC cable (section 2.2) provided on the contrary experimental pressure drops higher than predictions.

Table 2-2 shows discrepancies up to 50 % between theoretical calculations and measured coefficients. The empirical formula of Katheder is from now on divided by 1.5 to coincide with PFIS annular pressure drop measurements [Mari04] and extrapolate results to lower Reynolds values. This is a numerical example of the weak annular hydraulic model precision.

$$f_{A, \text{PFIS}} = f_{\text{Katheder}} / 1.5 \quad (2.1-11)$$

When PFIS experimental campaigns are scrutinized for thermal interpretation in chapter 3, the measured friction factor (2.1-11) will be used.

2.1.3 Bundle pressure drop model improvement

The currently available database of bundle channel pressure drop for different strand diameters, levels and lengths of twisting allows us to refine the Katheder model, ideally adding of new parameters. Remark that for example the influence of twisting lengths could be studied through the harmonic mean of the various twisting pitches.

Numerical simulation

An evaluation of possibilities to model central and annular channels with a code (Fluent) was performed by IUSTI (Marseille). Axisymmetric 2D and 3D calculations were performed. While spiral detailed modelling makes sense, a mean porous permeability seems more reasonable for the annular channel. The number of strands, level of geometric complexity, various geometric uncertainties and computer-intensive calculations subject to potential mistakes do not allow to reasonably well model the annular channel starting from the lower scale of strands. In fact, even for a spiral, a 2D gridding of a slice may be sufficient, with helical limit conditions.

The maximal reasonable number of volumes is 1 million to keep processing time low, and this number is easily reached in a 3D environment. Comparatively to 3D, 2D gridding is interesting because of simplicity and efficiency. The annular channel complexity seems more adapted to an experimental comprehension than to a detailed numerical model attempt. Future efforts should concentrate on a spiral period, which remains accessible to a finite elements modelling, while the annular channel can consent an anisotropic porous averaging [Top97].

The level of confidence that can be conceded to a predictive friction simulation decreases as the level of turbulence increases. Hydraulic codes indeed use the Navier-Stokes equations. Models and solutions are effective for laminar flows, but tend to diverge from experiments as the Reynolds number increases. Since the central channel spiral flow is characterised by $Re \sim 10^5$, the presence of micro-turbulence with multiple moving vortices cannot be well modelled and eventually becomes non-negligible, making the use of a code at high Reynolds ineffective.

The choice of adequate resolution parameters can only be done by comparison with experimental results with a Reynolds and Prandtl analogy, which requires experimental campaigns on spirals. It is easier to compare code results and experiments directly for the same fluid. The numerical simulation of a spiral would allow a parametric sensitivity study to the spiral geometry, helping design optimisation.

Experimental future efforts

An experimental characterisation of transverse annular porosity or transverse cable porosity may be realised on a small CICC sample stripped from its jacket and adequately pressurised in an existing thermohydraulic facility dedicated to tiny samples.

To obtain precise values of varying properties, the program must use a supercritical helium thermodynamic database. Thermal characterisation of the spiral may be possible as well.

Researcher from IUSTI are capable, through X-rays imaging, of numerically reconstructing porous objects. Local energy loss and pressure drop laws can be calculated from the material fine structure. Such technique is applicable to a superconductor bundle petal, and allows local evaluation of energy dissipation and heat exchanges, but at a high cost and effort.

It is important to know which tools are available, and where the limits of preceding work lie. Because limited resources must be concentrated on reasonable and critical design and optimisation objectives, the annular channel Katheder friction factor is considered a fair and practical tool to model annular pressure drop.

Hydraulic phenomena are scrutinized in the central spiral only for the following reasons:

- The central channel lacks a decent model, whereas the Katheder model is available for the annular channel.
- The annular channel is not an optimisation variable: coils limited size and superconductors electric contacts enforce a void fraction with little variation margin.
- Central spirals of same size, thought to be somewhat similar have proven friction to vary by a factor 100%.
- Small spiral modifications can bear heavily on CICC hydraulics (pressure drop and mass flow repartition).

2.2 Experimental spiral friction in nitrogen

The low impedance CICC central channel consisting of a stainless steel spiral pipe has a premium role in the distribution of mass flows and in the global pressure drop.

Two test facilities have been built at CEA/Cadarache to investigate the hydraulic behaviour of dual channel CICC samples: OTHELLO is dedicated to hydraulic resistance measurements using nitrogen at ambient temperature; HECOL is operated for thermal-hydraulic experiments using variable temperature liquid water up to 60°C.

A set of various spiral samples has been tested in these two facilities, providing a double database of friction factors in N₂ and H₂O flows. Results are to be compared as a function of the Reynolds number, and taking into account the Mach number during experiments (in the compressible N₂ case).

Section 2.2 is dedicated to pressure drop measurements in N₂ using the OTHELLO facility. Starting from the report by Nicollet [Nic03], the specific contributions added are the influence of Mach number in the compressible nitrogen, the choice of a hydraulic diameter, the comparison of results using external, internal or hydraulic diameter and modelling the role of geometric parameters.

The experimental campaign and samples instrumentation is first detailed. Friction factor calculation methodology is then explained, taking into account properly the Mach number of the fluid. Finally, results and precision are given.

2.2.1 Experimental campaign

The OTHELLO test facility was built at CEA/Cadarache to investigate the hydraulic behaviour of dual channel CICC samples. It is dedicated to hydraulic resistance measurements using nitrogen at ambient temperature. More information about this facility is developed in appendix A1.

Samples

The OTHELLO facility allows the high pressure testing of spirals in an open loop with disposable nitrogen. Spirals samples over 4 m long were mounted in soft pressurised tubing, and eventually mounted again in stainless steel pipes to check results and for more tests in the HECOL facility. For stainless steel tubing, spirals were inserted into pipe with the method called “Overtwist”. It consisted in twisting the spiral over an internal rod to reduce slightly its outer diameter, then relaxing it inside a pipe chosen for its internal diameter. Local brazing of the spiral through holes every half meter tied spiral and tube to avoid twist pitch variation and vibration.

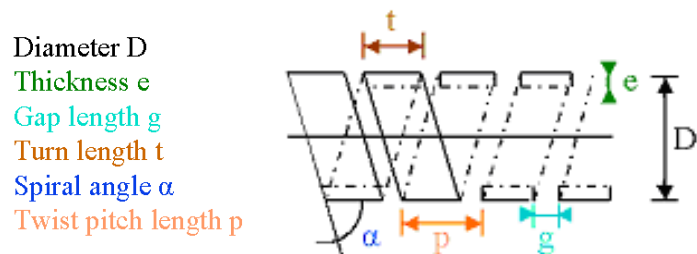


Figure 2-2: Spiral geometric parameters

A wide spectrum of sample geometries including ITER spirals manufactured by Showa (SHO), Cortaillod (COR) and later VNIIKP (PFCI only tested in HECOL) were provided by EFDA. Additionally, a set of spirals was manufactured by Mécaressorts: type CΦ, IΦ & SΦ, where Φ is the external diameter given in mm. The wide spectrum of spiral geometries tested is meant to understand and improve the thermohydraulic behaviour of the central channel spirals chosen for the ITER coils.

Spirals have constant thickness $e = 1$ mm and turn $t \approx 6$ mm. Their main variable characteristics are listed in Table 2-3. Spirals PFCI, S9, C9, I9 and I7.6 appearing in grey in the Table have not been tested in nitrogen, but only later in water (section 2.3). ST8 and ST10 are the names of the Smooth Tubes of internal diameters 8 and 10 mm respectively.

Table 2-3: Basic spiral geometry parameters values

| Spiral type | L [m] | D[mm] | e[mm] | d[mm] | g[mm] | t[mm] | p[mm] | S(e-5) [m²] | w[mm] | Dh[mm] |
|--------------------|--------------|--------------|--------------|--------------|--------------|--------------|--------------|-------------------------------|--------------|---------------|
| SH0wa | 4.87 | 11.9 | 1 | 9.9 | 2.4 | 6.25 | 8.65 | 8.64 | 34.8 | 9.93 |
| CORtaillod | 4.45 | 12.1 | 1 | 10.1 | 5.3 | 6.5 | 11.8 | 9.57 | 36.6 | 10.48 |
| PFCI | 3.38 | 12 | 1 | 10 | 1.93 | 6 | 7.93 | 8.69 | 34.9 | 9.95 |
| S-10 | 4.72 | 9.945 | 1 | 7.945 | 2.85 | 6.25 | 9.1 | 5.83 | 28.9 | 8.07 |
| C-10 | 4.56 | 9.74 | 1 | 7.74 | 5.84 | 6.5 | 12.34 | 6.00 | 29.3 | 8.20 |
| I-10 | 4.66 | 9.99 | 1 | 7.99 | 7.29 | 6.25 | 13.54 | 6.53 | 30.5 | 8.57 |
| S9 | 3.41 | 9.55 | 1 | 7.55 | 2.57 | 6.2 | 8.77 | 5.26 | 27.6 | 7.64 |
| C9 | 3.40 | 9.7 | 1 | 7.7 | 6.05 | 6.45 | 12.5 | 5.97 | 29.2 | 8.18 |
| I9 | 3.40 | 9.65 | 1 | 7.65 | 7.31 | 6.2 | 13.51 | 6.06 | 29.4 | 8.24 |
| S-8 | 4.72 | 7.88 | 1 | 5.88 | 3.75 | 6.25 | 10 | 3.52 | 22.8 | 6.18 |
| C-8 | 4.65 | 7.915 | 1 | 5.915 | 5.6 | 6.5 | 12.1 | 3.75 | 23.5 | 6.39 |
| I-8 | 4.75 | 8 | 1 | 6 | 6.08 | 6.25 | 12.33 | 3.91 | 23.9 | 6.53 |
| I7.6 ITER | 3.42 | 7.6 | 0.8 | 6 | 6 | 6.5 | 12.5 | 3.64 | 22.9 | 6.38 |



Figure 2-3: Photo of spiral samples

Experimental equipment of ~4 m samples in tubes includes absolute and differential pressure, temperature and mass flow rate sensors. Central channel spiral designs shown in Figure 2-3 have been investigated at CEA in the framework of a European task.

Calibration

Performing pressure drop measurements on smooth tubes ST8 and ST10, which have a measurable micro-roughness, provides validation of the results. The Blasius equation is the reference theoretical friction limit for a perfectly smooth tube. Its equation is [Idel'cik]:

$$f = \frac{1}{(1.8 \ln(Re) - 1.64)^2} \quad (2.2-1)$$

This equation is equivalent, for the hydraulically smooth case of turbulent flow, to the Karman-Nikuradse intrinsic formula [Tdi pdcA738]:

$$\frac{1}{\sqrt{f}} = 2 \ln(Re \sqrt{f}) - 0.8 \quad (2.2-2)$$

which is valid for Re up to 10^6 . Turbulent flow in stainless steel tubes becomes hydraulically rough beyond and f becomes independent of the Reynolds number.

The smooth tube asymptotic value $f = 1.7 \times 10^{-2}$ at large Reynolds corresponds to an apparent roughness $\epsilon/id = 5 \times 10^{-4}$. The roughness measured on the tubes, ϵ_{ss} between 3.2 and 7×10^{-7} m (half a micron) leads to a relative roughness ϵ/id between 4 and 8.75×10^{-5} , leading to smaller friction factor values. The OTHELLO facility hence provides slightly overrated friction factors. Smooth tubes calibration results were considered satisfying given that roughness was difficult to measure, and because comparison is done with empirical formulae that have an 8 to 10% measurement uncertainty [Tdi pdcA738].

All measurement points are averaged over at least 20 seconds of steady state experiment.

2.2.2 Compressibility

While the roughness in a smooth tube is stochastic with a constant friction factor along the tube, friction in a rib-roughened tube involves periodic phenomena. Several pressure drop mechanisms are hidden behind this global friction factor. Therefore small-scale shear and large-scale roughness should ideally not be treated in the same way. For example a spiral lineic friction may in fact hide a form drag friction per singularity. Following the example of the literature in the domain of helically ribbed tubes and rib roughened conduits, and by analogy with smooth tubes, a friction factor is related to an effective roughness. The same pressure drop formula is used and a mean friction factor calculated:

$$\Delta P = f \cdot \frac{1}{2} \rho U^2 \frac{L}{D_h} \quad (2.2-3)$$

This formula relates the pressure drop to the friction coefficient, the dynamic pressure (or kinetic energy) $\frac{1}{2} \rho V^2$, the length and hydraulic diameter for an ideal fluid in permanent, incompressible flow. It is equivalent to:

$$\rho \Delta P = \frac{w \cdot m^2}{8S^3} \cdot f \cdot L \quad (2.2-4)$$

In the more general case of compressible flow, the friction factor belongs inside an integral involving the Mach number.

$$\int_{P_{out}}^{P_{in}} \rho dP = \frac{w \cdot m^2}{8S^3} \int_0^L \left(1 + \frac{\gamma(x) \cdot M(x)^2}{1 - M(x)^2} \right) f \cdot dx \quad (2.2-5)$$

This formula is valid for an ideal gas, which is a reasonable assumption for the diatomic gas nitrogen, and takes into account properly the Mach number evolving along the streamlines in this permanent flow regime. P_{in} and P_{out} are the inlet and outlet pressures, respectively.

Technically, f should be considered a function of Re and M . Practically variations of f with Mach are small and neglected. $\frac{\partial f}{\partial Re}$ is also known to be insignificant for quadratic flow regime, i.e. for Re larger than 10^5 . So (2.2-5) becomes:

$$\int_{P_{out}}^{P_{in}} \rho dP = f \frac{w \cdot m^2}{8 \cdot S^3} \int_0^L \left(1 + \frac{\gamma(x) \cdot M(x)^2}{1 - M(x)^2} \right) dx \quad (2.2-6)$$

Pressure drop in the central channel was calculated from extrapolated spiral friction measurements at $Re = 10^5$ and assumed constant. A total variation of 8% is expected from measurements with error bars of 10% in the Reynolds number interval $[5 \times 10^4; 1.5 \times 10^5]$.

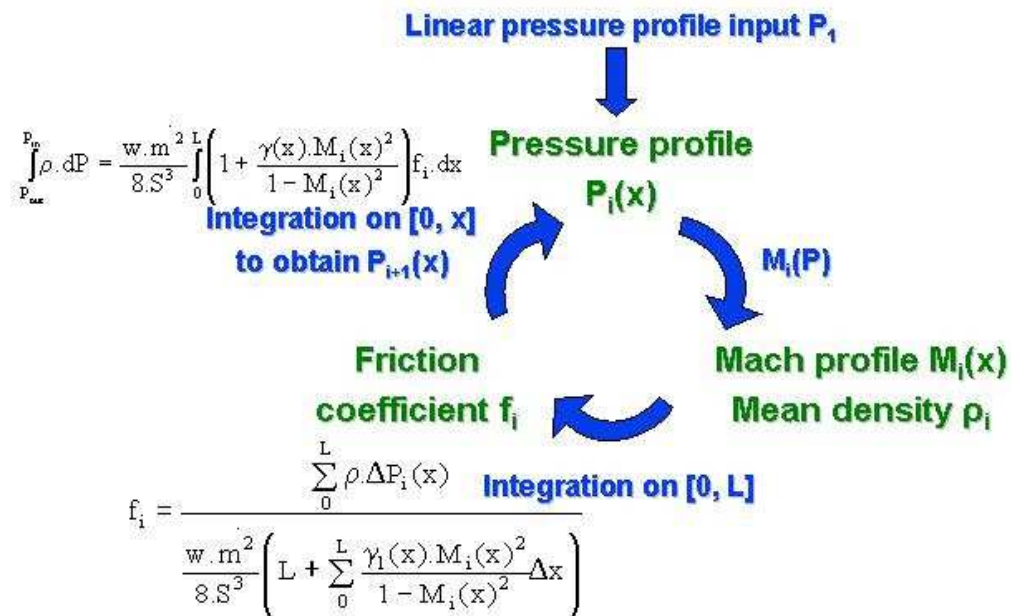


Figure 2-4: Numerical loop principle used to implement pressure drop with compressibility

Proof for the compressible relation (2.2-5) and its numerical application are developed in Appendix II. The calculation principle given in Figure 2-4, applied in a Visualbasic code and convergence is obtained in a few iterations. In the end, the friction factor is calculated from (2.2-7) where δ is the effect of compressibility:

$$f = \frac{8 \cdot S^3 \int \rho dP}{w \cdot m^2 (1 + \delta) L} \quad (2.2-7)$$

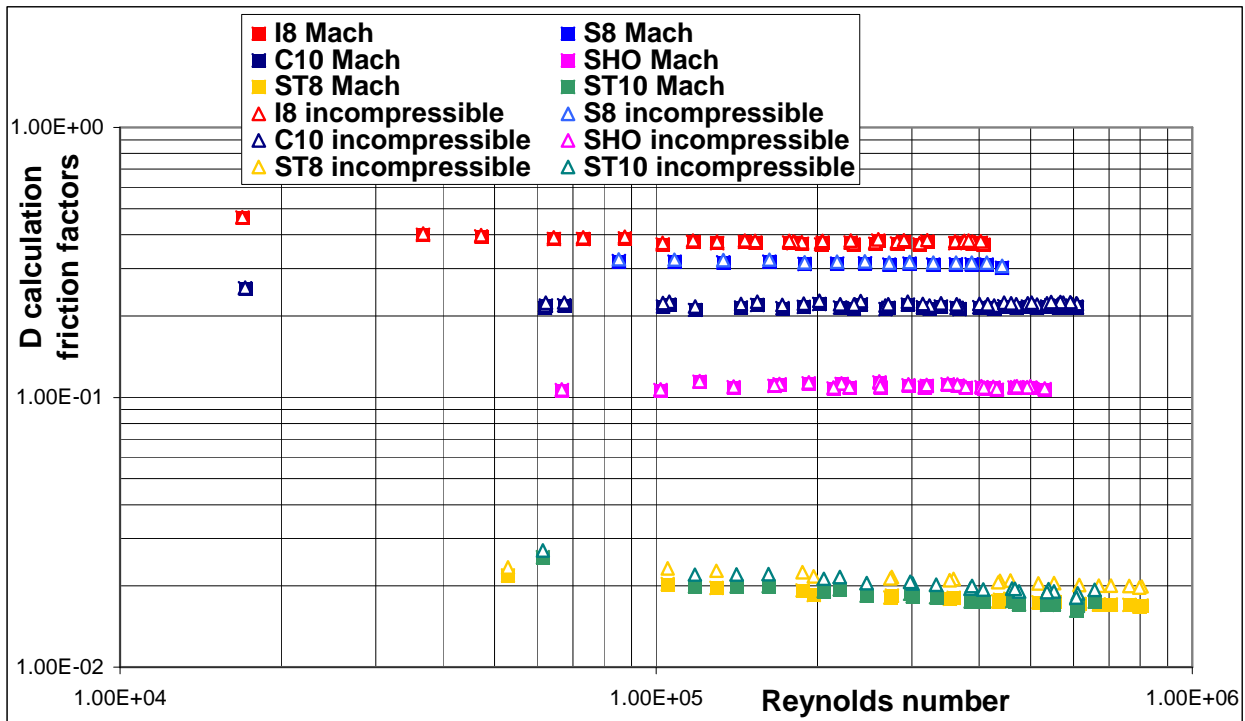


Figure 2-5: Friction factors effect of compressibility using the outer diameter od

Friction factors lead to slightly lower values when more rigorously using the compressibility effect through the Mach number. The relative difference with/without compressibility remains under 6% for spirals, and raises up to 11 and 17.5% only for ST10 and ST8 (Table A-1). On Figure 2-5 where only some of the spirals performances are represented for clarity reasons, we see that about 5% discrepancy due to compressibility does not appear as a major results modifier when plotted in logarithmic scale.

Joule-Thomson expansion

A Joule Thomson expansion describes a temperature variation that goes along the pressure release of an isolated gas. These experiments are indeed regarded as Joule-Thomson flows, where the thermodynamic law $\Delta H = 0$ is used.

$$dH = m.c_p.dT + \left(V - T \frac{\partial V}{\partial T} \right) dP = 0 \quad (2.2-8)$$

where dP is negative. In the general case we can introduce the coefficient $\beta_p = \frac{1}{V} \frac{\partial V}{\partial T} \Big|_p$ in order to get

$$dT = \frac{1}{\rho.c_p} (T\beta_p - 1)dP \quad (2.2-9)$$

The Joule-Thomson coefficient μ_{JT} is defined as the instant temperature variation (cooling or heating) that collocates a constant enthalpy Joule-Thomson expansion:

$$\mu_{JT} = \frac{\partial T}{\partial P} \Big|_H = \frac{(T\beta_p - 1)}{\rho.c_p} \quad (2.2-10)$$

The Joule-Thomson coefficient gives a value of the eventual temperature increase or decrease. Temperature variation due to a Joule-Thomson pressure drop can be either negative (shaded area of Figure 2-6) or positive depending on the local sign of μ_{JT} . Isenthalpic expansion moves the system along constant enthalpy curves with temperature varying vertically. The

inversion temperature occurs when the isenthalps change the sign of their slope [TdI thAF4040, Matyushov].

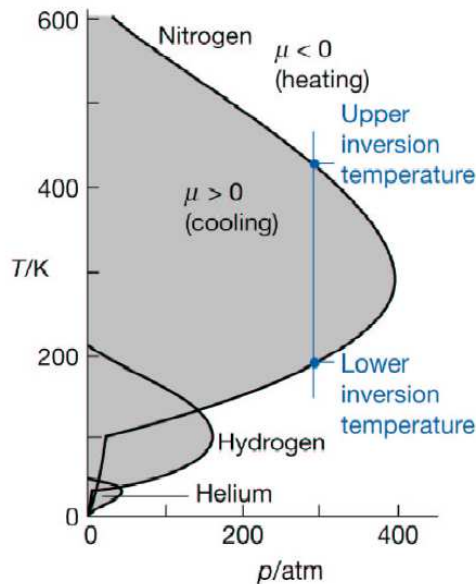


Figure 2-6: Temperature-pressure domain of Joule-Thomson coefficient for N₂ and He

Table 2-4: μ_{JT} as a function of P and T for H₂O (HECOL), N₂ (OTHELLO) & He (ITER)

| fluid | P [MPa] | T [K] | T [°C] | μ [K/MPa] |
|----------|---------|-------|--------|---------------|
| Water | 3 | 293 | 20 | -0.23 |
| Water | 3 | 333 | 60 | -0.20 |
| Water | 0.5 | 293 | 20 | -0.23 |
| Water | 0.5 | 333 | 60 | -0.20 |
| Nitrogen | 2.5 | 293 | 20 | -0.62 |
| Nitrogen | 2 | 30 | -243 | 0.13 |
| Nitrogen | 0.5 | 293 | 20 | -0.62 |
| Nitrogen | 0.5 | 73 | -200 | -0.44 |
| Helium | 0.5 | 293 | 20 | -0.62 |
| Helium | 0.5 | 73 | -200 | -0.44 |
| Helium | 0.5 | 4 | -269 | -1.48 |
| Helium | 0.5 | 5 | -268 | -0.50 |
| Helium | 0.5 | 6 | -267 | 1.38 |
| Helium | 0.4 | 4 | -269 | -1.36 |
| Helium | 0.4 | 5 | -268 | -0.17 |
| Helium | 0.4 | 6 | -267 | 3.14 |

Values of μ_{JT} for water, nitrogen and helium at various temperatures are in Table 2-4. This expansion is isothermal for an ideal fluid:

$$\beta_P = \frac{1}{V} \frac{\partial V}{\partial T} \Big|_P = \frac{1}{V} \frac{\partial}{\partial T} \left. \frac{nrT}{P} \right|_P = \frac{nr}{PV} = \frac{1}{T} \quad (2.2-11)$$

hence $dT=0$. In other words enthalpy is a function of T only for ideal fluids.

2.2.3 Results and precision

Starting with formula (2.2-3), the arbitrary choice of a diameter is important for the estimation of the friction factor. Physically the hydraulic diameter is the most appropriate diameter to be used in this calculation. Formula (2.2-8) illustrates the importance of this choice:

$$f_{od} = f_{id} \left(\frac{U_{id}}{U_{od}} \right)^2 \frac{od}{id} = f_{id} \left(\frac{od}{id} \right)^5 \quad (2.2-12)$$

The OTHELLO set of friction factors calculated for each sample, with measurement at every inlet/outlet pressure drop plateau is displayed in Figure 2-7 for spirals defined in Table 2-3. The Blasius equation (2.2-1) plotted as a black line below the data points is the theoretical friction limit for a perfectly smooth tube.

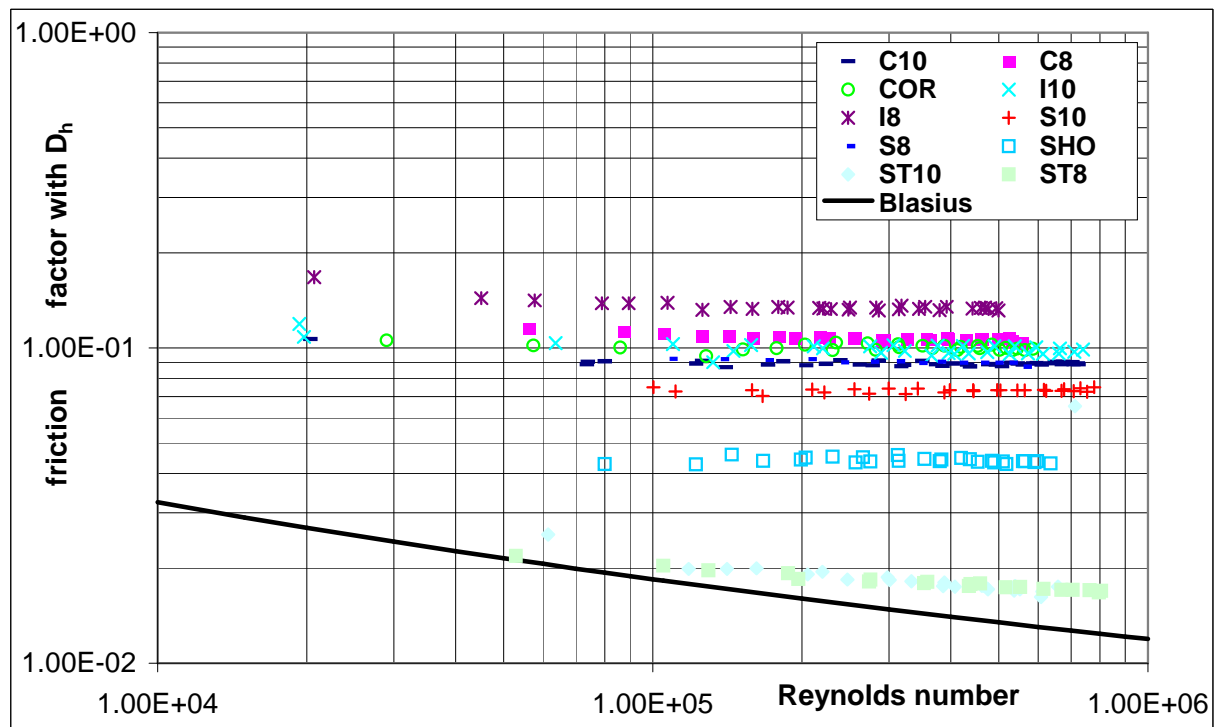


Figure 2-7: Friction coefficients calculated using the Mach number and the hydraulic diameter D_h as a function of the Reynolds number (Moody diagram)

Table 2-5: Friction factors calculated using hydraulic (D_h), internal (id) and external (od) diameters. roughness function is further defined in section 2.4

| Spiral type | $f D_h$ | $f id$ | $f od$ | $R^+ D_h$ | $R^+ id$ | $R^+ od$ |
|-------------|-----------------------|-----------------------|-----------------------|-----------|----------|----------|
| Showa | 4.39×10^{-2} | 4.33×10^{-2} | 1.10×10^{-1} | 6.49 | 6.55 | 3.56 |
| Cortaillod | 1.00×10^{-1} | 8.32×10^{-2} | 2.07×10^{-1} | 4.07 | 4.61 | 2.36 |
| S-10 | 7.32×10^{-2} | 6.74×10^{-2} | 2.14×10^{-1} | 5.49 | 5.75 | 2.79 |
| C-10 | 8.90×10^{-2} | 6.57×10^{-2} | 2.16×10^{-1} | 4.96 | 5.88 | 2.83 |
| I-10 | 1.01×10^{-1} | 6.99×10^{-2} | 2.22×10^{-1} | 4.56 | 5.64 | 2.73 |
| S-8 | 9.03×10^{-2} | 6.98×10^{-2} | 3.13×10^{-1} | 5.64 | 6.41 | 2.85 |
| C-8 | 1.07×10^{-1} | 7.14×10^{-2} | 3.17×10^{-1} | 5.18 | 6.33 | 2.82 |
| I-8 | 1.33×10^{-1} | 8.55×10^{-2} | 3.71×10^{-1} | 4.67 | 5.84 | 2.61 |

The Showa and Cortaillod external diameter measurements, 0.11 and 0.207 respectively, can be compared to the ITER design criteria correlations [Nic00] in the appropriate Reynolds range [$10^5, 10^6$] and with the external diameter:

$$f_{SHO} = 0.3024 \text{Re}^{-0.0707}, \text{ and} \quad (2.2-13)$$

$$f_{COR} = 0.7391 \text{Re}^{-0.1083} \quad (2.2-14)$$

that leads to f_{SHO} values of [0.11, 0.13] while f_{COR} values are within [0.17, 0.21].

Internal diameter results available in [Zan00] are inferior by a factor 4 to the internal diameter values of this study and to the ITER design criteria because they are expressed as US (as opposed to European) friction factors $C_f = f/4$.

The friction factor does not provide direct pressure drop or mass flow rates comparison because of the different spiral diameters and dynamic pressures. Only spirals of similar size may be compared, where the recurring classification occurs: $f_S < f_C < f_I$ (see Table 2-3). When looking for a friction factor reduction, the vertical classification of the probes is enlightening. In other words at constant diameter, thickness and turn length, the smaller the gap, the lower the f .

Whatever the diameter chosen, the recurrent surprise comes from the Cortaillod spiral aligned on the od10 spirals in Figure 2-7, and that displays high friction results for a 12 mm diameter spiral (COR).

Another way of modelling spiral friction is to look at the rib roughness as a series of diaphragms constituting singular friction. In fact, the slight declivity of spiral f as a function of Re appears to be that of a smooth tube. The spiral friction factors could be modelled as a micro-roughness (on the spiral turns), shifted upwards by a value defined by the gaps singular friction (a constant multiplied to dynamic viscosity).

Noise and precision

The noise level observed on the pressure probes is quasi constant, resulting in quite large relative error at low pressures and Re , while measurement uncertainty is kept very low as soon as P is above 0.2 Mpa, which is the case in OTHELLO measurements (see Appendix I). The friction factor is calculated from (2.2-8), which provides the possible sources of error:

$$\frac{\Delta f}{f} = \frac{\Delta \int \rho dP}{\int \rho dP} + 2 \frac{\Delta m}{m} + \frac{\Delta(\delta)}{(1+\delta)} \quad (2.2-15)$$

Calculation uncertainty on $\int \rho dP$ is about 1%, and sensor uncertainty on the averaged pressure measurement is no more than 1%. Uncertainty of $m = \rho Q_v$ is the measurement relative error on Q_v , in principle less than 1% according to the device manufacturers. Calculation uncertainty on δ (the effect of compressibility) is on the order of 1% (from iteration). Uncertainty on δ itself is also of 1%. We obtain a global friction factor uncertainty of 5%. Calibration and discrepancy with measurements in water presented in the next section show that real uncertainty may be larger than calculated uncertainty.

2.3 Experimental spiral friction in water [Ren06-3]

The pressure drop of spiral prototypes was investigated in pressurised water in order to cross-check N₂ results, to use better adapted rigid spiral tubing, to be free from compressibility effect and to complete the database.

2.3.1 Experimental campaign

The Heat Exchange Conductor Operational Loop (HECOL) test facility operated at Cadarache offers similar hydraulic measurement possibilities in H₂O as the OTHELLO facility in N₂. Appendix III details working pressure and temperature of the facility. The pressure drop of various CICC central spirals samples was investigated in HECOL, using pressurised ambient temperature water at Reynolds numbers relevant to ITER conditions (1.3×10^5). The test facility pumps and heat exchangers allow mass flow rate up to $1.5 \times 10^{-3} \text{ m}^3 \text{s}^{-1}$ and temperature ranging from 15 to 75°C.

Spirals previously tested had either their pressure and temperature sensors remanufactured, or were tubed using a better method called “Co-drawing”, realised with an industrial collaboration (Nexans). It consists in inserting the spiral inside a steel pipe 0.4 to 1 mm larger than the spiral diameter, and co-drawing the pipe with the spiral inside, reducing its outer diameter until the gap between the spiral and the tube is closed. All spirals were tested in HECOL. Spirals characteristics are listed in Table 2-3.

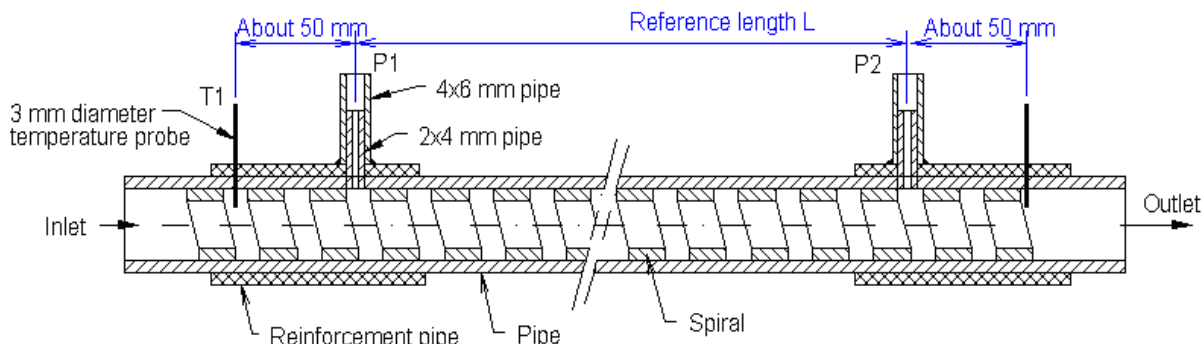


Figure 2-8: Sketch of sample spiral inserted and instrumented in a pipe

Samples were completed by hydraulic connections, temperature sensors and pressure drop holes at each end (Figure 2-8). ΔP data is used to avoid adding measurement errors.

2.3.2 Results

Although spiral roughness is macroscopic and stands as a series of singular turbulent patterns, spirals are simply modelled as rough tubes with a hydraulic diameter D_h and a friction coefficient f . The friction factors were derived for a volume flow rate Q_v , the fluid density ρ and the dynamic viscosity μ from:

$$f = \frac{\pi^2 \times \Delta P \times D_h^5}{8 \times L \times \rho \times Q_v^2} \quad (2.3-1)$$

$$Re = \frac{4 \times \rho \times Q_v}{\mu \times \pi \times D_h} \quad (2.3-2)$$

Table 2-6: Spirals advanced characteristics; friction factor f given for $Re = 2 \times 10^5$

| Spiral | Diameter D_h [mm] | Roughness e/D_h | Cavities g/e | Angle α [°] | Spatial freq. $1/p$ [m ⁻¹] | Perforation g/p % | f for $Re > 10^5$ |
|-------------|------------------------|----------------------|-----------------|-----------------------|---|----------------------|------------------------|
| SHO | 9.93 | 0.101 | 2.4 | 77.0 | 116. | 27.7 | 4.63×10^{-2} |
| COR | 10.48 | 0.095 | 5.3 | 72.8 | 84.7 | 44.9 | 9.42×10^{-2} |
| PFCI | 9.95 | 0.100 | 1.93 | 78.1 | 126. | 24.3 | 4.07×10^{-2} |
| C10 | 8.20 | 0.122 | 5.84 | 68.0 | 81. | 47.3 | 8.40×10^{-2} |
| I10 | 8.57 | 0.117 | 7.29 | 66.7 | 73.9 | 53.8 | 1.05×10^{-1} |
| S9 | 7.64 | 0.131 | 2.57 | 73.7 | 114. | 29.3 | 7.10×10^{-2} |
| C9 | 8.18 | 0.122 | 6.05 | 67.7 | 80. | 48.4 | 1.01×10^{-1} |
| I9 | 8.24 | 0.121 | 7.31 | 66.0 | 74. | 54.1 | 9.45×10^{-2} |
| S8 | 6.18 | 0.162 | 3.75 | 68.0 | 100. | 37.5 | 8.02×10^{-2} |
| C8 | 6.39 | 0.156 | 5.6 | 64.1 | 82.6 | 46.3 | 9.7×10^{-2} |
| I8 | 6.53 | 0.153 | 6.08 | 63.9 | 81.1 | 49.3 | 1.12×10^{-1} |
| I7.6 | 6.38 | 0.125 | 7.5 | 62.4 | 80. | 48. | 7.70×10^{-2} |

Pressure drop graphics are given in friction factors or linear pressure drop [Pa/m] as a function of Reynolds number in order to easily transpose results to any fluid through similarity laws. More classical flow rate-pressure drop curves do not provide easy similitude.

Previous spiral empirical laws [Nag86, ITER05] demonstrate very low dependence on Reynolds number. This low dependence is confirmed in Figure 2-9: friction coefficients do not change significantly after Re passes 10^5 . Curvature of results looks flat in this usual logarithmic scale and above $Re = 10^5$. In fact, the spiral friction factors' dependence on the Reynolds number is comparable to that of the smooth tube. The Blasius friction law for smooth tube could serve in the friction model retained for spirals in order to add the small Reynolds influence.

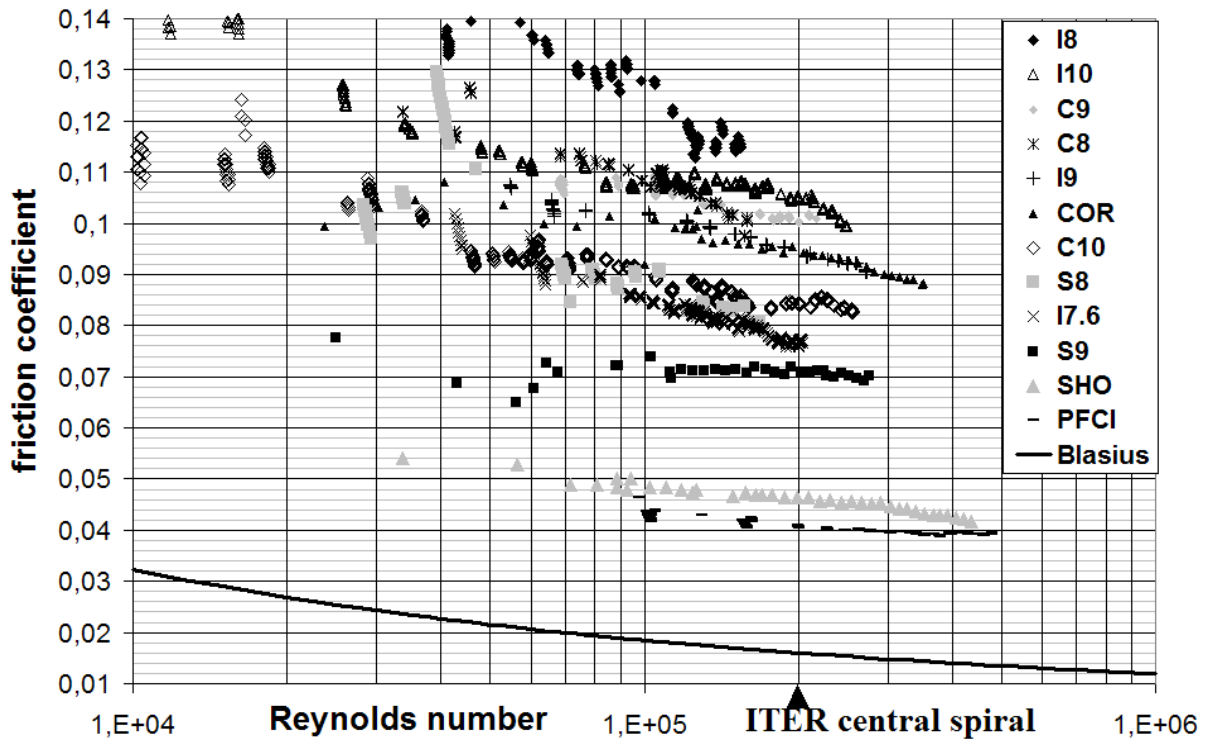


Figure 2-9: Moody diagram: friction factor as a function of Reynolds number

2.3.3 Precision

Calibration

The accuracy of the volume flow rate ultra sound sensor located at the outlet is better than 1%. The differential pressure drop ΔP measurement, recorded between pressure tubes on a reference length L , also has an accuracy better than 1%. Qualification of HECOL was conducted on smooth tubes, compared to the Blasius law and Colebrook intrinsic formulae (2.2-1 & 2). Measurements gave a friction factor surprisingly below the minimum friction of perfectly smooth tubes. Pressure intakes were therefore reduced to the smallest possible internal diameter of 2 mm sketched in Figure 2-10. Distance from end connexions was checked in order to guarantee state-of-the-art pressure intakes [TdI pdcA738].

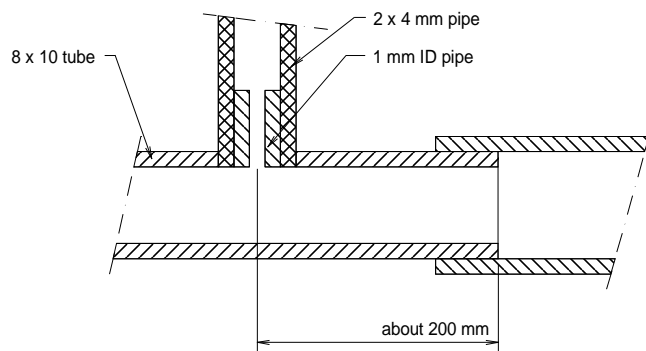


Figure 2-10: Pressure intake configuration: small and far from connexions ($> 20 \times id$)

Pressure intakes were visually inspected and deburred. The flow meter was also inspected, replaced, and checked by integrating and weighting flow. Results were confirmed: friction factors in HECOL may be slightly minimised. The difference between measured and expected values of friction factors from intrinsic formulae is within the 8 to 10 % accuracy of the formulae. Assuming that the absolute error is constant, which is a reasonable assumption, the maximum error reported on higher spirals friction becomes a relative error under 3%, which is similar to the experimental accuracy.

The qualification of the facilities (OTHELLO and HECOL) can be discussed when comparing overestimated friction factors in nitrogen to underestimated friction factors in water. Water experiments are retained as the reference experimental data for the following reasons:

- Tests conducted on the full set of spirals,
- Tubing dispositions identical or better,
- Finer and double-checked pressure intakes,
- The flow is incompressible, which is useful for high Re measurements (ITER conditions)
- The Joule-Thomson coefficient is closer to 0, therefore no thermal perturbation is present.

While it seems safer for cable designers to overestimate pressure drop, it is wiser to correctly evaluate flow repartition and the resulting heat transfer properties in the dual channel CICC.

Symmetry

Spirals tested in both directions should demonstrate a symmetric hydraulic behaviour. Experimental discrepancies observed up to 30% are attributed to the insufficient manufacture and tubing quality of spirals. S10, displaying 65% difference, was discarded. The dynamic pressure level –compared to the absolute pressure– is not sufficient to explain the variation due to flow direction. Because spiral turbulence can easily be augmented but not diminished, only the minimal friction factor is considered in Table 2-6.

Considering the results obtained in this investigation, and whatever the prediction system or parameter considered, one cannot help to think that the Cortaillod spiral behaves worse than all expectations, whereas the Showa spiral offers very good hydrodynamics performance. While essential geometric dimensions have been verified by direct measurement, there were different manufacturers for the whole set of spirals, and different fabrication process probably induce side effects in the spiral geometry. The most obvious differences observed on the prototypes are the sharpness of the angles and the slight bend of the metallic ribbon shown in Figure 2-11: spirals provided by different suppliers may not be strictly comparable.



Figure 2-11: Exaggerated ribbon geometrical defects

Furthermore, probes tested in reverse flow direction have provided pressure drop variations with up to 36% difference. It is believed that the spirals may not be perfectly symmetric and/or that spirals may not be attached to their testing pipe at sufficiently small intervals. Spiral geometric parameters (Figure 2-2) influence on pressure drop is sought from friction results reported in Table 2-6.

2.4 Friction factor model

The influence of the spiral geometric parameters: spiral hydraulic diameter, spatial frequency, thickness to diameter ratio (rib roughness), gap ratio etc. on the pressure drop is investigated. Theoretical works are required to select or discard relevant parameters among the pleiad of factors which intervene. Not all parameters in the experimental database have a range of values large enough to draw conclusions.

2.4.1 Parameters driving turbulence

Relative roughness and relative friction

The friction factor evaluates shear phenomena in the fluid layer at the interface with the wall. Spiral small-scale roughness is not relevant given the relative magnitude of smooth tube friction compared to spiral friction. The ratio f_{spiral}/f_{ST} is not very interesting because the roughness measured on all stainless steel smooth tubes and spiral ribbons are almost identical.

$$\epsilon_{ss} \approx 5 * 10^{-7} \quad (2.4-1)$$

Still it is interesting to measure the order of magnitude (3 to 10 times) between the pressure drop in a rib-roughened environment and that of a smooth canal. This observation tells us that the form drag (section variation) contribution to the pressure drop reaches one order of magnitude over the skin shear drag. High friction factors are driven by spiral geometric turbulence, or macroscopic roughness, and the Reynolds number.

For fully turbulent quadratic flow regime, f is a function of relative roughness only. The hydraulic diameter, while determining the section and mean velocity of the fluid, has no direct implication in the friction, a local phenomenon at the surface of the pipe. It appears only because relative roughness e/D_h is used instead of absolute roughness.

Spirals are said to have roughness similarity if the geometry of the ribs is the same in all aspects except for a scale factor. Only the use of the similarity law would lead to a strict comparison of spirals according to their hydraulic diameter.

Hydraulic diameter D_h

The calculated hydraulic diameter takes into account all the available volume. A physical interpretation of the fluid flow in the spiral will tell us however that all the volume is occupied but part of it cannot be used as flowing canal. The area behind the ribbon where a recirculation occurs does not contribute to the main flow and is called dead corner. It depends on g , α and Re . This detail is neglected in the geometry of the hydraulic diameter.



Figure 2-12: Hydraulic diameter surface S and wetted perimeter w

For the spectrum of spirals studied in this set of experiments, e is kept constant but a varying gap length g leads to slightly varying D_h and relative roughness e/D_h . The choice of D_h versus id or od is significant because it redefines the relative roughness.

D_h is a weighted average between $id\left(1 + \frac{2e}{\pi \cdot id}\right)^{-1}$ and $od\left(1 + \frac{2e}{\pi \cdot od}\right)^{-1}$ depending on the perforation (Figure 2-12).

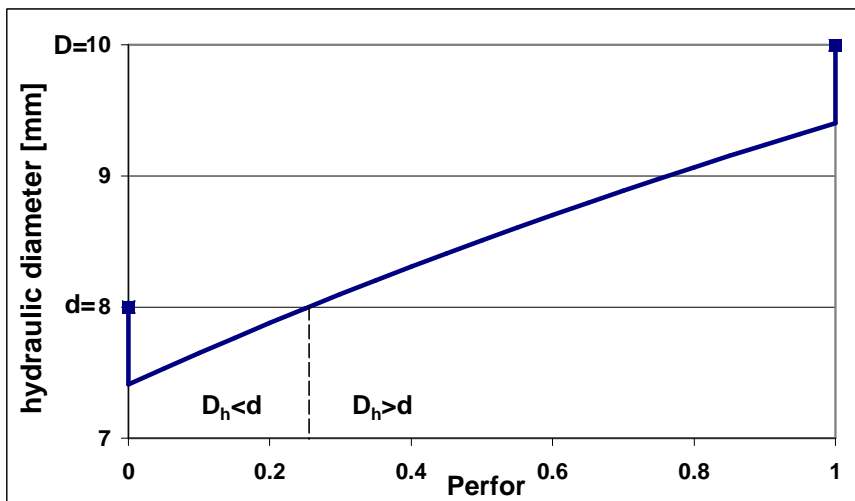


Figure 2-13: Hydraulic diameter evolution as a function of Perfor for a id8-od10 spiral of constant thickness 1mm

$$D_h = 4 \frac{S}{w} = \frac{od^2 - 4e(od - e)(1 - \text{Perfor})}{od - 2e((\pi - 1)/\pi - \text{Perfor})} \quad (2.4-2)$$

The additional lateral ribbon surface tends to bring D_h closer to id and even below id (Figure 2-13). The real space available for the flow –subtracted the dead corners– depends on the flow pattern and on the spiral angle α etc. It was therefore decided not to model the dead corners in order to keep the definition of the hydraulic diameter purely geometric.

D_h has a small incidence on f , but is extremely important to get the dynamic pressure and the global pressure drop. Substituting $w = \frac{m}{\rho S} \approx \frac{4m}{\rho \pi D_h^2}$ in (2.2-4), one gets:

$$\Delta P \approx f \cdot \frac{8m^2}{\rho \pi^2} \cdot \frac{L}{D_h^5} \quad (2.4-3)$$

Note that at quadratic regime where f is constant the pressure drop is varying as m^2/D_h^5 .

S. Nicollet et al. [Nic03] calculated f using od while a study from R. Zanino & al. [Zan00] used id , much closer to the definition of D_h .

Spiral perforation Perfor

The perforation is defined as $\text{Perfor} = t/p$, the percentage of open spiral surface (Figure 2-14). The two spirals represented in Figure 2-15 have the same perforation of 50%. Different gaps will clearly lead to different hydrodynamic behaviours, all other geometric parameters remaining equal. The sample spirals tested in the OTHELLO facility all have the same turn length t . As a result, spiral perforation relates directly to g in this set of samples. Perfor can be shown to have an artificial influence on friction.

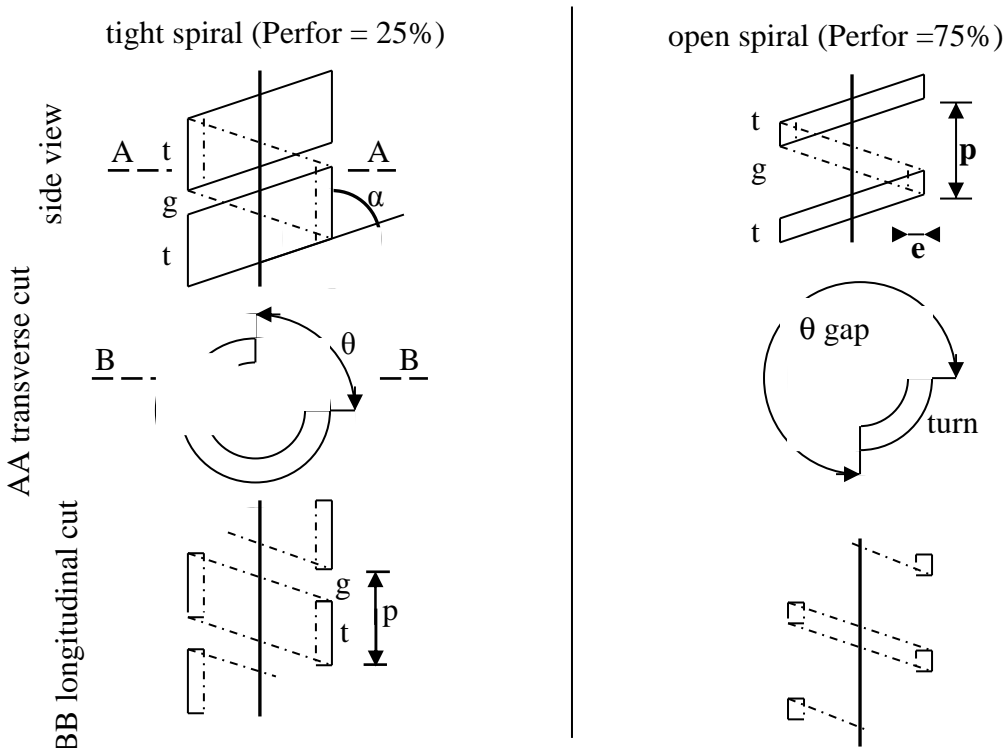


Figure 2-14: Sketch of spiral geometry side view, transverse cut and longitudinal cut

In the case of double channel cable with porous petals surrounding the spiral, perforation certainly has a leading role in the mass transfer across the spiral, combined with the type of vortices in the gaps, the relative roughness e/D_h and the Reynolds number. But concerning the pressure drop, the frequency of the accidents and the nature of the accidents would advantageously replace the perforation.

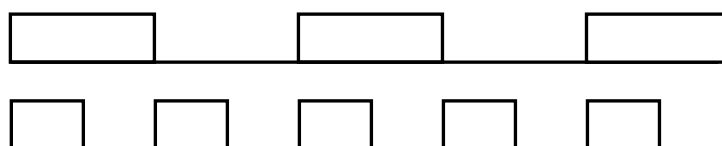


Figure 2-15: Various spiral gaps of equal perforation

Turn length t

The vortex created by the protuberance leads to a reduction of the central section available for the flow right after the gap (Figure 2-16). This vortex is short ($\sim e$), therefore t has little incidence on it as long as $t > e$. Most of all, this vortex has a much smaller part in the overall friction than the form drag in the gap due to the change in diameter and the long vortex. The large area behind the ribbon where a recirculation occurs is a dead corner that does not contribute to the main flow [Lew75, Kakaç].

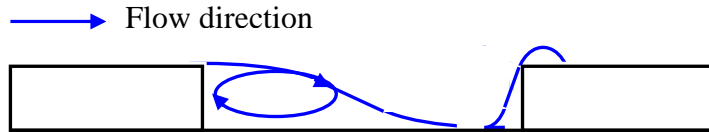


Figure 2-16: Average turbulent streamlines in spiral gap

Sketches of streamlines in Figure 2-16 are time average positions of turbulently moving and intermittent phenomena, including reverse flows and vortices.

Because form drag and vorticity effects have a much greater impact on ΔP than the shear drag, t has a secondary role compared to g . The gap length, which dominates the physical type of flow and turbulence in the gap hence the form drag, is one of the leading factors determining the total friction coefficient.

Gap and ratio g/e

While g is an important parameter, the flow pattern in the gap depends on e also: There can be a full reattachment with a growing boundary layer (Figure 2-17 a), just reattachment (Figure 2-17 b) or vortices independent of e (Figure 2-17 c) according to Webb [Web71, Kakaç].

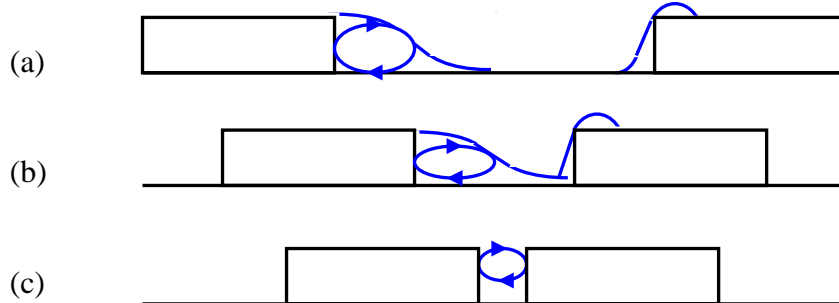


Figure 2-17: Reattachment patterns inside spiral gap

Hydraulic models are always based upon non-dimensional properties. The ratio g/e is thought to provide the general type of perturbation in the gap, while the Reynolds number and the relative thickness are important to the shape and frequency of the vortices.

The aspect ratio g/D_h does not offer a direct physical meaning, but notice that this dimensionless parameter is the product $(g/e)*(e/D_h)$, where both factors are already regarded as physically significant.

For small g/e , the vortex in the gap does not reach the depth e , and e/D_h does not evaluate the relative roughness anymore: only the gap upper part is in this case subjected to turbulent vorticity. In this case, g alone or g/D_h is the relevant parameter.

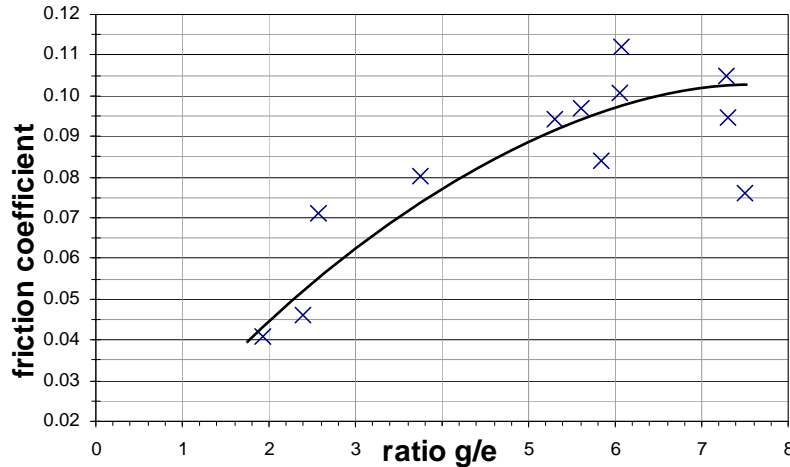


Figure 2-18: Influence of g/e on experimental spiral friction factor
The trend curve rises and is expected to fall again beyond $g/e \approx 9$

According to literature using square ribs with $t = e$ [Lew74], the most unfavorable p/e – leading to a local maximum of the roughness function and minimum the friction factor – is reached at the value $p/e \approx 10$. We can transfer this maximum to a value of $g/e \approx 9$ using the transformation (for $t = e$):

$$\frac{p}{e} = \frac{g + t}{e} = g/e + 1 \quad (2.4-4)$$

Above this limit, form drag is constant and shear drag becomes non-negligible. The spatial frequency is expected to drive f and the friction factor slightly drops as g/e increases.

This maximum is beyond the range of spirals g/e tested, but an observable behaviour change also occurs around $g/e = 3$ in Figure 2-18. This transition can be attributed to the physics of the drag led by vortices of a size directly proportional to g when g is small enough for the vortices not to reach the depth e . Above a certain threshold, for example $g/e = 3$, the boundary layer reattaches to the pipe in the spiral gaps. Between 3 and 10, reattachment pattern is varying. Above $g/e = 10$, reattachment patterns are similar: a friction layer grows in the gap and the singularity frequency becomes a leading parameter. Diaphragms of nearly identical singular friction (typically $\Delta P = \left(\frac{S_{id}}{S_{od}} - 1 \right)^2 \frac{1}{2} \rho U^2$) create turbulence at a given spatial frequency. Because our study is based on samples of high frequency without reattachment and constant thickness driving $\left(\frac{S_{id}}{S_{od}} - 1 \right)^2$, this interpretation of the observed phenomenon cannot be properly validated.

Period and spatial frequency

The friction due to small-scale roughness is negligible compared to the form drag due to large-scale roughness. Hence g is more significant than t to understand the mechanics of the drag because most of the form drag effects take place in the gap. As a result, the period p is not as adequate as the gap to characterise friction. g is the decisive parameter hidden behind p , but many studies using $t \ll p$ or t constant obtain interesting correlation with p/e nonetheless.

Beyond the critical value of $g/e \approx 10$, the singularities do not vary significantly as a function of g/e anymore, but the frequency of accidents takes more and more influence. At large period

values, the singularities become uncorrelated and we have three separate phenomena: shear stress on the external diameter on a length smaller than g , shear stress on the internal diameter on length t , and form drag once per period.

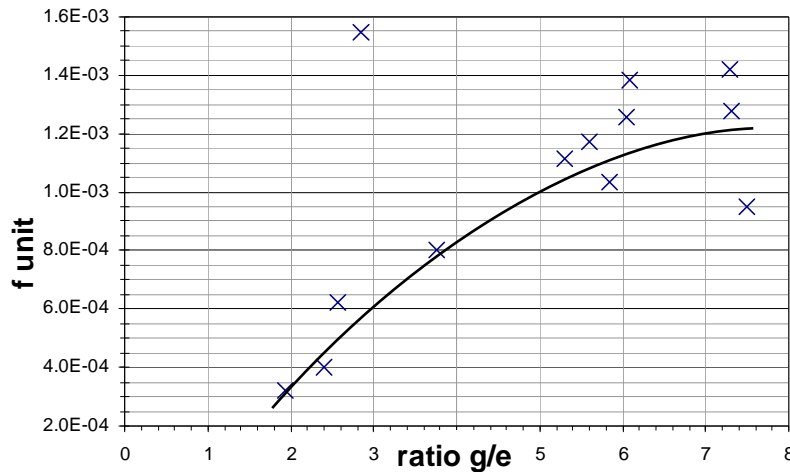


Figure 2-19: Unit friction coefficient as a function of g/e

Notice the aberrant datapoint on top, from S10 discarded because of asymmetry

Because the singularities have much more hydraulic significance than the linear friction unless the friction lengths considered are multiplied by a factor 10, the number of these accidents is a key parameter. the singularity frequency $1/p$ is defined. It is especially significant when the accidents are similar: same g/e and varying t or for g/e above a certain threshold (at least 10) where the form drag becomes constant. Neglecting linear shear, the unit drag coefficient $f_{\text{unit}} = f \cdot p$ –friction coefficient per singularity– could be expected to be constant. This consequence is not observed in Figure 2-19 because of the measly values of g/e .

The predominating form drag could be modelled as a series of diaphragms of constant spatial frequency although the ribs would be parallel with a “spiral” angle $\alpha=90^\circ$, which is impossible in a spiral. A singularity here consists of both section augmentation and reduction. A singularity is independent of another if the distance in-between is at least 7 to 10 times the pipe diameter. If not, the velocity profile is affected and the singular pressure drop is usually reduced. In this case, formula (2.3-5) allowing to calculate ΔP for a singularity cannot be used, or would need to be altered by a proximity factor. Spirals are a good example of non-independent singularities, with ribs in the hydraulic shadow of each other.

$$\Delta P = \zeta \frac{1}{2} \rho V^2 \quad (2.4-5)$$

A diaphragm model does not seem indicated for spirals with a great frequency of hydraulic accidents. Diaphragm friction is much higher than spiral friction.

Spiral cross-sectional shape

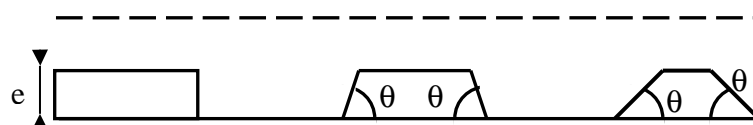


Figure 2-20: Ribbon attack angle

Edges shape (Figure 2-20) remains square and its angle $\theta=90^\circ$ perpendicular to the flow. Although the diaphragm interpretation is unsatisfactory, a hydraulic section reduction coefficient α is inspiring: the edges of the spiral cross-section could be accommodated to reduce both the section reduction and the gap turbulence [Mey79, Saj95]. Just like a wing, a rounded inside leading edge is necessary to avoid going into a stall. In other words, flow separation leads to a reduction of the section available for the flow and surely augments pressure drop while reducing heat transfer between the spiral and the fluid.

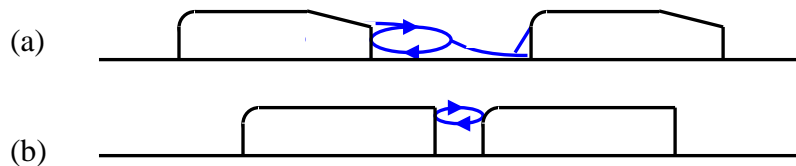


Figure 2-21: Ideal spiral cross-section with edges alteration

If flow reattachment occurs in the gap, the trailing edge should also be bevelled so that the flow leaving the turn tangentially will result in a reduced thickness e from the hydraulic point of view, with less vortex shedding (Figure 2-21 a). If no reattachment occurs however, the trailing edge should be kept rectangular to keep the gap small and the spiral as close to the smooth pipe as possible (Figure 2-21 b). This proposed geometry would still need to comply with fabrication methods and undergo further pressure drop testing.

Coolant is flowing from the center to the ends of pancakes, so the cable is necessarily symmetrical to optimise flow in both directions. The edge is an important parameter. Edge shape seems but a detail, and no variation of edge geometry was conducted. Nevertheless, it is advisable to have smooth round edges.

Spiral angle α

Spiral angle α may induce a mild axial rotation of the flow; this effect is not specifically quantified in the literature. It may contribute to the fact that measured friction is not as unfavourable as diaphragms perpendicular to the flow. Han showed that friction drops with the angle α , while the Stanton number (and consequently the heat transfer) remains almost constant for values of α above 50° in the studied surfaces [Han78]. The angle varies only from 63.9° to 77° in the set of spirals benchmarked here so influence of α cannot be extracted. Because existing models take α into account, this available correlation is used.

Parameters retained

Many parameters, while more simple to grasp or visualize are not relevant or would be poor choices for friction interpretation. Choices must be made in the vast array of variable parameters.

The number of unrelated macroscopic parameters necessary to fully characterise a rectangular ribbon spiral is five. Four adimensional independent parameters and one length are enough to know all other characteristics, hence its hydraulic behaviour:

- the hydraulic diameter D_h , calculated using the wetted perimeter and flow surface in the cavities
- the relative rugosity e/D_h (also called rib roughness)
- the shape of the cavities g/e (related to the perforation g/p),
- the angle of the spiral α ,
- the spatial frequency of hydraulic singularities (related to the period p)

Table 2-7: Advanced spiral geometric parameters (calculated from geometry and from Re)

| Spiral | Diameter Dh [mm] | Roughness e/Dh | Perforation % | Cavities g/e | Angle α [degrees] | Spatial freq. 1/p |
|------------|------------------|----------------|---------------|--------------|--------------------------|-------------------|
| Showa | 9.93 | 0.101 | 27.7 | 2.40 | 77.0 | 115.6 |
| Cortaillod | 10.48 | 0.095 | 44.9 | 5.30 | 72.8 | 84.7 |
| PFCI | 9.95 | 0.100 | 24.3 | 1.93 | 78.1 | 126.1 |
| S10 | 8.07 | 0.124 | 31.3 | 2.85 | 73.8 | 109.9 |
| C10 | 8.20 | 0.122 | 47.3 | 5.84 | 68.0 | 81.0 |
| I10 | 8.57 | 0.117 | 53.8 | 7.29 | 66.7 | 73.9 |
| S9 | 7.64 | 0.131 | 29.3 | 2.57 | 73.7 | 114.0 |
| C9 | 8.18 | 0.122 | 48.4 | 6.05 | 67.7 | 80.0 |
| I9 | 8.24 | 0.121 | 54.1 | 7.31 | 66.0 | 74.0 |
| S8 | 6.18 | 0.162 | 37.5 | 3.75 | 68.0 | 100.0 |
| C8 | 6.39 | 0.156 | 46.3 | 5.60 | 64.1 | 82.6 |
| I8 | 6.53 | 0.153 | 49.3 | 6.08 | 63.9 | 81.1 |
| I7.6 | 6.38 | 0.125 | 48.0 | 7.50 | 62.4 | 80.0 |

2.4.2 Elaboration of the model

Interpretation of the results is based upon literature assessment of the relevant parameters, and includes reduced coordinates that are used by many authors.

Friction function and roughness Reynolds

In order to account for the friction similarity and reduce the spread of the data, Nikuradse [Nik50] used a change the coordinates (Re , f) into (e^+ , R^+) to reduce data spread, defining the roughness Reynolds e^+ (2.4-6):

$$e^+ = \frac{e}{D_h} Re \sqrt{\frac{f}{2}} \quad (2.4-6)$$

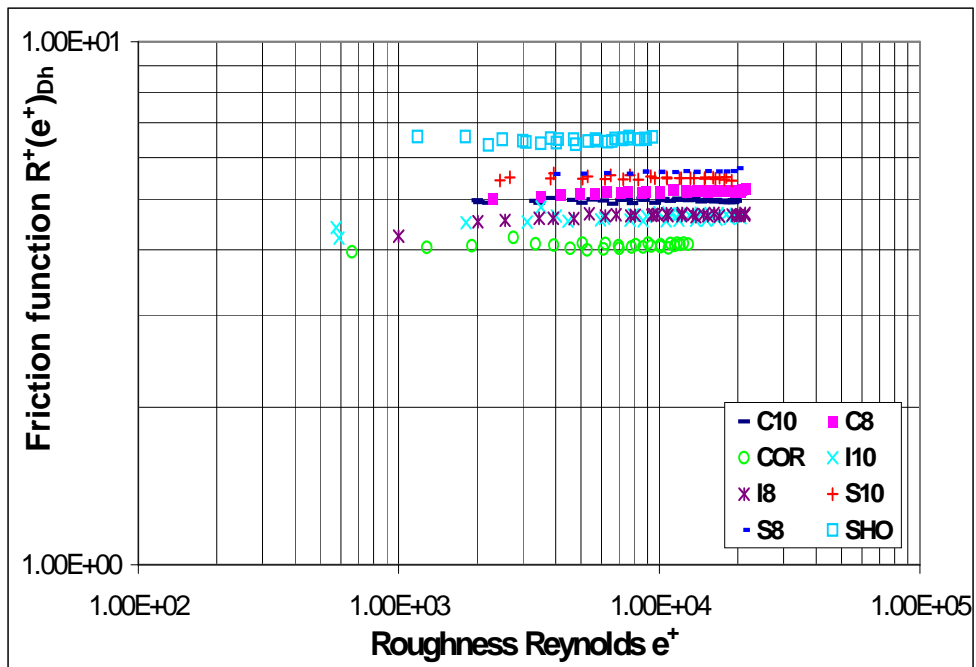
and proposed a roughness function $R^+(e^+)$ (2.4-7) taking into account the relative roughness:

$$R^+(e^+) = \sqrt{\frac{2}{f}} + 2.5 \ln\left(\frac{2e}{D_h}\right) + 3.75 \quad (2.4-7)$$

For liquid helium at 0.5 MPa and 4 K we have the density $\rho = 143 \text{ kg/m}^3$ and the dynamic viscosity $\mu = 4 \times 10^{-6} \text{ kg.m}^{-1}.s^{-1}$. Values of velocity of the order of 1m/s and a diameter of about 1cm yield: $Re \approx 400\ 000 > 10^5$, hence a quadratic flow regime. In this case ($Re > 10^5$ or $e^+ > 2 \times 10^3$) the quadratic or fully turbulent regime is characterised by a constant friction coefficient, R^+ is therefore not a function of the roughness Reynolds e^+ anymore.

This complex change of coordinates leads to Figure 2-22, which replaces favourably Figure 2-9 without any loss of information. The entire data set is here represented in this new coordinate system, where the data spread is reduced. Surprisingly the 10-12 mm spirals SHO and COR have an either much better or worse behaviour.

Webb & al. [Web71] used the roughness function $R^+(e^+)$ and found for $P/e > 10$ a successful friction correlation expressed as $R^+(e^+) = k_1 \left(\frac{P}{e} \right)^{k_2}$. Because of g/e is more physical, and as chosen by Zanino [Zan00], p/e is replaced by g/e .

Figure 2-22: Re^+ with hydraulic diameter D_h vs. e^+ for all spirals

Regression on g/e

A complete regression of $R(e^+)$ needs to exploit all the parameters involved in the physical process of the friction: Re or e^+ , θ , g/e and α . The model of Han, based upon lower Reynolds number experiments, was created of the form (2.4-8) [Han78]:

$$R^+ = 4.9 \left(\frac{e^+}{35} \right)^m \left(\frac{\theta}{90} \right)^{-0.35} \left(\frac{p}{10e} \right)^n \left(\frac{\alpha}{45} \right)^{-0.57} \quad (2.4-8)$$

- f and $R^+(e^+)$ are considered constant for quadratic flows, unlike previous spiral empirical laws [ITER05], hence e^+ is not longer a variable.
- θ has the invariant value of 90° , for spirals tested in this study all have rectangular cross-section; its effect is therefore left as previously modelled.
- The cavities shape g/e , physically linked to the turbulence patterns, replaces advantageously p/e .
- Dependence on α remains unrevised given its narrow variation range here (19% variation between 62.4° and 77°)

As α increases, the friction factor drops faster than does the Stanton number, indicative of heat transfer. Gee and Webb found that the value $\alpha=45^\circ$ provides the maximum St/f [Gee80]. A power regression (2.4-9) provides the friction power dependency on the parameter g/e , with the coefficient of determination $R^2=82.4\%$. This expression provides a full friction function correlation (2.4-10) at large Reynolds numbers [Ren06-3]:

$$R^+(e^+) * \left(\frac{\alpha}{45} \right)^{0.57} = 10.9 \left(\frac{g}{e} \right)^{-0.31} \quad (2.4-9)$$

$$R^+ = 10.9 \left(\frac{\theta}{90} \right)^{-0.35} \left(\frac{\alpha}{45} \right)^{0.57} \left(\frac{g}{e} \right)^{-0.31} \quad (2.4-10)$$

The understanding of the friction phenomenon and choice of parameters to model pressure drop may be biased by the fact that the spirals tested in this research have constant e , almost constant t and limited extension of g . Because of the limited studied geometry range, results interpretation and validity is not expected to be transposable to another geometry.

Influence of Reynolds number

We have seen in sections 2.2.3 and 2.3.2 that spirals friction factors slightly decrease as Reynolds increases. Blasius provided an explicit expression (2.2-1) of this skin layer Reynolds dependence. When this shear drag Blasius friction is subtracted from the data, spiral friction factors become independent of Reynolds (Figure 2-23).

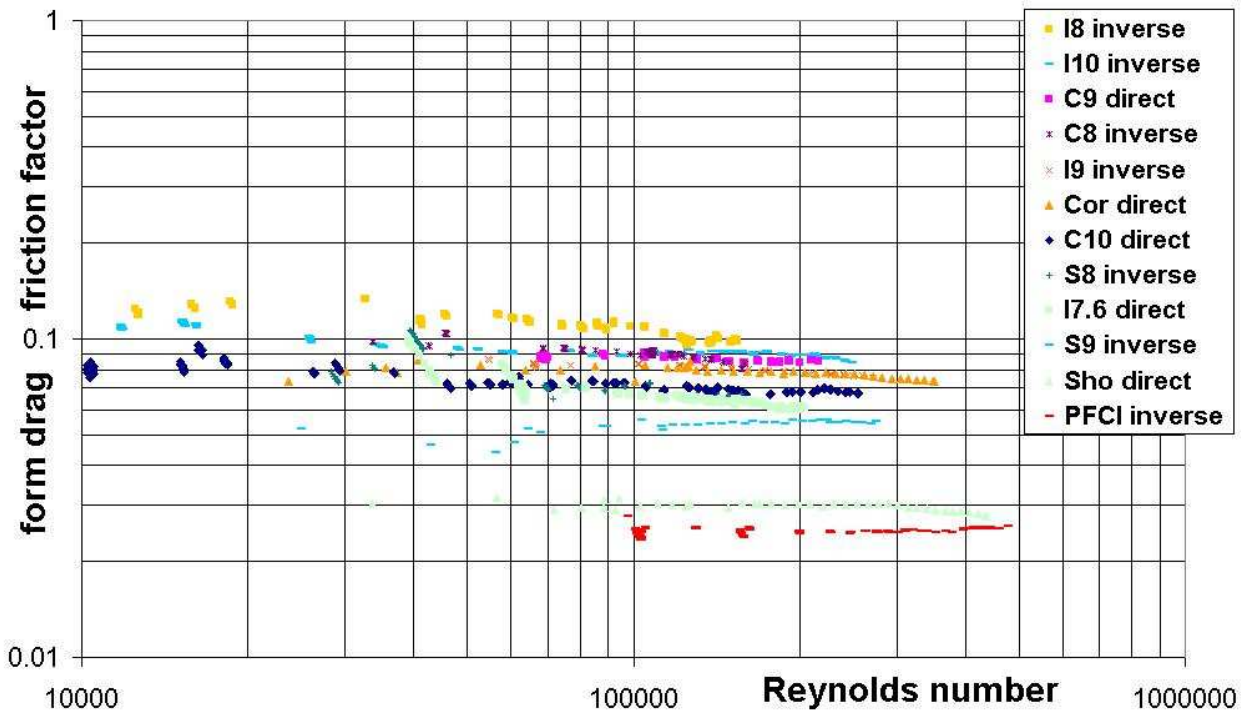


Figure 2-23: Drag component of the spiral friction factor

The total friction factor is considered to be the sum of shear and form drag friction coefficients:

$$f_{\text{spiral}} = f_{\text{shear drag}} + f_{\text{form drag}} \quad (2.4-11)$$

A regression performed on the form drag component (Figure 2-24) leads to (2.4-12):

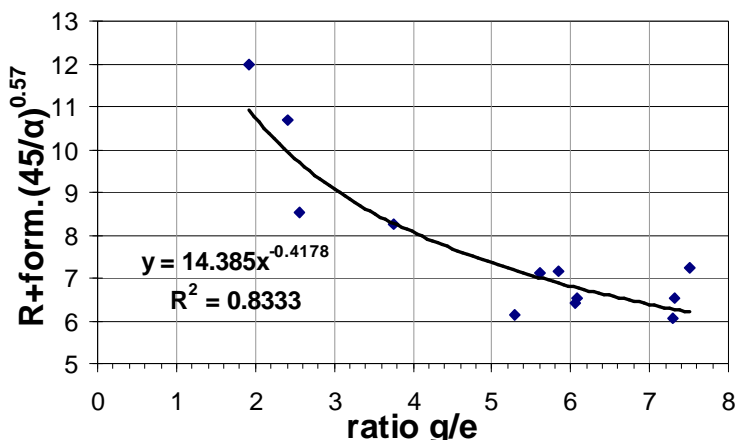


Figure 2-24: Dependence on g/e and α of the form drag friction function R^+_{form}

$$R^+ = 14.4 \left(\theta / 90 \right)^{-0.35} \left(\alpha / 45 \right)^{-0.57} \left(g / e \right)^{-0.42} \quad (2.4-10)$$

2.4.3 Application

Predictive friction analysis

The friction function definition (2.4-5) is reversed, using correlation (2.4-10), which allows to propose (2.4-11) as a predictive assessment tool for the form drag of a regular spiral of rectangular cross-section in a quadratic turbulent flow.

$$f_{\text{form drag}} = \frac{2}{\left(14.4 \left(\frac{\theta}{90} \right)^{-0.35} \left(\frac{\alpha}{45} \right)^{-0.57} \left(\frac{g}{e} \right)^{-0.42} - 2.5 \ln \left(\frac{2e}{D_h} \right) - 3.75 \right)^2} \quad (2.4-13)$$

Friction factors function trends are given in Figure 2-25 for constant diameters and angles. Experimental data has been added to this graph to serve as indicative values. The cavities shape ratio g/e has a positive influence on friction: to reduce the rough tube friction factor, reduce the gap g.

The spiral was assumed to be inserted inside a smooth tube, similar to the hydraulic test configuration used. This includes a smooth outer diameter in the gap and the possible reattachment of the flow. The reality of a dual channel CICC is quite different: the annular petals form an arch around the spiral with edges free for the flow.

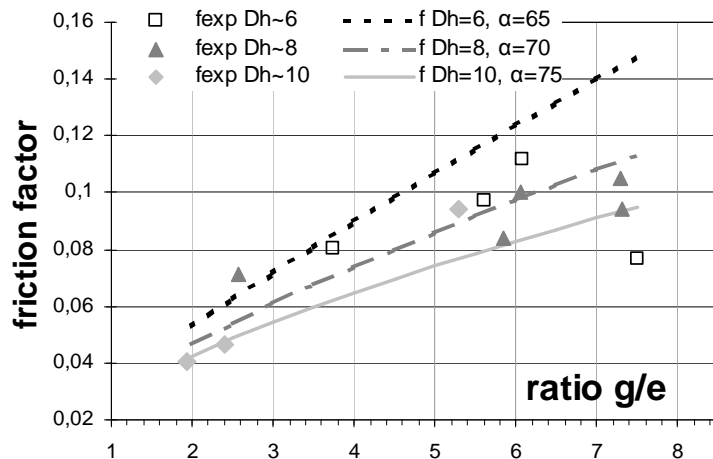


Figure 2-25: Friction factors predictions (shear at $Re = 2 \times 10^5$ + form drag) for an array of hydraulic diameters D_h and spiral ribbon angles α (at constant attack angle $\theta = 90^\circ$) as a function of spiral gap to thickness ratio.

Rigorously each spiral experimental data has a distinct D_h and α

It is complicated to measure simultaneously the respective channel mass flow rates. Channel mass flow balance is calculated, but uncertainty remains in the empirical law used. Similarly, it is Herculean to evaluate mass exchange between annular and central channels (through the use of a colour marker such as Methylen blue in an open circuit). Of course the respective mass flows strongly influence physical phenomena and heat transfer rates.

Conclusion on pressure drop

The annular channel hydraulic model is preserved.

Central channel spirals pressure drop is tested and provides a database in pressurised nitrogen and water. Spiral modelling parameters are proposed: hydraulic diameter D_h , gap over thickness g/e , relative thickness e/D_h , spiral angle α , as well as the drag singularity frequency $1/p$. The influence of these parameters on the pressure drop is demonstrated when possible and a model is given to guide ITER design. Additionally the attack and trailing edge angle θ or the specific cross-section shape of the spiral and the Reynolds number are needed for a complete hydrodynamic picture of the channel.

Spiral pressure drop is subdivided into shear friction (Blasius model) and form drag, which is modelled from a friction function correlation. The following hydraulic pressure drop prediction model is proposed for CICC spirals:

$$f_{spiral} = \frac{1}{(1.8\ln(Re)-1.64)^2} + \frac{2}{\left(14.4\left(\frac{\theta}{90}\right)^{-0.35}\left(\frac{\alpha}{45}\right)^{-0.57}\left(\frac{g}{e}\right)^{-0.42} - 2.5\ln\left(\frac{2e}{D_h}\right) - 3.75\right)^2}$$

Improvement of the CICC central channel will be obtained as a compromise between mechanical and heat exchange properties: turbulence is hydraulically negative, but can have a positive influence on thermal properties by intensifying convection coefficients.

3 Interchannel heat exchange

Temperature difference between the two channels leads directly to an increase in the temperature of the superconducting strands, and therefore to a loss of temperature margin for the properties of the strands, as compared to an isothermal conductor. We must ensure good thermal coupling so that helium circulating at higher velocity in the thermal exchanger central channel will efficiently extract power from the annular channel.

Thermal exchanges are here studied in order to understand and model both nominal superconducting conductor temperature operation and transient forced flow coil cooling, such as phases of coil current increase and decrease.

In this chapter the steady state thermal behaviour of a CICC is first modelled (3.1) and experimented (3.2); the transient behaviour is similarly modelled and tested (3.3 & 3.4). These experimental investigations lead to an analytical heat transfer model (3.5).

3.1 Steady state analysis [Ren06-1]

The principle of thermal behaviour investigation always consists in using a heat excitation of the conductor and in measuring resulting temperatures on a real size dual channel conductor. In a steady state CICC behaviour investigation, interest lies in the channels temperature homogenisation downstream from the heat excitation length characterised by a strong temperature imbalance.

3.1.1 Principle and hypothesis

Under a series of simplifying assumptions a simple bithermal model of the CICC allows to fully solve the heat equation in steady state [Nic04ICEC]:

- invariant mass flow distribution, and
- each channel isothermal,
- temperatures invariant in time,
- no longitudinal heat transport in metallic parts or fluid other than mean mass transport,
- constant heat capacity for small temperature variations,
- perfect heat distribution.

Let us consider a dual channel conductor, uniformly heated along a length L , for the purpose of modeling an experimental test configuration (Figure 3-1):

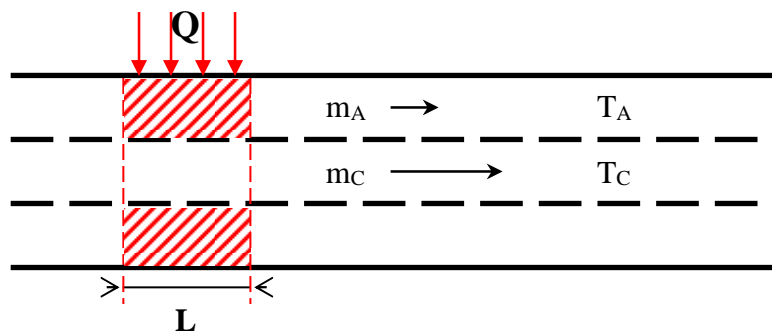


Figure 3-1: Heat flux model on the CICC bundle region

Supposing the annular (T_A) and central (T_C) temperatures are uniform in each cross-section, their spatial rates of change is given by:

$$\begin{cases} \dot{m}_A C_p \frac{dT_A}{dx} = -H p(T_A - T_C) + Q \\ \dot{m}_C C_p \frac{dT_C}{dx} = H p(T_A - T_C) \end{cases} \quad (3.1-1)$$

where the distributed heat source Q is present on a heated length L , \dot{m}_A and \dot{m}_C designate the annular and central mass flow rates, $C_p = C_p(T_{out})$ the specific heat calculated at the common outlet temperature and H the global heat exchange coefficient through the spiral of external perimeter p . Spiral external diameter od is used, although a mean perimeter would be more physical, in order to allow a valid comparison of spirals of different thickness for a given cable central channel available space.

Because we consider a boundary condition of uniform heat load, and the longitudinal conduction in the jacket is neglected, we have a jacket temperature (T_J) difference imposed under the resistive heaters by the heat flux condition:

$$T_J - T_A = \frac{Q}{h_A p_{AJ}} \text{ in the heated zone} \quad (3.1-2)$$

where h_A is the annular channel convection coefficient. $\Delta T_{JA} = 0$ outside the heated zone. In fact, for a CICC under AC field losses, heat load is brought directly to the metallic parts in the annular channel, so jacket and annular temperatures are expected to concord everywhere. We define the annular-central heat exchange characteristic length as [Duc04]:

$$\Lambda = \frac{\dot{m}_A \dot{m}_C C_p}{H \cdot p \cdot m} = \frac{\alpha_A (1 - \alpha_A) m C_p}{H \cdot p} \quad (3.1-3)$$

Λ is strongly dependant on the flow repartition stepping in with the fraction of annular mass flow percentage α_A . The system of equations (3.1-1) combines into (3.1-4).

$$(T_A - T_C) - \Lambda \frac{d(T_A - T_C)}{dx} = -\beta_A \Lambda \quad (3.1-4)$$

The power Q is hidden behind β_A , rate of temperature increase when the heat load is supported by the annular mass flow only, $\beta_A = Q / (\dot{m}_A C_p)$.

3.1.2 Heat equation solution

In the case of a semi-infinite heater, the solution of (3.1-4) for annular and channel temperatures is given by the everywhere valid temperature difference:

$$(T_A - T_C) = \beta_A \Lambda (1 - e^{-x/\Lambda}) \quad (3.1-5)$$

leading to the temperatures system:

$$\begin{cases} T_C = \beta_{iso} \left(x - \Lambda \left(1 - e^{-x/\Lambda} \right) \right) \\ T_A = \beta_{iso} x + (\beta_A - \beta_{iso}) \Lambda \left(1 - e^{-x/\Lambda} \right) \\ T_J = \beta_{iso} x + (\beta_A - \beta_{iso}) \Lambda \left(1 - e^{-x/\Lambda} \right) + \Delta T_{AJ} \end{cases} \quad (3.1-6)$$

where ΔT_{AJ} is given by (3.1-2), and β_{iso} is the rate of temperature increase in an isothermal conductor, $\beta_{iso} = Q / (\dot{m} C_p)$

For a finite heater, the temperatures solutions for bundle [Nic02], center and jacket [Ren04-2] are (see Appendix V):

- before the heated region $[-\infty, 0]$:

$$T_c = T_A = T_J = 0 \quad (3.1-7)$$

- in the heated region $[0, L]$, (3.1-6) applies.

- after the heated region $[L, +\infty]$: equation (3.1-1) finds a solution with:

$$\begin{cases} T_c = \beta_{iso} L - \beta_{iso} \Lambda \left(1 - e^{-L/\Lambda}\right) e^{-(x-L)/\Lambda} \\ T_A = T_J = \beta_{iso} L + (\beta_A - \beta_{iso}) \Lambda \left(1 - e^{-L/\Lambda}\right) e^{-(x-L)/\Lambda} \end{cases} \quad (3.1-8)$$

These equations are illustrated in Figure 3-2. Outside the heated region, the jacket temperature is equal to the bundle temperature. The conductionless assumption ($\lambda \rightarrow 0$ in the jacket) leads to a non-physical temperature discontinuity at the end of the heated zone. Practically, conductionless means the temperature gradient in the jacket due to conduction varies over a characteristic length small compared to Λ . The annular temperature is continuous but its derivative experiences discontinuities at the heater ends. The central temperature is continuous and can be derived with an inflection point at the heater ends.

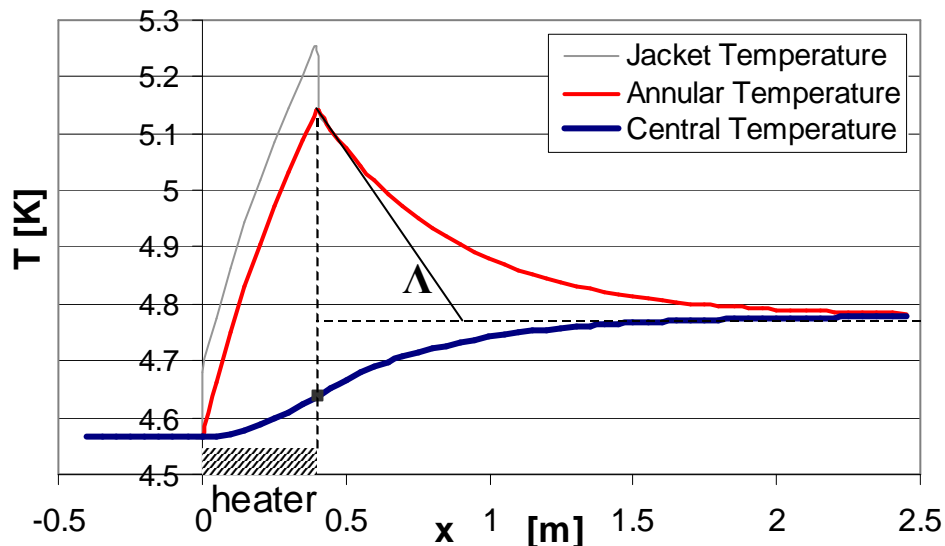


Figure 3-2: Bithermal conductionless model temperatures

Annular temperature rises sharply on the heating length and homogenises beyond
Central temperature rises slowly, with an inflection point at the end of the heating length.

3.1.3 Applications

From (3.1-6), it is useful to define $T_{iso} = \beta_{iso}x$ as the average cable temperature giving the uniform temperature of mixed helium, considering the conductor is isothermal as a unique channel. From (3.1-5) we know that even with an infinitely long distributed power, the temperature gradient between the two channels can never increase beyond the limit [Duc04thermosiphon]:

$$(T_A - T_C)_{max} = \beta_A \Lambda = \frac{Q\Lambda}{m_A C_p} \quad (3.1-9)$$

where the temperatures are given by:

$$T_A = T_{iso} + (T_A - T_C)_{max} \frac{m_C}{m} (1 - e^{-x/\Lambda}) = \beta_{iso}x + \frac{Q\Lambda}{m_A C_p} \frac{m_C}{m} (1 - e^{-x/\Lambda}) \quad (3.1-10)$$

and similarly:

$$T_C = \beta_{iso}x - \frac{Q\Lambda}{m_A C_p} \frac{m_A}{m} (1 - e^{-x/\Lambda}) \quad (3.1-11)$$

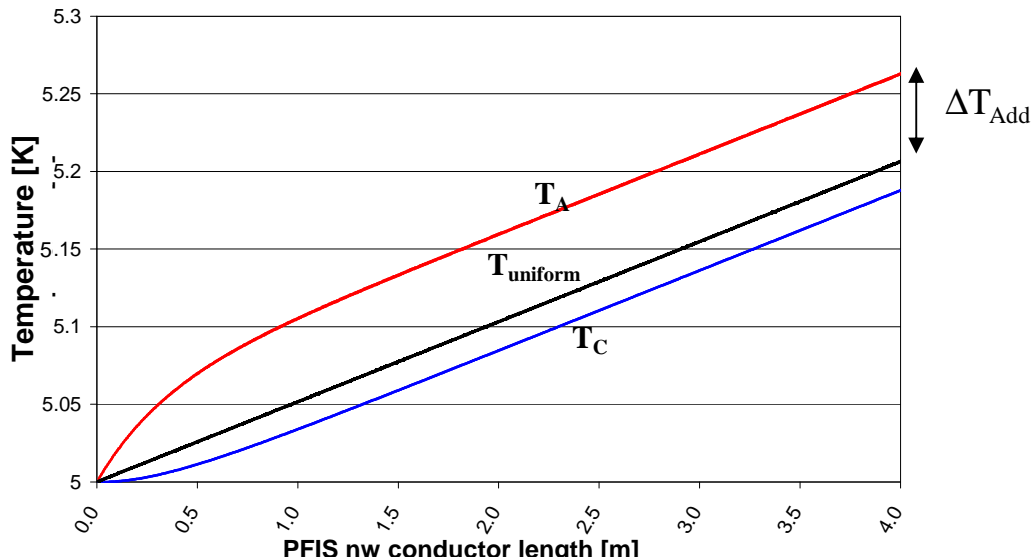


Figure 3-3: Evolution of annular, central and uniform temperatures in a steady state infinite annular heating environment: the difference reaches an asymptotic value.

Illustration for the PFISnw conductor subject to a heat distribution of $Q = 2 \text{ W/m}$

This is illustrated in Figure 3-3, where the temperature difference between annulus and center reaches an asymptotic value after a few Λ . This very important result means we can assert an upper boundary to interchannel temperature difference and thus evaluate the maximal acceptable T required at the coil inlet in a given heating configuration in order to keep the superconductor temperature under the appropriate margins from T_{CS} . We will also extract from ΔT_{CA} the maximal density gradient $\Delta \rho_{CA}$ that serves the risk of a thermosiphon discussed in section 4.1.

The characteristic length Λ provides both a measurable value to get H , and physical information on the length necessary to transfer heat from one channel to the other.

Although this additional temperature term $\Delta T_{Add} = (T_A - T_C)_{max} \frac{\dot{m}c}{m}$ seems reasonably small (a few hundredths of Kelvin for TF conductors), it is not taken into account in the ITER coils that only use $T_{uniform}$ at the critical magnetic field location for the superconducting strands.

Hence ΔT_{Add} is to be subtracted directly from the nominal superconducting magnets temperature margins, and may not be negligible compared to these margins.

3.2 Assessment of the heat transfer coefficient in steady state

The purpose is here to experimentally measure the global interchannel heat transfer coefficient H by means of a characteristic length Λ . Compared to hydraulic experiments, heat transfer experimental campaigns are always more difficult to conduct with rigour, because heat transfer is not directly measurable and any heat bridge can lead to a compromised thermal balance through heat leaks. The principle of steady state experiment consists in imposing a heat flux on the conductor jacket and observing the annular temperature decline downstream, as fluid temperature homogenises in the channels.

3.2.1 Preliminary comments on experimental set-up

Spiral thermal properties including mass exchange between central and annular channels can only be assessed in a full CICC sample, where many parameters interfere. It should be possible to evaluate a heat transfer coefficient in a spiral alone, inserted in a tube. But such an experimental campaign would only provide convection coefficients, and the absence of mass exchange in the gaps wouldn't allow a direct comparison with the heat transfer conditions happening in a real conductor.

The HECOL facility, used for the hydraulic characterisation of conductor and spirals, was designed for the thermal characterisation of CICC conductors in pressurised ambient temperature water (Appendix III). The SULTAN facility, operated in supercritical helium by EPFL at CRPP/Villigen in Switzerland, allows electromagnetic as well as thermohydraulic testing of the superconducting cables (Appendix IV).

Full size samples have been used for all hydraulic and thermal tests.

Heat load simulation by annular heaters

Practically, the experimental simulation of heat load deposition is made by external heating of the jacket: this simulation used in steady experimental operation is imperfect and brings questions about the temperature homogeneity of the petals and of heat exchange between helium and jacket.

However this corresponds to the situation of a neutron irradiation which heats mostly the metal of the jacket, and the conductor through convection and further penetration. Solving the complex experimental conditions in the analysis is thus useful for ITER.

Homogeneity of water temperature and thermometer precision

Given the extreme geometric complexity of the annular channel that includes strands twisted in petals, empty corners and eventually wrappings, this anisotropic porous medium is hydraulically turbulent and thermally nearly uniform. Temperature uniformity is obvious in the (ITER) case of strand heating. The temperature homogenisation is generated by forced convection, conduction in the copper, mechanical transposition (various twisting levels) and turbulent fluid advection.

In the experimental facilities, jacket heaters provide the heating simulation of neutronic heating. Temperatures homogeneity in the annular area and inhomogeneity at the channel interface (the spiral) is an imperfect superposition.

The cable jacket has been perforated to place thermometers 1 mm inside the annular channel in the water experiments. Because heaters are located on the jacket, and thermometers make a localised measurement, it is wise to check the thermal transfers to assess both that the annular channel is well heated, and homogeneously thermalised.

The power transmitted longitudinally through conduction in the jacket is proportional to $\frac{\lambda_{ss} A_{ss}}{l}$, where l is a chosen length of CICC, chosen equal to Λ in order to compare to transverse heat transfer, while heat transfer to the bundle is driven by $h_{AJ} p_J l$. These factors appear under a square root in the equations driving the conduction in steel at ambient water temperature:

$$\sqrt{\frac{h_{AJ} p_J \Lambda^2}{\lambda_{ss} A_{ss}}} = \sqrt{\frac{h_{AJ} \Lambda^2}{\lambda_{ss} e_{Jss}}} \approx \sqrt{\frac{46000 * 1.11^2}{15 * 4 * 10^{-3}}} = 971 \gg 1 \quad (3.2-1)$$

which proves –with a theoretical heat characteristic Λ assumption further given in section (3.5)– that conduction should not disturb the heat transfer from the jacket to the annular water, at least on the scale of Λ . The same type of calculation to evaluate conduction in the copper strands at ambient temperature water leads to a much more disputative conclusion:

$$\sqrt{\frac{h_{AJ} p_{Cu} \Lambda^2}{\lambda_{Cu} A_{Cu}}} \approx \sqrt{\frac{46000 * 0.126 * 1.11^2}{400 * 404.1 * 10^{-3}}} = 6.65 \quad (3.2-2)$$

Over the scale of Λ , conduction does not prevail. But if a smaller length of interest is chosen, conduction in the copper may not be negligible compared to heat transfer between copper and water at ambient temperature. Although thermal conditions are not ideal with ambient temperature water, the transmission of energy to the annular channel is much more efficient than longitudinal conduction, which makes the theoretical developments in section (3.1) receivable to model these experiments.

Water density decrease in the bundle region theoretically reduces bundle mass flow but by values so insignificant that this effect can be neglected without any doubt.

Homogeneity of helium temperature and thermometer precision

Two samples tested in SULTAN (Appendix IV) were subject to a thorough thermohydraulic experimental investigation: the Poloidal Field Full Size Joint Sample (PF-FSJS) tested only with downward flow [Dec02-2, Dec03-3], and the Poloidal Field Coil Insert (PFIS), tested in upward and downward flow directions [Duc05].

Contrary to the PF-FSJS, the PFIS is asymmetric because the superconducting subcable petals are 80% wrapped (W80) in stainless steel tape of thickness 0.055mm in the left leg, whereas on the right side these petals have been stripped of their wrappings before insertion in the jacket (NW), which required a slightly higher compaction in order to keep the annular void fraction constant.

Because helium circulation cannot admit leaks, thermometers are located on the cable jacket. They are not ideally distributed because copper conditioning blocks could not be located in the AC losses region where they would heat up from Foucault currents. The stainless steel jacket, trimmed at the sensors locations down to a thickness < 2 mm, has a high thermal diffusivity and negligible thermal inertia compared to supercritical He at 5 K, so jacket measurements can rigorously be assimilated to annular temperatures if appropriately glued.

The same temperature homogeneity question arises for cryogenic helium temperature experiments. Comparing similarly longitudinal conduction to transverse convection leads to:

$$\sqrt{\frac{h_{AJ} p_J \Lambda^2}{\lambda_{ss} A_{ss}}} = \sqrt{\frac{h_{AJ} \Lambda^2}{\lambda_{ss} e_{Jss}}} \approx \sqrt{\frac{1500 * 1.11^2}{0.3 * 4 * 10^{-3}}} = 1230 \gg 1 \quad (3.2-3)$$

in the steel jacket, again with a theoretical Λ from section (3.5), and in the copper strands:

$$\sqrt{\frac{h_{AJ} p_{Cu} \Lambda^2}{\lambda_{Cu} A_{Cu}}} \approx \sqrt{\frac{1500 * 0.126 * 0.5^2}{800 * 404.1 * 10^{-3}}} = 0.38 \quad (3.2-4)$$

Steady state experiments with the central channel blocked could assess whether there is a residual Λ due to metallic conduction. In fact the inertia of superconducting strands is 2 orders of magnitude lower than the enthalpy of helium, which guarantees the stability of the superconductors and limits the thermal influence of metals on the helium temperature.

Transverse conduction in the inhomogeneous bundle region is a weighted average between conduction in copper and in helium. It depends strongly on contact surfaces between the copper strands and on fluid turbulence, and cannot simply be calculated from the void ratio.

Calibration

Thermometers are calibrated from a reference measure before being fixed to the cable. In order to eliminate the Joule-Thomson heating along the CICC, the temperature offsets are measured when the additional heater is turned off, for the same pressure drop. We obtain a (Joule-Thomson) reference for each thermocouple, which is subtracted from temperature readings with annular heating in order to be left with the sole temperature elevation from AH (Figure 3-4). This calibration deals with temperature rise from the Joule-Thomson expansion and zeroes sensor offsets.

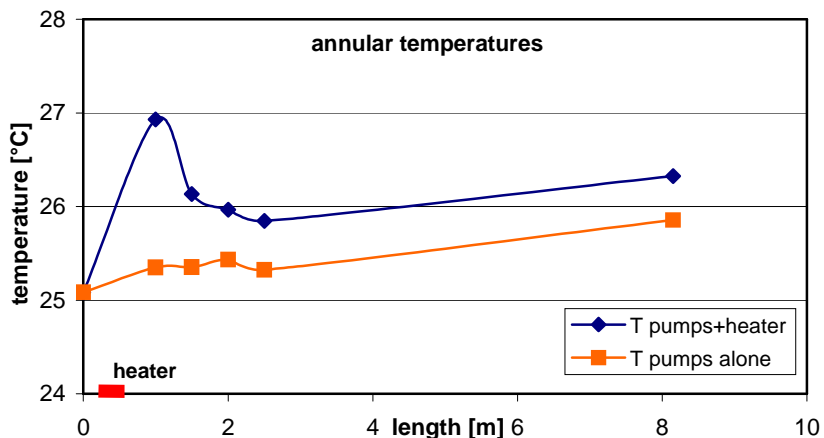


Figure 3-4: Raw heated vs. non-heated annular temperature evolution in water at 0.85L/s

Temperature differences should be large enough to be accurately measurable, and as small as possible to avoid undesirable heat leaks and non-linearities, i.e. ~ 2 K in water and ~ 0.5 K in helium. Low mass flow rates are required on some water experiments to reduce temperature differences, a necessity that leads to shorten the Reynolds number and draw away from the validity domain of the annular friction Katheder formula as well as from the Prandtl similitude for cryogenic cooling.

Similarly, SULTAN temperature data are first linearly calibrated using reference data with and without heating (Figure 3-5 for SULTAN). For further accuracy and to discard Joules-Thomson perturbation, only temperature differences are used [Rou04].

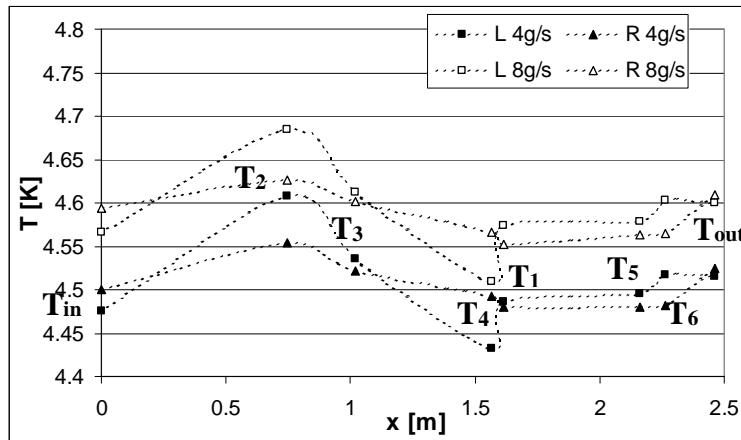


Figure 3-5: PF-FSJS raw helium temperatures data without any heat source showing the need for calibration

Following calibration inconsistency on the PFIS, temperature data are first linearly normalized using reference data from external temperature sensor with and without heating [Rou04]. For universality and further accuracy, temperatures differences are used and reduced to variations between 0 and 1. Indeed absolute values are not needed to interpret experimental temperature variations velocities and offsets.

3.2.2 Measure of the heat transfer coefficient in water

Theoretical calculations of heat transfer coefficient H , used to compare with experimental data, are developed in section 3.5. In the bundle region $f=f_{\text{Katheder}}$ with a void ratio of 0.36 is in principle valid for Re within [1000; 6000] while solving the equilibrium of bundle and central pressure drop leads to a more laminar Reynolds value (Experimental variable parameters are provided in Table 3-1).

Table 3-1: Water thermal experiments properties

| Experimental parameters | | | Model parameters | | |
|---------------------------------------|-----------------------|-------|-------------------------|--------|--------------------|
| parameter | value | unit | parameter | value | unit |
| T | 303 | K | α_A | 25 | (%) |
| P_{in} | 1.525 | MPa | \dot{m}_A | 0.20 | kg/s |
| P_{out} | 0.511 | MPa | \dot{m}_C | 0.61 | kg/s |
| $\Delta P_{measured}$ | 1.014 | MPa | $\Delta P_{calculated}$ | 1.41 | MPa |
| \dot{m} | 0.81 | kg /s | f_A | 0.456 | - |
| Q | 8 630 | W/m | Re_A | 337 | - |
| Total power | 3.28 | kW | h_A | 46000 | W/m ² K |
| $p=p_{bc}=\pi \times D_{mean}$ | 0.0374 | m | f_C | 0.136 | - |
| $p_{bj}=\pi \times 40 \times 10^{-3}$ | 0.126 | m | Re_C | 84700 | - |
| id | 9.9×10^{-3} | m | h_C | 130000 | W/m ² K |
| D_h | 10.9×10^{-3} | m | H | 17200 | W/m ² K |
| Perfor | 28 | (%) | H_p | 580 | W/mK |
| C | 4180 | J/kgK | Λ | 1.10 | m |

h_c is the convection coefficient inside the central channel, and one of the thermal resistances in series composing the global interchannel heat exchange coefficient $H=H_{AC}$. h_A –used on the jacket and on the spiral side– and the heat load impose the temperature difference between jacket and bundle in the heated zone: $\Delta T_{AJ}=1.47K$.

Model and measurements comparison

In Figure 3-6, experimental data points are plotted together with central channel and annular region model temperatures. The final mixing temperature is expected to be:

$$\Delta T_\infty = \beta_{iso} L \approx 2.56 * 0.38 = +0.97K \quad (3.2-1)$$

The asymptotic mixed temperature expectation shows excellent similitude with measures. We observe that the model temperature curve does not appropriately fit the observed temperature evolution along the bundle. After extracting all data from these temperature profiles, possible explanations shall be brought.

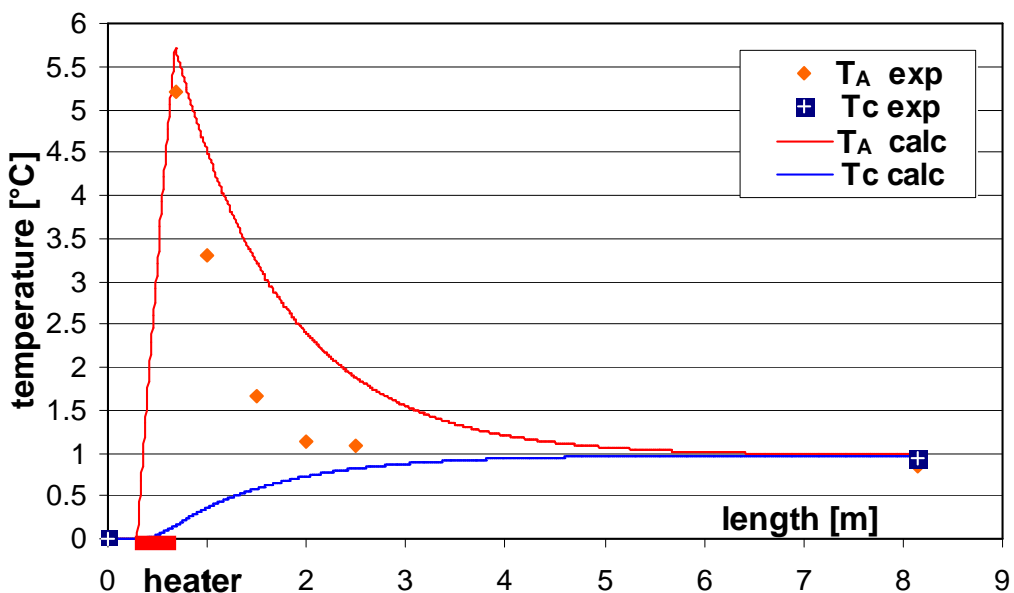


Figure 3-6: Model and measured temperatures evolution in central (T_c) and annular (T_A) regions; water at 0.85 L/s and $T=30^\circ C$

Even if supposing annular and central channel are thermally isolated in the heated zone the annular temperature should never rise above:

$$\Delta T = \frac{Q \cdot L}{m_A \cdot C_p} \approx \frac{3280}{0.21 * 4180} = 3.74K \quad (3.2-2)$$

A temperature difference almost as high is observed at a significant distance from the heater. Conduction in the jacket seems to bring some of the heat load downstream of the heater, furthermore the location of the thermocouples near the jacket may strongly bias the bundle measurement: the temperature recorded may not be the average bundle temperature but a temperature closer to that of the jacket.

If we consider annular temperature to be non homogeneous, whether because of the dead corners between the wrappings and the jacket or because of the laminar flow and poor mixing within each petal, we expect an external bundle temperature higher than the internal one. This would artificially stimulate a higher temperature that would drop back with a smaller Λ .

Experimental steady state Λ value

The five measurements downstream of the heater are used to calculate an experimental Λ , and supposing that the asymptotic common temperature T_∞ value has been reached before the sample end (8.15m). T_0 is the first measurement, and the expected exponential behaviour is recorded regardless of the distance from the heater (0.32m).

$$\frac{T - T_\infty}{T_0 - T_\infty} = \exp\left(-(x - x_0)/\Lambda\right) \quad (3.2-3)$$

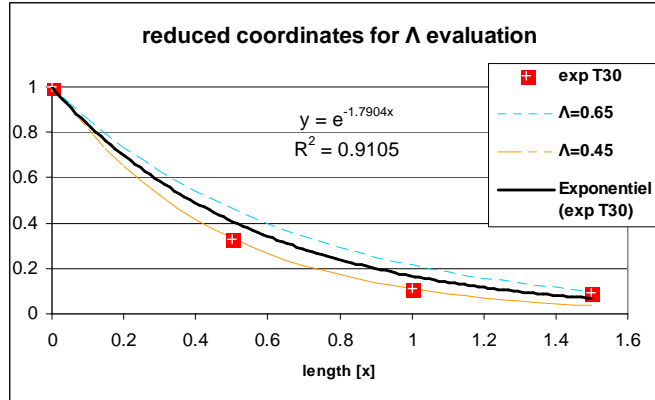


Figure 3-7: Steady state hence stationary characteristic length Λ calculation

The exponential regression provides (Figure 3-7):

$$\Lambda_{water} \approx \frac{1}{1.7904} = 0.56m \quad (3.2-4)$$

The observed higher external bundle temperature and small characteristic length are compatible with the diagnosis of a “third channel” in the CICC. The isothermal channel hypothesis is indeed based on either turbulent mixing which can be objected, or some conduction.

Even with this tentative explanation, the extrapolated bundle temperature should not possibly rise above the jacket temperature, as it does in Figure 3-8: we see that the conductionless model applied with the experimental Λ value of 0.56 m does not fit the experimental data well either. This jacket temperature calculated through $\Delta T_{AJ} = Q/(h_{AJ}p_J)$ carries a high uncertainty because of the value calculated for h_{AJ} .

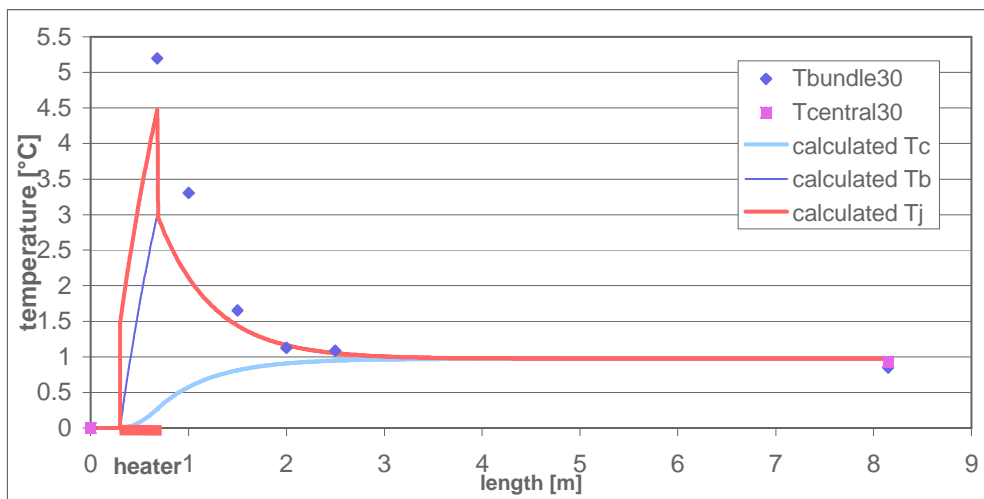


Figure 3-8: Jacket temperature (T_J) calculated from Λ_{exp} , and T_A extrapolation at heater end

Imposing a heat flux rather than a jacket temperature may explain the high overheating of the annular channel if its temperature homogenisation is not efficient enough. This hypothesis would clarify the anomalous annular temperatures close downstream from the heater.

The analytical model assumes a uniform annular temperature. A corresponding thermometer measure should ideally be performed in the center of a strands bundle petal, rather than just 1 mm away from the jacket, which is not self-consistent with modeling.

If “the” annular temperature was to be divided into a few temperatures evolving separately, it could take into account the concentric geometry of the entire cable (e.g. dead corner T, outer annular T, inner annular T) or the geometry of each petal (e.g. dead corner T, external petal T, petal heart T).

Discussion on α_A value

The conductionless thermo-hydraulic problem solutions are entirely known when both the bundle mass flow proportion α_A and the heat exchange characteristic length Λ are given. In order to make an experimental best fit of the model to the data α_A must be evaluated from experimental values. An easy way to do so is to use equation (3.1-8) and fit the maximal bundle temperature to the extrapolated experimental value $T_A(L)$ at the end of the heated zone:

$$(\beta_A - \beta_{iso}) = \frac{T_A - \beta_{iso}L}{\Lambda(1 - e^{-L/\Lambda})} \approx \frac{5.19 - 2.56 * 0.38}{0.56(1 - e^{-0.38/0.56})} = 15.3 K/m \quad (3.2-5)$$

from $(\beta_A - \beta_{iso}) = \frac{Q}{mC_p} \left(\frac{1}{\alpha_A} - 1 \right)$ we get:

$$\alpha_A = \left(\frac{(\beta_A - \beta_{iso})mC_p}{Q} + 1 \right)^{-1} = \left(\frac{15.3 * 0.81 * 4180}{8630} + 1 \right)^{-1} = 0.143 \quad (3.2-6)$$

As was expected, a higher bundle temperature is associated to a lower bundle mass flow.

$m_A = 0.14 \text{ kg/s}$ instead of 0.25 kg/s .

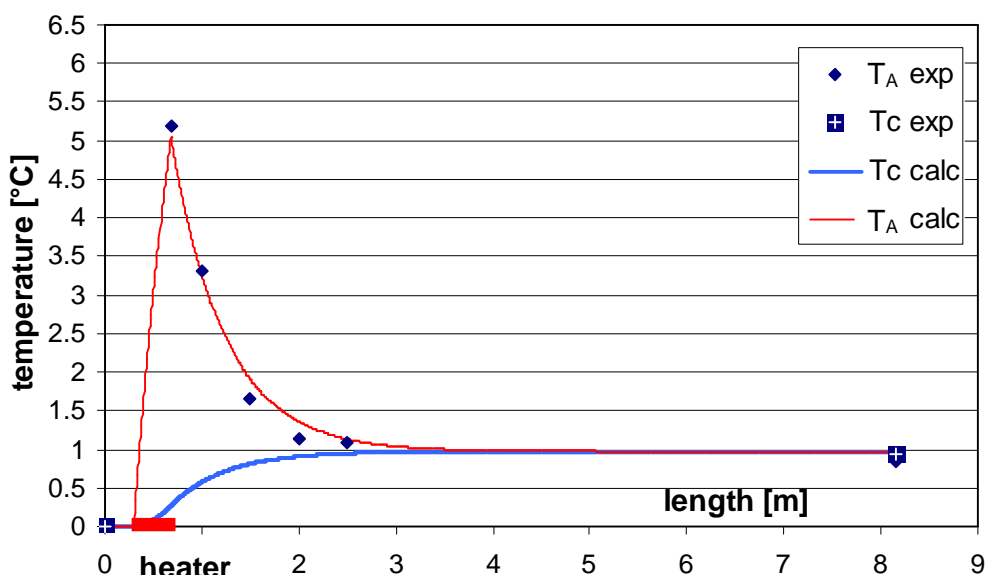


Figure 3-9: Thermal model applied with experimental (α_A, Λ)

In Figure 3-9, we observe that the steady state thermocouples data obtained on HECOL is perfectly compatible with the conductionless model developed at CEA but with experimental values of α_A and Λ far from theoretical previsions.

Table 3-2: Summary table of theoretical and experimental α_A and Λ results

| | α_A (%) | Λ [m] |
|--------------------|----------------|---------------|
| Theoretical value | 25 | 1.10 |
| Experimental value | 14.3 | 0.56 |

The value α_A could in principle be checked with transient experiments annular heat front travel times. Practically this hypothesis of extremely low annular mass flow rate is hardly thinkable because the total CICC pressure drop is even lower than expected, while a higher overall pressure drop for a constant mass flow would be necessary assuming the pressure drop for spirals is correctly known.

Discussion

Jacket and strands thermal inertia are suppressed in a steady state data collection. Because the HECOL loop temperature is very hard to stabilise, experiments are conducted in slowly drifting temperatures (<2K/min). The difference between the heater on and heater off cases leads to a different drift speed and averaged temperatures may be biased.

Thermocouples absolute error bars are as high as 0.2 K, The relative precision to be used here is somewhat smaller, but cannot be expected to drop below the order of magnitude of 0.1 K. Because our steady-state measurement of Λ is based upon a very limited number of thermocouples (five), precision and redundancy are poor. But the uncertainty on temperature measurements is not high enough that it could explain by itself the divergence between model and results. There must be an additional phenomenon not taken into account in the model.

The measured value of Λ (0.56 m) is much less than the value expected from the calculations (1.11 m) with the model for h_{AC} . Furthermore, the experimental temperatures do not follow a simple model of localised heat load and redistribution between homogeneous temperature channels: the annular temperature raises more and falls off more quickly than expected.

Hints to explain the discrepancies are listed hereafter:

- The heater may provide a wide heat load with a jacket temperature overheat distributed over a width greater than that of the heater itself, if longitudinal conduction in the jacket is non-negligible. This may lead to a peak annular temperature shifted downstream at $x>L$;
- The bundle mass flow may be smaller than what models predict (low α_A) This is incoherent with measures of a low global pressure drop, but would explain both a higher temperature rise and a reduced value of Λ ;
- The bundle temperature may not be homogeneous. If the dead corners and possibly the outside of the petals do not mix well with the heart of the petals, it can lead to a higher external bundle temperature measurements, with a reduced Λ ;
- As far as heat losses through the jacket insulation are concerned, cooling jacket and annular temperature will tend to reduce the observed Λ value, while on the central temperature no influence is expected other than a reduced asymptotic final temperature. Because the power balance is recovered at the outlet thermometer, losses are not a good explanation.

The results obtained in permanent regime conditions can only show good accordance with model previsions if both α_A and Λ are reevaluated with experimental values. Discrepancies in

Λ and temperature after the heated zone leads to a discussion of possible explanations, including conduction in the jacket (unlikely), low bundle mass flow (unlikely), incomplete model of heat coefficient (likely), with inhomogeneous bundle temperatures (likely) and a possibly strong dead corners disturbance (likely).

3.2.3 Measure of the heat transfer coefficient H in cryogenic helium

The thermohydraulics of full size conductor samples has been explored at low temperatures in the SULTAN facility at CRPP/Villigen, where superconductive cable critical properties are also being investigated (Appendix IV).

Experimental campaigns with supercritical helium offer the tremendous advantage of providing measurements that do not require a similitude law to be applicable to a conductor design. There is a small disadvantage however: thermometers can only be located on the cable jacket because of leak concerns.

PFIS AC losses

Due to the thermometer layout of the PFIS, this study was carried out using only the AC loss deposition provided by a dipole on a conductor section. The two legs of the PFIS are asymmetric because the superconducting strand petals are directly inserted in the jacket in the right leg, whereas they are wrapped in stainless steel tape in the left leg. The eddy currents created by the AC field and generating heat have a reduced intensity on the left leg, which is presently the main option for ITER.

An example of results and theoretical expectations of heat transfer coefficient is given for each leg at 10 g/s with AC heating in Figure 3-10, with results summarised in Table 3-3. These experiments do not provide accurate thermal results concerning the space constant Λ and associated heat transfer coefficient H between the two conductor channels, nevertheless this kind of heating is instructive given its representativeness of AC losses in the final coil use. The main reason for the deficient experimental result quality is that the exact length and homogeneity of the heat deposition is uncertain: clues of an extended heating width arise especially on the left leg with wrappings, both from the upstream T₅ slight temperature rise at extremely low levels of input power, and from high downstream T₃ measurements compared to T₄, which can only be explained by a heat source in-between. This point is further discussed in section 5.3.

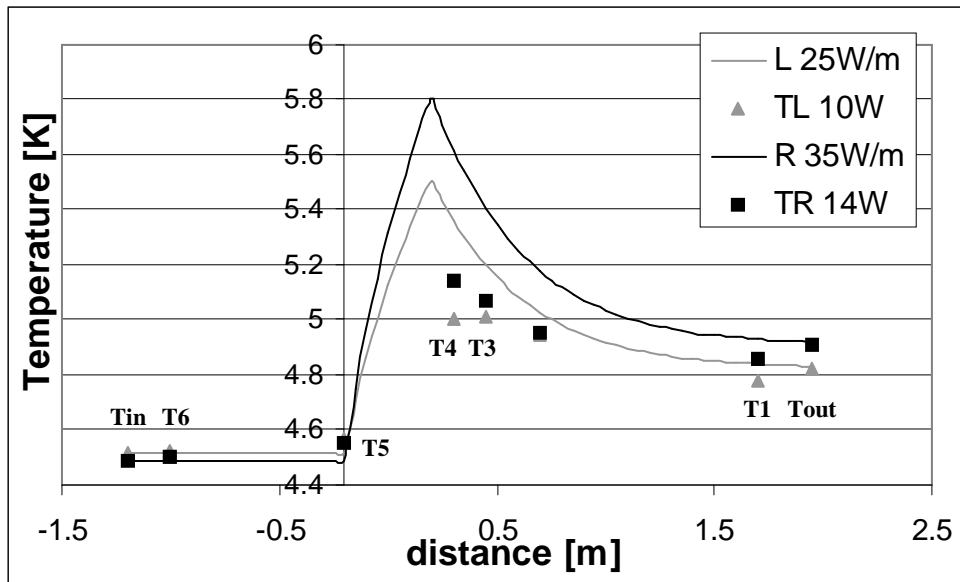


Figure 3-10: PFIS annular (jacket) temperature for 1 Hz AC heating (annular) at 10 g/s

Table 3-3: PFIS AC power, characteristic length Λ and resulting heat transfers at 10 g/s

| Expected values ($\Phi=0$) | | $\Lambda = 0.48 \text{ m}$ | $H = 418 \text{ Wm}^{-2}\text{K}^{-1}$ | $H_p = 13.1 \text{ Wm}^{-1}\text{K}^{-1}$ |
|---------------------------------|--|------------------------------------|--|---|
| AC frequency | 4 Hz | 3 Hz | 2 Hz | 1 Hz |
| w80 measures (L) | $W = 37 \text{ W}$ | 25 W | 15 W | 10 W |
| | $\Lambda = 0.7 \text{ m}$ | 0.75 m | 0.8 m | 1 m |
| | $H = 285 \text{ Wm}^{-2}\text{K}^{-1}$ | $265 \text{ Wm}^{-2}\text{K}^{-1}$ | $250 \text{ Wm}^{-2}\text{K}^{-1}$ | $200 \text{ Wm}^{-2}\text{K}^{-1}$ |
| w0 measures (R) | 54 W | 36 W | 21 W | 14 W |
| | $\Lambda = 0.35 \text{ m}$ | 0.35 m | 0.4 m | 0.4 m |
| | $H = 570 \text{ Wm}^{-2}\text{K}^{-1}$ | $570 \text{ Wm}^{-2}\text{K}^{-1}$ | $500 \text{ Wm}^{-2}\text{K}^{-1}$ | $500 \text{ Wm}^{-2}\text{K}^{-1}$ |

On the PFIS experiments, AC losses heat up the NW leg more than the W, as expected. The minimum power used in these 10g/s experiments is 25W/m assuming a deposition length of 0.4 m. The NW leg temperatures heat up especially less than expected. The PFIS AC loss upstream temperature is slightly rising even at very low power, which is disturbing and may be also a sign of wide heating length.

PF-FSJS AH stimulation

PF-FSJS-results of annular temperature profiles at 8 g/s in each leg are shown for symmetrical 0.4 m AH power of level 10, 15 & 20 W/m (Figure 3-11) and 25, 30 & 35 W/m (Figure 3-12). In each case, a constant inlet temperature upstream of the heated region is observed, followed by an annular temperature sinking downstream the heater and reaching isothermal channels asymptotic value.

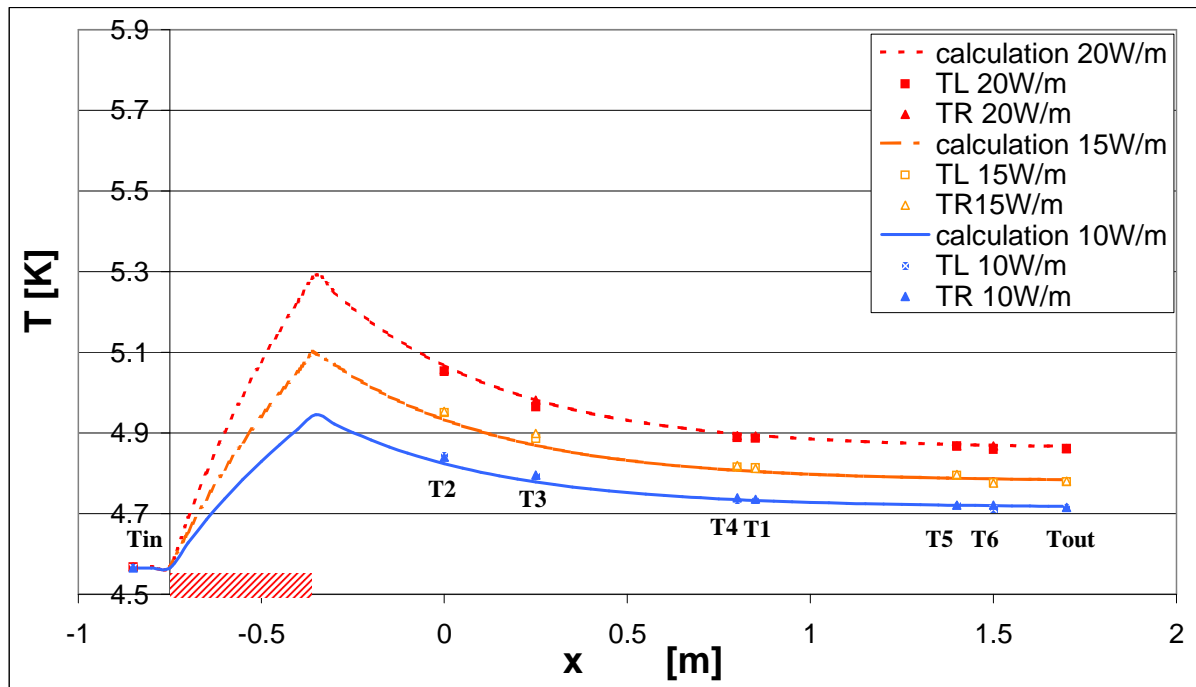


Figure 3-11: PF-FSJS calculated (lines) and measured (points) annular temperatures for 10, 15 & 20 W/m AH per leg at 8 g/s

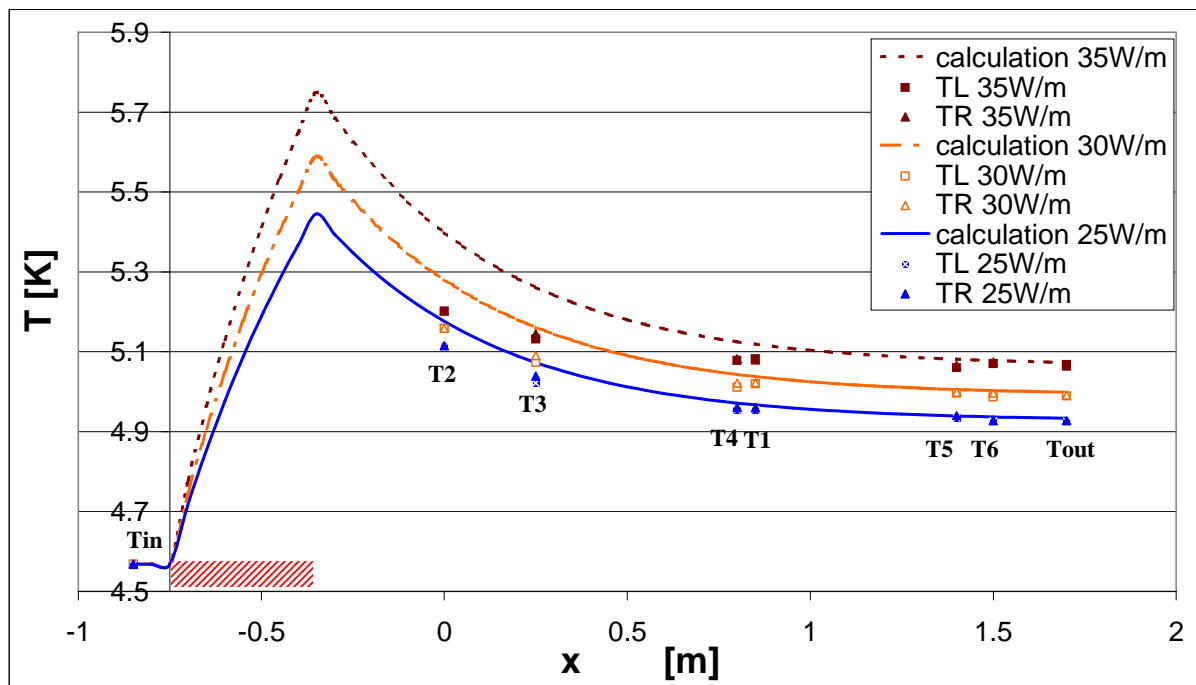


Figure 3-12: PF-FSJS calculated (lines) and measured (points) annular temperatures for 25, 30 & 35 W/m AH per leg at 8 g/s

Temperature differences should be high for better measurement precision, but low enough to avoid the distortion between theory and nonlinear experiments.

Table 3-4: Heating power and Λ for PF-FSJS annular heating at 8 g/s in the model, Left and Right leg experiments.

| P distributed | 10 | 15 | 20 | 25 | 30 | 35 | W/m | |
|------------------------|-------|------|------|------|------|------|-------|-------|
| P electric per leg | 4 | 6 | 8 | 10 | 12 | 14 | W | |
| ΔH in-out | (R) | 508 | 731 | 1012 | 1250 | 1482 | 1555 | J/kg |
| (L) | 506 | 728 | 1012 | 1244 | 1473 | 1565 | J/kg | |
| P from ΔH | (R) | 4.06 | 5.85 | 8.09 | 10.0 | 11.9 | 14.0 | W |
| = $m \Delta H$ | (L) | 4.05 | 5.82 | 8.09 | 9.95 | 11.8 | 14.1 | W |
| Λ model | 0.457 | | | | | | m | |
| H model | 360 | | | | | | W/m²K | |
| Λ experimental | (R) | 0.45 | 0.58 | 0.43 | 0.47 | 0.49 | 0.3 | m |
| Λ experimental | (L) | 0.48 | 0.53 | 0.41 | 0.42 | 0.43 | 0.3 | m |
| H experimental | (R) | 365 | 283 | 382 | 350 | 335 | 547 | W/m²K |
| H experimental | (L) | 342 | 310 | 401 | 391 | 382 | 547 | W/m²K |

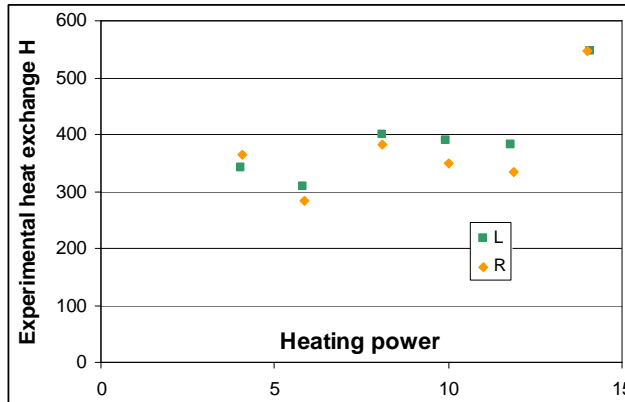


Figure 3-13: Heat transfer H_{exp} [$\text{W.m}^{-2}\text{K}^{-1}$] as a function of experimental heating power P_{electric} conditions per leg [W] at 8 g/s, while its theoretical value should remain constant

Analyses with numerical values of the heat transfer characteristic length are summarised in Table 3-4 and visible in Figure 3-13. The heat distribution power is the total power divided by the heating length, here 0.4 m. The ratio r appearing in this table will be introduced in section 3.6.

Experiments and predictions using the model of Appendix V are in good agreement only at lower power ($\leq 20\text{W/m}$) for reasons discussed in section 4.1, but low power tends to minimise ΔT_{CA} and leads to higher relative uncertainty on the measurements. Data acquisition ranges set absolute thermometer uncertainty at most at 0.16 K. The quality of the agreement between result and model prediction for the sensor T_2 is provided by the second column of Table 3-5.

Table 3-5: Experiment-calculation discrepancy and linearity limit comparison to r-values in PF-FSJS AH at 8g/s for various distributed powers

| Distributed power [W/m] | Relative difference at T_2 experiment-calculation (%) $(T_{2\text{calc}} - T_{2\text{exp}}) / (T_{2\text{exp}} - T_{\text{in}})$ | | risk ratio r |
|--------------------------------|---|----------|---------------------|
| | L | R | |
| 10 | -2.2 | -5.7 | 0.69 |
| 15 | -0.04 | -0.42 | 1.03 |
| 20 | 8.7 | 2.0 | 1.38 |
| 25 | 17.2 | 11.1 | 1.73 |
| 30 | 26.6 | 20.6 | 2.07 |
| 35 | 38.9 | 31.0 | 2.42 |

While absolute heat transfer values are the parameters driving the physics of the temperature variations, the space constant provides explicit information about the scale of absorption of heat load in a CICC.

3.3 Transient analysis [Ren06-2]

The purpose of a transient analysis is to obtain an analytical solution for the measurable annular temperature as a function of time and distance. This analytical solution requires the knowledge of the interchannel heat transfer coefficient we seek, but a numerical inverse method will allow revert from the temperature back to H . Analytical procedures to characterise transient behaviour of heat exchangers have also been reported for other geometries [Hen91].

3.3.1 Principle and hypothesis

Another means of measuring the heat transfer coefficient between the two channels is to observe the transient behaviour of the conductor in time and space when a temperature step is suddenly sent as admission fluid temperature at the inlet (Figure 3-14).

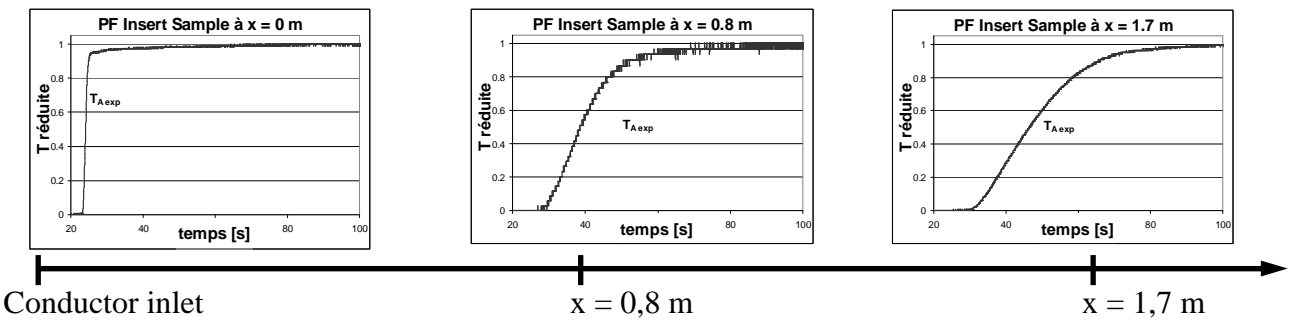


Figure 3-14: Evolution of an experimental temperature step (Heavyside) as it transits along a PF conductor.

The central and annular temperatures evolutions are dictated by the energy conservation equations in an incompressible fluid flow, again with the assumption of two uniform temperature channels:

$$\begin{cases} \frac{DT_A}{Dt} + \gamma_A (T_A - T_C) = Q \\ \frac{DT_C}{Dt} - \gamma_C (T_A - T_C) = 0 \end{cases} \quad (3.3-1)$$

where $\frac{D}{Dt}$ is the derivative following the fluid particles,

Q the power deposited in the annular channel,

γ the ratio of the linear heat transfer coefficient over the channel linear heat capacity:

$$\gamma_i = \frac{H \cdot p}{\rho_i \cdot A_i \cdot C_{pi}} \quad \text{for } i=A, C \quad (3.3-2)$$

H the unknown transverse heat transfer coefficient, p the spiral external perimeter, $\rho(T)$ the density, A the channel cross-sectional area, and C_p the channel helium heat capacity.

3.3.2 Heat equation solution

An analytical solution can be given for a heating (or cooling) step entering the CICC and progressively replacing the fluid present in the cable at $t = 0$ (Figure 3-15).

The different fluid velocities generate a space window of interest $[U_A \cdot t ; U_C \cdot t]$ which is expanding and shifting in space as time goes by, where U_i is the mean velocity in channel i. The upper part of Figure 3-15 illustrates snapshots of the temperatures in the conductor.

For $x \leq U_A \cdot t$, all temperatures are set to 1 because He flowing at that distance has been fully replaced. For $x \geq U_C \cdot t$, all temperatures in the cable are set at 0 because the heating wave has not yet reached this point.

The very first central fluid particle entering at $\theta_c(0,0) = 1$, and exchanging with a uniform annular temperature $\theta_a(x, x/U_c) = 0$, provides with its temperature derivative at the entrance

(0,0) a graphic evaluation of a heat exchange characteristic length $\Lambda = \frac{U_c m_A}{\gamma_c m}$.

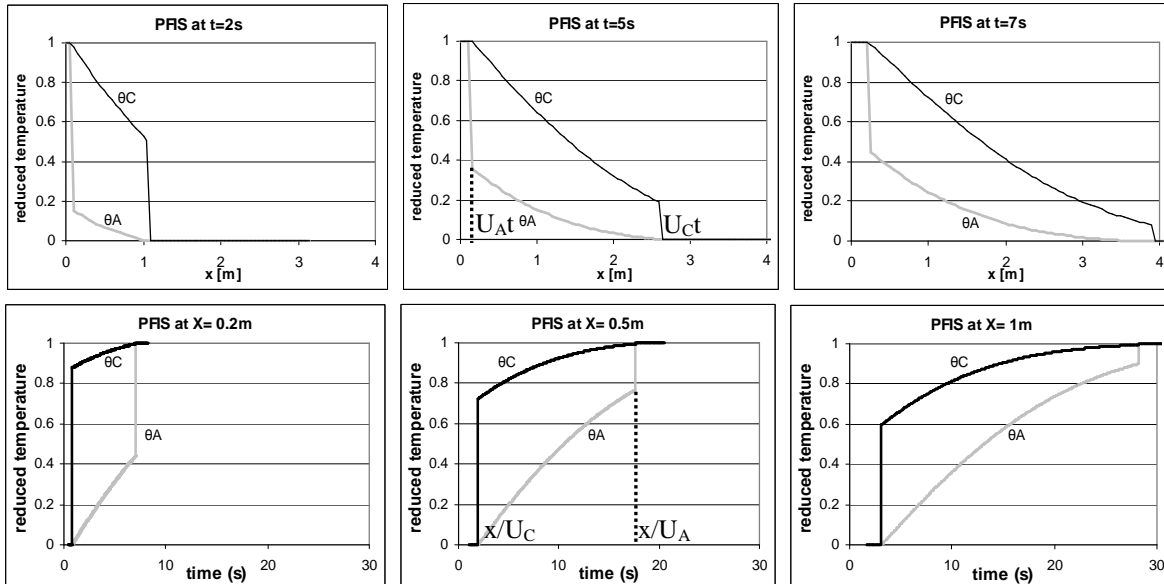


Figure 3-15: Illustrations of PFIS W (L) space (top) and time (bottom) windows at 8 g/s

Similarly, The dual channel model is characterised by a time window of interest $[x/U_A ; x/U_C]$, expanding and shifting in time. The lower part of Figure 3-15 illustrates the theoretical time evolution of temperatures as could be sensed by an observer, depending on the distance from the conductor isothermal inlet.

In these representations at fixed positions, we see that a temperature derivative can provide a measurable transition time providing a practical way of evaluating H. The transition time τ is quantified precisely in appendix VI and discussed in section 3.3.3.

Laplace transform and integration, detailed in appendix VI, lead to the implicit solution:

$$\begin{aligned} (\theta_c - \theta_a)(x, t) &= \exp(-\alpha - \alpha\delta^2) \cdot I_0(2\alpha\delta) \\ \frac{d\theta_c}{dt}(x, t) &= \frac{\exp(-\alpha - \alpha\delta^2)}{\Delta U} \cdot \left(\gamma_c U_A I_0(2\alpha\delta) + \frac{\gamma_A U_C I_1(2\alpha\delta)}{\delta} \right) \end{aligned} \quad (3.3-3)$$

where I_0, I_1 , are modified Bessel functions of the first kind,

$$\Delta U = (U_c - U_A) \quad (3.3-4)$$

$$\alpha(x, t) = \gamma_c (x - U_A t) / \Delta U \quad (3.3-5)$$

$$\delta(x, t) = \sqrt{\frac{(U_c t - x) \gamma_A}{(x - U_A t) \gamma_c}} \quad (3.3-6)$$

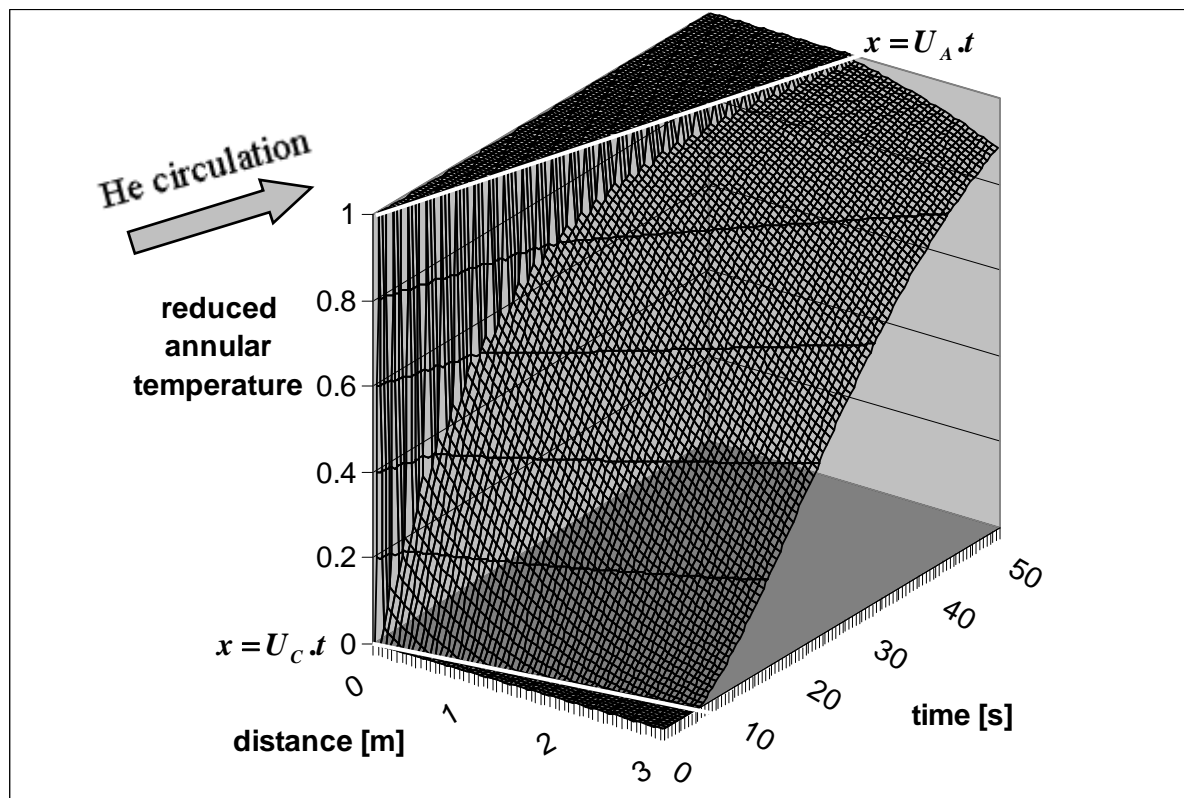


Figure 3-16: Calculated annular temperature $\theta_A(x, t)$ as a function of time and space on PFIS W (L) at 8 g/s.

Explicit and practical use of these implicit equations is detailed in Appendix VI. These equations are illustrated in Figure 3-16. He circulating in the central channel enters on the side ‘distance=0’ and advances parallel to the line $x = U_A t$, while temperature sensors experience annular time evolutions at fixed distances (Figure 3-16). The conductionless assumption ($\lambda \rightarrow 0$ in the jacket) leads to a non-physical temperature discontinuity at line $x = U_A t$ shown in white.

3.3.3 Application: Transition time τ

The transient analysis is a useful tool to understand how a coil temperature transient is operated, whether operational or accidental.

The first application of this analytical solution lies of course in the evaluation of H . But a computation of temperatures first requires the knowledge of the interchannel heat transfer coefficient we seek. Determining the heat transfer coefficient H is possible using an identification (inverse) method, comparing the experimental and analytical data.

An evaluation \hat{H} of H is found as solution minimising the distance between analytical and experimental temperature evolutions:

$$\hat{H} = \arg \left\{ \min \left(\sum_{\text{thermometers}} \sum_{\text{time}} (T_{\text{analytical}} - T_{\text{experimental}})^2 \right) \right\} \quad (3.3-7)$$

A minimisation of the residual difference done automatically through an iterative method of conjugated gradients is a practical way to fit the analytical solution to the experimental data. One of the limits of this method is the fact that distance between temperature curves is calculated and minimised only in the vertical direction.

The other important application of the temperatures analytical solution is the transition time. The transition time is a concept illustrated in Figure 3-16 that can easily be applied to the future ITER conductors in order to provide temperature transient durations. The transient duration is a coil property that a cooling loop should match, but does not need to over-match: cryogenic circulation over-capacity would not bring any benefit in terms of recooling time. The cooling of each double pancake, likely to be realised with an increased circulation rate, pressure drop in this configuration should not be a limiting factor, which should preferably be inertia, heat exchange coefficients and maximal acceptable temperature gradients. The recooling time must be known for a reasonable planning of successive plasma shots in the reactor.

A front velocity is defined as:

$$\bar{U} = \frac{U_A (\rho \cdot A \cdot C_p)_A + U_C (\rho \cdot A \cdot C_p)_C}{(\rho \cdot A \cdot C_p)_A + (\rho \cdot A \cdot C_p)_C} \quad (3.3-8)$$

simply expressed by:

$$\bar{U} = \frac{U_C \gamma_A + U_A \gamma_C}{\gamma_A + \gamma_C} \quad (3.3-9)$$

Remark that this mean velocity \bar{U} of the heat front becomes $\bar{U} = \frac{\dot{m}_A + \dot{m}_C}{A_A + A_C}$ when simplifying $\rho_A = \rho_C$ and $C_{p_A} = C_{p_C}$. More about \bar{U} characteristics is presented in appendix VI.

The transition time τ is defined as the inverse of the slope at the point verifying $x = t \cdot \bar{U}$, it counts the duration of the transient between two temperature equilibria:

$$\frac{1}{d\theta_{\bar{U}}/dt} \approx \tau(x) = \frac{2\Delta U \sqrt{\pi \gamma_A \gamma_C x}}{(\gamma_A U_C + \gamma_C U_A)^{3/2}} \quad (3.3-10)$$

Half of the transition time $\tau(L)/2$ is approximately the additional time required beyond L/\bar{U} to extract heat from a dual channel CICC of length L. The transition time is a measurable constant τ and could be used to experimentally assess H:

$$H = \frac{4\pi\rho C_p L \cdot A_C^2 A_A^2 \Delta U^2}{\tau^2 p \left((A_C U_C)^{3/2} + (A_A U_A)^{3/2} \right)^2} \quad (3.3-11)$$

Fitting the temperature data time evolution with an exponential curve has been performed as a practical way to achieve heat transfer coefficient measurements [Bot06CHATS]. This Heavyside thermal step is a convenient experimental excitation to explore heat transfer between the two channels. A Heavyside step is also representative of the re-cooling of the cable after a long experiment where the coil temperature would have drifted. The analytical

coil recooling time $\frac{L}{U} + \frac{\tau}{2}$ is an operating constraint useful to design the cryoplant helium bath, potentially dimensioned for a nominal power well below the maximal instantaneous cooling demand.

3.4 Assessment of the heat transfer coefficient in transient

The purpose is here to experimentally measure the interchannel heat transfer coefficient H by means of an inverse method (3.3-7), or by using the transition time τ (3.3-10).

3.4.1 Transient experimental campaigns

Transient experiments in the HECOL facility (Appendix II) in water are made possible by the large pressurized tank, which allows to suddenly switch from direct water feed to tank water feed at a different temperature.

The two SULTAN samples (Appendix IV) were subject to a thorough thermohydraulic experimental investigation. The PF-FSJS instrumentation allowed for steady state experiments, while only the PFIS tested in upward and downward flow directions [Duc05], was scrutinized through a series of transients providing a full set of measurements at various mass flow rates and temperatures.

Water temperature and thermometer precision

The validity of the transient bithermal model developed in section 3.3, and of the resulting temperature calculations, is not the same as the steady state bithermal check conducted in section 3.2.1. Thermometer placement and calibration remains unchanged.

Steady state experiments raised the question of temperature homogeneity in the annular channel subject to transverse heat. Transient experiments feed each channel directly, therefore annular temperature inhomogeneity is not the important issue. In fact, the central channel cable cooling necessarily leads to weak annular radial gradients even in these transient experiments. Turbulent smoothing of the front is neglected in the transient approach. There is, however, a concern about metal inertia and about thermometer time response.

All metallic parts (spiral, strands and jacket) have a thermal inertia. The energy required to thermalise this hardware is taken from the heat front, tampers and weakens it. Metals inertia should be compared to the coolant enthalpy. Using ambient temperature water, the energy swallowed by steel and copper heating rapidly integrates and the heat front is weakened after a few tenths of meter. A direct analytical resolution is not interesting in these unsatisfactory testing conditions.

Helium temperature and thermometer precision

The thermal perturbation from the conductor metallic parts is neglected in supercritical helium given the strands and jacket low inertia. Contributions from viscous heating, heat conduction in helium and mass exchange between the channels can also be neglected [Bot06CHATS]. It is necessary to verify whether jacket measurements can be assimilated to annular temperatures with a fast enough response. The driving parameter in this case is the thermal diffusivity:

$$D_j = \frac{\lambda}{\rho C_p} \approx \frac{0.28}{7.9 * 2} * 10^{-4} = 1.77 \times 10^{-6} \text{ m}^2/\text{s}, \text{ high enough compared to usual values of } \sim 10^{-6}.$$

Thermometer data are again linearised for consistency and precision. Linearity of temperatures may not be respected beyond temperatures differences of 0.5 K [Ren05], which is the case here, because of otherwise neglected phenomena and the resulting thermosiphon [Nic04ICEC, Zan04]. In these cryogenic helium experiments, it is important to control mass flow rate. Supercritical helium thermal expansion is indeed non negligible, although this fluid can be considered incompressible in the nominal pressure drop range expected in a CICC.

3.4.2 Water transient applicability

Time step experiments [Dec02-2] & [Dec03-1] are another means of measuring the CICC internal heat transfer coefficients. In both steady state and transient case, we have seen that ambient temperature water does not provide optimal experimental conditions. Diffusivity of metallic parts must remain low compared to that of the fluid. Because metallic inertias must be used in these water experiments, only a code simulation can compute cable calorific capacity and transient temperature evolution [Mar03, Zan04]. The model for the heat transfer coefficient H seems to be coherent with these numerical time-steps analyses of HECOL measurements.

On the contrary, the analytical approach is not suitable for ambient temperature water tests, because the strong hypothesis that allow simplification of the system (3.3-1) are invalid. H may have to be altered but this alone will not explain the discrepancies between the analytical resolution and the experimental transients

Still transient experiments could provide a way of checking the mass flow repartition α_A by looking at the transit time of a first move and half-step temperature of the central or annular channel. Data of successive temperature rise and fall (up and down steps) are also interesting because their signature can reveal eventual problems of thermal diffusion if it is not symmetrical.

Furthermore, an ideal similitude to transfer results to supercritical helium would need not only to match Reynolds number and Nusselt number, but also the conduction coefficient in the fluid. Because such simultaneous similitude on all three parameters is not possible, results with ambient temperature water, though simple and rich in questioning, have been left aside to concentrate on available experiments conducted in supercritical helium close to ITER cooling conditions.

3.4.3 Helium transient application

The PFIS leg samples of section 1.1 are fed with a rising temperature step as defined in 2.2, and provide experimental temperature data at sensors as shown in Figure 3-17.

External temperature evolutions allow to understand the internal cable behaviour and to measure the transverse heat exchange, with comparable responses whether with upward or downward helium flow. The analytical formulae of the temperature are numerically integrated in a datasheet using a time step of at most 0.1s and helium thermodynamic properties. An appropriate choice of starting delay and a simple inverse method minimising the distance between analytical and experimental temperature θ_A for sensors 2, 3, 4 (upward); 2, 3, 4, 5 (downward) provides a best fit of H. Time dependence agreement is excellent between temperature sensors more than a metre from the He inlet and conductor joint (Figure 3-18). A confidence margin on the best heat transfer coefficient H value is given according to sensitivity (Figure 3-19).

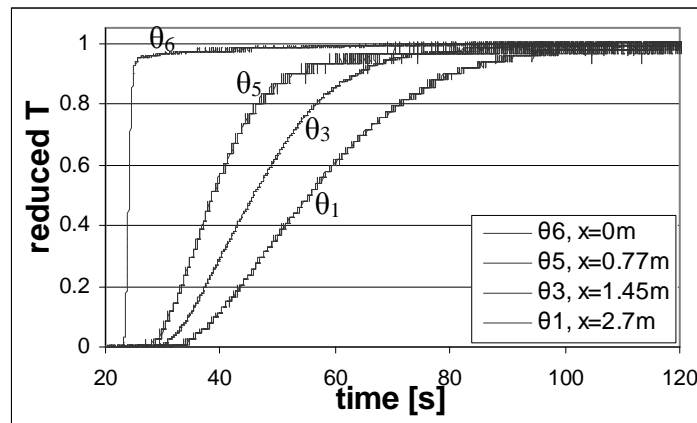


Figure 3-17: PFIS W (L) upward $T_6, T_5, T_3, \& T_1$ reduced temperature data steps at 8 g/s

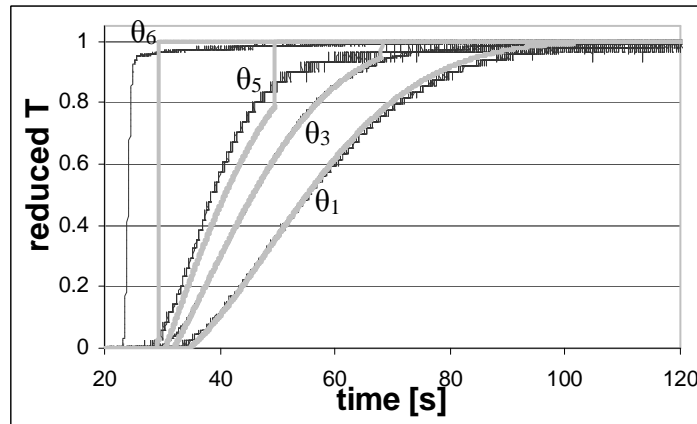


Figure 3-18: PFIS W (L) upward reduced temperatures $T_6, T_5, T_3, \& T_1$ at 8 g/s vs. calculation (in light grey) with $H=400 \text{ W/m}^2\text{K}$

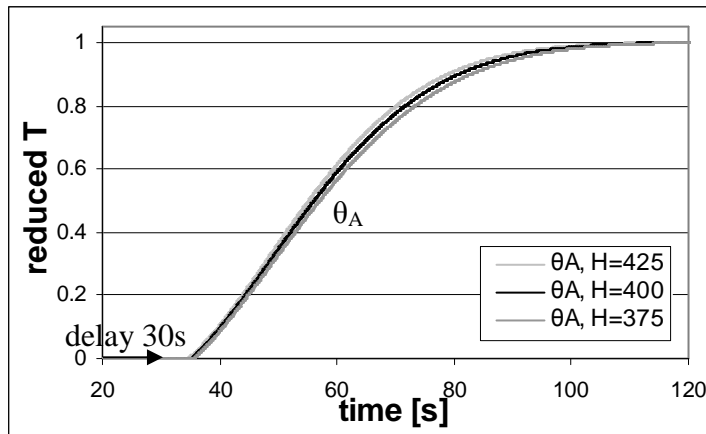


Figure 3-19: PFIS W (L) calculated temperature at $x=2.7$ m (LT1) 8 g/s sensibility to the value of the heat transfer H around $400 \text{ W.m}^{-2}\text{K}^{-1}$

This heat transfer assessment method seems more precise than the alternative steady state approach [Ren05]. Both were never compared on the same sample: steady state tests cannot be conducted on the PFIS with inappropriate annular heaters. Contrary to steady state experiments, fits of transients offer a consistent set of measurement on the full range of mass flow rate, for each leg and in both flow directions.

Agreement between transient, steady state and modelled heat transfer coefficients values allows to give some credit to the calculated forecasts.

Upward and downward heat transfer results are illustrated in Figure 3-20 with their fitting error bars. This fitting uncertainty remains under 10%, but there are other sources of uncertainty listed in the following discussion. As temperature rises, mass flow rate reduces in each leg, by up to ~4% (upward) or ~2% (downward); the smaller final mass flow rate is arbitrarily used for computation of channel balance and heat transfer coefficients.

No heat transfer estimation between the two zones, based on cold supercritical helium in full size CICC samples, was available before the simultaneous publications of the CHATS conference [Bot06CHATS, Ren06-2]. A. Long measured heat transfer through central channel cylindrical springs alone [Lon95], while A. Martinez and R. Zanino interpreted CICC measurements in water [Mar03, Zan05]. This thesis uses the displacement of a temperature front –method suggested by L. Bottura [Bot06CHATS]– through a simple analytical treatment never proposed before. This approach coupled to a simple model enables to account for the resulting experimental observation of heat transfer coefficient in a typical CICC.

Although a refined modelling of the heat transfer requires a better understanding of forced convection and mass exchange through the spiral, the calculated influence of the mass flow rate on the heat exchange coefficient illustrated in Figure 3-20 is in agreement with experimental results.

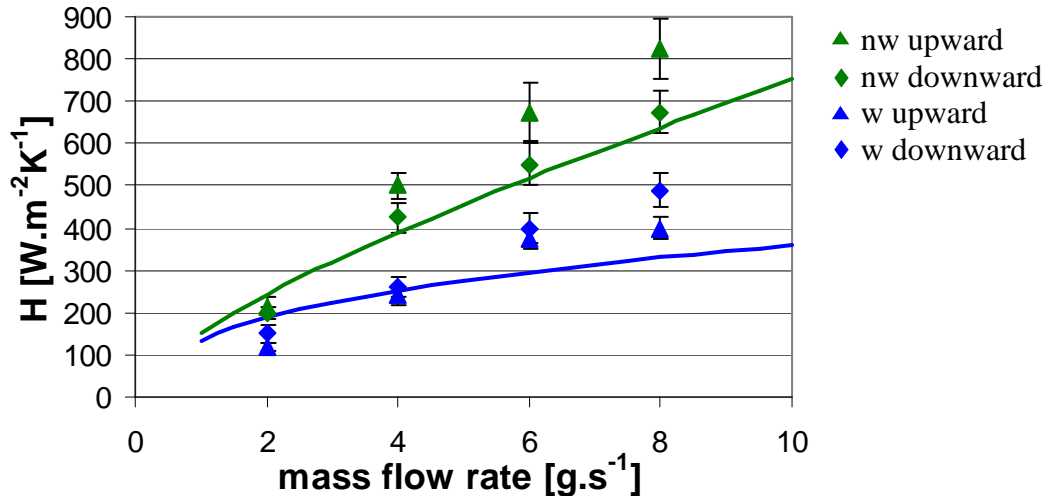


Figure 3-20: PFIS W (L) and NW (R): heat transfer coefficient H measurements (points) and expectation calculated from the model developed in section 3.5 (lines)

Striking graphic agreement between transient temperature data and analytical curves show that the simplification hypothesis and Laplace resolution match the experimental mode. It is not possible on this sample to fit all sensor data with the same delay because the joints –not taken into account in the model– perturbate time delays for thermometers 1 and 5 near the inlet and outlet.

It is difficult to experimentally evaluate the respective channel mass flow rates. Results must be extrapolated to the right Reynolds number, and uncertainty remains in the empirical laws used [Mari04]. Of course the respective mass flows strongly influence physical phenomena and experimental evaluation of heat transfer rates. Only the global interchannel heat transfer is measured via the characteristic length Λ , while the fine modeling of heat transfer requires to separate annular and central forced convection, and to evaluate conduction and mass exchange in the spiral. A fine hydraulic understanding is a prerequisite for a thermal understanding. The calculated influence of the global mass flow rate on the heat exchange coefficient is illustrated in Figure A-5; a different flow balance would alter this projection.

It is demonstrated on the PFIS sample that wrappings lead to a substantial reduction of the heat exchange coefficient between the CICC channels. This shortcoming is compensated by the electrical benefit of the wrap: under AC loss stimulation, the thermal power received by the cable is scaled down by the wrap, outmatching their thermal draw back. Most of all, the local wrap thermal downside brings the global benefit of tapering the cryoplant power required for magnetic field operation CICC cooling.

3.5 Heat transfer model

The analytical thermal model for dual channel CICC was built progressively, published [Nic04ICEC, Ren05], and used to demonstrate the orderly running expected from fusion coils cooling circulation. An evaluation of the heat exchange H is helpful to provide fully analytical steady state and transient temperature solutions. It is necessary to serve as comparison reference to experimental measurements. Most importantly, the heat transfer model must serve the thermal optimisation of the CICC central channel.

3.5.1 Unhomogeneous thermal resistances

Heat transport is most hindered through the thick spiral turns. In this case three heat transport mechanisms and corresponding coefficients are in series :

- heat convection from central region to steel (h_C)
- eventually heat conduction in steel spiral (e/λ_s)
- heat convection from steel to annular region (h_A)

The mechanism of heat transport from central channel to annular region is substantially affected by the existence of the subcable wrappings. When present, wrappings force heat to cross a metallic barrier in the travel between central channel and annular region. In practice the heat conduction in the thin wrappings (0.055 mm) can be neglected, but heat transport requires convection on each side. The wrappings' presence results in the sealing of the subcable and imposes the superposition of the two convective processes on each side of the metallic barrier. A first model imposed either 0% or 100% wrappings coverage in the spiral perforated interstices [Nic04ICEC]. A refined model includes the wrappings coverage ratio in the perforated parts, just like the perforated ratio defines parallel thermal resistances:

The model for the heat exchange coefficient through the spiral is an arithmetic mean of the coefficients through closed and perforated areas, proportionally to their applicable surfaces.

λ_{ss} : stainless steel thermal conductivity [W/mK]

H : global heat exchange coefficient [W/m²K]

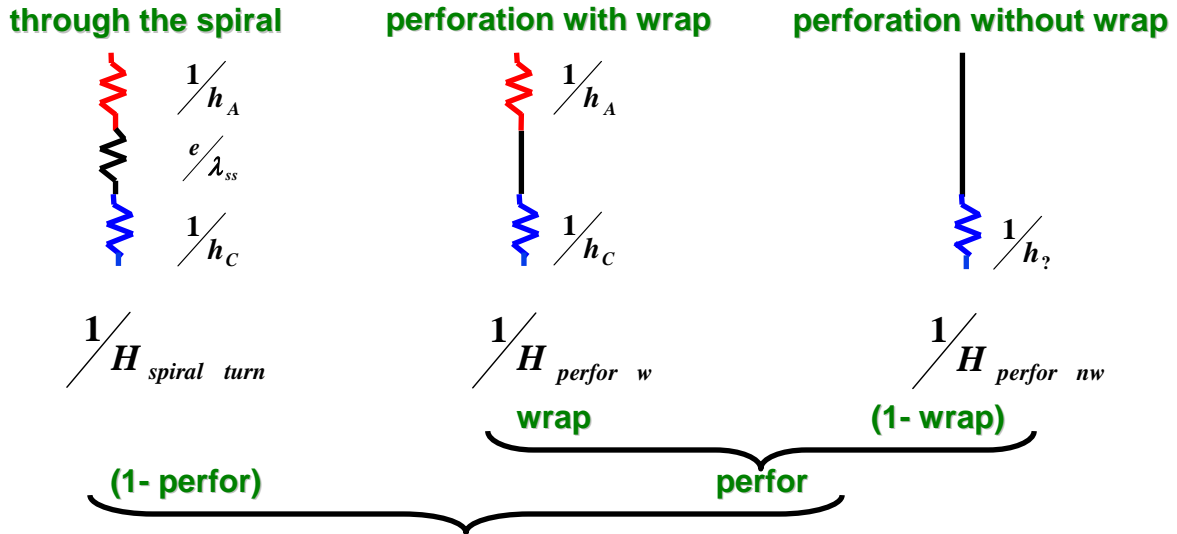


Figure 3-21: Areas closed and perforated, with or without wrappings are set in parallel proportionally to their surface; thermal resistances are in series in each area

The spiral is modeled as a sealed tube with infinite conductivity in the gaps, although it is obvious that mass transfer contributes efficiently to heat transport, even with a null net exchange. The simple heat exchange representation through the spiral now differentiates the two legs, which was not the case before because the wrappings do not alter annular void. Wrappings tend to block the transverse mass flow; this is not considered in the model of H nor in Λ . Putting the thermal resistances in series and parallel [Nic04] according to Figure 3-21 leads to the formulae:

$$H = H_{\text{turn}} (1 - \text{perfor}) * + H_{\text{Perfor W}} * \text{perfor} * \text{wrap} + H_{\text{Perfor NW}} * \text{perfor} * (1 - \text{wrap}) \quad (3.5-1)$$

with

$$H_{\text{spiral turn}} = \frac{1}{\pi \cdot \text{od} \cdot h_{\text{convA}}} + \frac{1}{\pi \cdot D_{\text{mean}} \cdot \frac{e}{\lambda_{ss}}} + \frac{1}{\pi \cdot id \cdot h_{\text{convC}}} \quad (3.5-2)$$

$$H_{\text{perfor W}} = \frac{1}{\pi \cdot \text{od} \left(\frac{1}{\pi \cdot \text{od} \cdot h_{\text{convA}}} + \frac{1}{\pi \cdot id \cdot h_{\text{convC}}} \right)} \quad (3.5-3)$$

$$H_{\text{perfor NW}} = \frac{1}{\pi \cdot \text{od} \left(\frac{1}{\pi \cdot id \cdot h_?} \right)} \quad (3.5-4)$$

where $h_?$ indicates an unknown heat transfer coefficient that depends on interchannel mass exchange and turbulence in the spiral gap. The spiral helium being able to convect on the subcable strands, $h_? = h_C$ (more conservative than h_A , used with (3.5-7)) or $h_? = (h_C + h_A)/2$ (used with (3.5-10)) provide an order of magnitude for $h_?$.

$$H_{\text{perfor NW}} = \frac{1}{\pi \cdot \text{od} \left(\frac{2}{\pi \cdot id \cdot (h_{\text{convC}} + h_{\text{convA}})} \right)} \quad (3.5-5)$$

The heat coefficient can be calculated with a more rigorous radial conductivity, replacing (3.5-2) by:

$$H_{\text{spiral}} = \frac{1}{\pi \cdot \text{od} \cdot h_{\text{convA}}} + \frac{1}{2\pi \lambda_{ss}} \ln \left(\frac{\text{od}}{\text{id}} \right) + \frac{1}{\pi \cdot id \cdot h_{\text{convC}}} \quad (3.5-6)$$

Heat exchange is calculated considering that convection takes place in a tight helix. In other words no transverse mass exchange is modeled. Mass exchange is obviously non zero, but is simply considered to increase turbulence on each side.

In these experimental temperature steps between 4.5 and 5 K, evidence of mean temperature or Prandtl number influence cannot be made; H is here considered to be a function of the mass flow rate only.

This evaluation of the heat transfer coefficient H only intends to provide a reference order of magnitude, since a refined value, depending on the complex CICC geometry and turbulent thermal boundary layers, is difficult to assess theoretically.

3.5.2 Convection coefficients

From convection coefficients, the global interchannel heat transfer coefficient is calculated and plugged into the steady state or transient thermal models to resolve the temperature profiles. Local convection coefficients h_{conv} must be evaluated in each channel.

The central spiral is highly turbulent; the annular channel is a tortuous medium where turbulence and Nusselt number are expected to rise. h_{conv} for fully developed turbulent flow in rough tubes is applied to both central and annular channels, as a default and arbitrarily simple convection model. The Nusselt number is defined from the convection coefficient with the general expression $\text{Nu} = (h_{\text{conv}} \cdot D_h) / \lambda_{\text{He}}$, and allows to calculate a non-dimensional convection.

An expression of the Nusselt number is now necessary to evaluate h_{conv} in the channels. The expression proposed by Dittus-Boelter [Dit30] for Reynolds number under 1.2×10^5 , leads to

the famous correlation $h_{\text{conv}} = 0.0259 \frac{\lambda_{\text{He}} \cdot \text{Re}^{0.8} \cdot \text{Pr}^{0.4}}{D_h}$. Values of this Dittus-Boelter correlation

for the central channel ($h_{\text{convC}} = 1100 \text{ W.m}^{-2}\text{K}^{-1}$) have proved to deliver convection coefficients two to three times under the observed values.

A simple Nusselt number expression, derived from the expression of Nu for fully developed turbulent flow in rough tubes $\text{Nu} = \frac{f}{8} \text{Re} \cdot \text{Pr}^{1/3}$ [Holman], and directly proportional to the friction factor f, could also be used [Ren06-1]:

$$h_{\text{conv}} = f \frac{\lambda_{\text{He}} \cdot \text{Re} \cdot \text{Pr}^{1/3}}{8 \cdot D_h} \quad (3.5-7)$$

In this case a numerical value of $h_{\text{convC}} = 2800 \text{ W.m}^{-2}\text{K}^{-1}$ is satisfactory when compared to experimental measurements as shown in Figure 3-20.

While the literature justifies Reynolds and Prandtl dependence, a previous contribution seems to contradict linear variation of the Nusselt number as a function of the friction factor [Lon95]. In Long's work, h_{conv} has not been measured for the same kind of rectangular spiral geometry. This thesis is the first attempt to model h_{conv} in such high-turn low-gap spirals, very different from the springs studied by Long. Geometries of springs vs PFIS spirals sketched at the same scale in Figure 3-22, show that turbulence is not directly comparable:

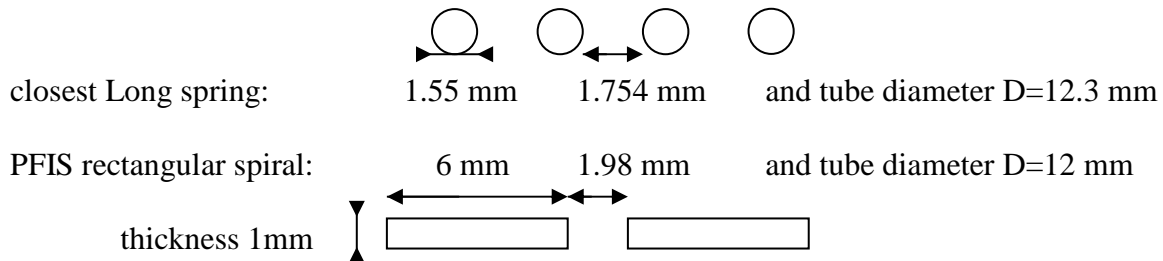


Figure 3-22: Comparative geometries of CICC central helix

Nusselt number dependence on friction reported in the Master's thesis of Long provides $\text{Nu}/\text{Nusmooth}$ values between 2 and 4 (widespread data) for springs characterised by f/f_{smooth} between 12.5 and 45. The (comparable od) rectangular spiral used in the PFIS sample is reported with $f/f_{\text{smooth}} = 4.5$. The rough tube hypothesis is clearly not perfect but goes along with the hydraulic assumption of the CICC channel.

Another experimental study seems to call for a 0.4 power dependance on friction [Nun56]. A detailed study of convection in helically roughened tubes with rectangular spirals is the only way to have a serious model of convection. A more general expression of h_{conv} can take the form:

$$h_{\text{conv}} = \zeta(f) \cdot \frac{\lambda_{He} \cdot \text{Re} \cdot \text{Pr}^{1/3}}{8 \cdot D_h} \quad (3.5-8)$$

Further work more dedicated to the sensitivity of heat transfer to mass flow, and with different spiral geometries could give the opportunity to refine a model for $\zeta(f)$ in each channel or contradict these simple laws.

The experimental values of the heat transfer coefficient H plotted in Figure 3-20 as a function of mass flow rate display a linear behaviour. Calculated H values are not far from being linear, because h_{conv} is modelled proportional to the Reynolds number hence to m . Linearising heat exchange is a possibility that was used to simplify the optimisation of complex thermohydraulic systems [Cos98]. Simple heat transfer predictions can be given by setting $\zeta_A(f_A) = f_A$ and $\zeta_c(f_c) = f_c$ in the convection coefficient model (3.5-8) –using the Nu correlation proposed by Holman for rough tubes [Holman]. This choice offers good experimental correlation (Figure 3-20) and seems acceptable in the range of annular Reynolds, without claiming universal validity.

Other Nusselt number expressions are provided by Prandtl [Pra44] and Von Karman [Kar39] for low Prandtl values. Petukhof et al [Pet58, Pet63] and Gnielinski [Gni76] provide Nusselt number correlations in the central channel validity domain. The explicit law proposed by Gnielinski is the most interesting for simplicity and precision:

$$\text{Nu} = \frac{(f/2)(\text{Re} - 1000) \cdot \text{Pr}}{1 + 12.7 \sqrt{f/2} (\text{Pr}^{2/3} - 1)} \quad (3.5-9)$$

leading to an explicit expression, function of the friction factor f

$$h_{\text{conv}} = \frac{(f/2)(\text{Re} - 1000) \cdot \text{Pr} \cdot \lambda_{He}}{(1 + 12.7 \sqrt{f/2} (\text{Pr}^{2/3} - 1)) D_h} \quad (3.5-10)$$

but this correlation provides numerical values of h_{convC} under the observed values of global heat transfer, which is unacceptable when thermal resistances are added.

Uncertainty on heat transfer coefficients is very large even for academic geometries with well known hydrodynamics. Here we have poor knowledge of the turbulence patterns in the CICC channels. The convection models are precisely dependant on the type of turbulence and skin layer thickness on the spiral walls, therefore a convection coefficient cannot be accurately predicted.

H is considered to be a function of the mass flow rate, but not of the temperature. Interchannel helium mass transfer contributes to heat transport through increased convection. It is unknown and results in a null net exchange, therefore its precise contribution remains hidden in the global –diffusion and convection– heat exchange coefficient in the spiral openings.

Conclusion on interchannel heat transfer

Steady state temperature measurements were interpreted on two conductor samples, reaching excellent agreement between model and data only at a low AH power threshold. The steady state experimental campaign has allowed to grade temperature margins of the superconducting strands and to validate the thermal behaviour of the CICC.

Transient experiments provide a robust heat transfer coefficient H evaluation method with a best fit uncertainty of $\pm 10\%$. The transient resolution offers a precise way of measuring H and a clearer understanding of a CICC Heavyside step response in time and space. Behaviours of central and annular temperatures under a step stimulation bring insight about the thermal characteristics of a CICC through its recooling time.

While steady state model limits lie in the homogeneous channel temperatures assumption and non-linearities at high power, transients heat transfer measurements find their limit with the precision of the temperature step shape and the joint perturbation.

Non measurable calculated channel mass flow balance is quite uncertain due to the empirical formulae used to determine the friction factor coefficients. Of course the respective mass flows strongly influence the physical phenomena behind heat transfer rates, while only a limited number of global CICC behaviours are observed.

A complete CICC simulation is a double-nested model: the thermal solution is based on H , itself based on h_{conv} . The model proposed is the following:

$$H = \frac{(1 - perfor)}{\pi \cdot od \left(\frac{1}{\pi \cdot od \cdot h_A} + \frac{1}{2\pi \lambda_{ss}} \ln \left(\frac{od}{id} \right) + \frac{1}{\pi \cdot id \cdot h_C} \right)^{+}} + \frac{perfor * wrap}{\pi \cdot od \left(\frac{1}{\pi \cdot od \cdot h_A} + \frac{1}{\pi \cdot id \cdot h_C} \right)^{+}} + \frac{perfor * (1 - wrap)}{\pi \cdot od \left(\frac{2}{\pi \cdot id \cdot (h_C + h_A)} \right)}$$

using $h_C = h_{conv} = f_C \frac{\lambda_{He} \cdot Re_C \cdot Pr_C^{1/3}}{8 \cdot D_{hC}}$ and $h_A = h_{conv} = f_A \frac{\lambda_{He} \cdot Re_A \cdot Pr_A^{1/3}}{8 \cdot D_{hA}}$ respectively in the central and annular channel.

While steady state and transient measurements are in good agreement with predictions, the model of the heat transfer coefficient H remains coarse. These heat transfer coefficients can be useful for code users and help extrapolate, through simple albeit improvable laws, heat transfer coefficients to predict performances of other CICC geometries.

4 Central channel spiral improvement

Is the preliminary design of ITER spirals optimal? If not, how should their geometry be altered in order to gain on performance? What performance is most crucial: pressure drop, heat exchange, cryogenic power, recooling time, investment cost, operating cost? These are the questions at stake in this chapter.

Section 4.1 is dedicated to the danger of thermosiphon. The spiral design sensitivity to friction and heat transfer is studied (4.2), leading to the proposal of an optimal central channel (4.3). Finally (4.4), other issues and alternative CICC designs are discussed.

4.1 Danger of thermosiphon

The thermosiphon phenomenon was unexpected when it was discovered with these PF-FSJS Sultan experiments (Figure 4-1) [Cia03, Zan04, Par03]. Experiments are steady state annular heating tests described in section 3.2. The vertical configuration of Sultan appears useful to assess the vertical flow behaviour in a heated CICC.

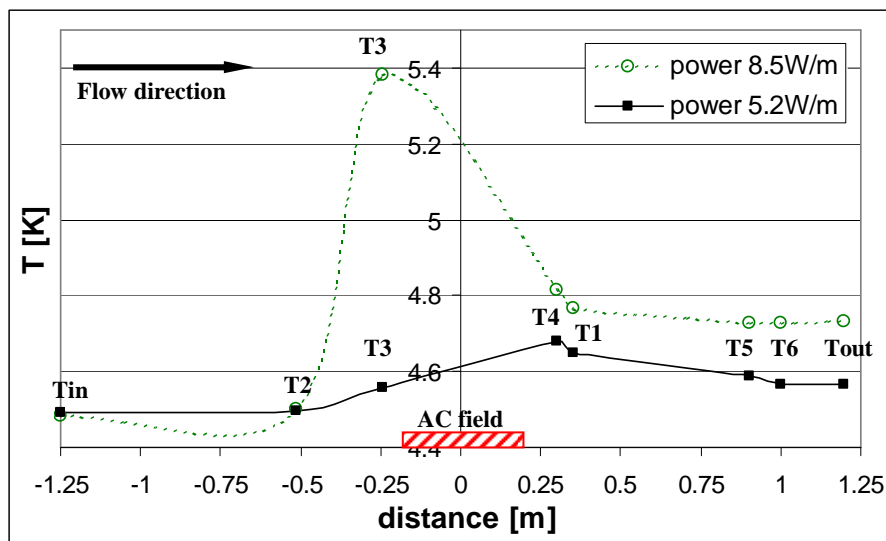


Figure 4-1: Experimental temperatures upstream and downstream of the magnetic heater in PF-FSJS at 4 g/s, 2 and 4Hz AC heating

4.1.1 The thermosiphon principle

Unbalance of heat load between channels in a vertical dual channel cable leads to a coolant density unbalance among channels and to a related mass flow disturbance (Figure 4-2). This configuration of heat load is reproduced in power intensive AH or AC annular heating steady state experiments described in section 3.2. The PF-FSJS sample (Appendix IV) being tested in a downward flow, it is subject to possible mass flow inversion for high heating input. This phenomenon is witnessed in Figure 4-3 where an abnormally high upstream temperature is measured on sensor T₃ after about a minute of heating.

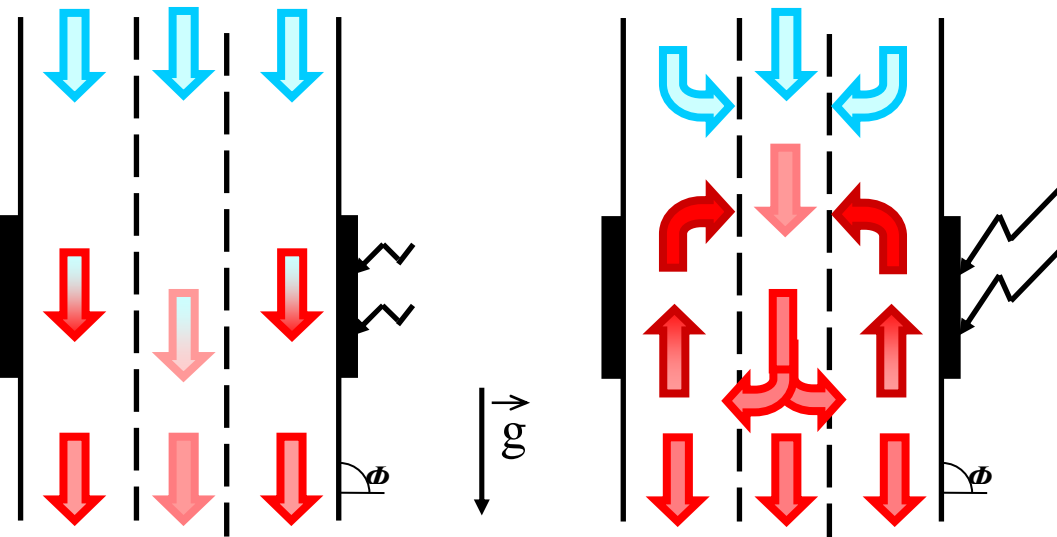


Figure 4-2: Principle of CICC annular mass flow inversion because of thermosiphon:
moderate heating on the left, strong heating flow configuration on the right

An upstream temperature rise is somewhat abnormal, but could be due to conduction. But when upstream temperature is above downstream, the only possible solution is a reverse flow. This inverse flow can also be observed with the PFIS experiments (Appendix IV) in downward flow direction, where in that case T₃ (upstream from heat) rises over T₅ (downstream) after some unstable transient behaviour (Figure 4-3). This abnormal temperature rise is a concern for sensitive superconducting strands. Note the evolution of mass flow rate sinking from 7.73 to 6.94 g/s as the steady state heating phase settles: this 10% reduction in coolant circulation is also critically deprecative for conductor performance.

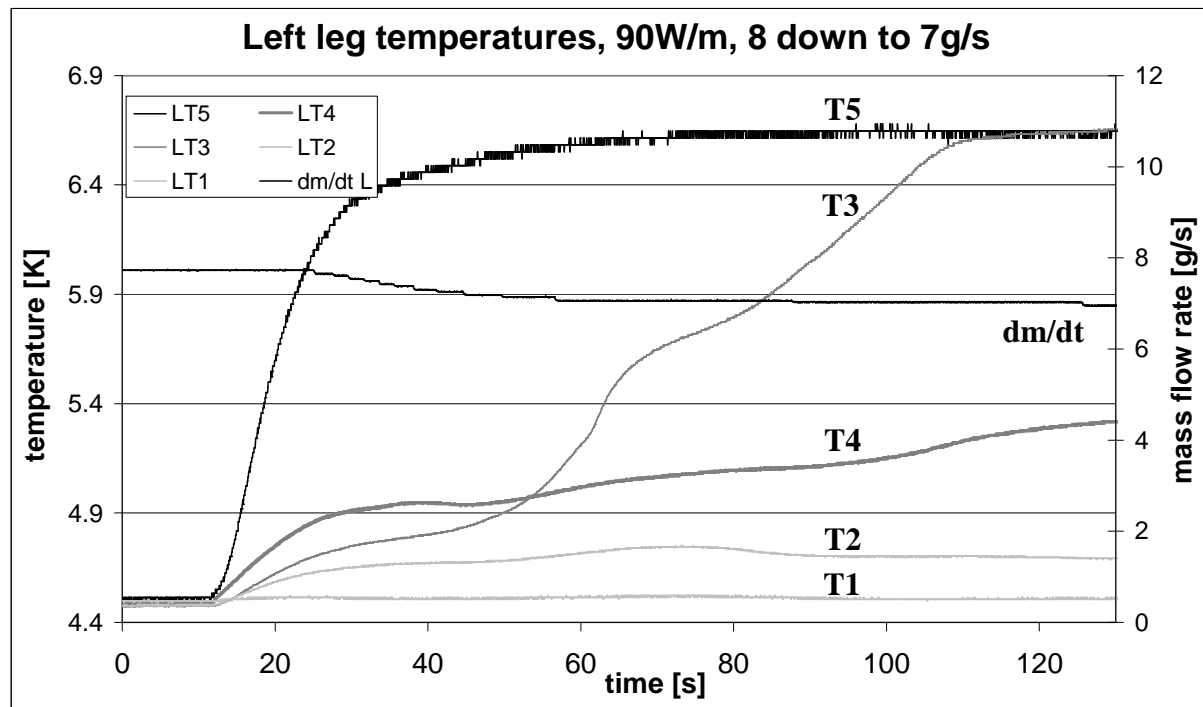


Figure 4-3: Evidence of thermosiphon in PFIS AC heating left leg with downward flow: upstream temperature T_3 rises irregularly over T_5 after a transient phase

There are yet many issues not precisely predictable, such as the maximal rise of T_3 above T_4 in full thermosiphon examples obtained on the PFIS and visible in Figure 4-3. This figure shows that a transient thermal behaviour is induced by a not-too-high power input, but experiments cannot be carried long enough to assert whether equilibrium is always reached. Apart from the stream inversion, gravity may well introduce a progressive flow disturbance, such as a nonlinear behaviour clearly observed in Figure 4-4 above 15 W/m of rising distributed power in the PF-FSJS experimental annular temperatures. From this figure, we have evidence that downstream annular temperatures converge to a uniform CICC temperatures mixed by the thermosiphon as heat load grows. The bottom line illustrating the linear behaviour of the mixed outlet temperature is slightly curved downward because of increasing $C_p(T)$.

Of high importance, an assessment of the flow reduction or inversion risk is being first investigated.

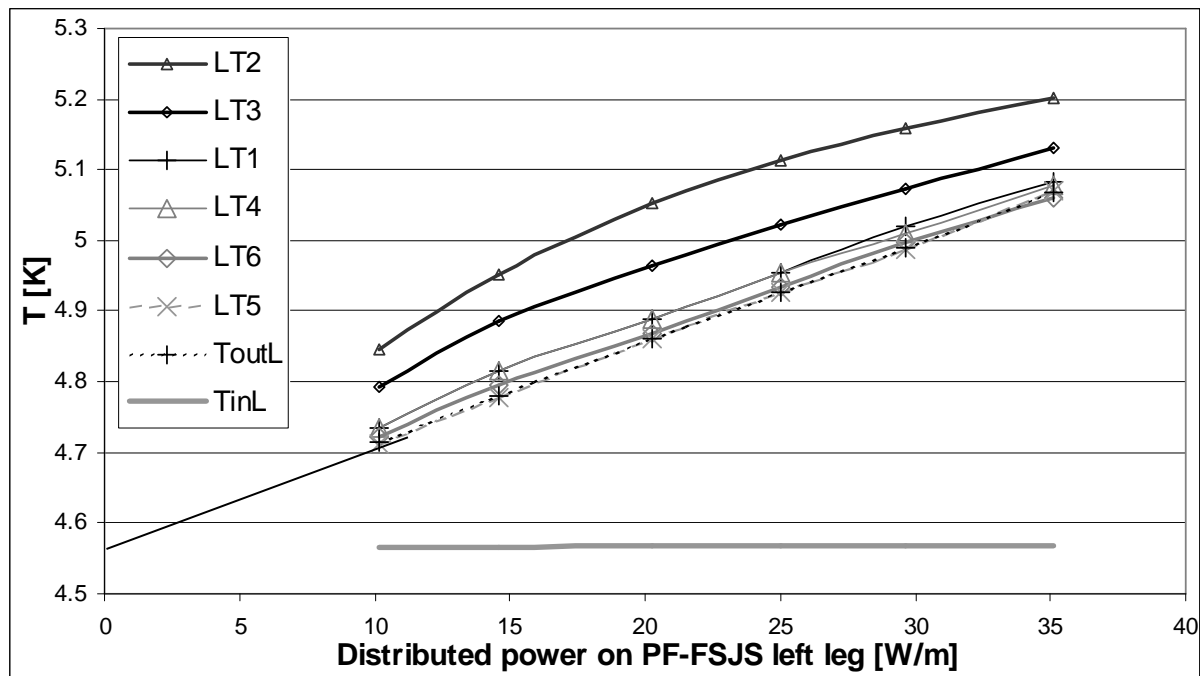


Figure 4-4: PF-FSJS evaluation of thermosiphon power threshold for annular heater at 8g/s: the experimental annular temperatures have a linear behaviour up to ~15W/m only

4.1.2 Evaluation of the risk

A precise modelling of the thermosiphon phenomenon would imply to be able to model transverse hydraulic resistance, i.e. to provide a law of mass flow redistribution given a pressure difference between the two channels.

In a CICC, thermosiphon phenomenon is very complex to model in detail because of unknown interchannel pressure gradient, hydraulic resistance and associated transverse mass diffusion. It has been decided that an evaluation of the risk and of the maximal acceptable power to avoid annular flow halt would be more effective than the use of a model requiring adaptable but not mastered parameters [Zan04]. In order to evaluate the relative importance of the “gravity pressure”, we compare its static pressure, assuming two distinct temperatures which leads to different densities, to the cable pressure drop calculated with dynamic balance of mass flows in the channels without any thermosiphon hydraulic alteration [Duc04thermosiphon].

$$\Delta P_{\text{thermosiphon}} = \Delta \rho_{CA} \cdot g \cdot L_t \cdot \sin \Phi \quad (4.1-1)$$

with the density ρ , the gravity g , a conductor length L_t and angle Φ with horizontal.

$$r = \frac{\Delta P_{\text{thermosiphon}}}{\Delta P_{\text{friction}}} \quad (4.1-2)$$

Annular mass flow inversion is obtained for $r=1$ if the circulating pumps behave as a pressure generator (Figure 4-5), and for $r>1$ if they behave as a mass flow generator (Figure 4-6), because the conductor pressure drop would increase as thermosiphon disturbs the flow, making r a conservative risk ratio. Note that the pressure-flow rate relation is quadratic and that pressure increase is very high to maintain total mass flow in the conductor.

Circulating pumps are commonly assimilated to a pressure generator, and evaluation of the power needed to inverse the flow uses $\Delta P_{\text{friction}}$, with (reduced) total mass flow forced through

the central channel only. In short, m reduced to m_C unchanged and $m_A=0$. This is an unstable situation given the continuous heat load, and may lead to either a bi-stable annular mass flow hysteresis or to a positive and negative annular mass flow cyclical alternation.

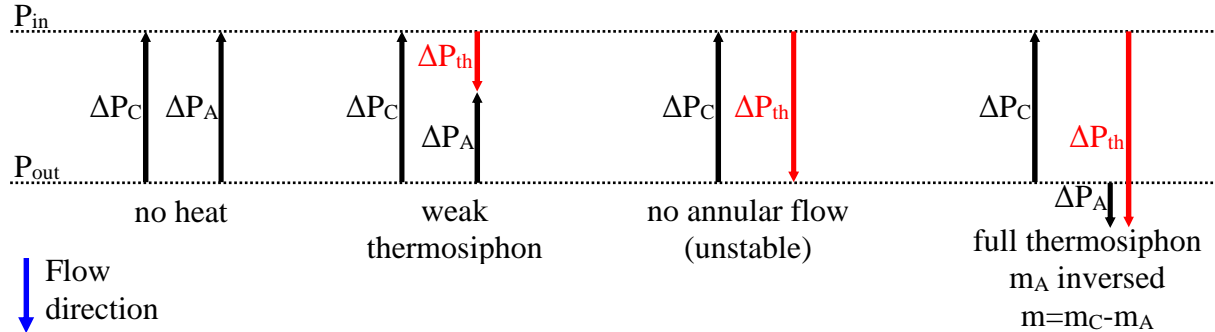


Figure 4-5: CICC pressure evolution for a pressure generator circulating pump

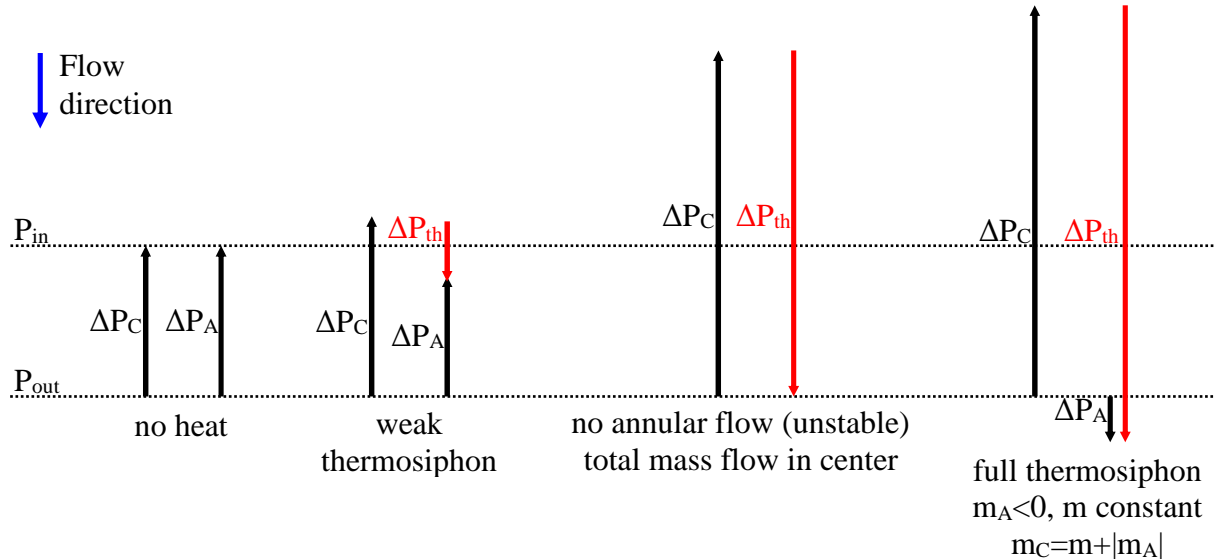


Figure 4-6: CICC pressure evolution for a mass flow generator circulating pump

The simple parameter r is hence valid when $\Delta P_{\text{thermosiphon}} \ll \Delta P_{\text{friction}}$. We can simply state there is no danger of poor annular refrigeration if $r \ll 1$ [Duc04], because $m_A \sim \sqrt{\Delta P_A}$ will not vary significantly. Figure 4-7 provides values of $r(m)$ at various power inputs for the two samples studied in SULTAN. Note that the definition of r is valid for an infinitely long heater, or more practically for a length of at least $3 \times \Lambda$, while the experiments are heated on $L \sim \Lambda$ and therefore affected by less density difference than r . Calculated on an infinite length, r provides the greatest possible asymptotic temperature gradient obtained for a given heat load and places a coil designer on the safe side. The behaviour of the PF-FSJS AH experiments in Figure 4-7 seems corroborated by values of r in section 3.4: nonlinear above $r=1$.

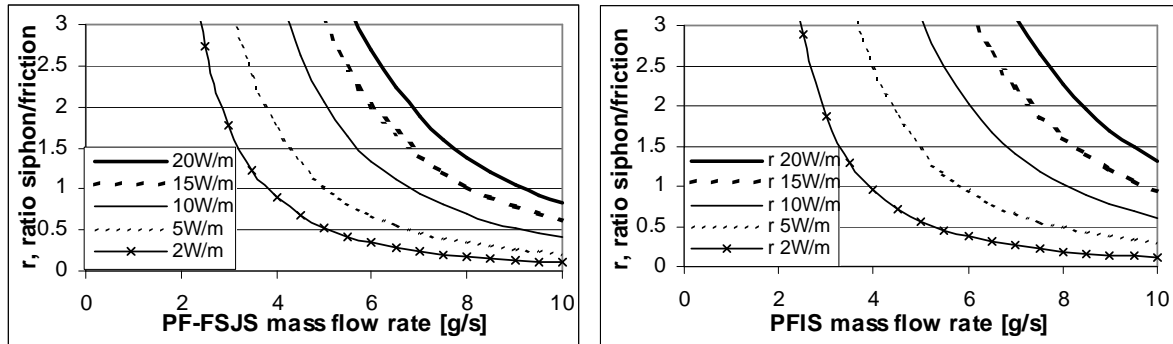


Figure 4-7: Thermosiphon risk ratio in PF-FSJS and PFIS for an array of mass flow rates

4.1.3 Thermosiphon risk in ITER coils

The temperature difference between the two channels of a CICC adds an additional superconductors temperature increase to that calculated when the heat load is taken by the total isothermal mass flow. In order to keep working specifications below superconductors chosen margins, it may require to further drop the temperature at the inlet of the coil. This raised the concern in the community that if we could diagnose thermosiphon on a sample heated on a very short length (0.4 m), the 15 m high ITER TF coils could choke and come up with unacceptably low cooling performances.

Due to the reasonable expected distributed heat load in the vertical ITER TF inner leg, $Q=1.6 \text{ W/m}$ [Bes05], the r ratio is evaluated at 2% and no thermosiphon blocking is expected. This r ratio is calculated with an isothermal cable mass flow rate hypothesis, the resulting 2% perturbation leads to the belief that the simple mass flow hypothesis is correct and no recursive evaluation of r is needed. Furthermore, from (3.1-9) a maximal annular relative temperature difference is calculated independently of the heated length, with $L \rightarrow \infty$. This central to annular temperature difference given for each geometry in Table 4-1 should be accounted for in the machine design of the superconductor margins.

Table 4-1: ITER TF Temperature margins and extreme central channel choices comparison

| ITER TF conductor | | | |
|--|------------|-------------|-----------------------|
| Perfor 50% ITER reference spiral | Perfor 29% | Smooth tube | no central channel |
| id/od [mm] | 7/9 | 7/9 | 7/9 |
| r risk ratio at 2 W/m and 8 g/s | 0.018 | 0.036 | 0.22 0 if sealed |
| interchannel tempe- rature difference ΔT_{CA} at 2 W/m | 0.03 K | 0.04 K | 0.18 K 0 K |

It can be understood in Table 4-1 that the single channel CICC eradicates both the interchannel thermal difference and the risk of thermosiphon, at the expense of a high ΔP . The opposite design would be a smooth tube, which cannot experience local recirculation unless it is pierced to allow mass transfer. In fact, a sealed tube is not desirable because in a quench situation the fast pressure rise in the annular channel is more limited if the volume of central helium is accessible. Piercing a tube is a complicated and costly industrial operation compared to twisting a spiral from a manufacturer point of view.

Furthermore, in a vertical coil where the cryogenic fluid is flowing alternatively up and down, the buoyancy effect does not accumulate and the channel mass flow repartition can only be altered because of one coil height. It should remain unaltered in a seal tube, but the price to be paid is an excessive superconductors temperature rise as reported in Table 4-1.

Sensors linearity and thermosiphon discussion

With increased power, PF-FSJS experiments become highly nonlinear above $r=1$ and the downstream temperatures tend to drop (Figure 4-4). But does a weak conductor annular heating invariably lead to an alteration of mass flow balance and of the expected channel temperature evolutions?

A weak thermosiphon also reduces the annular mass flow rate and tends to increase on the contrary the temperature in the annular channel. The low experimental PF-FSJS downstream temperature may be interpreted as a reduction of Λ : helium expansion leads to a smaller bundle mass flow ratio α_A that reduces Λ . The associated mass transfers (annular He escape to the central channel, then partial refueling after the heaters) tend to increase H and again locally reduce Λ . This could explain a low downstream annular temperature rise.

Another side effect of feeding high power to the conductor is that temperatures significantly high may result in a non-negligible jacket longitudinal conduction. Note that AH experiments give evidence of progressive non-linearities above $r=1$ while experiments reflect sudden changes at certain temperature thresholds. AH and AC field experiments are not directly comparable, whatever the value of r is.

AC losses experiments have a more complex distribution and thermal behaviour; they provide evidence of thermosiphon in the two conductor channels, with a reduction of their cooling functionality. Instead of modeling this intricate phenomenon, its occurrence risk is evaluated using a simple ratio r , where hydraulic and thermal aspects of the conductor are intrinsically linked.

4.2 Design sensitivity to friction and heat transfer

The interdependency of spiral hydraulic and thermal responses is here under focus. It is important to comparatively determine how spiral design influences CICC thermohydraulics. Mass exchange between channels through the spiral is still considered an underlying parameter, that remains hidden in the heat exchange intensity and is not directly measurable, nor necessary to evaluate.

4.2.1 Friction sensitivity to spiral design

Spiral friction is calculated according to the chapter 2 experimental model, and conducted on spirals of various gaps and diameters (Figure 4-8). With close friction factors values, the diameter is the primary factor leading pressure drop:

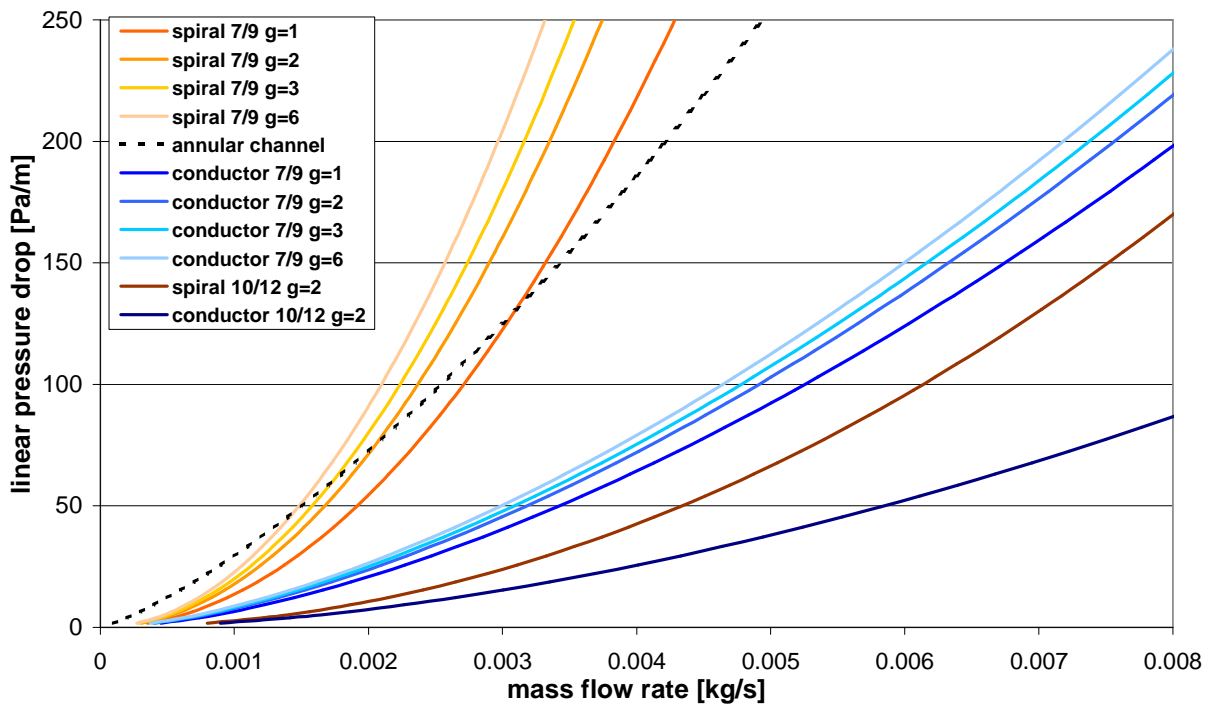


Figure 4-8: Calculated pressure drop for spirals of various gaps and constant 50% conductors wrappings

Perforation: The ITER project raises the question of an optimal perforation for a 7/9 spiral. Wrapping being equal (50%), lowering perforation leads to enhanced hydraulic behaviour with reduced friction. A friction factor difference among spirals becomes less significant between conductors equipped with these spirals, because of the common presence of the annular channel.

All this Table 4-2 is calculated assuming a 33% void fraction which is the specified ITER value. Due to the sensitivity of Nb₂Sn to flexion, it could be considered to decrease the void fraction of TF conductors down to 28%. In this case the linear pressure drop increases to 256 Pa/m.

Variations of the gap lead to variations of the angle α of the spiral, which decrease friction faster than heat exchange as it drops from 90° to 45°. Gee and Webb reported a maximum value of St/f for $\alpha=45^\circ$ [HSPCHT]. α may be reduced by increasing the turn length t , which would also result in a smaller frequency of the spiral singularities.

Table 4-2: Thermohydraulic performance of TF conductor at 8 g/s with variable perforation (gaps from 1 to 6), 33% void fraction and 50% wrappings

| | TF g1w50 | TF g1.5w50 | TF g2w50 | TF g3w50 | TF g6w50 | unit |
|----------------------------|-----------------------|-----------------------|-----------------------|-----------------------|-----------------------|-------------|
| Perforation | 14.3 | 20 | 28 | 33.3 | 50 | (%) |
| Turn gap | 0.006 | 0.006 | 6.15×10^{-3} | 0.006 | 6.15×10^{-3} | m |
| f_C | 0.001 | 1.5×10^{-3} | 2.35×10^{-3} | 0.003 | 6.15×10^{-3} | m |
| \dot{m}_C | 0.037 | 0.046 | 0.057 | 0.838 | 0.12 | - |
| Lineic pressure drop | 3.98×10^{-3} | 3.74×10^{-3} | 3.72×10^{-3} | 3.38×10^{-3} | 3.22×10^{-3} | kg/s |
| H | 185 | 200 | 204 | 227 | 239 | Pa/m |
| Λ | 358 | 466 | 614 | 840 | 1384 | W/m^2K |
| $(T_A - T_C)_{asymptotic}$ | 0.88 | 0.68 | 0.512 | 0.367 | 0.219 | m |
| ΔT_{Add} | 0.98 | 0.071 | 0.054 | 0.0355 | 0.0206 | K |
| r | 0.049 | 0.034 | 0.025 | 0.0151 | 0.0084 | K |
| | 0.089 | 0.054 | 0.040 | 0.024 | 0.013 | (-) |

The shape of the spiral attack angle is important to the turbulence. Spirals fabrication method generates rounded edges on one side of the ribbon before it is helically shaped into a CICC spiral. ITER design recommends the external twisting of the rounded side of the spiral, in order to avoid local pinching of the fragile superconducting strands. In fact, it would be desirable to have the spiral inside edges rounded as well (Figure 4-9). Turbulence pressure drop is highly responsive to flow separation and sharp trailing edges; these should absolutely be avoided. Of course, because helium is fed in the middle of a double pancake and flows in both directions, spirals must be symmetrical and there can be no difference between attack and trailing edge. The operation of edge smoothing should not raise the price of spirals much above its value of ~10€ per meter, that remains ludicrous compared to the tons of valuable superconducting strands.

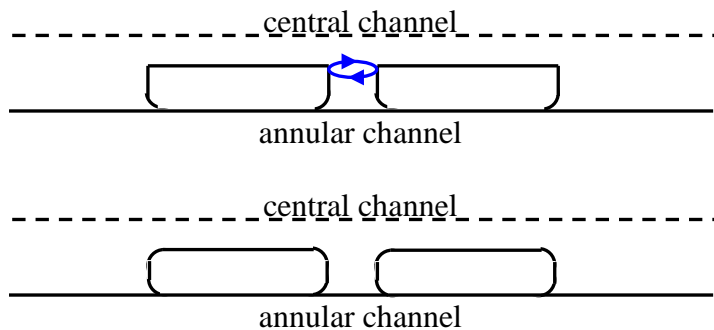


Figure 4-9: Spiral angle shape: ribbon fabrication rounded edges are set outside additional rounded edges would allow to both preserve superconducting strands from local pinching, and reduce trailing turbulence.

A reduction of the spiral gap provides a mechanical and hydraulic benefit: the strands petals are better sustained and the pressure drop is reduced (see Table 4-2). From the pressure drop point of view, it is recommended to reduce spiral perforation. The down side is thermal: because the perforation is smaller (combined with a larger quantity of helium flowing in the central channel), all thermal properties are degraded when the spiral gap shrinks.

4.2.2 Interchannel heat exchange sensitivity to spiral design

The steady state analysis from section 3.3 illustrates the maximal temperature difference that appears in an infinitely long conductor subject to a permanent heat load. A real conductor heating of finite length and finite duration will naturally lead to a somewhat smaller temperature difference. The thermal barrier between the channels of a CICC being alternatively made of central spiral perforated and closed parts, the local thermal resistance is varying and local temperature differences have been calculated in Appendix V. Numbers prove that the spiral step scale is too small and that this additional level of complexity is unnecessary. The average heat exchange properties allow an accurate macroscopic evaluation of the maximal interchannel temperature difference.

Providing an upper limit to these thermal differences is fundamental to superconducting strand temperature control, and allows to assess the optimal geometry that should be assigned to the CICC central spiral.

Given the extreme geometric complexity of the annular channel, which includes twisted strands, wrap around petals and empty corners, this porous medium is more isothermal when heat load is applied to the strands directly. The hypothesis of a high lateral heat transfer is important to temperature homogeneity, carried by forced convection and turbulent mass exchange. The various twisting levels of the strands lead to a pitch of mechanical transposition of the subcable of at most 0.45 m.

Conduction has a major impact on the heat exchange through the spiral: the heat resistance through the spiral closed parts is 5 to 10 times more than the resistance through the perforated area. The thermal characteristics of the spiral are hence very sensitive to the perforation.

Because reducing perforation is the most efficient way to reduce pressure drop, it is vital to demonstrate how perforation acts on the CICC interchannel heat exchange. Table 4-2 shows how perforation influences H, all other geometric parameters remaining constant. Note that heat exchange measurements were performed only on spirals of diameters 10-12 mm, and that thermal data in Table 4-2 is derived from the model in chapter 3.

As expected, a smaller perforation degrades temperature homogenization properties. While the trend is clear, the reasonable values of heat transfer in Table 4-2 (a few hundreds of $\text{W.m}^{-2}\text{K}^{-1}$) allow to advocate that it is acceptable to reduce perforation as low as ~0.15 to 0.2. It is clear that benefits outweigh drawbacks; therefore the author recommends to minimise the perforation, keeping a gap of 1 to 2 mm.

Table 4-3: performance of TF conductor joint

| TF joint | Tube 6/12 | unit |
|---------------------------------------|-----------------------|-------------------------------|
| Perforation | 0 | (%) |
| m_c | 6.15×10^{-3} | kg/s |
| Lineic pressure drop | 435 | Pa/m |
| H | 58 | $\text{W}/\text{m}^2\text{K}$ |
| Λ | 2.9 | m |
| Q | 10 | W/m |
| $(T_A - T_C)_{asymptotic}$ | 2.69 | K |
| ΔT_{Add} after $\sim \Lambda$ | 4.27×10^{-2} | K |
| r | 0.223 | (-) |

In the limit case without perforation, as in the joints mounted with tight tubes, mass exchange is no longer possible, turbulence is strongly reduced and heat transfer becomes poor. As shown in Table 4-3, the combined effect of a dangerously small annular flow, also contributes to a poor heat exchange coefficient value, although the central channel diameter has been reduced to 6 mm.

4.2.3 Wrappings

The purpose of conductor wrappings is to reduce undesirable currents induced in the copper strands.

Manufacturing the two PFIS sample legs differently was intended to assert whether the wrappings electrical benefit in AC losses reduction was mitigated by their thermal penalty. On the PFIS experiments, AC losses heat up the NW leg (right) without wrappings more than the W one (left), as expected. The heat generated by the eddy currents resulting from an AC field excitation has a reduced intensity on the PFIS W (L) leg.

From temperatures evolution, the heat transfer coefficients without wrappings reported in Table 3-3 are twice as good as their twins with wrappings. However, the temperature rise with the wrappings remains much lower than without (Figure 3-11). At first sight, it means the wrap electrical advantage (less heat) overcomes the thermal coupling reduction (less cooling) for superconductor's temperature. In fact, the two legs may not be directly comparable because of a different heat distribution. The AC field experiments conducted in SULTAN create a magnetic field on a narrow length, and it seems the induced heating length is longer than the field itself. The flat temperature evolution is evidence of a longer heating distribution in AC losses with wrappings as compared to without. The PFIS AC loss upstream temperature T_5 is slightly rising even at very low power, which is disturbing and may be a sign confirming a wider W heating length. Results should therefore not be extrapolated to any length or any power. It is not certain that a reduced power is always preferable, from a temperature point of view, to an increased heat transfer.

Wrappings results are more dependent on gravity: Figure 3-21 shows H_w upward is lower than H_w downward. This is probably not due to the value of H itself, but artificially linked to the transient measuring method: a change of mass flow repartition α_A (and velocities) directly impacts the transient thermal response (Figure 4-10). In the case of an upward flow, when the wrappings reduce heat transfer and keep the subcable petals tight, the central channel front advancing faster is warmer, contrary to previous PF-FSJS experiments exhibiting thermosiphon [Ren05]. The density of the He decreases with temperature; this effect increases U_C and reduces U_A and α_A . The rising temperature slope is decreased and it looks as if H_w was smaller, from a constant velocity and temperature independent material properties model point of view. Without wrappings, the opposite effect observed could be explained by faster upward central channel circulation again, but this time transmitted more efficiently through mass exchange and higher heat transfer to the annular channel, thus leading to an increased rising temperature slope.

A conductor without wrappings is more permeable and less subject to thermosiphon.

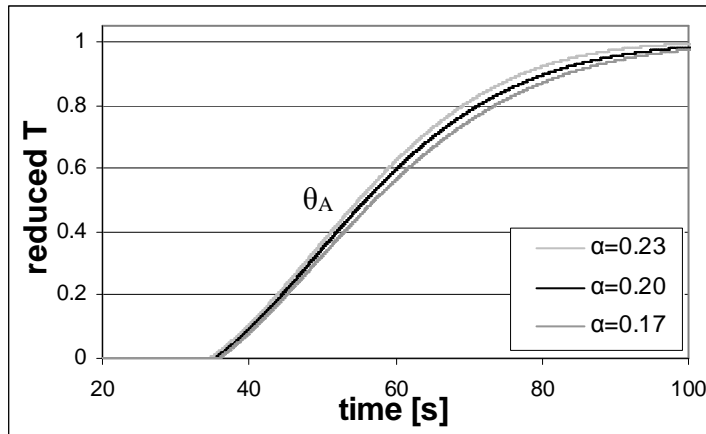


Figure 4-10: Annular T calculation sensitivity to annular flow ratio α_A value (+/-15%),
at $x=2.7$ m (LT1) 8 g/s W (L), H being constant

The wrappings covering percentage will affect the heat transfer performance of spirals, according to the model developed in (3.5-1). Contrary to the choice of spiral gap that has a significant hydraulic impact, the percentage of wrappings coverage has a negligible influence on the pressure drop. The thermal downside is to be balanced with the electrical benefits. The following Table 4-4 is given for a constant perforation of 33%:

Table 4-4: influence of wrappings on conductor thermohydraulic performance

| | TF g33nw | TF g33w50 | TF g33w80 | unit |
|----------------------------|----------|-----------|-----------|--------------------|
| Perforation | 33.3 | 33.3 | 33.3 | (%) |
| Wrap coverage | NW | 50 | 80 | (%) |
| H | 1197 | 840 | 625 | W/m ² K |
| Λ | 0.257 | 0.367 | 0.493 | m |
| $(T_A - T_C)_{asymptotic}$ | 0.0249 | 0.0355 | 0.0477 | K |
| ΔT_{Add} | 0.0106 | 0.0151 | 0.0202 | K |
| r | 0.0166 | 0.0237 | 0.0320 | (-) |

The presence of wrappings has a significant impact on the interchannel heat exchange according to the model (section 3.5). This locally negative impact on H seems acceptable and wrappings are more than welcome when considering that their presence not only reduces the local heat load, but also total temperature increase and refrigeration power [Nij04].

When measuring a reduction of H with the presence of wrappings, the physics of this heat transfer setback is not well known. It is thought that the wrappings impede the contribution of heat transport due to mass transfer, while the convection in the spiral remains unchanged. A serious heat transfer characterisation requires the knowledge of the interchannel helium mass transfers.

ITER wrappings specifications will be of 50 % subcable coverage instead of the 80 % manufactured on the PFIS. This raises H and ensures an easy transverse thermal coupling. The wrappings do not constitute or burden any critical design point for dual channel CICCs. Even if the local impact of wrappings is balanced and may be discussed, there is still a fundamental certitude to their thermal effect: wrappings reduce the global heat load supported by the coil and the associated cryoplant power. Wrappings reduce investment and operational refrigerating costs dictated by the coil design, hence wrappings are good.

4.2.4 Central channel diameter and thickness

The size of the central channel is also a variable parameter that can be justified and optimised. The cable pressure drop and cooling time depend on this diameter: the spiral diameter is more significant than the spiral roughness in determining the respective channels flow rates and velocities.

A large diameter central channel best carries the dual channel principle of fast and easy helium flow. However, a variety of reasons lead to balance the choice of spiral diameter. In the case of toroidal coils the diameter was chosen (small enough) to keep coils compact, in relation with the high current density required by the ITER project to reduce the reactor size and thereby the cost. In these TF vertical coils subject to critical heat loads, the spiral diameter should also be chosen (small enough) in order to maintain a small thermosiphon risk ratio r . Thirdly, strands temperature –the priority in these high heat load coils (ITER TF & CS)– require a small enough diameter to maintain annular helium surface and mass flow rate high. Indeed, annular helium flow surface around the strands (linked to the void fraction) is the only volume of coolant considered in the case of a quench. ITER design has reduced annular void fraction from 36% to 32%, but the void impact on electromagnetic issues is more critical than on thermohydraulic issues, and the void is here considered firm. In practice, temperature criteria lead to an annular helium mass flow rate of about half the total mass flow rate.

In the case of horizontal poloidal coils, with no stringent heat load and compactness conditions, a large spiral conveying most of the mass flow rate is acceptable for the superconducting strands, and certainly a better choice to reduce pressure drop. The design of the ITER PF coils should consequently call for spiral of diameters 10-12 mm.

The spiral has an important mechanical role of pressure distribution when the petals are subject to the Laplace force. Thermohydraulic inserts would not offer this regularly distributed support [Bos95]. The mechanical constraints impose the minimal thickness of the spiral. Proposed spirals have a constant default thickness of 1 mm. A design improvement (a reduction) of this spiral property is possible, but only with a mechanical calculation that should justify the minimum acceptable thickness given other spiral properties and expected pressure conditions.

4.3 Optimal central channel proposal

4.3.1 Spiral improvement criteria

Experimental CICC testing and modelling has provided in-depth understanding of temperature variations mechanisms.

Beyond model validity and accuracy, their physical meaning and parametric trend allows to better understand how design changes the cable thermohydraulic properties and cryogenic needs. The improvement first consists in defining risk situations and keeping cable operation away from it. An accurate annular channel additional temperature ΔT_{Add} above the average conductor temperature can be calculated. A thermosiphon risk ratio has been defined (section 4.1).

An appropriate mass flow repartition is desirable (section 4.2.4). From this frame it is possible to choose a minimal safe interchannel heat transfer coefficient. While a monochannel CICC is isothermal, it is the heat transfer coefficient in a dual channel conductor that governs the temperature increase in the annular region. A heat transfer coefficient of a few hundreds of $\text{W.m}^{-2}\text{K}^{-1}$ for a nominal magnet mass flow rate of 8 g/s leads to an efficient temperature homogenization. The expected temperature difference $T_A - T_c$ is $\leq 0.04 \text{ K}$ with the most stringent ITER local heat load deposition scenario of $Q=1.6 \text{ W/m}$ [Bes05].

Given this minimal interchannel heat transfer coefficient, an improvement consists in minimising costly pressure drop according to the spiral thermohydraulic laws in Figure 4-11. Once a spiral is chosen, a global conductor properties check can guarantee that conductor cooling operation will contain strands temperature increase even when calling for minimum pumping power. The recooling time is a parameter that may not be critical, but should nevertheless be minimised to gain time during reactor operation.

Behind the physical properties, the characteristics of the cooling system feeding the coils provide the cost function in terms of pumping losses and cooling power. This cost function will ultimately set the optimal choice. In summary, constraints other than thermohydraulic first set the frame of possible modifications. Spiral design improvement is conducted from a sensitivity analysis on three criteria: pressure drop, annular channel temperature and thermosiphon risk. Other properties are simply checked.

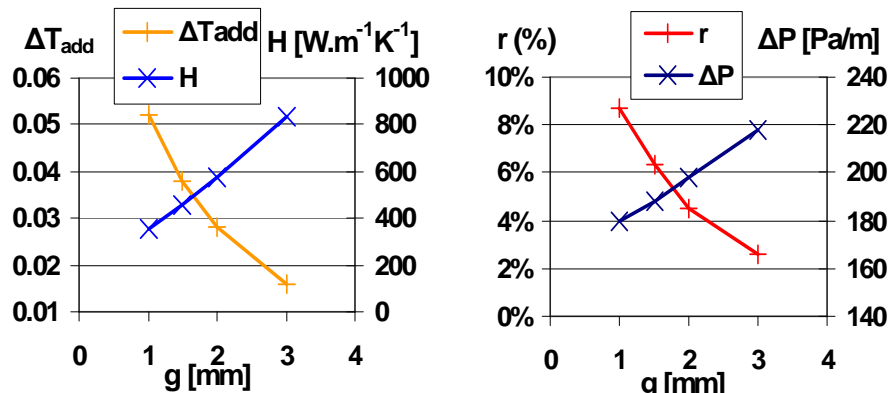


Figure 4-11: Sensitivity analysis of the additional temperature ΔT_{Add} , the heat transfer H , the risk ratio r and the conductor lineic pressure drop ΔP on the gap length g

4.3.2 Proposal of spiral design

A simple and efficient way to optimise a complex system is to work on the variables separately, tuning parameters again after all others have been modified, in order to converge towards a solution obeying the optimisation law of each variable [Siarry]. Reducing the perforation offers a reduced hydraulic pressure drop but reduces thermal exchange. A look at the global conductor hydraulic and thermal properties allows to advocate that the benefits of small gaps spirals outweigh the thermal drawbacks. Additionally, it is wiser to seek a best thermohydraulic compromise at small perforation values, where the spiral keeps its mechanical strength. The author hence pleads for spirals with a small perforation ratio between 0.15 and 0.2 (Table 4-5). TF and CS coils, sensitive to thermosiphon, must be equipped with spirals of external diameter no larger than 10 mm. Higher diameter central channel spirals are a better hydraulic choice, possible only for PF coils unresponsive to thermosiphon.

Table 4-5: Example of proposed ITER spirals of diameters 7/9 and associated dual channel Cable-In-Conduit Conductor performance

| Central spiral | | Dual channel conductor | |
|--------------------------------------|--------|---------------------------------------|-------|
| id [mm] | 7 | Flow repartition α_A % | 47 |
| od [mm] | 9 | m_C [g/s] | 3.74 |
| e [mm] | 1 | m_A [g/s] | 4.26 |
| t [mm] | 6 | Pressure drop [Pa/m] | 203 |
| g [mm] | 1.5 | Wrap coverage % | 50 |
| p [mm] | 7.5 | H_{turn} [W/m ² K] | 196 |
| Diameter Dh [mm] | 6.89 | $H_{Perfor\ w}$ [W/m ² K] | 864 |
| Roughness e/Dh | 0.145 | $H_{Perfor\ nw}$ [W/m ² K] | 2162 |
| Perforation % | 20 | H [W/m ² K] | 458 |
| Cavities g/e | 1.5 | Λ [m] | 0.69 |
| Angle α [degrees] | 75 | $(T_A - T_C)_{asymptotic}$ [K] | 0.071 |
| Spatial freq. 1/p [m ⁻¹] | 133 | ΔT_{Add} [K] | 0.034 |
| Friction factor | 0.0465 | r | 0.054 |

Although this study cannot experimentally sustain the choice of spiral edges, rounded instead of square inside edges of the spirals' rectangular cross section are proposed with the intention to further reduce friction turbulence.

4.4 Other issues and alternative CICC design

Large superconducting coil design is on the frontier of knowledge in the fields of superconductivity, electromagnetism, cryogenics, thermohydraulics and mechanics. This section evokes interdisciplinary issues, open questions and possible future experiments.

4.4.1 Strands compression

The current supported by superconducting strands in a CICC, characterised by the current density J_c , is negatively affected by:

- The compression of petals by the magnetic field and Lorentz forces, flexion that creates curvature and local pinching of strands. ($J_c - \sim 20\%$)
- The thermal differential expansion between stands and jacket, which compress strands when cooling after the heat treatment (steel expands and contracts more than copper) ($J_c - \sim 30\%$).

Both mechanical effects generate a performance loss of 50 to 60% between tested CICC samples and the individual performance of a healthy strand, extrapolated to the number of cable strands. Strands with higher performance levels are hence being studied, in order to keep a sufficient CICC current after mechanical degradation.

The magnetic force on each strand is proportional to B^*I .

$$\vec{F} = \vec{J} \wedge \vec{B} \quad (4.2-1)$$

Pressure integrates with the number of strands carrying current; therefore it integrates on the conductor height [Ren95].

The effect of pressure could be alleviated. Several possible ways to reduce strand movement have already been thought: bigger superconducting strands [Lib05-2], conductors filled with brazing [Pas04], or conductors with a reduced void fraction. A solution to keep helium volume high and provide a mechanical continuity in the annular channel could consist in filling the void fraction with metallic foam (Figure 4-12). The choice between copper and stainless steel would depend on the desirable electric contacts between strands.

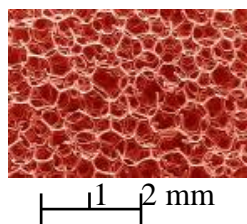


Figure 4-12: Copper foam with open porosity
(courtesy of ‘Société de Conseil et de Prospective Scientifique’)

The thermohydraulics of the conductor would be changed because of a seriously impeded annular helium circulation. In short, an idea that requires to rethink the concept of CICC, and cannot be implemented on the short term, except possibly in a conductor joint.

The pressure itself could be lowered by reducing the cable height. Instead of petals, the bundle channel is formed by subpetals, and a permutation such as that of the Rutherford cable

provides the conductor relative electrical symmetry. Figure 4-13 provides a graphic example for a half-cable, but it is possible to draw a flat cable having any number of strands.

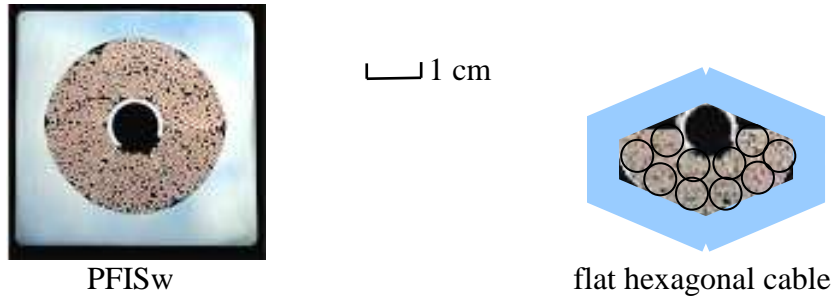


Figure 4-13: Proposition of a flat dual channel CICC

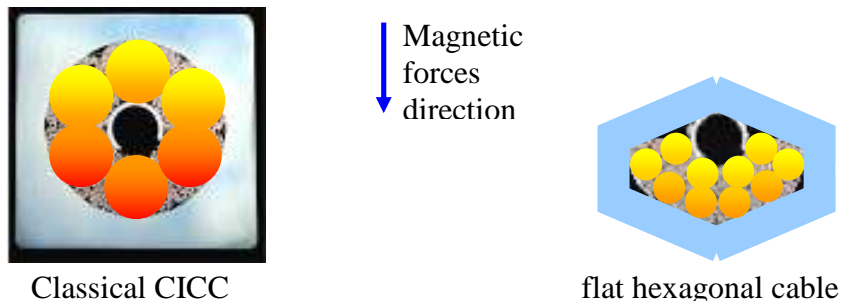


Figure 4-14: Comparative pressure level on strands

The thickness of the bundle channel is the same everywhere, therefore it is minimal anywhere and magnetic pressure does not accumulate to crush strands. The dual channel concept, with pressure drop reduction and faster helium circulation is still possible. Wrappings should limit undesired lateral currents, if possible. Coil fabrication using such conductors with half coverage is not a space loss, because a trapezoidal fusion coil cross-section is well filled with a half widths increments grid.

The potential gain on superconductor performance in a flat dual channel conductor deserves a more thorough study.

Superconducting material is produced through diffusion of a metal in another. This is achieved with a heat treatment of hours at temperatures of 700°C of the fragile conductors in their final shape. Heated metals become lax and copper stretches to match the expansion of steel. The thermal differential expansion between stands and jacket becomes a concern during cool-down, when limp copper becomes resilient: steel contracts more than (stretched) copper, curving and compressing strands. Curvature adds to the complexity of the differential expansion, as observed during the TFMC fabrication [Raf03]. Strands current transport capacity is strongly compromised by mechanical deformation [Zani04]. The jacket-strands differential expansion should be minimised to avoid massive coil performance loss. Low contraction jacket metal was tested, but easy manufacture and soldering remain a priority for the helium-tight conductor jacket.

Jacket stretching –either during cool-down or when placing pancakes in their casing– could be an efficient way of zeroing the strands compression. Preliminary calculations demonstrate that small displacements with a high precision and reproducibility are required, making this a delicate process [Dec97]. Because a high performance gain is at stakes through this seemingly simple mechanical touch, it seems worth a thorough examination.

Superconductor strand stability depends on local temperature and heat transfer properties [Bot98, Cia05, Bot06LHC]. It is however not possible, to extrapolate strand properties to a

cable properties, whether hydraulic, mechanical or electrical [Duc76]. Empirical models prove to be simpler and more efficient than trying to bring small-scale models to a larger scale.

4.4.2 Future investigations to optimise CICC thermohydraulics

The pressure drop testing of smoothed spirals (i.e. spirals with rounded inside edges), would be interesting, as the edge shape can hardly be taken into account in a model, while it certainly can affect trailing edge turbulence and pressure drop.

Water testing should maximize the number of temperature sensors at various depths on a short distance, and benefit from the possibility to move the heater in order to obtain the multiple measurements sensitivity to distance from the annular heater. Ideal thermometer locations include the bundle dead corners, a petal heart and the central spiral, helpful to better understand temperature behaviours. Jacket temperature underneath the heaters would be desirable as well. Given the short thermal homogenisation length Λ , a CICC sample length of a couple of meters is enough, plus a hydraulic settlement length.

A set of water experiments in a configuration of closed central channel would allow measurements of the bundle pressure drop and the bundle to jacket heat transfer coefficient. This data would be pertinent to the understanding of the full CICC complexity.

Next conductor samples in Sultan will be appropriately instrumented with the PF-FSJS configuration: long AH and thermometers regularly set, close downstream and away from the joints –where mass flow repartition is disturbed.

It would be wise to obtain both steady state and transient experimental measurements of the heat transfer coefficient on the same piece of prototype CICC, in order to validate the values obtained by the two experimental procedures and separate calculation methods [Cia06].

A parametric study of the global interchannel heat transfer coefficient H as a function of the volume flow rate Q_v and the temperature T (or the Reynolds and Prandtl numbers [Vic04]) would qualify the thermal CICC properties at higher temperatures and complete the model.

CEA\Grenoble disposes of a cryogenic helium loop equipped with a 4.5g/s pump in a horizontal sample configuration (about half the mass flow rate needed for the forced cooling of a CICC). This loop has been used weekly for CERN coils testing among other samples. This testing loop provides an opportunity of getting measures on CICCs, with the possibility of imposing electric losses in the copper strands to simulate Joules losses occurring during current rise or decrease.

A numerical study of the hydraulic and thermal turbulent flow patterns is an important tool. After a proper validation with experimental data, the numerical model should allow the parametric study, understanding of turbulent phenomena, extrapolation of the geometries, validation of the analytical models and improvement of the spiral.

Conclusions

Dual channel Cable-In-Conduit Conductors

A forced flow cooling circulation through large high-field superconducting coils Cable-In-Conduit Conductors is an efficient way to remove variable heat load and maintain the low temperature, critical to superconductor reliable operation. The necessity to balance the fusion reactor ITER pancakes pressure drop is demonstrated in this thesis. A free-flow central channel is justified to reduce pressure drop in the forced cooling circulation, highly expensive in cryogenic cooling. The dual channel concept, however, introduces a problem of temperature homogenisation and requires design improvement. This improvement is the grail that was sought in this work; it requires to understand the driving parameters of the central channel spirals thermo-hydraulics.

Pressure drop

Models for helium flow through a bundle of superconducting strands exist and are useful, even though they have stringent limitations. Existing data of spiral hydraulic pressure drop in nitrogen were studied, adding compressibility and Joule-Thomson expansion. An experimental campaign focused on a dozen spirals' hydraulics in water was further conducted with a better precision, obtained after redundant checking. A slight Reynolds dependence was modelled as shear drag. The high form drag is modelled by choosing appropriate parameters from turbulence patterns and available models. Shear and form drag are added in an explicit parametric friction factor model, proposed for (helically roughened tubes) spirals.

Thermal coupling

The thermal coupling between the hydraulic channels was investigated using water and low temperature supercritical helium, taking part in two European campaigns in the test facility SULTAN. Imprecise water testing was rapidly set aside to focus on steady state and Heavyside transient helium experiments. Two different methodologies have been developed for the two kinds of experiments, respectively based upon a characteristic length and a thermal wave traveling propagation, or characteristic time. Despite annular conductor temperatures measurement difficulties, experimental campaigns have led to validate analytical bithermal laws of dual channel conductor temperature evolutions under local heat load excitation or during a coil cooling phase. These developments unveiled the interchannel heat exchange behaviour, key to the spiral improvement. A simple explicit model of heat exchange coefficient was built. Maximal temperature difference in the conductor, thermosiphon risk and recooling time have been defined and estimated.

Conductor design improvement

The now available pressure drop and heat exchange models are explicitly simple albeit already quite elaborate, given the tenuous and high uncertainty experimental database they are each drawn from. Based on these models and on the new understanding of Cable-In-Conduit Conductors thermohydraulic behaviour, a central spiral optimisation could be initiated, in order to propose a best central channel design for fusion reactors (ITER). The risk of thermosiphon choke must be avoided and an enlightened minimum to the intensity of heat exchange is set. Within this frame, a pressure drop reduction is possible by reducing spirals gaps down to 1.5 mm, with a perforation of 15 to 20%.

Perspectives

More experimental work is required to complete the database and validate the choice of a low perforation spiral with rounded edges. A numerical validation of this experimental and analytical contribution would help to complete and refine the understanding of the spiral geometry impact on its thermohydraulic properties. In order to alleviate mechanical degradation of superconducting strands performances, a study of a reduced annular void fraction or increased strands diameter could be performed. The circular geometry of the cable itself, less adapted to the high mechanical constraints in the new Nb₃Sn strands, may have to be flattened or reduced in size. The newly developed models provide tools to accompany the design of a dual channel Cable-In-Conduit Conductor from a thermo-hydraulic point of view. Though forced flow dual channel Cable-In-Conduit Conductor coils could be replaced by bath or dry coils technologies in the future, they provide an established way to stabilise the temperature of high discharge voltage superconducting coils operating in transients.

Personal conclusion

The success of a research lies in the art of questioning, sustained in this Ph.D. thanks to the rich scientific environment of “Groupe CRYomagnétisme” that holds competences in cryogenics, mechanics, superconductivity and thermohydraulics. Preparing this long term project forced me to seek the right questions, to separate the message from the pedagogic vector, to be open-minded, to develop my scientific knowledge, skills, creativity, tenacity, autonomy and responsibility. I had to surpass myself and to demonstrate an innovating mind, intellectual honesty and the ability to grasp complex intellectual developments with the ambition of providing a state of the art answer. This experimental and theoretical work, which contributes to an international energy project, also includes technological, numerical and economic aspects.

Résumé détaillé :

Comportement thermo-hydraulique des supraconducteurs de type câble-en-conduit à double canal pour ITER

Introduction

Les besoins croissants d'énergie pour la consommation mondiale poussent les chercheurs à trouver des solutions alternatives aux énergies fossiles. La fusion thermonucléaire fait partie des énergies propres susceptibles d'être fournies en grande quantité. Pour obtenir et contrôler la réaction nucléaire similaire à celle qui chauffe notre soleil, un mélange deutérium-tritium est porté à une centaine de millions de degrés sous forme de plasma qu'il faut confiner efficacement afin de limiter les pertes thermiques. Plusieurs systèmes de confinement existent ; le plus étudié et prometteur est le tokamak. Le plasma est confiné dans un tore au moyen de champs magnétiques intenses. La densité de particules y est faible (10^{-5} fois celle de l'air) mais le temps de confinement de l'énergie est grand (quelques secondes). Dans un tokamak, le confinement du plasma est assuré par la faculté qu'ont des particules chargées de décrire des trajectoires hélicoïdales autour d'une ligne de champ. La configuration magnétique d'une telle machine comprend des systèmes de champ toroïdal (TF), poloïdal (PF), ainsi qu'un solénoïde central (CS) et le champ propre du courant plasma (Figure R-1).

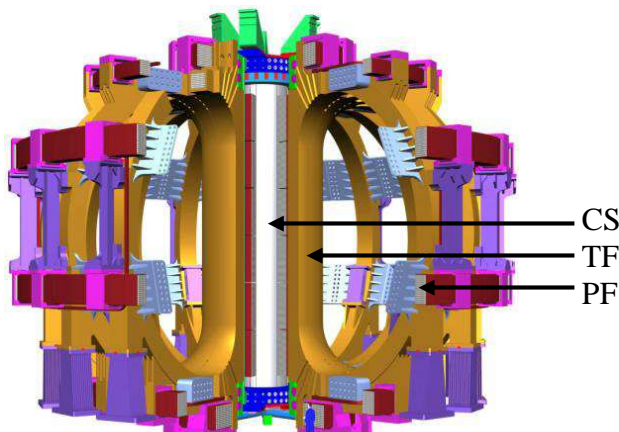


Figure R-1 : Configuration magnétique d'ITER pour le confinement du plasma (source ITER)

Projet ITER

Des partenaires internationaux regroupent depuis une quinzaine d'années leurs efforts de recherche sur la fusion contrôlée par confinement magnétique, en vue de la construction d'une machine nommée ITER (chemin ou International Thermonuclear Experimental Reactor). Le projet ITER, décidé en 2005 et dont l'implantation sera à Cadarache, a pour but de démontrer que la fusion thermonucléaire est une source d'énergie possible pour l'humanité.

Les bobines des systèmes de champ magnétique du projet ITER nécessitent des courants électriques importants sur de longues périodes, ce qui justifie l'utilisation de matériaux supraconducteurs. Les conducteurs doivent être produits puis bobinés ; un refroidissement cryogénique leur confère l'état supraconducteur. Le projet ITER a concentré un important travail dans les technologies cryogéniques pour les supraconducteurs, dans les bobines et dans les réseaux de distribution d'hélium supercritique. Ces programmes de développement des conducteurs offrent une mine d'expérimentation visant à comprendre et modéliser les conducteurs supraconducteurs de type câble-en-conduit, utilisables pour toute bobine à haut champ (>5 T).

1. Conducteurs de type Câble-en-conduit à double canal

Supraconductivité

C'est la propriété remarquable qu'ont certains métaux ou alliages de voir s'annuler leur résistance électrique à très basse température. Les matériaux utilisés à échelle industrielle (le niobium-titan et le niobium-étain) doivent être refroidis par de l'hélium liquide à 4,2 K pour devenir supraconducteurs. Ces matériaux ont les paramètres critiques suivants :

- Densité de courant critique J_c

La densité de courant qui circule dans un matériau supraconducteur s'établit à la densité de courant critique J_c . C'est une fonction du champ, de la température, et des sollicitations mécaniques pour certains matériaux.

- Champ critique B_c

Si le champ magnétique dépasse B_c , le matériau perd son état supraconducteur.

- Température critique T_c

Au delà de la température critique T_c , le matériau perd sa supraconductivité. Cette température est très basse, au plus 23 K pour les supraconducteurs conventionnels.

- Contraintes mécaniques

Certains matériaux ont leurs paramètres critiques (B_c , T_c , J_c) sensibles aux déformations mécaniques (traction/compression). Les contraintes ne sont pas une limite à proprement parler, mais peuvent occasionner une dégradation des performances du supraconducteur.

Si au moins l'un des trois paramètres (B , T , J) dépasse sa valeur critique, le caractère supraconducteur du matériau est perdu. Maintenir basse la température du supraconducteur est incontournable. Les brins supraconducteurs sont constitués majoritairement de cuivre, pour leur stabilité thermique et pour porter le courant en cas de perte de la supraconductivité. Ils contiennent des filaments de niobium-titan et de niobium-étain. Ces derniers sont fragiles, moins ductiles que le NbTi et nécessitent un traitement thermique à environ 650 °C pendant trois semaines, mais supportent des champs magnétiques plus élevés et sont donc requis pour ITER.

Conducteurs de type câble-en-conduit

Les conducteurs de la fusion, caractérisés par des fortes valeurs de champ magnétique (5-13 T), de courant (40-70 kA) et de tension (5 kV/masse) ont évolué vers la géométrie de câble en conduit caractérisée par une gaine d'acier, une isolation électrique et une circulation forcée de réfrigérant.

Les câbles du projet ITER sont circulaires et constitués de 1000 à 1500 brins supraconducteurs de diamètre 0,81 mm, torsadés en niveaux successifs (Figure R-2).

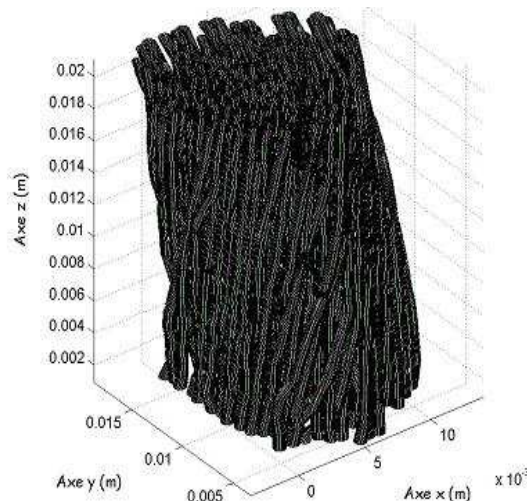


Figure R-2 : Torsadage d'un pétalement de câble supraconducteur (source CEA/DRFC)

Le câble ainsi formé est inséré dans sa gaine d'acier inoxydable, dans laquelle circule l'hélium pour la réfrigération. Ces conducteurs ont les avantages suivants:

- courants forts jusqu'à 70 kA
- symétrie circulaire favorable à une distribution de courant homogène
- refroidissement local des brins efficace par une circulation d'hélium
- faibles pertes magnétiques en champ variable
- isolation électrique externe efficace (comme pour un conducteur ordinaire)
- fabrication maîtrisée du conducteur en tirant le câble dans sa gaine.

La conception des conducteurs ITER a conduit à la construction de nombreux prototypes de câble, joint et même de deux bobines modèles représentatives du système de champ toroïdal et du solénoïde central.

Charges thermiques P_{hl} sur les bobines à 4,5 K

Des sources de chaleur variées occasionnent des charges thermiques sur les bobines supraconductrices du système TF du tokamak ITER :

- pertes de courant variable dans les structures des bobines et dans le conducteur supraconducteur (en moyenne 7,3 kW)
- pertes dues aux amenées de courant (~1 kW)

Pour limiter les pertes dans le conducteur, un enrubannage d'acier d'épaisseur 0,55 mm isole entre eux les six pétales au sein du conducteur pour réduire les boucles de courant. Des échantillons PF avec et sans enrubannage, ont été testés afin d'étudier l'efficacité des enrubannages.

- chauffage nucléaire résiduel derrière les écrans neutroniques

Le rayonnement neutronique échauffe les volumes métalliques, plus intensément les parties les plus proches du plasma. La puissance neutronique de fusion du plasma d'ITER (~400 MW) est écrantée par des modules activement refroidis à l'eau pressurisée et par la chambre à vide elle-même. Ainsi seule une puissance résiduelle peut atteindre les bobines du système TF, avec une puissance instantanée de 10 kW et moyenne de 3 kW pour un scénario de décharge de 500 s toutes les 1800 s.

- pertes résistives dans les joints des bobines, pertes statiques par rayonnement à partir des écrans et conductions dans les supports des bobines et les connexions (11,9 kW)

Les charges statiques peuvent être en partie évacuées par une circulation de réfrigérant externe à la bobine. Un système complexe d'écrans thermiques refroidis à 80 K à l'azote liquide limite encore le rayonnement du cryostat et de la chambre à vide. L'hélium liquide maintient finalement la température des bobines à 5 K.

Circulation forcée d'hélium supercritique

Toutes ces charges thermiques sont irréductibles et constituent l'hypothèse de travail pour le refroidissement cryogénique. Un débit d'hélium minimal de $8 \times 10^{-3} \text{ kg.s}^{-1}$ est déterminé afin d'évacuer P_{hl} et de maintenir les supraconducteurs sous la température limite nominale de 4,7 K. Une perte de pression de 0,06 à 0,1 MPa apparaît dans les circuits hydrauliques élémentaires du système TF (galettes) [ITER05]. Le travail de pompage de l'hélium P_{circ} pour combattre cette perte de charge introduit un échauffement (11,4 kW) qui s'ajoute à P_{hl} au niveau du réfrigérateur (Figure R-3).

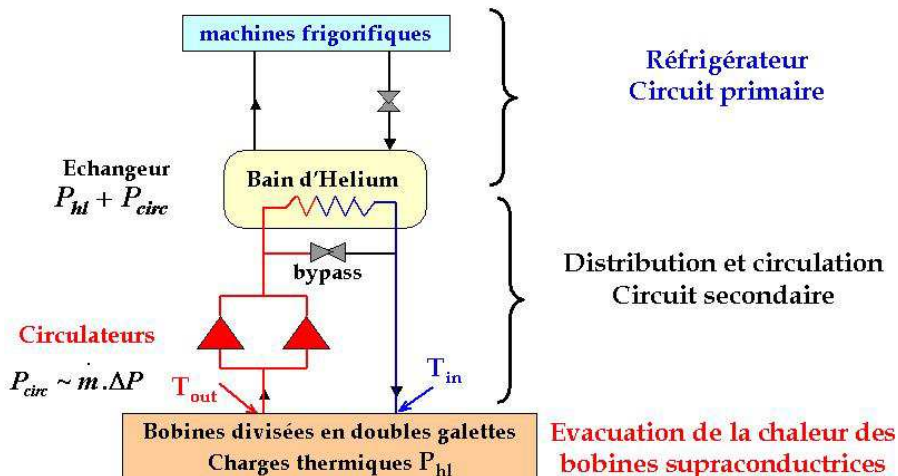


Figure R-3 : Principe des circuits Cryogéniques et pertes de pression de circulation d'ITER

La puissance électrique associée à cette puissance cryogénique additionnelle à 4,5 K est coûteuse : environ 2,9 MW. Un bypass permet de limiter la charge instantanée de l'échangeur du réfrigérateur, mais provoque alors une dérive de la température d'entrée des bobines.

Le but de cette thèse est d'optimiser la circulation de l'hélium supercritique dans les conducteurs supraconducteurs de type câble-en-conduit à double canal d'ITER, pour minimiser le travail de la pompe et la puissance cryogénique, sans compromettre le refroidissement des brins supraconducteurs.

Equilibrage des doubles-galettes

Les bobines d'ITER sont divisées en doubles galettes dont les conducteurs mesurent environ 700 m. Pour réduire la longueur hydraulique dans laquelle circule le réfrigérant, des entrées d'hélium sont introduites au milieu du conducteur des galettes ; l'hélium coule en direction opposée, partant de cette entrée hydraulique vers les connexions électriques des extrémités de galettes. Le système TF d'ITER comprend 18 bobines, chacune constituée de 14 galettes. La position idéale pour l'entrée d'hélium de chaque galette est en réalité le milieu hydraulique – et non géométrique – du conducteur en cas d'asymétrie.

A titre d'exemple, les essais de réception des conducteurs du stellarator W7-X montrent des différences de débit massique jusqu'à +/- 20%, pour des conducteurs théoriquement similaires et des pressions d'entrée et sortie normalisées. La présence d'un canal central devrait réduire ces différences pour les galettes d'ITER. Pour chaque satellite de distribution d'hélium, la galette la plus défavorable, c'est à dire ayant la plus grande perte de charge, impose la pression de distribution d'hélium qui assure le débit massique minimal m_{min} recherché. Une fois cette pression de fonctionnement fixée, les galettes peuvent éventuellement avoir des débits différents mais supérieurs à m_{min} . Comme le travail de la pompe est proportionnel au débit total $m = \sum_{i=1}^n m_i \geq n \times m_{min}$ y circulant, il est obligatoire de limiter les débits au strict

nécessaire en effectuant un équilibrage hydraulique des galettes à l'aide de vannes d'équilibrage.

Canal central

Pour réduire la perte de pression de l'hélium circulant dans le conducteur, et le travail de pompage qui lui est inhérent, les brins supraconducteurs sont torsadés autour d'une spirale perméable qui délimite un canal central à faible impédance (Figure R-4).



Figure R-4 : Vue éclatée des six pétals et de la spirale centrale d'un câble-en-conduit (source CEA/DRFC)

Le conducteur supraconducteur de type câble-en-conduit à double canal ainsi conçu a été sélectionné pour les bobines d'ITER. Un tel conducteur offre l'avantage d'une résistance hydraulique faible et d'un refroidissement poussé avec une compacité maximale. L'hélium y circule en parallèle dans la spirale centrale et dans la zone annulaire où il baigne les brins supraconducteurs. Le débit de réfrigérant est donc assuré par une circulation rapide d'hélium dans la spirale, permettant l'évacuation des calories moyennant un bon transfert thermique de la zone des brins vers la spirale centrale. Le canal central joue un rôle prépondérant dans la répartition des débits d'hélium et dans la caractéristique hydraulique globale du conducteur, donc sur les circulateurs, l'enthalpie de pompage, l'échangeur cryogénique qui combat cette enthalpie, les réfrigérateurs, la consommation énergétique et les coûts d'investissement et de fonctionnement. La Table R-1 montre que le canal central a un impact important sur un projet comme ITER, avec des conséquences économiques significatives.

La spirale garantit la dimension du canal central et prévient qu'il ne soit bouché ; elle assure un rôle mécanique lorsque le conducteur est soumis à des sollicitations magnétiques. Mais si le canal central permet de réduire les pertes de pression, il introduit une complexité géométrique et thermique.

Table R-1: Simulation comparée des propriétés du conducteur pour le système TF d'ITER et différents choix du canal central.

| Projections du conducteur ITER TF à canal central variable 0.6 MPa, 5 K, 8 g/s, 1400 brins, taux de vide 33% | | | | |
|---|--|--------------------------------------|--------------------------------------|--|
| | Spirale 7/9 mm Perfor 50% référence ITER | Spirale 7/9 mm Perfor 28% | Tube lisse 7/9 mm | Conducteur plus petit sans canal central |
| Coefficient de friction du canal central | 0,12 | 0,057 | 0,017 | ∞ |
| Répartition de débit | 5,1 g/s (anneau) 2,9 g/s (centre) | 4,2 g/s (anneau) 3,8 g/s (centre) | 3,5 g/s (anneau) 4,5 g/s (centre) | 8 g/s (brins, homogènes) |
| Perte de charge | $0,99 \times 10^5$ Pa | $0,77 \times 10^5$ Pa | $0,58 \times 10^5$ Pa | $1,9 \times 10^5$ Pa |
| Puissance cryogénique pour circuler l'He (TF) | 2,6 kW | 2,0 kW | 1,53 kW | 5,15 kW |
| Puissance électrique du réfrigérateur (TF) | 650 kW | 500 kW | 382 kW | 1,29 MW |
| Coût d'investissement frigorifique | 1,56 M€ | 1,2 M€ | 0,92 M€ | 3,1 M€ |
| Coût total sur 20 ans d'opération | 0,86 M€ | 0,67 M€ | 0,5 M€ | 1,7 M€ |

Echanges thermiques entre les deux canaux

Si le but affiché d'une spirale centrale est de faciliter la circulation d'hélium pour refroidir le conducteur, elle n'est pas sans conséquence sur le comportement thermique du conducteur, en particulier sur la température des brins supraconducteurs. Comme l'hélium central a été détourné de sa fonction de refroidissement du conducteur, les débits et vitesses annulaires au contact des brins sont réduits. Sous sollicitation thermique, le canal annulaire du conducteur reçoit de l'énergie et sa température s'élève. Par rapport à un conducteur de température homogène, une différence de température entre les deux canaux représente donc une perte de marge thermique pour le supraconducteur. La spirale centrale ne peut se contenter de minimiser les pertes de pression, ce qui conduirait à choisir un simple tube lisse, mais il faut trouver le compromis qui assure un échange thermique suffisant entre l'hélium annulaire et l'hélium central. Un bon couplage thermique des canaux doit permettre à l'hélium circulant plus vite dans la spirale faisant office d'échangeur thermique interne, d'extraire et d'évacuer efficacement la puissance thermique loin des brins supraconducteurs. En plus de la différence de température qui peut être un phénomène statique, la différence de vitesse entre les circulations dans chaque canal introduit des phénomènes dynamiques de propagation d'une sollicitation thermique.

Les phénomènes physiques complexes et transitoires, tels que les échanges de masse à travers la spirale, ne peuvent être compris que sur des échantillons à taille réelle. De nombreux aspects de la thermohydraulique des conducteurs de type câble-en-conduit à double canal nécessitent une meilleure compréhension. Les concepts et les technologies ne demandent qu'à être optimisés. Bien que de nombreux travaux thermohydrauliques expliquent et modélisent les phénomènes liés à une rugosité macroscopique, ce type d'échangeur poreux à très haut Reynolds n'a encore jamais été traité dans la littérature scientifique.

Contenu de la thèse

Des études énergétiques portant sur les écoulements cryogéniques dans un environnement complexe (porosité, turbulence) et sur les échanges thermiques entre l'hélium réfrigérant et les brins supraconducteurs (physique du transfert et du transport) sont nécessaires pour

s'assurer du bon dimensionnement des conducteurs supraconducteurs de type câble-en-conduit, de leur système cryogénique, et pour garantir le fonctionnement nominal de bobines supraconductrices à haut champ.

Le premier chapitre montre pourquoi les conducteurs développés pour le projet ITER sont à double canal, avec une spirale centrale à faible perte de charge et un canal annulaire contenant les brins supraconducteurs. Afin d'optimiser la géométrie de la spirale centrale, cette thèse étudie son comportement thermohydraulique.

Le chapitre 2 est consacré à l'étude expérimentale et la modélisation hydraulique des spirales [Ren06-3].

Le chapitre 3 est consacré à l'étude et la modélisation thermique, en régime permanent [Ren06-1] et transitoire [Ren06-2], de la spirale au sein d'un conducteur.

A l'aide des nouveaux modèles hydrauliques et thermiques développés, une optimisation des conducteurs d'ITER est proposée dans le chapitre 4.

2. Pertes de pression

L'hydraulique est étudiée en priorité car la thermique est subordonnée au type d'écoulement et de turbulence. Les pertes de charges, dont la loi est différente dans le canal central et dans le canal annulaire, régissent l'équilibrage des débits. Le canal annulaire voit son torsadage des brins supraconducteurs et son taux de vide fixés par des considérations électriques. Bien que le canal annulaire ne fasse pas l'objet de cette étude, il faut se pencher sur sa caractéristique pour résoudre la loi hydraulique (débit-pression) du conducteur. De plus une erreur d'appréciation de la répartition de débit $\alpha_A = \dot{m}_A / \dot{m}$ introduit automatiquement une incertitude sur le coefficient d'échange thermique entre les canaux, et sur toutes les caractéristiques thermohydrauliques du conducteur.

Pertes de pression annulaires

L'hélium circule dans la zone des brins à travers un entrelacement qui s'apparente à un milieu poreux anisotrope. Pourtant les lois hydrauliques des milieux poreux (Darcy et Forchheimer) ne sont vraiment utiles qu'à très faible vitesse, et requièrent une connaissance expérimentale de la perméabilité. Katheder a proposé un modèle de coefficient de friction [Kat94] pour la circulation de réfrigérant dans les conducteurs de type câble-en-conduit monocanal, qui ne dépend que du nombre de Reynolds Re et du taux de vide (void) :

$$f_A = \frac{(0.0231 + (19.6/Re^{0.7953}))}{void^{0.742}}$$

Le canal annulaire est ici assimilé, comme la spirale, à un canal circulaire avec un diamètre hydraulique et un coefficient de friction f . Ce modèle a l'avantage d'être simple. Sa validation expérimentale est acquise, mais avec une marge d'incertitude qui atteint (+/-) 40%, ce qui donne un avant-goût des difficultés de mesure expérimentale. Il est évident qu'il ne prend pas en compte certains paramètres de la géométrie réelle, tels les pas de torsadages (ou leur moyenne harmonique) qui modifient la perte de charge à taux de vide constant. On peut noter aussi que ce modèle a été défini pour $Re > 1000$, alors que l'introduction du canal central baisse Re à des valeurs généralement entre 700 et 1100.

Aujourd'hui la base de donnée expérimentale pour la zone des brins permettrait d'affiner le modèle de Katheder, idéalement en y ajoutant des paramètres justifiés. La modélisation numérique du canal annulaire semble inutilement intensive à cause de la forte turbulence et du nombre de petits canaux de géométrie incertaine. Cette simulation est donc inappropriée sauf pour comprendre par exemple l'influence locale de la taille des brins. La simulation numérique de l'écoulement dans une spirale est certainement beaucoup plus intéressante et

devrait permettre une étude de sensibilité à certains paramètres géométriques, pour aider à son optimisation.

Pertes de pression dans la spirale centrale

Les efforts sont désormais concentrés sur les phénomènes hydrauliques de la spirale car :

- Il n'existe que des modèles empiriques ponctuels, tandis que le modèle de Katheder fournit une loi générale, même imparfaite, pour le canal annulaire.
- Le canal annulaire n'est pas une variable d'optimisation : la compacité des bobines et les contacts électriques imposent le taux de vide sans marge de manœuvre.
- Des spirales de mêmes tailles et assez similaires ont montré des coefficients de friction variant de 100%,
- La spirale centrale a un impact fort sur l'hydraulique du conducteur (perte de charge et répartition de débit).

Les pertes de pression dans une spirale sont très sensibles aux caractéristiques géométriques, de par leur influence complexe sur la turbulence. Les campagnes expérimentales de pertes de pression de spirales visent à comprendre et modéliser de manière paramétrique cette influence géométrique. La spirale est assimilée à un tube rugueux caractérisé par un coefficient de friction. Cependant, cette modélisation ne constitue pas une comparaison directe des lois débit-pression dans des spirales de diamètres différents.

Campagne expérimentale en azote de perte de pression de spirale

Une campagne expérimentale de mesure des pertes de charge de spirales dans l'azote à température ambiante a été réalisée avant cette thèse sur la station d'essai OTHELLO (Annexe 1). La valeur ajoutée réside ici dans le dépouillement des résultats avec une analyse et de la compressibilité (Annexe 2). Une douzaine de spirales de dimensions variables sont insérées dans un tube souple ou dans un tube d'acier, de la manière la plus jointive possible ; température et débit sont enregistrés pour différentes pertes de pression lors de la circulation d'azote. L'étalonnage du banc d'essai sur des tubes lisses est laborieux et les résultats semblent systématiquement majorés, mais les résultats de référence (Blasius, Karman-Nikuradse) sont eux-mêmes donnés avec une incertitude de 8 à 10 %.

Les coefficients de friction sont calculés par une boucle numérique convergente intégrant l'influence du nombre de Mach pour la compressibilité de l'azote. Le coefficient de Joule-Thomson, qui quantifie la variation de température associée à une détente isenthalpique, est évalué mais n'affecte pas les résultats car la densité varie peu. Un calcul d'erreur fournit une incertitude de 5% pour ces mesures, mais l'étalonnage et la comparaison aux essais en eau des mêmes spirales laissent penser que la précision est moindre.

Campagne expérimentale en eau de perte de pression spirale

Une campagne expérimentale de mesure des pertes de charge de spirales dans l'eau pressurisée et chauffée de 15 à 75°C a été organisée. Le montage du banc d'essai doit beaucoup à MM. Cloez, Decool, Serriès et Tena. Les résultats expérimentaux permettent d'accéder aux variations du coefficient de friction, en fonction du nombre de Reynolds. Un étalonnage par rapport au tube lisse indique cette fois une sous-évaluation des coefficients de friction, qui a conduit à une vérification systématique et redondante de tout le matériel de mesure. Finalement les résultats en eau sont retenus plutôt que ceux en azote pour les raisons suivantes :

- Eventail de spirales testées plus large,
- Fixation identique ou meilleure des spirales dans les tubes tous en acier,
- Prises de pression plus fines et toutes vérifiées,
- L'eau permet de s'affranchir des problèmes de compressibilité pour des écoulements à très grand Re nécessaires pour reproduire les conditions ITER,
- Pas de perturbation thermique due à la détente Joule-Thomson,

- Etalonnage plus proche de la théorie que celui des essais en azote.

Bien qu'il puisse sembler plus sécurisant de surestimer la perte de pression (cas de l'azote), il est préférable d'évaluer la chute de pression le plus rigoureusement possible pour ne pas biaiser la répartition des débits dans le conducteur à double canal, avec des conséquences thermiques. Etant donné la précision expérimentale hydraulique disponible dans la littérature, en particulier la précision attendue de la formule de Katheder pour le canal annulaire, l'incertitude de mesure sur les spirales est satisfaisante.

Paramètres géométriques qui régissent la turbulence

Les spirales théoriquement symétriques suivant le sens de circulation de l'hélium, montrent expérimentalement une asymétrie qui peut s'élèver jusqu'à 30%, attribuée à la qualité de fabrication des spirales et de montage des échantillons, mais sans pouvoir identifier de défaut corrigible. Finalement une spirale est écartée des résultats car elle montre 65% de différence reproductible selon le sens de l'essai. De nombreux paramètres peuvent servir à définir hydrauliquement une spirale, le choix s'est porté sur des paramètres adimensionnels si possible, et déterminant le type de turbulence (Table R-2).

Table R-2 : Paramètres géométriques avancés (issus de la géométrie et du Reynolds)

| Spirale | Diamètre D _h [mm] | Rugosité e/D _h | Perforation % | Cavités g/e | Angle α [degrés] | fréq. spatiale 1/p [m ⁻¹] |
|-------------------|---------------------------------|------------------------------|------------------|----------------|---------------------|--|
| Showa | 9.93 | 0.101 | 27.7% | 2.40 | 77.0 | 115.6 |
| Cortaillod | 10.48 | 0.095 | 44.9% | 5.30 | 72.8 | 84.7 |
| PFCI | 9.95 | 0.100 | 24.3% | 1.93 | 78.1 | 126.1 |
| S10 | 8.07 | 0.124 | 31.3% | 2.85 | 73.8 | 109.9 |
| C10 | 8.20 | 0.122 | 47.3% | 5.84 | 68.0 | 81.0 |
| I10 | 8.57 | 0.117 | 53.8% | 7.29 | 66.7 | 73.9 |
| S9 | 7.64 | 0.131 | 29.3% | 2.57 | 73.7 | 114.0 |
| C9 | 8.18 | 0.122 | 48.4% | 6.05 | 67.7 | 80.0 |
| I9 | 8.24 | 0.121 | 54.1% | 7.31 | 66.0 | 74.0 |
| S8 | 6.18 | 0.162 | 37.5% | 3.75 | 68.0 | 100.0 |
| C8 | 6.39 | 0.156 | 46.3% | 5.60 | 64.1 | 82.6 |
| I8 | 6.53 | 0.153 | 49.3% | 6.08 | 63.9 | 81.1 |
| I7.6 | 6.38 | 0.125 | 48.0% | 7.50 | 62.4 | 80.0 |

- Un diamètre hydraulique proche du diamètre interne id est défini.

Les résultats quantifiés d'après un choix arbitraire de diamètre sont transposables avec les lois

$$f_{Dh} = f_{id} \left(\frac{Dh}{id} \right)^5 \text{ et } Re_{od} = Re_{Dh} \left(\frac{id}{Dh} \right)^2.$$

- La rugosité relative e/D_h représente l'épaisseur relative des singularités de la spirale
- La forme des cavités g/e (en lien avec le taux de perforation g/p) (Figure R-5),

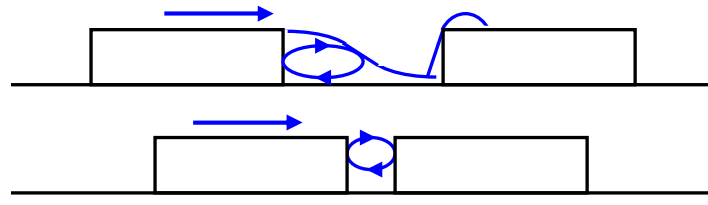


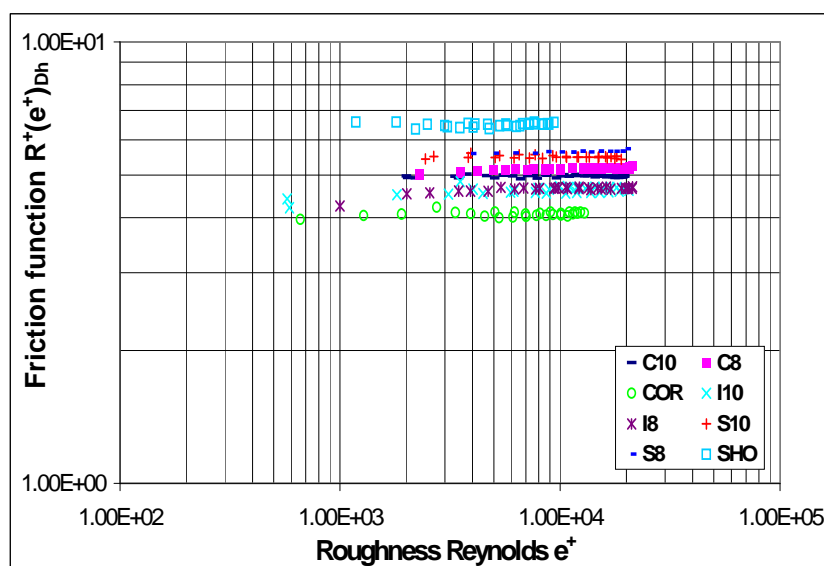
Figure R-5 : Détachement de veine dans les cavités de la spirale

- L'angle α de la spirale,
 - La fréquence spatiale des singularités hydrauliques (en lien avec la période p), et
 - L'angle d'attaque et de fuite θ du ruban de la spirale, qui pourrait aussi être une courbe.
- Ce dernier paramètre est fixé à 90° pour ces spirales qui présentent une section rectangulaire.

Modélisation du coefficient de friction ; friction visqueuse

Les courbes f fonction du nombre de Reynolds sont quasi horizontales, ce qui indique un régime d'écoulement quadratique, en accord avec une très faible dépendance en Reynolds des lois empiriques existantes pour quelques spirales. Alors que les coefficients de friction des spirales sont de deux à quatre fois supérieurs à ceux de tubes lisses, la courbure en Reynolds est identique. Il est donc décidé de séparer d'une part la friction de peau correspondant aux forces internes de viscosité le long des surfaces mouillées, modélisée depuis un siècle pour les tubes lisses (Blasius), et d'autre part le facteur de forme correspondant à la résistance de déformation des lignes de courant dans chaque singularité de la spirale. Le facteur de forme a une valeur prédominante, constante en fonction du Reynolds (Figure R-6) et qui représente une moyenne des singularités hydrauliques très fréquentes dans une spirale semblable à une suite de diaphragmes. La formule explicite de Blasius $f_{\text{Blasius friction}} = \frac{1}{(1,8 \ln(\text{Re}) - 1,64)^2}$ est par

conséquent retranchée des coefficients de friction bruts pour obtenir le facteur de forme linéaire.

Figure R-6 : Pertes de pression de spirales exprimées en fonction de la fonction de friction Re^+ et du Reynolds rugueux e^+

Modélisation du coefficient de friction ; facteur de forme

La modélisation du facteur de forme a été élaborée en s'appuyant sur le changement de variable classique [Nik50] (f , Re) → (R^+ , e^+) en introduisant la fonction de rugosité

$$R^+(e^+) = \sqrt{\frac{2}{f}} + 2.5 \ln\left(\frac{2e}{D_h}\right) + 3.75 \text{ et le Reynolds rugueux } e^+ = \frac{e}{D_h} Re \sqrt{\frac{f}{2}}.$$

e/D_h est pris en compte. Une régression sur R^+ doit pouvoir faire intervenir les autres paramètres des spirales. Han propose un modèle pour des spirales largement ouvertes et à faible Re [Han78] :

$$R^+ = 4.9 \left(\frac{e^+ / 35}{35} \right)^m \left(\theta / 90 \right)^{-0.35} \left(\frac{p / 10e}{10e} \right)^n \left(\alpha / 45 \right)^{-0.57}$$

- e^+ prend une valeur constante pour une spirale donnée car toute variation en Re est désormais négligée,
- θ est invariant à 90° , car toutes les spirales testées dans cette étude sont à section rectangulaire ; son modèle est laissé intact,
- La forme des cavités g/e , physiquement reliée aux types de turbulence, remplace avantageusement p/e ,
- La dépendance en α demeure encore inchangée étant donné la faible plage de valeurs disponibles dans l'échantillonnage testé (19% de variation entre $62,4^\circ$ et 77°).

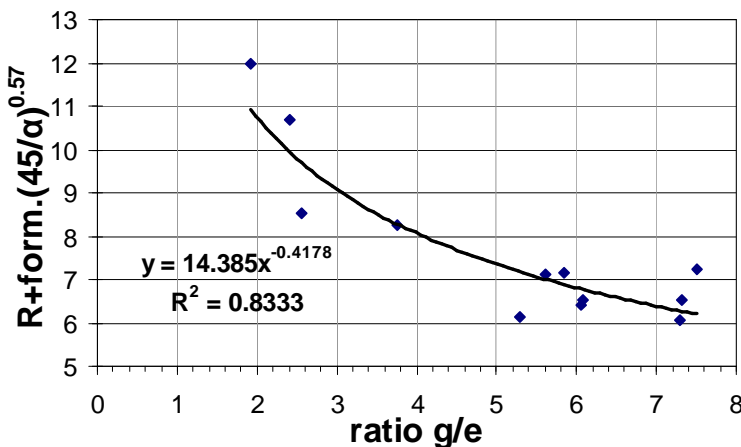


Figure R-7 : Dépendance de R^+_{forme} à l'ouverture de spirale (g/e)

Une régression de la fonction R^+ en fonction de g/e avec une loi de puissance (Figure R-7) fournit :

$$R^+ = 14.4 \left(\theta / 90 \right)^{-0.35} \left(\alpha / 45 \right)^{-0.57} \left(\frac{g}{e} \right)^{-0.42}$$

L'inversion des expressions de la fonction de rugosité et du Reynolds rugueux permet de remonter au facteur de forme linéaire :

$$f_{\text{form drag}} = \frac{2}{\left[14.4 \left(\frac{\theta}{90} \right)^{-0.35} \left(\frac{\alpha}{45} \right)^{-0.57} \left(\frac{g}{e} \right)^{-0.42} - 2.5 \ln\left(\frac{2e}{D_h}\right) - 3.75 \right]^2}$$

Cette formule expérimentale est basée sur un nombre de spirales qui reste faible, avec des épaisseurs et des largeurs de ruban quasi-constantes. Les conditions d'expérimentation (tube externe) sont différentes des conditions limites rencontrées au sein d'un conducteur supraconducteur.

Conclusion sur les pertes de pression

Le modèle de Katheder pour le canal annulaire est utilisable tel quel.

Les mesures de pertes de pression de spirales ont fourni une base de donnée en azote et en eau. Des paramètres de modélisation ont été proposés : le diamètre hydraulique D_h , la forme des cavités, l'épaisseur relative e/D_h , l'angle α de la spirale, et la fréquence des singularités $1/p$. De plus, l'angle d'attaque et de fuite θ ou la forme de la section du ruban formant la spirale et le nombre de Reynolds sont nécessaires pour une image hydrodynamique complète de la spirale centrale. L'influence de ces paramètres sur les pertes de pression est montrée dans la mesure du possible, et un modèle construit pour guider la conception des conducteurs d'ITER, en scindant le coefficient de friction des spirales en une friction visqueuse (modèle de Blasius) et un facteur de forme linéique :

$$f_{spiral} = \frac{1}{(1.8\ln(Re) - 1.64)^2} + \frac{2}{\left(14.4\left(\frac{\theta}{90}\right)^{-0.35}\left(\frac{\alpha}{45}\right)^{-0.57}\left(\frac{g}{e}\right)^{-0.42} - 2.5\ln\left(\frac{2e}{D_h}\right) - 3.75\right)^2}$$

La largeur des ouvertures de spirale ayant une action positive sur les pertes de charge, il serait souhaitable de réduire la perforation des spirales, mais un compromis thermique doit pour cela être recherché : la turbulence est négative du point de vue hydraulique, mais peut avoir une influence thermique positive par modification systématique de la couche limite.

3. Echange thermique

Si l'échange thermique entre les canaux n'est pas satisfaisant, la température des brins supraconducteurs dans l'anneau s'élève, réduisant la marge qui sépare le supraconducteur de son état résistif. Le but est ici de comprendre et modéliser les opérations de fonctionnement nominal du conducteur, ainsi que les phases transitoires de remise en froid et d'échauffement (montée du champ magnétique, chauffage neutronique).

Le principe des investigations expérimentales consiste à utiliser une sollicitation thermique et à mesurer les températures qui en résultent sur un conducteur à double canal de taille réelle.

Comme on le verra ici, les mesures les plus productives ont été effectuées directement à basse température d'hélium, sur le stand d'essai européen SULTAN situé en Suisse. En effet il a été possible de greffer des essais thermiques aux tests électriques d'échantillons de conducteur d'ITER à l'échelle 1.

3.1 Analyse stationnaire

Lors d'une étude en régime stationnaire, on s'intéresse à l'homogénéisation des températures en aval d'une section de chauffage dissymétrique (chauffage de l'hélium des brins uniquement), qui introduit un déséquilibre des températures. Un modèle bicanal permet de résoudre le problème moyennant certaines hypothèses simplificatrices :

- Répartition de débit invariante,
- Chaque canal est isotherme : unique température centrale (T_C) et annulaire (T_A),
- Invariance des températures au cours du temps,
- Pas de transport thermique longitudinal dans les métaux ni le fluide autre que le débit,
- Capacité calorifique massique C_p constante pour des faibles variations de température,
- Chauffage parfaitement réparti et transmis.

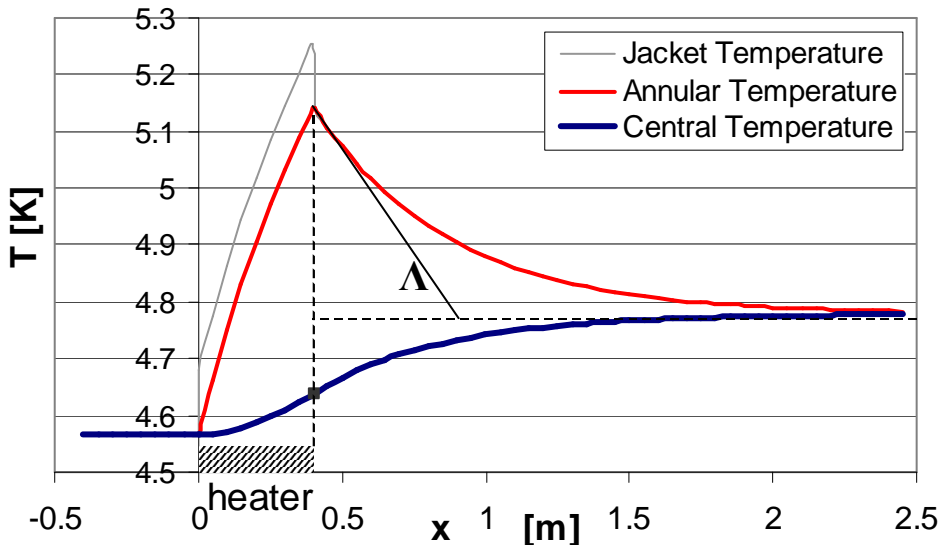


Figure R-8 : Modèle bicanal de températures en régime stationnaire

L'équation de la chaleur ainsi obtenue pour les températures annulaires admet une solution de type exponentiel (Figure R-8) comportant une longueur caractéristique d'échange inversement proportionnelle au coefficient d'échange thermique et au périmètre p de la spirale délimitant les deux canaux :

$$\Lambda = \frac{\alpha_A(1-\alpha_A)mC_p}{H \cdot p}$$

Λ dépend fortement de la fraction de débit annulaire α_A , tandis que le coefficient d'échange H dépend aussi des nombres de Reynolds et Prandtl donc de la répartition hydraulique dans le conducteur. L'annexe V fournit plus de détails sur une résolution thermique de ce problème stationnaire prenant en compte l'inhomogénéité longitudinale de la spirale centrale.

Cette méthode est simple et la longueur caractéristique d'échange Λ est mesurable par une connaissance exclusivement externe de la température annulaire. Elle donne en plus une information physique sur la longueur nécessaire pour transférer de l'enthalpie du canal annulaire vers le canal central.

Différence de température ΔT_{CA} maximale

Si le canal annulaire du conducteur est uniformément chauffé sur une longueur semi-infinie, les températures croissent, après une zone transitoire, le long de rampes parallèles avec $T_A > T_{uniform} > T_C$ (Figure R-9). Dans ces conditions la différence de température ne peut dépasser :

$$(T_A - T_C)_{\max} = \frac{Q\Lambda}{m_A C_p}$$

et l'écart de température par rapport à une situation isotherme ne peut dépasser

$$T_A - T_{iso} \leq \frac{Q\Lambda}{m_A C_p} \frac{m_c}{m} = \frac{\alpha_A(1-\alpha_A)}{H \cdot p} \frac{Q m_c}{m_A}$$

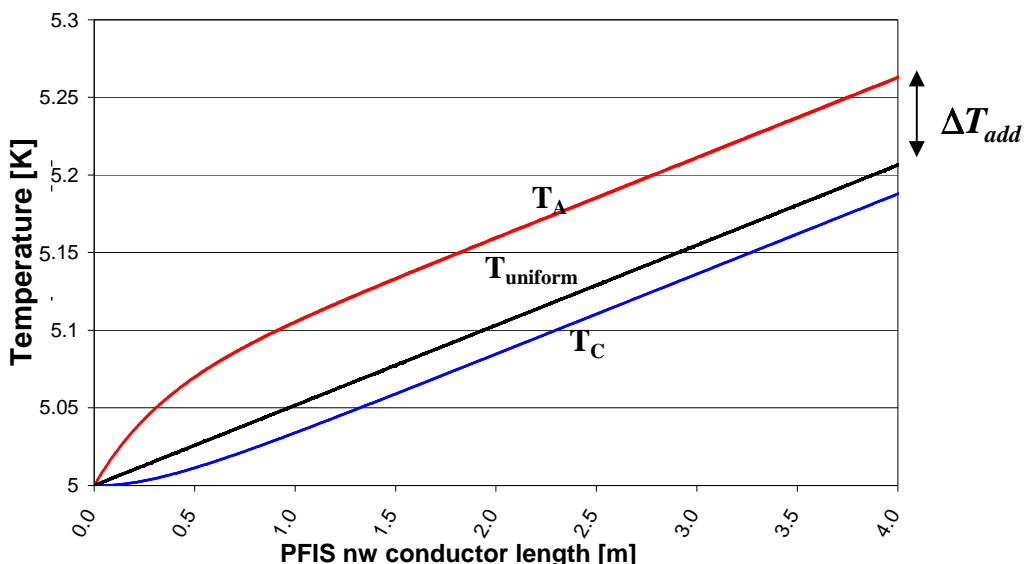


Figure R-9 : Evolution des températures annulaires, centrales et uniformes pour un chauffage annulaire stationnaire infini uniforme : la différence atteint une valeur asymptotique.
Illustration calculée pour le PFISnw soumis à un chauffage $Q = 2 \text{ W/m}$

Jusqu'à présent la température d'hélium avait toujours été considérée uniforme. Il apparaît que la température du supraconducteur T_A doit prendre en compte une marge en température supplémentaire dans la mesure où l'anneau est surchauffé. Il est heureux de pouvoir majorer cette différence de température à prendre en compte, qui s'élève en fait à quelques centièmes de kelvin, ce qui n'est pas forcément négligeable vis-à-vis d'une marge en température d'un degré.

Mesure stationnaire du coefficient d'échange H

Il s'agit de mesurer Λ pour calculer H expérimentalement. Les essais thermiques sont toujours plus subtils que des tests hydrauliques car de simples bilans d'énergie sont souvent compromis par le moindre pont thermique. Comme dans la théorie, le principe consiste à fournir de l'énergie au canal annulaire par l'intermédiaire de chaufferettes, puis de mesurer par des thermomètres en aval la baisse de température qui va de pair avec l'homogénéisation thermique du conducteur.

Mesures en eau

Ces mesures ont été tentées dans l'eau à température ambiante (Annexe III) puis dans l'hélium supercritique (Annexe IV). Si le chauffage de la gaine est imparfait pour le transfert d'enthalpie vers l'anneau, il est en revanche représentatif d'une situation de chauffage neutronique. L'homogénéité des températures et l'absence de conduction longitudinale sont vérifiées. L'étalonnage et l'utilisation de différences de températures sont systématisés. Les températures expérimentales s'élèvent plus et chutent plus vite que dans les calculs, ce qui correspondrait à un Λ et un débit annulaire deux fois plus petits que prévu. Les causes invoquées sont :

- Gaine transmettant l'énergie des chaufferettes sur une longueur plus grande (conduction longitudinale dans la gaine). Ceci décalerait en aval le maximum de T_A ;
- Débit annulaire plus faible que prévu (faible α_A). Incohérente avec la perte de pression, cette hypothèse expliquerait les températures élevées et le petit Λ ;
- T_A inhomogène. Si l'hélium externe se mélange mal avec le cœur des pétales, on a un phénomène à $n > 2$ températures ;

Comme la température de la boucle fluide est instable, que la similitude est impossible simultanément avec Re , Pr et λ , et que l'imprécision des mesures n'explique pas les

incohérences observées, il est probable qu'une des hypothèses simplificatrices ne soit pas négligeable dans l'eau à température ambiante. Les mesures en hélium supercritique à basse température sont donc privilégiées, elles ne nécessitent pas d'extrapolation ni de similitude.

Mesures en hélium supercritique

La participation à deux campagnes sur la station européenne SULTAN, avec la conception de programmes d'essais, l'analyse et le dépouillement des résultats ont permis d'effectuer des mesures à basse température. Le même principe de chauffage annulaire est utilisé, avec l'hypothèse supplémentaire justifiée de températures mesurées sur la gaine donnant les températures annulaires (Annexe IV). Tandis qu'un chauffage par pulsation magnétique de répartition incertaine fournit des résultats discutables, les chauffelettes classiques conduisent à des mesures parfaitement conformes au modèle tant que ΔT reste faible (Figure R-10). Le coefficient d'échange thermique a une valeur du coefficient d'échange $H \sim 400 \text{ W/m}^2\cdot\text{K}$ et l'homogénéisation thermique se fait sur une distance qui obéit à la longueur caractéristique d'échange thermique $\Lambda \sim 0,5 \text{ m}$.

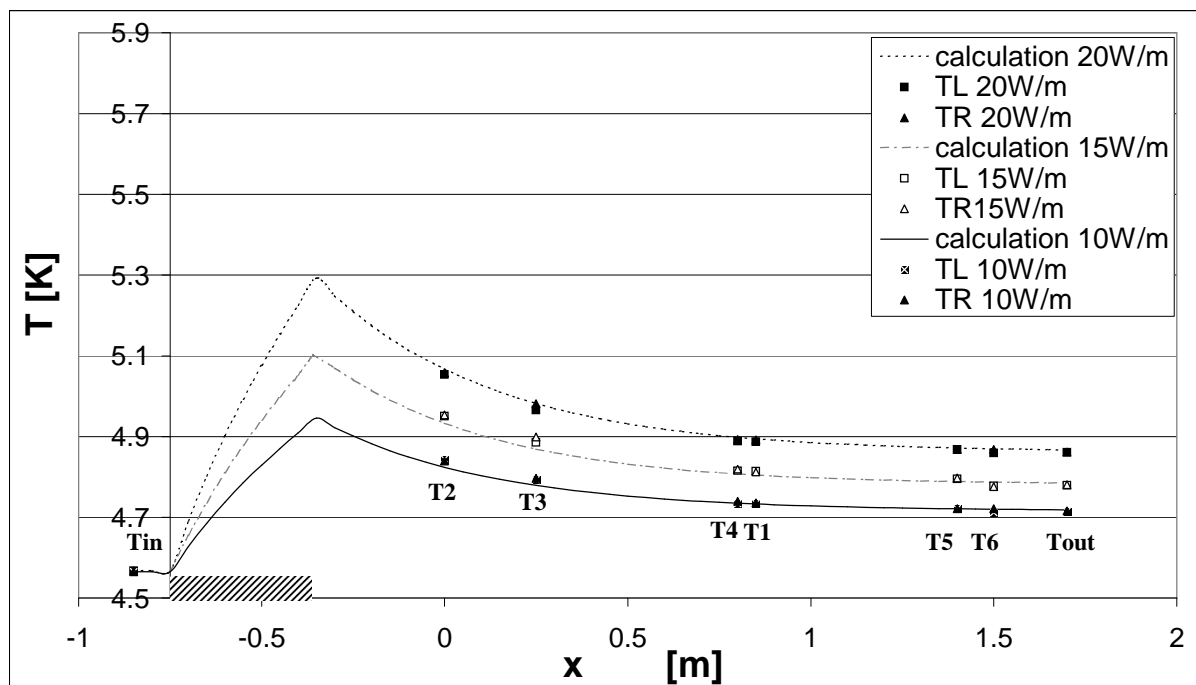


Figure R-10 : Températures annulaires calculées (lignes) et mesurées (points) du PF-FSJS pour 10, 15 & 20 W/m à 8 g/s

3.2 Analyse transitoire

La réponse transitoire du conducteur à un échelon de température d'entrée est un autre moyen de mesurer l'intensité des échanges thermiques en son sein (Figure R-11). Le but de l'analyse transitoire est de proposer une solution analytique dans le temps et l'espace, des deux températures qui caractérisent le conducteur. Le même modèle bicanal utilisant des hypothèses simplificatrices permet de résoudre les équations de conservation de l'énergie dans des écoulements incompressibles.

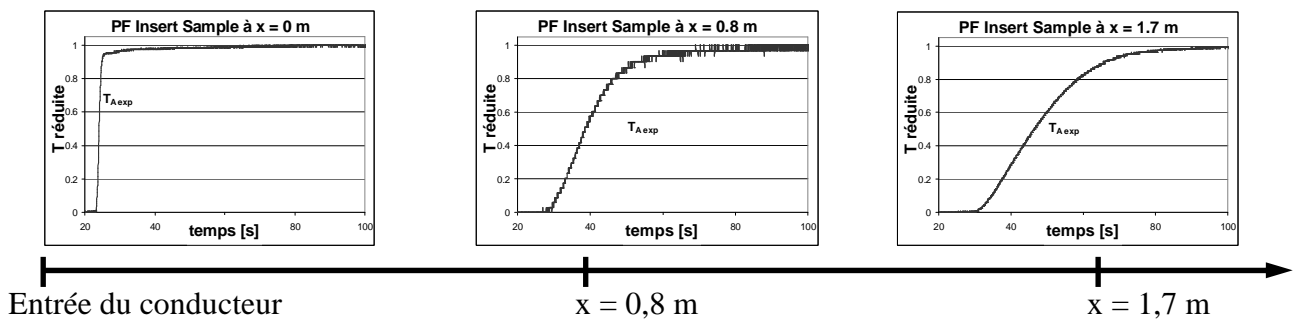


Figure R-11 : Evolution d'un échelon de température expérimentale (Heavyside) lors de sa propagation dans un conducteur PF.

$$\frac{DT_A}{Dt} + \gamma_A(T_A - T_C) = Q \text{ et } \frac{DT_C}{Dt} - \gamma_C(T_A - T_C) = 0, \text{ où } \gamma_i = \frac{H \cdot p}{\rho_i \cdot A_i \cdot C_{pi}}, \frac{D}{Dt} \text{ est la dérivée}$$

particulaire, Q une source d'énergie, p le périmètre externe de la spirale, $\rho(T)$ la densité, A la section d'hélium et C_p la chaleur spécifique de l'hélium du canal concerné. Entre l'avancée des deux fronts de température dans les canaux aux vitesses U_A et U_C se situe une zone d'échange thermique entre les canaux, qui avance et s'étend (Figure R-12).

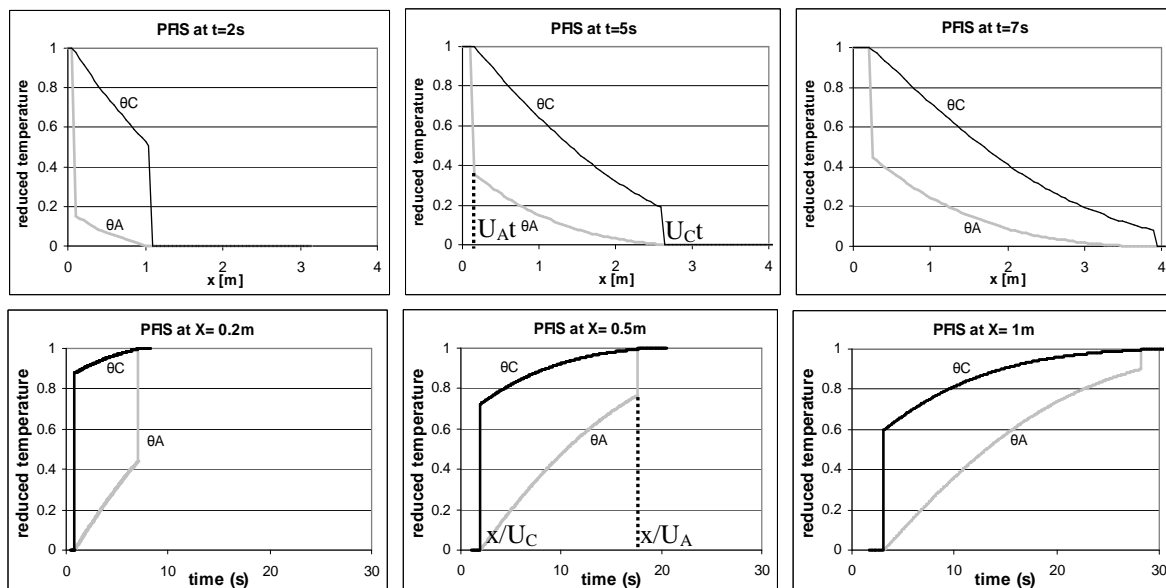


Figure R-12 : Fenêtre d'espace (haut) et de temps (bas) d'un conducteur PF W à 8 g/s

La résolution des équations de la chaleur par transformation de Laplace et intégration par partie (Annexe VI) conduit à une solution implicite pour des variations de températures normalisées entre 0 et 1 :

$$(\theta_C - \theta_A)(x, t) = \exp(-\alpha - \alpha \delta^2) I_0(2\alpha \delta) \text{ et } \frac{d\theta_C}{dt}(x, t) = \frac{\exp(-\alpha - \alpha \delta^2)}{(U_C - U_A)} \left(\gamma_C U_A I_0(2\alpha \delta) + \frac{\gamma_A U_C I_1(2\alpha \delta)}{\delta} \right)$$

où I_0 et I_1 sont des fonctions de Bessel modifiées du premier type,

$$\alpha(x, t) = \gamma_C (x - U_A t) / (U_C - U_A) \text{ et } \delta(x, t) = \sqrt{\frac{(U_C t - x) \gamma_A}{(x - U_A t) \gamma_C}}.$$

La différence et la dérivée permettent de remonter à une unique solution en température.

Temps de remise en froid d'une bobine supraconductrice à circulation forcée

La représentation dans deux dimensions espace-temps des températures permet de visualiser le rôle d'une longueur caractéristique et d'un temps caractéristique de l'échange thermique. La réponse à un échelon est un outil efficace, qui permet de comprendre comment se propagent dans le conducteur les variations de température opérationnelles ou accidentelles, toujours décomposables en série d'échelons. Les définitions d'une vitesse moyenne pivot \bar{U} et d'une constante de temps à partir de la dérivée de la température au pivot

$$\frac{1}{d\theta_{\bar{U}}} \approx \tau(x) = \frac{2\Delta U \sqrt{\pi \gamma_A \gamma_C x}}{(\gamma_A U_C + \gamma_C U_A)^{3/2}} \quad (\text{Annexe VI})$$

(Annexe VI) permettent de chiffrer la durée de la zone transitoire, et d'accéder au temps de refroidissement d'un conducteur, qui est la durée nécessaire pour refroidir entièrement sa longueur. Cette durée comprend la durée moyenne de circulation auquel on ajoute la moitié du transitoire $\frac{L}{U} + \frac{\tau(L)}{2}$. Cette durée de transition des

doubles-galettes d'ITER entre deux équilibres en température est une propriété importante sur laquelle le système de réfrigération devrait idéalement s'aligner, mais qu'il est inutile de dépasser : une surcapacité de la circulation cryogénique n'apporterait aucun bénéfice. Le facteur limitant la puissance de mise en froid devrait être le gradient de température maximal admissible, tandis que le débit dans les doubles-galettes peut être augmenté provisoirement ou réduit lors d'un simple maintien en température.

Mesure du coefficient d'échange H

La première application de la méthode transitoire est la mesure du coefficient d'échange thermique H. Des courbes exponentielles fournissent une méthode pratique sur une idée de Bottura pour calculer le temps de réponse de l'échange thermique et accéder à H [Bot05]. La constante de temps permet un calcul direct de l'échange thermique :

$$H = \frac{4\pi\rho C_p L A_c^2 A_a^2 (U_c - U_a)^2}{\tau^2 p ((A_c U_c)^{3/2} + (A_a U_a)^{3/2})^2}$$

La solution analytique n'est comparable à des mesures de température qu'à partir d'un calcul utilisant le coefficient d'échange H supposé inconnu. Une méthode d'identification permet d'estimer la valeur (expérimentale) de H qui minimise l'écart entre les courbes de température théoriques et mesurées sur l'un des thermomètres (Figure R-13).

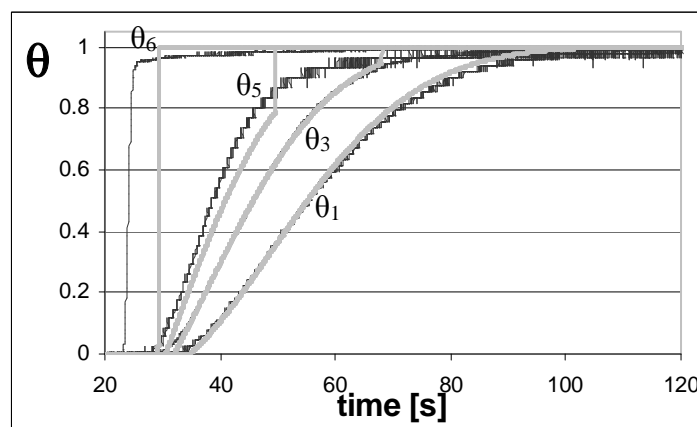


Figure R-13 : Températures expérimentales et théoriques (gris clair) à différentes distances avec $H=400 \text{ W/m}^2\text{K}$ pour un conducteur PF à 8 g/s. θ_5 et θ_6 situées trop proches du joint du conducteur non modélisé ne coïncident pas avec leurs courbes théoriques.

Mesures en eau

La température de la boucle fluide peut être brutalement modifiée en basculant la circulation amont de l'eau sur un réservoir (Annexe II). La validité du modèle n'est pas identique à celle des essais stationnaires : ces derniers demandaient de vérifier l'homogénéité de la température annulaire, tandis que des essais transitoires sont concernés par les inerties des métaux et le temps de réponse des thermomètres. A température ambiante, l'inertie thermique du conducteur est importante face à celle de l'eau, et modifie le front de température. Bien que ces expériences aient permis de progresser sur de nombreuses questions concernant la validité des conditions d'expérimentation et la répartition des débits, la résolution analytique n'est pas intéressante ici : seul un code de calcul peut prendre en compte les inerties pour un calcul détaillé pas à pas. Le modèle du coefficient d'échange thermique H développé suite à ces campagnes de mesures est par contre également applicable à température ambiante.

Mesures en hélium

Les mesures en hélium sont réalisées à froid (SULTAN) sur des échantillons PF verticaux, avec une circulation montante ou descendante de débit et température variable. Les perturbations thermiques liées aux inerties métalliques sont négligeables à très basse température : l'enthalpie de l'hélium est deux ordres de grandeur au dessus de la capacité calorifique du cuivre. Une forte diffusivité dans l'acier permet d'affirmer que le temps de réponse des températures mesurées à l'extérieur de la gaine est faible. La concordance des réponses mesurées et calculées est grande pour les thermomètres éloignés de plus d'un mètre des connexions non modélisées (Figure R-13). Une barre d'erreur ne dépassant pas 12% est donnée sur les mesures du coefficient d'échange H en fonction de la sensibilité des mesures (Figure R-14).

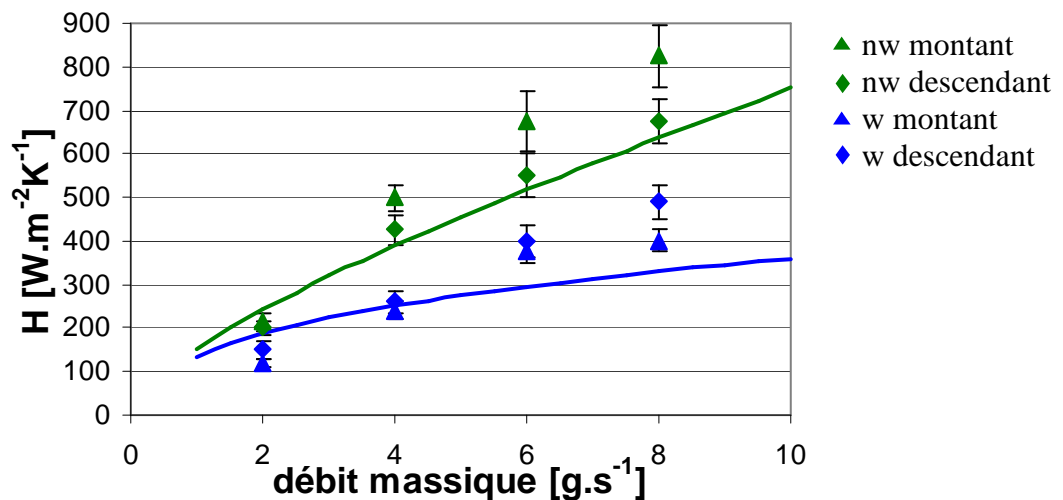


Figure R-14 : Mesures de H et prédictions sur le PFIS avec (W) et sans (NW) enrubannages

A cause de l'équipement des échantillons et des programmes d'essais, les méthodes d'essai transitoire et stationnaire n'ont pu être directement comparées sur le même conducteur, mais concordent avec un unique modèle du coefficient d'échange H. L'analyse transitoire semble plus précise et elle fournit une gamme de mesures complète même à bas débit. L'analyse reste assujettie à une évaluation correcte des débits respectifs des canaux, dont l'incertitude est grande, et le débit global subit une chute négligée de 2 à 4% lors de la montée transitoire de température. Aucune mesure du coefficient d'échange au sein d'un supraconducteur de type câble-en-conduit à double canal n'était disponible dans l'hélium supercritique avant ces contributions originales.

On démontre que les enrubannages des pétales de brins supraconducteurs affectent fortement le coefficient d'échange H (Figure R-14). Pourtant cet inconvénient est compensé par les

avantages électriques : un échauffement par champs variable est moindre avec les enrubannages, et conduit à une élévation de température inférieure malgré le faible H. Même si l'action locale des enrubannages est mitigée, les enrubannages réduisent les pertes variables dans la bobine et l'échauffement total combattu par la boucle cryogénique, donc ces enrubannages sont bénéfiques.

Modélisation du coefficient d'échange thermique H

La création d'un modèle analytique de H, initiée au CEA [Nic04ICEC], a pour but de doter un conducteur de type câble-en-conduit de valeurs prédictives et de réponses analytiques complètes à l'intensité des échanges thermiques entre ses canaux. Un tel modèle peut ensuite servir d'outil d'optimisation du conducteur. Trois types de surface d'échange sont placés en parallèle de manière proportionnée : les zones fermées de la spirale, les zones ouvertes avec enrubannage et les zones ouvertes sans enrubannage (Figure R-15).

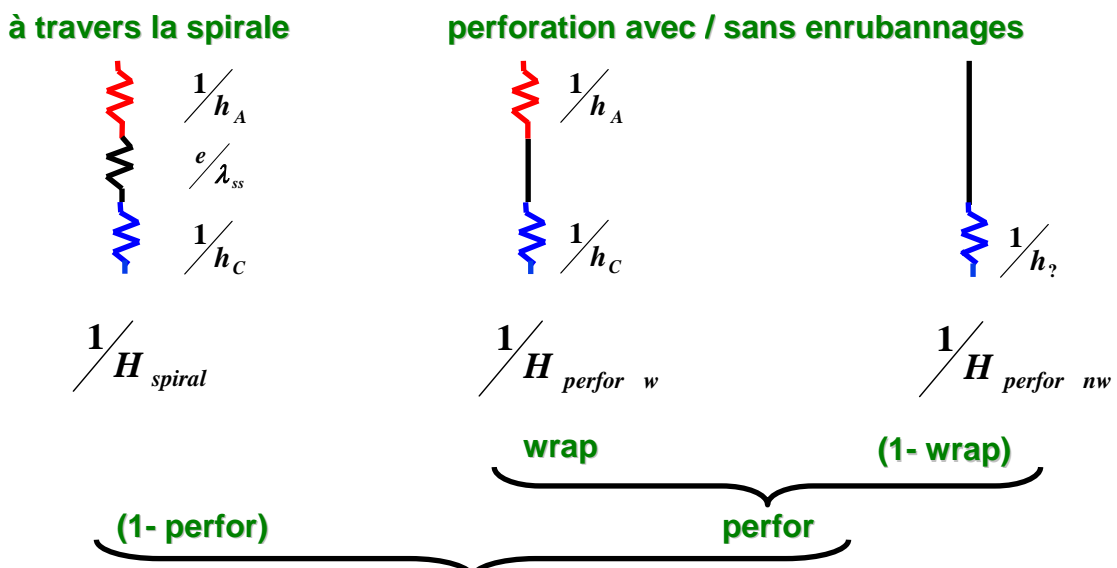


Figure R-15 : Surfaces d'échange fermées ou perforées, avec ou sans enrubannages en parallèle proportionnellement à leur aire ; résistances thermiques en série dans chaque surface

$H = H_{turn}(1 - perfor) * + H_{perforW} * perfor * wrap + H_{PerforNW} * perfor * (1 - wrap)$ avec le taux d'ouverture de la spirale « perfor » et le taux de recouvrement des enrubannages « wrap ». A travers la spirale on considère la conduction et un coefficient de convection de chaque côté (h_A ou h_C), appliqué au diamètre interne id ou externe od.

$$H_{spiral} = \frac{1}{\pi \cdot od \left(\frac{1}{\pi \cdot od \cdot h_A} + \frac{1}{2\pi \lambda_{ss}} \ln \left(\frac{od}{id} \right) + \frac{1}{\pi \cdot id \cdot h_C} \right)}$$

La conduction dans les enrubannages d'épaisseur 0,55 mm est négligée, mais ils constituent une barrière étanche qui justifie l'utilisation des deux coefficients de convection h_A et h_C .

$$H_{perforW} = \frac{1}{\pi \cdot od \left(\frac{1}{\pi \cdot od \cdot h_A} + \frac{1}{\pi \cdot id \cdot h_C} \right)}$$

En l'absence d'enrubannage, on considère un unique coefficient de convection (la moyenne des deux), utilisé comme ordre de grandeur, faute d'une meilleure connaissance de la convection et des échanges massiques, dont la contribution demeure cachée derrière la convection.

$$H_{perforNW} = \frac{1}{\pi \cdot od \left(\frac{2}{\pi \cdot id \cdot (h_C + h_A)} \right)}$$

Les coefficients de convection sont calculés à partir de l'expression du nombre de Nusselt $Nu = (h_{conv} \cdot D_h) / \lambda_{He}$. L'expression du nombre de Nusselt donné par Holman [Holman] finalement choisie pour les deux canaux, compte tenu de son domaine de validité pour les écoulements turbulents, de sa simplicité et de sa pertinence par rapport aux mesures, conduit à

l'expression explicite $h_{conv} = f \frac{\lambda_{He} \cdot Re \cdot Pr^{1/3}}{8 \cdot D_h}$ des coefficients de convection en fonction du

coefficient de friction du canal observé. Le coefficient d'échange H est ainsi considéré comme une fonction du débit massique, mais de la température seulement indirectement par Re et Pr. L'incertitude attachée à des coefficients d'échange thermique est grande même pour des géométries académiques. Ce modèle peu affiné d'échange thermique est satisfaisant par rapport à la précision des mesures et aux incertitudes des modèles hydrauliques sous-jacentes.

Conclusion sur l'échange thermique

Une compréhension analytique bicanal du comportement thermique des conducteurs de type câble-en-conduit à double canal en régime permanent et en régime transitoire permet de mieux appréhender la distance d'homogénéisation des températures, les marges en températures pour les brins supraconducteurs, la propagation d'un transitoire thermique, sa durée et le rôle du coefficient d'échange thermique.

Des mesures du coefficient d'échange thermique H entre les canaux ont été effectuées pour la première fois, en régime permanent et en régime transitoire en fonction du débit massique, permettant la validation des solutions analytiques. Alors que les essais en régime stationnaire sont limités par l'hypothèse d'homogénéité de la température annulaire, et par la non-linéarité pour une puissance trop forte, les expériences en régime transitoire sont limitées par la précision temporelle des thermomètres et par la perturbation des joints du conducteur.

Un modèle simple et explicite de H :

$$H = \frac{(1 - perfor)}{\pi \cdot od \left(\frac{1}{\pi \cdot od \cdot h_A} + \frac{1}{2\pi \lambda_{ss}} \ln \left(\frac{od}{id} \right) + \frac{1}{\pi \cdot id \cdot h_C} \right)} + \frac{perfor * wrap}{\pi \cdot od \left(\frac{1}{\pi \cdot od \cdot h_A} + \frac{1}{\pi \cdot id \cdot h_C} \right)} + \frac{perfor * (1 - wrap)}{\pi \cdot od \left(\frac{2}{\pi \cdot id \cdot (h_C + h_A)} \right)}$$

a été développé, basé sur un choix de coefficient de convection dans chaque canal:

$$h_{conv} = f \frac{\lambda_{He} \cdot Re \cdot Pr^{1/3}}{8 \cdot D_h}$$

où le coefficient de friction, le nombre de Reynolds, le nombre de Prandtl et le diamètre hydraulique doivent être calculés dans la spirale et dans la zone annulaire.

Tandis que les résolutions analytiques des équations de la chaleur sont rigoureuses et applicables avec une circulation d'hélium supercritique, le modèle du coefficient d'échange H reste simple. Il a pour vocation de donner rapidement des valeurs pour les utilisateurs de codes, et de permettre l'extrapolation prédictive de la géométrie de la spirale, donc son optimisation thermique.

4. Dimensionnement de la spirale centrale

Comment optimiser la spirale centrale des conducteurs d'ITER ? Quel compromis faut-il trouver, en particulier pour la turbulence qui est néfaste du point de vue hydraulique, mais susceptible de favoriser les échanges thermiques ?

Le danger de thermosiphon

Le thermosiphon est une pompe autogénérée par une différence de densité. Lorsqu'un conducteur de type câble-en-conduit à double canal est vertical, un chauffage excessif de la seule zone annulaire peut déséquilibrer la température des canaux et générer une différence de densité d'hélium au point de modifier et même d'inverser localement le débit annulaire (Figure R-16).

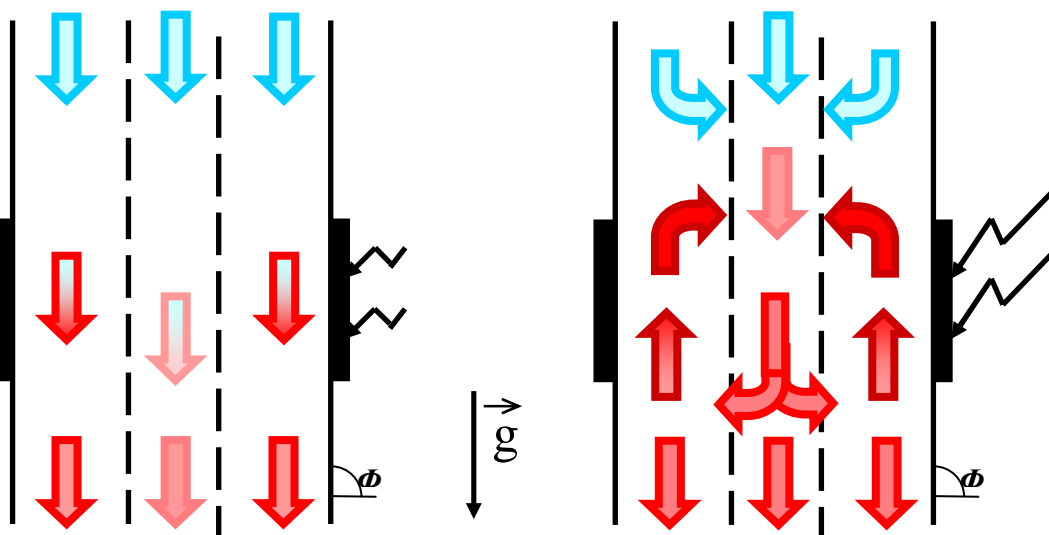


Figure R-16 : Principe de l'inversion de débit annulaire cause par un thermosiphon : chauffage modéré à gauche et intense à droite

Diagnostiquée expérimentalement par des températures les plus élevées paradoxalement en amont de la zone de chauffage, le thermosiphon montre que les canaux sont relativement étanches et l'échange thermique nécessaire. Ce phénomène gravitaire perturbe la circulation d'hélium dans le conducteur de manière très néfaste lors d'un écoulement vers le bas.

Le thermosiphon a certes été détecté à des niveaux de puissance locale bien supérieurs à la puissance reçue sur ITER, mais on constate une non-linéarité progressive de l'élévation de température en fonction de la puissance reçue (Figure R-17). Comme il est difficile de modéliser la porosité transverse du conducteur indispensable pour modéliser le thermosiphon, et que ce phénomène est instable dans le temps et variable d'un échantillon à l'autre, il a été décidé de simplement le majorer. Le ratio de la pression de thermosiphon sur la pression d'écoulement dans le conducteur est utilisé pour définir un facteur de risque :

$$r = \frac{\Delta P_{\text{thermosiphon}}}{\Delta P_{\text{friction}}}$$

Le thermosiphon n'apparaît pas dès que le facteur de risque r est égal à un, parce que le thermosiphon modifie la pression de l'écoulement, que seule une modélisation complexe ou un calcul itératif peut évaluer. Le facteur de risque est par contre valide tant que $\Delta P_{\text{thermosiphon}}$ (calculé sans prendre en compte la perturbation de débit) est très inférieur à $\Delta P_{\text{friction}}$, ce qui correspond à $r \ll 1$ et signifie qu'il n'y a pas de danger gravitaire pour le refroidissement

forcé du conducteur. r est calculé pour une charge thermique linéaire et un débit massique donnés.

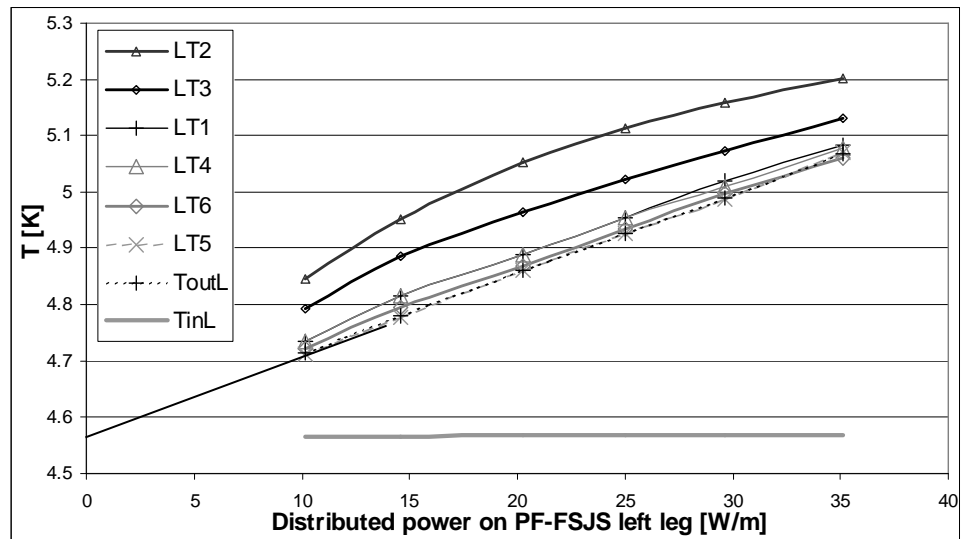


Figure R-17 : Températures annulaires et non-linéarités de thermosiphon sur les thermomètres LT2 et LT3 d'un échantillon PF à 8 g/s

Le thermosiphon dans ITER

La puissance linéaire maximale reçue par un conducteur d'ITER est de $Q=1,6 \text{ W/m}$ du côté du plasma de la jambe interne verticale d'une bobine TF [Bes05]. Cette puissance permet dans un premier temps d'évaluer une différence de température maximale entre les canaux, qui est un acquis de l'analyse de la réponse thermique stationnaire du conducteur. Le facteur de risque r peut ainsi être évalué à moins de 2%, ce qui signifie que la perturbation gravitaire est négligeable et l'hypothèse de calcul de r valide.

Pourtant l'optimisation de la spirale centrale consiste à réduire sa perte de pression, donc à augmenter la proportion de débit qui y circule. Ceci a pour conséquence la diminution du débit annulaire et, mais pour d'autres raisons, du coefficient d'échange thermique. Ces conséquences entraînent toutes deux une augmentation préoccupante de r . Le facteur de risque est donc un critère d'optimisation qui doit être surveillé pour demeurer assez faible.

Critères d'optimisation

Le canal central doit demeurer symétrique car l'hélium s'écoule dans une double galette dans les deux sens, en partant du milieu. Une spirale demeure le meilleur moyen de produire industriellement un tube avec des ouvertures nécessaires pour limiter l'augmentation de pression lors d'un échauffement rapide accidentel. La dimension de la spirale centrale et son épaisseur sont imposées par la compacité du conducteur et par la résistance mécanique. Un calcul de variation locale de température à l'échelle du pas de la spirale, dans laquelle les parties ouvertes permettent un meilleur transfert thermique, démontre qu'il n'est pas utile de se préoccuper de la fréquence des singularités de la spirale (Annexe V). Seul l'angle de torsadage de la spirale joue un rôle sur le coefficient de friction.

L'étude paramétrique du conducteur est conduite à l'aide des modèles hydrauliques et thermiques nouvellement développés, ce qui limite à leurs domaines de validité et l'entache de leurs barres d'erreur. L'optimisation de la spirale se fait sur les trois critères : perte de pression, température annulaire et risque de thermosiphon.

Les enrubannages des pétales de brins supraconducteurs ont une incidence complexe sur la perméabilité de la spirale et sur l'intensité des échanges thermiques. Pourtant ces échanges thermiques ne sont pas un chemin critique de la conception du conducteur (Table R-3), tandis que la réduction des pertes magnétiques apporte un gain sur la puissance cryogénique très

coûteuse. Il n'y a pas de contre-indication thermique à l'utilisation d'enrubannages par ailleurs souhaitables.

Table R-3 : Performances thermohydrauliques du conducteur TF à 8 g/s pour des cavités variables (perforations de 14 à 50%) et un enrubannage constant de 50%

| | TF g1w50 | TF g1,5w50 | TF g2w50 | TF g3w50 | TF g6w50 | unité |
|---------------------------------------|-----------------------|-----------------------|-----------------------|-----------------------|-----------------------|--------------|
| Perforation | 0,143 | 0,20 | 0,28 | 0,34 | 0,50 | (%) |
| r largeur fermée | 0,006 | 0,006 | $6,15 \times 10^{-3}$ | 0,006 | $6,15 \times 10^{-3}$ | m |
| g ouverture | 0,001 | $1,5 \times 10^{-3}$ | $2,35 \times 10^{-3}$ | 0,003 | $6,15 \times 10^{-3}$ | m |
| f_c | 0,043 | 0,046 | 0,057 | 0,838 | 0,12 | - |
| \dot{m}_C | $3,81 \times 10^{-3}$ | $3,74 \times 10^{-3}$ | $3,72 \times 10^{-3}$ | $3,38 \times 10^{-3}$ | $3,22 \times 10^{-3}$ | kg/s |
| Perte de charge | 198 | 200 | 204 | 227 | 239 | Pa/m |
| H | 377 | 466 | 614 | 840 | 1384 | W/m^2K |
| Λ | 0,84 | 0,68 | 0,51 | 0,37 | 0,22 | m |
| $(T_A - T_C)_{max}$ | 0,089 | 0,071 | 0,054 | 0,035 | 0,021 | K |
| $\Delta T_{1,Add}$ | 0,043 | 0,034 | 0,025 | 0,015 | 0,0084 | K |
| r | 0,069 | 0,054 | 0,040 | 0,024 | 0,013 | (-) |

Amélioration de la spirale centrale

Le paramètre principal qui régit le coefficient de friction est la longueur *g* des cavités de la spirale, mais la caractéristique hydraulique débit-pression des conducteurs dépend plus du diamètre que des faibles gains sur le coefficient de friction (Figure R-18). Pourtant le diamètre doit rester petit pour la compacité, et pour maintenir la moitié du débit dans le canal annulaire des bobines TF.

Bien que la preuve n'en soit pas faite sur des essais de spirale, il est souhaitable d'arrondir les angles internes de la spirale. Diminuer l'ouverture de la spirale *g* apporte un bénéfice hydraulique accompagné d'un meilleur soutien mécanique, mais réduit la perforation donc l'intensité de l'échange thermique, parce que la conduction à travers les parties fermées constitue la barrière thermique la plus importante. Une réduction de la longueur des ouvertures *g* jusqu'à 1 mm conduit à une différence de température entre les canaux de presque 0,1 K, qui devient inacceptable, tandis que *r* reste maîtrisé à des valeurs d'1 à 2% (Table R-3). La tendance est donc la bonne, et l'intensité des échanges thermiques de plusieurs centaines de $W.m^{-2}K^{-1}$ permet d'abaisser *g* raisonnablement jusqu'à une perforation de 15 à 20%, pour un bénéfice hydraulique sans risque thermique.

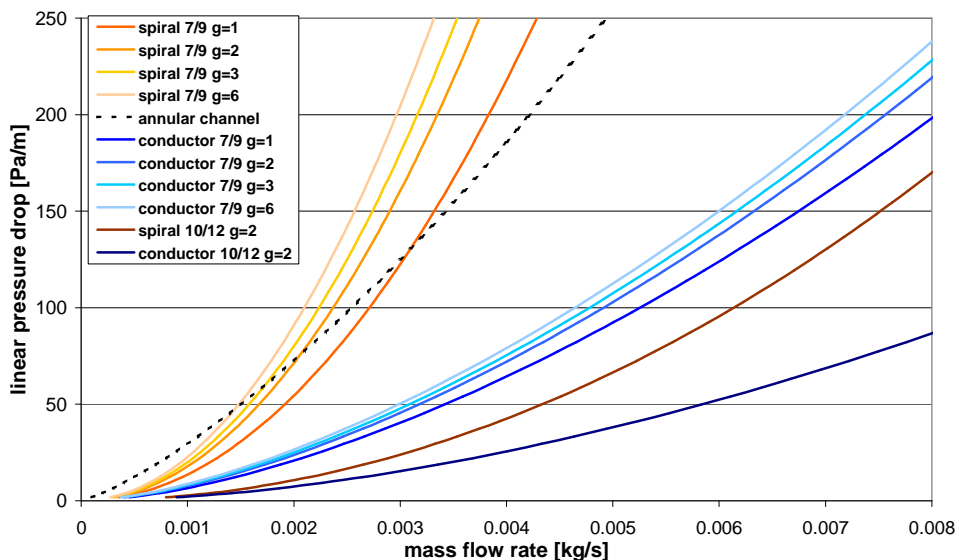


Figure R-18 : Perte de pression en fonction du débit pour des spirales et conducteurs d'ouverture variable à enrubannage constant de 50% et taux de vide de 33%

Conducteur alternatif

Les performances des brins supraconducteurs en Nb_3Sn sont détériorées par les contraintes et par les déformations mécaniques à la fois transverses, liées aux forces magnétiques cycliques dans le conducteur d'une bobine à haut champ, et longitudinales, dues au retrait thermique différentiel entre le câble et sa gaine après la cuisson de fabrication. La combinaison des deux effets génère une chute de la densité de courant maximale admissible qui dépasse les 50% pour le niobium-étain très fragile.

Un meilleur maintien mécanique pourrait donc avantageusement remplacer une partie des brins très coûteux, d'abord en réduisant le taux de vide annulaire ou en augmentant le diamètre des brins supraconducteurs. Une autre piste serait la réduction de l'épaisseur du conducteur pour éviter l'intégration des efforts sur une grande hauteur. Un conducteur plat de type Rutherford, mais réalisé avec des centaines de brins torsadés sous forme de petits pétales pourrait proposer cette géométrie. Le concept du double canal reste d'actualité et le principe d'une géométrie « plate » empilable (hexagonale) de conducteur supraconducteur de type câble-en-conduit à double canal est proposé avec la Figure R-19.

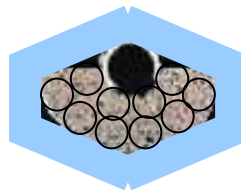


Figure R-19 : Proposition de conducteur hexagonal de type cable-en-conduit à double canal

Contre les contraintes longitudinales, il est envisageable d'imposer une précontrainte à la gaine d'acier, pendant ou après le refroidissement suite au traitement thermique. La réalisation pratique de ce principe sur des bobinages de courbure irrégulière, pour imposer des déplacements à une précision millimétrique serait extrêmement complexe.

Futurs travaux

Il serait utile de compléter la base de données des spirales, en particulier avec des spirales « optimales » pour valider les tendances du modèle hydraulique et le choix d'optimisation. L'amélioration du modèle hydraulique annulaire, l'efficacité d'un arrondi des angles, la répartition des débits central et annulaire, la comparaison thermique stationnaire et transitoire

du même échantillon, ou l'amélioration du modèle de coefficient d'échange thermique pour prendre en compte le niveau de température par le nombre de Prandtl, sont des pistes pour la poursuite des travaux de recherche thermohydraulique sur les conducteurs d'ITER.

Conclusion et perspectives

Le concept de conducteur de type câble-en-conduit supraconducteur à double canal a été présenté et justifié, en vue d'être optimisé. Les résultats de campagnes expérimentales de pertes de pression en azote et en eau ont permis de construire un modèle explicite de coefficient de friction des spirales. La résolution de l'équation de la chaleur avec un modèle bicanal a permis de comprendre le comportement thermique stationnaire et transitoire du conducteur. Un modèle explicite de l'échange thermique a été créé, conforme aux mesures cryogéniques réalisées dans la station européenne SULTAN. La température maximale des brins supraconducteurs, le risque de thermosiphon et le temps de remise en froid du conducteur ont été définis et évalués. A partir de cette compréhension du comportement thermohydraulique et des nouveaux modèles disponibles, une optimisation de la spirale a été initiée, réduisant ses ouvertures à 1,5 mm.

Les bases de données expérimentales pourront être enrichies à l'avenir par un choix de spirales peu ouvertes et arrondies. Des essais thermiques en régime permanent et transitoire réalisés sur le même échantillon, ainsi qu'une étude du coefficient d'échange H en fonction du nombre de Prandtl seraient désirables. La validation numérique de cette étude expérimentale et analytique aiderait à compléter la compréhension de l'impact géométrique d'une spirale sur ses propriétés thermohydrauliques. Des raisons électromécaniques nécessiteront probablement de diminuer le taux de vide annulaire, de modifier la géométrie du câble ou d'augmenter le diamètre des brins. Les modèles analytiques développés pourront accompagner ces évolutions. Le câble-en-conduit à double canal demeure un moyen éprouvé de maintenir en froid des bobines supraconductrices à haut champ.

Appendix I: Test facility OTHELLO

The OTHELLO test facility built at CEA/Cadarache to investigate the hydraulic behaviour of dual channel CICC samples is dedicated to hydraulic resistance measurements using disposable nitrogen at ambient temperature. A set of various spiral samples has been tested in 2003, providing friction factors in N₂ flow [Lib03].

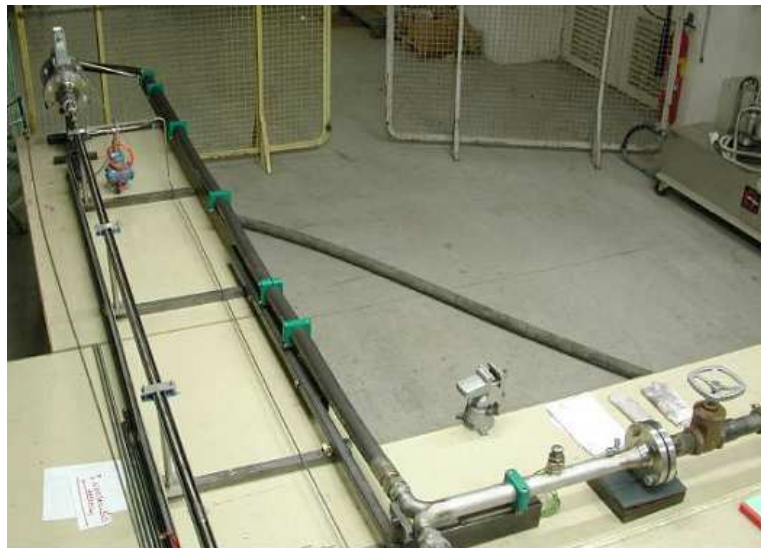


Figure A-1: OTHELLO test facility

The experimental setup allows to set the entrance pressure and observe its temperature, the mass flow rate, the exit pressure and exit temperature. Entrance pressure is adjusted and kept steady in order to reach a steady state pressure drop plateau. Each plateau is subsequently averaged over at least 20s of data to obtain a single friction factor value. A differential pressure sensor is available for precision and redundancy. This test facility comprises a pressurised nitrogen alimentation at 4.0 MPa (through a pressure reducer). The mass flow rate is estimated from the volumetric mass flow rate measurement at the outlet of the sample [Nic03].

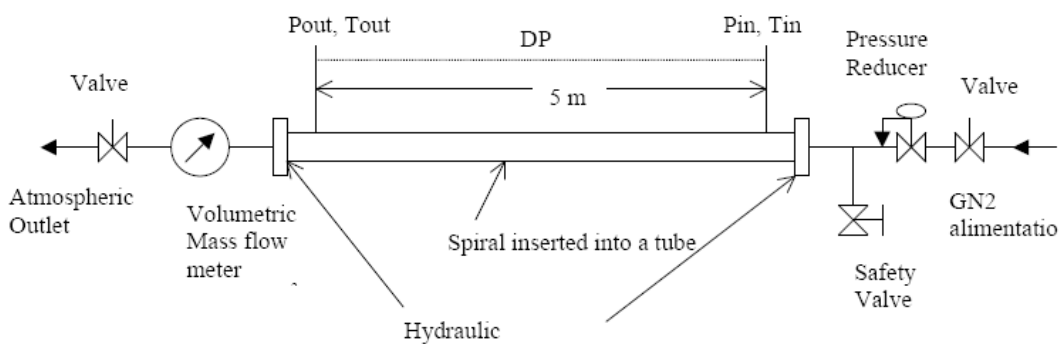


Figure A-2: OTHELLO spiral test setup

This test facility permits Reynolds numbers in the range of those expected for the coils of ITER at cryogenic normal operating temperature. The experimental test facility is first validated by measuring the pressure drop and friction factor on two smooth tubes. Experiments are conducted with care and every security procedure is used regarding the danger arising from pressurized gaz.

Appendix II: Pressure drop measurements

This appendix provides a detailed calculation of the pressure drop as a function of the friction coefficient in a compressible flow, where the Mach number is involved. The purpose is to evaluate friction coefficients of Cable-In-Conduit Conductors and spirals samples tested in the OTHELLO facility with a pressurized ambient temperature nitrogen flow.

Incompressible Fluid

Pressure drop is traditionally given by:

$$\Delta P = f \cdot \frac{1}{2} \rho v^2 \frac{L}{D_h}$$

This formula relates, for an ideal fluid in permanent incompressible flow, the pressure drop to : the friction coefficient f ,

the dynamic pressure $\frac{1}{2} \rho v^2$,

the length L and

the hydraulic diameter D_h .

This formula is equivalent to:

$$\rho \cdot \Delta P = \frac{U \cdot m^2}{8 \cdot S^3} \cdot f \cdot L$$

with the wetted perimeter U ,

the hydraulic surface S , so that $D_h=4S/U$

and the mass flow rate $m=\rho \cdot v \cdot S$

Compressible fluid

The governing equations for a compressible adiabatic viscous ideal gas flow in a circular pipe are given by :

Conservation of mass

$$\left\{ \begin{array}{l} \frac{1}{P} \frac{dP}{dx} + \frac{1}{v} \frac{dv}{dx} - \frac{1}{T} \frac{dT}{dx} = 0 \end{array} \right. \quad (\text{AII-1})$$

Conservation of energy

$$\left\{ \begin{array}{l} \rho \cdot v^2 \frac{dv}{dx} + \rho \cdot C_p \cdot v \frac{dT}{dx} = 0 \end{array} \right. \quad (\text{AII-2})$$

Conservation of momentum

$$\left\{ \begin{array}{l} \frac{1}{2} \rho \cdot v^2 \frac{dP}{dx} + \frac{2}{v} \frac{dv}{dx} = - \frac{f}{D_h} \end{array} \right. \quad (\text{AII-3})$$

In this last equation (AII-3), the velocity term dV/V is neglected in the incompressible case and must be evaluated to provide the result we seek.

Using $C_p = \frac{\gamma \cdot R}{\gamma - 1}$ and introducing the Mach number $M^2 = \frac{v^2}{C^2} = \frac{v^2}{\gamma \cdot R \cdot T}$, equation (AII-2) becomes:

$$v^2 \frac{dv}{v} + \frac{\gamma \cdot R \cdot T}{\gamma - 1} \frac{dT}{T} = 0$$

$$\frac{dT}{T} = -(\gamma - 1) M^2 \frac{dv}{v} \quad (\text{AII-4})$$

reporting (AII-4) in (AII-1), we get:

$$\frac{dP}{P} = -\frac{dv}{v} (1 + (\gamma - 1)M^2) \quad (\text{AII-5})$$

furthermore P can be expressed as

$$P = \rho \cdot R \cdot T = \frac{\rho \cdot v^2}{\gamma} \frac{\gamma \cdot R \cdot T}{v^2} = \frac{\rho \cdot v^2}{\gamma \cdot M^2}$$

plugging this expression of P in equation (AII-5) leads to

$$\frac{dP}{\frac{1}{2} \rho \cdot v^2} = \frac{-2}{\gamma \cdot M^2} \frac{dv}{v} (1 + (\gamma - 1)M^2) \quad (\text{AII-6})$$

reporting (AII-6) in (AII-3), we get:

$$2 \frac{dv}{v} \left(\frac{-1}{\gamma \cdot M^2} (1 + (\gamma - 1)M^2) + 1 \right) = -\frac{f \cdot dx}{D_h}$$

$$2 \frac{dv}{v} \left(\frac{1 - M^2}{\gamma \cdot M^2} \right) = \frac{f \cdot dx}{D_h}$$

hence

$$\frac{dv}{v} = \frac{1}{2} \left(\frac{\gamma \cdot M^2}{1 - M^2} \right) \frac{f \cdot dx}{D_h} \quad (\text{AII-7})$$

reporting in (AII-6) provides the result:

$$\frac{-dP}{\frac{1}{2} \rho \cdot v^2} = \left(\frac{1 + (\gamma - 1)M^2}{1 - M^2} \right) \frac{f \cdot dx}{D_h}$$

or

$$-dP = \frac{1}{2} \rho \cdot v^2 \left(1 + \frac{\gamma \cdot M^2}{1 - M^2} \right) \frac{f \cdot dx}{D_h} \quad (\text{AII-8})$$

which provides the incompressible linear pressure drop multiplied by the correction $\left(1 + \frac{\gamma \cdot M^2}{1 - M^2} \right)$, with

(AII-8) can also be written :

$$-\rho \cdot dP = \frac{U \cdot m^2}{8 \cdot S^3} \left(1 + \frac{\gamma \cdot M^2}{1 - M^2} \right) f \cdot dx \quad (\text{AII-9})$$

Therefore the corrective term for compressibility is in a compressible adiabatic viscous ideal gas flow in a circular pipe is $\left(1 + \frac{\gamma \cdot M^2}{1 - M^2} \right)$

Other compressible fluid demonstration

Another means to evaluate compressible pressure drop is to start from the balance of mass, momentum and energy with negligible viscosity but significant friction, and write them in terms of pressure, velocity and temperature [Bot00]:

$$\begin{cases} \frac{dv}{dt} + v \frac{dv}{dx} + \frac{1}{\rho} \frac{dP}{dx} = -F \\ \text{where } F \text{ is the friction force, and} \end{cases} \quad (\text{AII-10})$$

$$\frac{dP}{dt} + \rho \cdot C^2 \frac{dv}{dx} + v \frac{dP}{dx} = (\gamma - 1) \rho v F \quad (\text{AII-11})$$

for ideal adiabatic gas.

Multiplying (AII-10) by $\rho \cdot dx$ and (AII-11) by $\frac{dx}{C^2}$ leads to expression which can be subtracted to eliminate the term $\rho \cdot v \cdot dv$ in each expression.

Replacing F by:

$$F = \frac{f \cdot v^2}{2D_h} \quad (\text{AII-12})$$

leads to the final result (AII-8)

Mach number integration hypothesis and iteration

The friction factor calculation strategy consists in starting from a linear pressure drop profile, evaluating the Mach number effect and the friction factor and deducing a second pressure drop profile. Iterations are numbered with indices from 1 to 3.

A numerical evaluation of

$$\sum_{i=0}^n \left(1 + \frac{\gamma(x) \cdot M(x)^2}{1 - M(x)^2} \right) \frac{L}{n} \quad (\text{AII-13})$$

requires knowledge of nitrogen thermodynamic parameters along x. Temperature and pressure are used to obtain density, γ and Mach number. The temperature rise in the sample of length L is limited to 1 or 2 K, directly related to the Joule-Thomson expansion, which slightly differs from a linear law. It is therefore possible to linearise temperature elevation with a negligible error.

Similarly, pressure is linearised as $P_1(x)$. A first evaluation of the friction factor can be done with $M_1(x)$ and $\gamma_1(x)$, where ΔP is the pressure drop numerical step,

$$\Delta x = \frac{L}{n} \quad (\text{AII-14})$$

and n=500 is the number of space steps used:

$$f_1 = \frac{\sum_0^L \rho \cdot \Delta P_1(x)}{\frac{U \cdot m^2}{8 \cdot S^3} \left(L + \sum_0^L \frac{\gamma_1(x) \cdot M_1(x)^2}{1 - M_1(x)^2} \Delta x \right)} \quad (\text{AII-15})$$

Using this first calculation of the friction factor f_1 , we can come back to our linear pressure assumption and evaluate the pressure at each X, where x is an integration variable. For this purpose ρ is linearized as a function of P

$$\rho = \alpha P + \beta \quad (\text{AII-16})$$

$$\begin{cases} \alpha = 0.000012564 \quad [m^{-2}s^{-2}] \\ \beta = -0.1201 \quad [kg \cdot m^{-3}] \end{cases}$$

with $R^2=1$ for P varying between 5×10^4 and 10^7 Pa while pressure in the various experimental data is in the range 9×10^4 to 3.8×10^6 Pa. $\int_{P(X)}^{P_{in}} \rho \cdot dP$ hence integrates into

$$\frac{\alpha}{2} (P^2(X) - P_{in}^2) + \beta (P(X) - P_{in}) \quad (\text{AII-17})$$

$$\text{or } \frac{\alpha}{2} P^2(X) + \beta P(X) - \beta P_{in} - \frac{\alpha}{2} P_{in}^2 + f_1 \frac{U \cdot m^2}{8 \cdot S^3} \sum_0^X \left(1 + \frac{\gamma_1(x) \cdot M_1(x)^2}{1 - M_1(x)^2} \right) dx = 0 \quad (\text{AII-18})$$

which we solve in order to extract P(X) by integrating on x from 0 to X and obtain

$$P_2(X) = \frac{-\beta + \sqrt{\beta^2 - 2\alpha \left(f_1 \frac{U \cdot m^2}{8 \cdot S^3} \sum_0^X \left(1 + \frac{\gamma_1(x) \cdot M_1(x)^2}{1 - M_1(x)^2} \right) \Delta x - P_e^2 \frac{\alpha}{2} - \beta P_e \right)}}{\alpha} \quad (\text{AII-19})$$

Mach integration convergence

Iteration following the same principle provides f_2 , $P_3(x)$ and f_3 . No further iteration is needed because a sufficient precision convergence in P is reached:

$$\max \left(\frac{|P_3(x) - P_2(x)|}{P_2(x)} \right) \leq 0.022 \text{ for the smooth tubes experiments and } \leq 0.009 \text{ for all spirals values.}$$

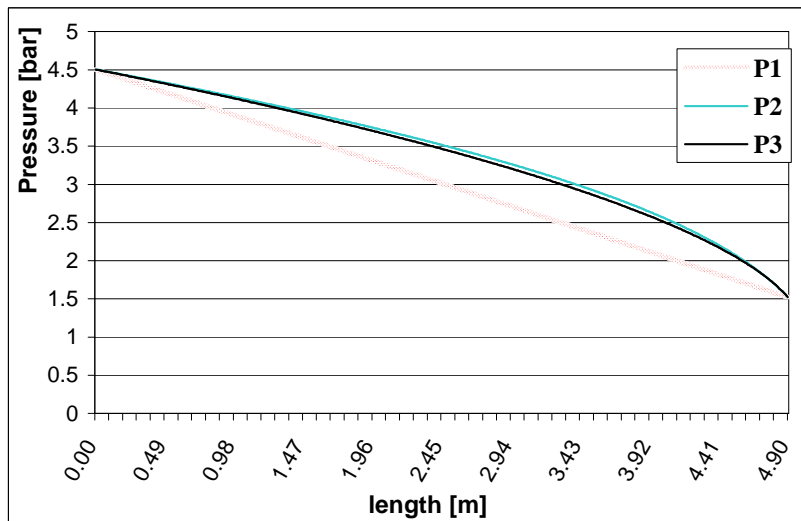


Figure A-3: ST8 pressure variation along probe

This ST8 pressure drop along the flow shows the non-linearity induced by the Mach number, and the rapid convergence with three iterations. Pressure was always integrated by dividing the probe length into five hundred steps. This pressure evolution graphic (Figure A-3) corresponds to a single plateau of steady state pressure measurements, the very plateau leading to the largest divergence between P_2 and P_3 . These calculations then lead to one friction factor evaluation.

Note that the pressure drop is boosted towards the outlet of the pipe: the pressure drop rate keeps increasing as the fluid progresses in the tube. Reynolds number variation between inlet and outlet is less than 5%, results are further presented with mean inlet-outlet Reynolds value.

Mach number absolute influence

The Mach number absolute variation range is [0; 0.64] for the smooth tubes and [0; 0.35] with the set of spirals tested. The extremes are reached with ST8 and I8, which have the largest friction factors in their respective category.

From the definitions $M = \frac{V}{a}$ and $V = \frac{\dot{m}}{\rho S}$, and according to (AII-16), we have:

$$M = \frac{\dot{m}}{a(\alpha P + \beta)S} \quad (\text{AII-20})$$

varying with a good approximation as $\frac{1}{P}$. The Mach number therefore rises as pressure sinks, and the high values of Mach are found at the tube outlet.

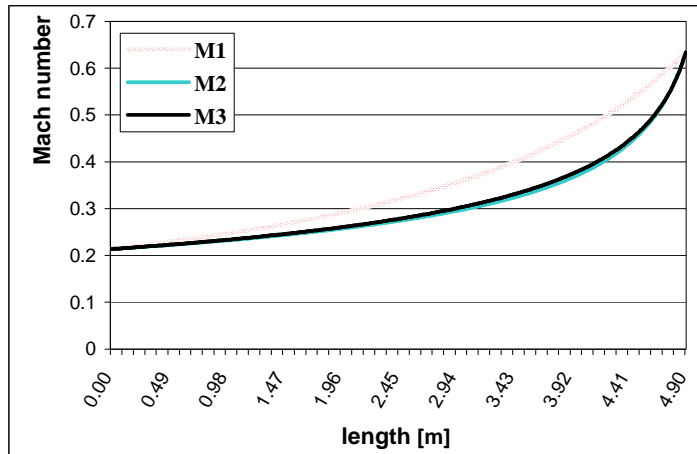


Figure A-4: Mach number evolution along smooth tube ST8 probe in 3 iterations for pressure conditions $P_{in}=4.5\times 10^5$ and $P_{out}=1.5\times 10^5$ Pa

Furthermore, large Mach number effects are present with high velocities, in turn obtained with high pressure drop. The highest velocities are obtained with the smallest diameters 6-8 mm and for the smallest values of friction factor (Figure A-4): an increased friction leads to mass flow and Mach number cut, although the concomitant pressure drop increase attenuates Mach number reduction (results in chapter 2). Hence the reduced Mach number effect on greater friction spirals. Because of their reduced rugosity, the smooth tubes endure higher mass flows and the flow is subject to the highest Mach numbers.

Mach relative influence

The numerical influence of the Mach number on the friction factor can be defined as:

$$f_{\text{without}} = f_{\text{Mach}}(1 + \delta) \quad (\text{AII-21})$$

where:

$$\delta = \int \left(\frac{\gamma(x) \cdot M(x)^2}{1 - M(x)^2} \right) dx / L \quad (\text{AII-22})$$

In Figure A-4, we observe that the compressibility leads to a reduction of the friction factor. δ values show that the omission of the Mach number introduces an error from 1.1 to 5.7% for the spirals, and up to 17.5% for the smooth tubes. The single friction factor values retained for each probe corresponds to a quadratic regime average: it is the constant value of f at large Reynolds numbers. This independence of Re is observed graphically for all spirals with Re above 10^5 , but the smooth tube reach this fully turbulent flow regime only above $Re=10^6$.

Table A-1: Friction factor experimental results with influence of Mach number

| Spiral type | f with Mach (D_h) | f without Mach (D_h) | Maximum relative difference δ (%) |
|-------------|-------------------------|----------------------------|--|
| Showa | 4.39×10^{-2} | 4.46×10^{-2} | 1.48 |
| Cortaillod | 1.00×10^{-1} | 1.01×10^{-1} | 1.13 |
| S-10 | 7.32×10^{-2} | 7.74×10^{-2} | 5.68 |
| C-10 | 8.90×10^{-2} | 9.40×10^{-2} | 5.58 |
| I-10 | 1.01×10^{-1} | 1.06×10^{-1} | 5.04 |
| S-8 | 9.03×10^{-2} | 9.53×10^{-2} | 5.65 |
| C-8 | 1.07×10^{-1} | 1.11×10^{-1} | 3.70 |
| I-8 | 1.33×10^{-1} | 1.37×10^{-1} | 3.01 |
| ST-10 | 1.70×10^{-2} | 1.88×10^{-2} | 10.83 |
| ST-8 | 1.75×10^{-2} | 2.05×10^{-2} | 17.42 |

Appendix III: Test facility HECOL

The Heat Exchange Conductor Operational Loop (HECOL) test facility was thought [Mar02] and designed [Dec03] for the evaluation of thermal characteristics of a superconducting Cable-In-Conduit Conductor (CICC) in transient experiments using pressurized ambient temperature water. Small additions soon allowed to conduct steady state operations and test hydraulic properties as well.

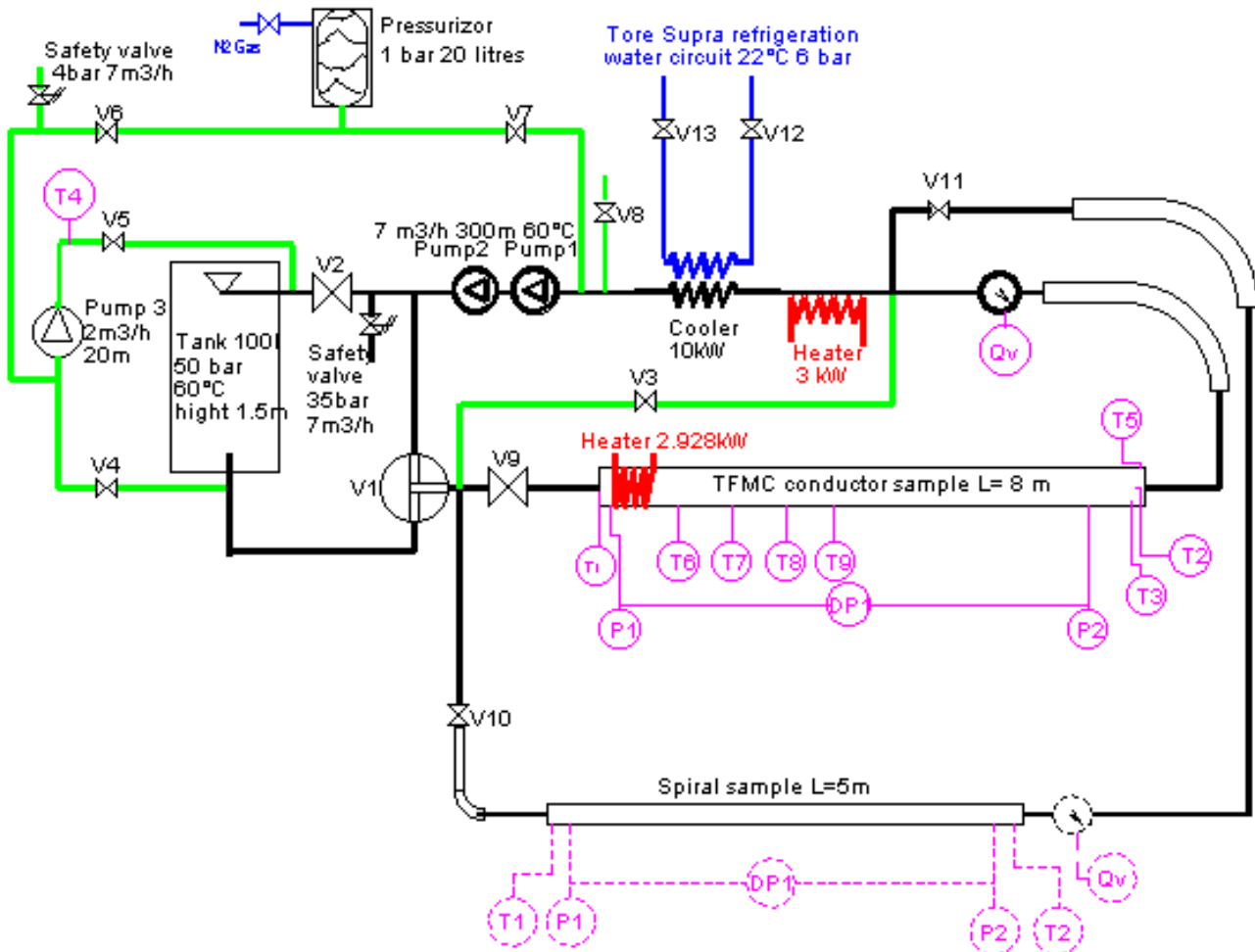


Figure A-5: HECOL test loop setup

Hydraulic tests

The pressure drop of various CICC central spirals samples was investigated in the test facility operated at Cadarache at Reynolds numbers relevant to ITER conditions. The loop is filled from a network of decarbonated water. The test facility pumps and heat exchangers allow mass flow rate up to $1.5 \times 10^{-3} \text{ m}^3/\text{s}$ and temperature ranging from 15 to 75°C.

The pressure in the loop is not controlled, but a variable mass flow rate is obtained using one or both of the two pumps (of different characteristics) in series, and eventually opening a bypass for a continuous testing of sample pressure/mass flow rate characteristics.

Pressure drop ΔP measurements qualification resulted in a very consistent minimization of pressure drop by 10% compared to the smooth tube Blasius law [Idel'cik] and Colebrook intrinsic formula [Col38], that remains within the accuracy reported in the experimental elaboration of these empirical laws, a hundred years ago. Pressure tubes were chosen as small as possible, and checked to have state-of-the art ends.



Figure A-6: HECOL facility

The heaters of the facility are also useful in purely hydraulic experiments because the fluid dynamic viscosity μ significantly diminishes when temperature increases, thus allowing the operator to reach higher Reynolds numbers. The HECOL facility being in configuration for heat exchange coefficient tests, the conductor instrumentation is as follows:

Spirals

Spirals samples over 4 m long are inserted with the “Overtwist” or “Co-drawing” method (see section 2.2 & 2.3) into a stainless steel pipe. Sample were equipped by hydraulic connections, pressure drop holes (2 mm inside diameter) and temperature sensors at each end.

Spirals unsymmetric hydraulic behaviour is discussed in chapter 2.

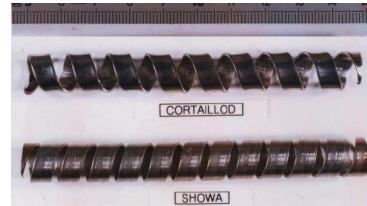


Figure A-7: COR and SHO spiral samples

TFMC (Toroidal Field Model Coil [Ulb05])

It is the Niobium-tin conductor used for the manufacture of the model coil of ITER toroidal field coils. This same conductor was used to design a SULTAN sample. The SULTAN cable sample is referred to as TFMC-FSJS (Full Size Joint Sample). It has a 1.6 mm thick round sheath out of stainless steel 316LN.

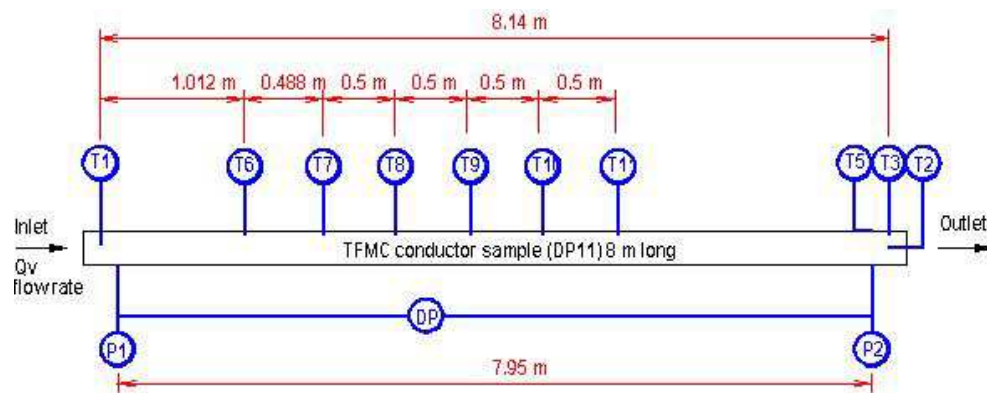


Figure A-8: TFMC thermometer configuration



Figure A-9: Section of the TFMC conductor

The sample tested in HECOL is an 8 m long TFMC sample, equipped with pressure probes, thermometers every 0.5 m. HECOL annular heaters are providing a fixed power of 3.28 kW when turned on.

Steady state thermal tests

A better understanding of the inter-channel heat exchange is sought for characterisation and modelling or validation of existing models [Nic02]. This appendix addresses steady-state experiments carried out in the facility with the TFMC-1 conductor sample.

The steady-state measurement principle developed in chapter 3 calls for a continuous heating of the jacket in a localized area. HECOL testing procedure consists in using a jacket heater of length $L=0.38$ m and power 3.28 kW (contrary to the reading on Figure A-5). The (movable) heater is bolted with thermal grease to the conductor jacket at 0.32 m from the conductor inlet. If more steady state experiments were to be conducted on HECOL, it would be preferable to densely concentrate instrumentation on a narrow section of the CICC, inside as well as outside. The moving capability of the heater could then be used to observe temperatures at different distances from it.

When conducting tests on a full size CICC sample, the same outlet flow rate Q_v Ultra Sound meter is used when testing spirals inserted in much smaller tubes, but the sensor is reconfigured, recalibrated and readings were checked both with another type of mass flow rate device and by weighing the integrating mass flow. The constructor provides a theoretical inaccuracy value under 1%.

Transient thermal tests

Transient experiments are obtained by storing water in the tank, bringing the loop water to a different temperature and suddenly shifting water circulation path to the tank.

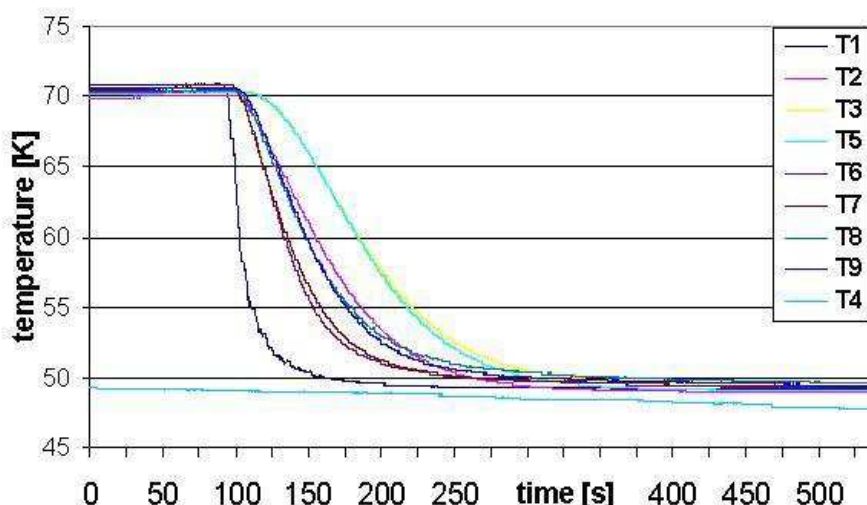


Figure A-10: HECOL transient temperature step

Appendix IV: Test facility SULTAN

Helium supply parameters from the SULTAN facility are a constant inlet pressure of 1.02 MPa and a mass flow rate varying between 2 and 10×10^{-3} kg/s.

PF (Poloidal Field) samples

It is the model Niobium-titanium conductor for the ITER poloidal coils, referred to as PF conductors. Two SULTAN samples of this conductor were manufactured out. The first is the PF-FSJS, made with two different types of strands. The second is the PFCI-FSJS, made from a Russian strand. This last conductor is to be tested in the CSMC (Naka, Japan). PF conductors have a square 51 mm 316LN stainless steel jacket.

Table A-2: Geometry of the PFIS and PF-FSJS CICC

| | symbol | PFIS W (L) | PFIS NW (R) | PF-FSJS | unit |
|------------------------------|--------------------------------|-----------------------|---|-----------------------|--------------------------------------|
| Spiral diameters | id/od | | 10/12 | | 9.9/11.9 mm |
| spiral helium surface | Ac | | 8.70×10^{-5} | | 7.74×10^{-5} m ² |
| spiral wetted perimeter | w _C | | 3.49×10^{-2} | | 3.12×10^{-2} m |
| spiral perforation | Perfor | | 24 | | 27.75 % |
| spiral id friction factor | f _C | | 0.043 | | 0.044 - |
| copper cross-section | A _{Cu} | | 353 | | mm ² |
| strand diameter | | | 0.73 | | mm |
| number of strands | | | 1440 | | - |
| bundle area void fraction | void | 33.5 | 34.3 | 36.85 | % |
| bundle area helium surface | A _A | 3.33×10^{-4} | 3.28×10^{-4} | 3.55×10^{-4} | m ² |
| bundle area wetted perimeter | w _A | 3.68 | 3.46 | 3.193 | m |
| bundle hydraulic diameter | | 3.61×10^{-4} | 3.79×10^{-4} | 4.45×10^{-4} | m |
| bundle friction factor | f _A | | $(0.0231 + 19.6/Re^{0.7953})/\text{void}^{0.742}$ | | - |
| total CICC helium surface | A _A +A _C | 4.19×10^{-4} | 4.15×10^{-4} | 4.32×10^{-4} | m ² |

The characteristics and dimensions reported in Table A-2 are used to compute all hydraulic and thermal properties of the PF-FSJS and PFIS samples studied. The PFIS is similar to the PF-FSJS, with a central channel characterised by less pressure drop, very short annular heaters near the joint and a testing program in both downward and upward flow directions. While the PF-FSJS is representative of a TF conductor with $\alpha_A \sim 60\%$, the PFIS is characterised by a very low pressure drop in the central channel and low α_A .

Mass flow balance and pressure drops summarized in Figure A-11 are calculated from Katheder's f_A and f_C extrapolated from spiral friction measurements (chapter 2).

He flow in the annular channel is assumed uniform and isothermal (3.1 and 3.2).

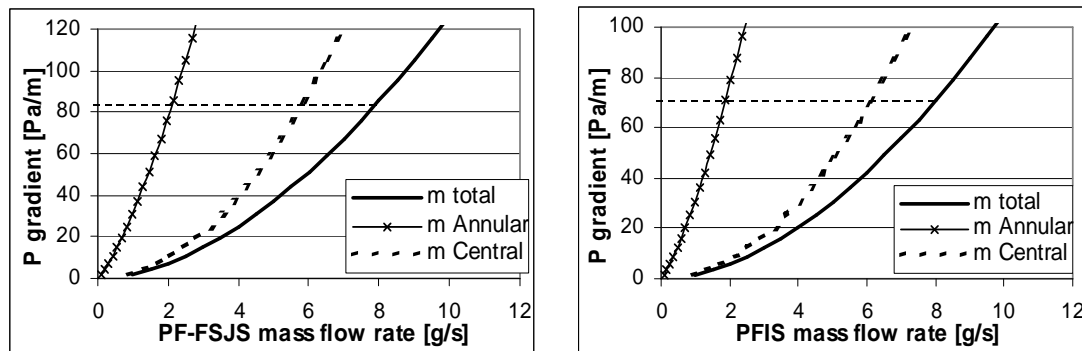


Figure A-11: Mass flow balance in PF-FSJS & PFIS specimen

The PF-FSJS is formed of two CICC legs, both with electric joints and hydraulic collectors at each end. The legs are wrapped and hydraulically similar in all characteristics except for a slight difference in annular petal twisting lengths.

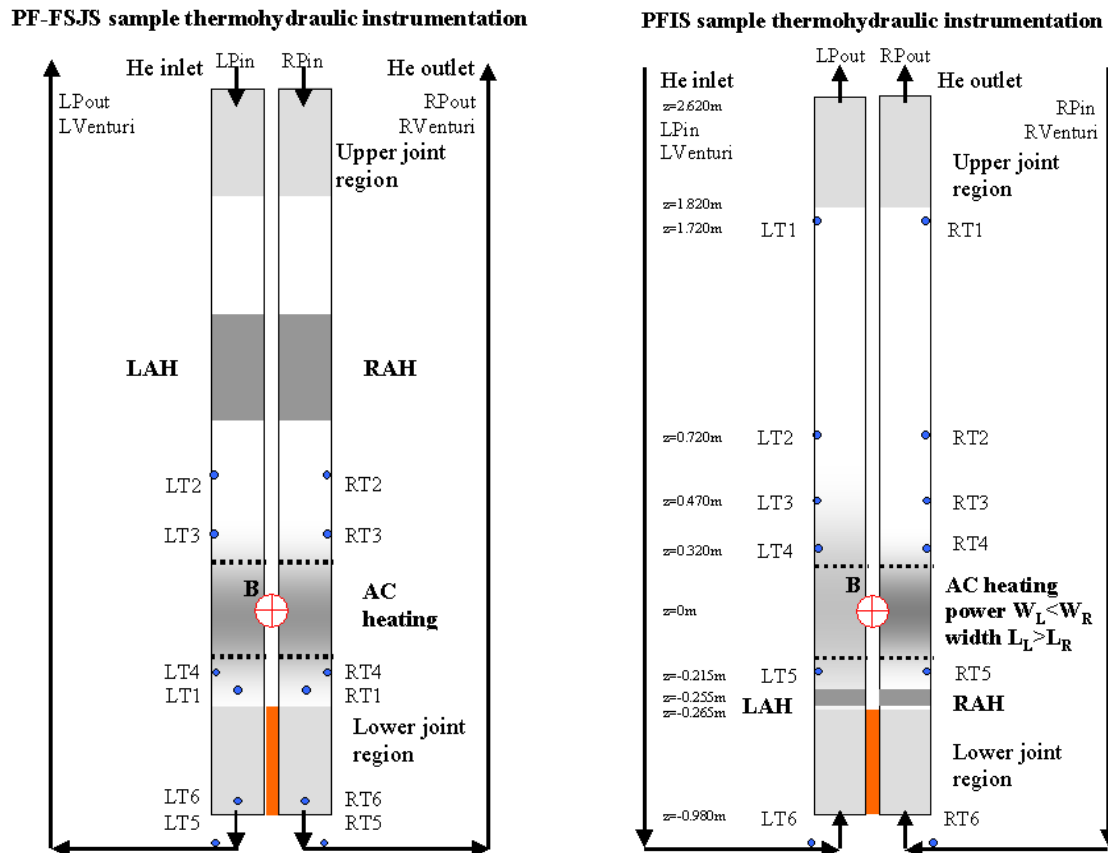


Figure A-12: Schematic view of the PF-FSJS (downward flow only), and of the PFIS (upward direction shown), including thermal-hydraulic equipment and sensors

There are two ways to apply steady state power to the annular helium flow: resistive annular heaters of defined lengths glued on the jacket provide radial heat through conduction; a pulsed magnetic field generates AC losses in conducting metallic parts, strands especially.

The jaws of the pulsed magnet are 0.4 m wide, the effective length of the field is 0.39 m, but the AC loss power distribution is not clearly defined in length nor in its profile, due to possible circulating currents in the cable. For each leg thermally insulated from its mate, the power obtained from a particular AC frequency must be evaluated from the inlet/outlet calorimetric enthalpy balance.

PF-FSJS heaters

SULTAN samples PF-FSJS was best equipped and instrumented for steady state experiments. In the PF-FSJS instrumentation, we dispose only of two close-together thermometers downstream of the AC field region, therefore we cannot use AC heating to observe a temperature evolution in space, needed to use a heat transfer length method. PF-FSJS AC results are thus not presented here. Even in the serviceable Annular Heaters (AH) experiments, the distance between AH and T₂ as well as the sparse repartition of downstream thermometers are not optimal.

The PFIS could on the contrary not use AH heaters, and was nevertheless tested with AC heating: Due to the thermometer layout of the PFIS where a large region of the sample reserved for AC losses cannot be instrumented, the short annular heaters cannot provide data of interest to thermal heat exchange.

There are two ways to apply steady state power to the annular helium flow: resistive annular heaters of defined lengths glued on the jacket provide radial heat through conduction; a pulsed magnetic field generates AC losses in conducting metallic parts, strands especially.

Information about both samples is detailed in Appendix IV.

PFIS heaters

The Poloidal Field Coil Insert Full-Size Joint Sample (PFCI-FSJS or PFIS) was manufactured and tested in 2004 [Hur05]. The PFIS is formed of two CICC legs, each with electric joints and hydraulic collectors at each ends, and thermally insulated from its mate (Figure A-12). The sample tested in upward and downward flow directions [Nic02] is also designed for steady state experiments of two types:

1. applying power with either resistive annular heaters glued on the jacket or
2. with a pulsed magnetic field generating AC losses in conducting strands [Nic04].

These two types of heaters are representative of two categories of heat deposition, which can take place in a fusion magnet during operation:

1. external heat deposition propagating through conduction in insulation and jacket,
2. inter-strand heat deposition due to variable magnetic field.

Helium supply parameters from the SULTAN facility are a constant inlet pressure of 1.02 MPa and a mass flow rate varying between 2 and 10×10^{-3} kg.s⁻¹.

Appendix V: Stationary thermal resolution

The thermal barrier between the channels of a CICC being alternatively made of central spiral perforated and closed parts, the local thermal resistance is varying and leads to local temperature heterogeneities. While the average heat exchange coefficient allows a fast macroscopic approach, the use of a space average between spiral closed and perforated heat transfer coefficients does not reflect the real complexity of local temperatures and the maximal local temperature difference between the two channels. Providing an upper limit to these thermal gradients at the spiral step scale allows to assess the optimal geometry that should be assigned to the CICC central spiral.

Mean temperature difference ($T_A - T_C$)

In reality spiral perforation is not evenly distributed, but is periodic with each spiral step p . The mean thermal heat exchange H only provides a mean behaviour for the thermal barrier generated by the presence of the spiral. Small periodic variations in ΔT , corresponding to real local heat exchanges H_{Closed} et H_{Perfor} allow a fine modeling of ΔT and of its maximal local intensity between the two channels.



Figure A-13: SHOWA helix

A conductor subject to a constant linear heat load distribution Q in the annular channel has a thermal response that can be subdivided into:

- A mean isothermal or uniform conductor temperature rising linearly as a function of distance:

$$T_{iso}(x) = T_0 + \frac{Q \cdot x}{m C_p} \quad (\text{AV-1})$$

- A temperature difference between the channels that can never vanish because it is necessary to transfer part of the power to the central channel, according to the heat exchange coefficient H . This temperature difference is labeled “mean” when the mean spiral properties are used, with mean H .

$$(T_A - T_C)(x) = \frac{Q \Lambda}{m_A C_p} (1 - e^{-x/\Lambda}) = \frac{Q m_C}{m \cdot H \cdot p} (1 - e^{-x/\Lambda}) \quad (\text{AV-2})$$

Note that there is a duality $H-\Lambda$, where Λ is the heat exchange characteristic length [Par03] :

$$\Lambda = \frac{m_A m_C C_p}{H \cdot p \cdot m} \quad (\text{AV-3})$$

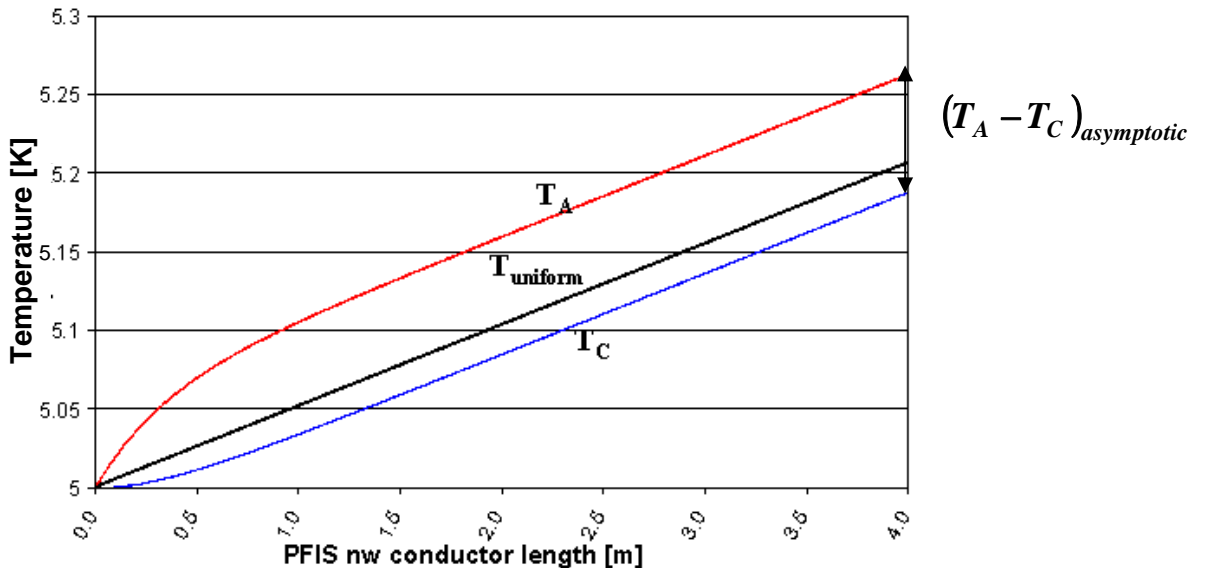


Figure A-14: Isothermal temperature and mean temperature in each channel [Ren04] for the PFISnw conductor subject to a heat distribution of $Q = 2 \text{ W/m}$

Hence the asymptotic temperature difference:

$$(T_A - T_C)_{asymptotic} = \frac{Q\Lambda}{m_A C_p} = \frac{Q \dot{m}_c}{m \cdot H \cdot p} = \frac{Q_c}{H \cdot p} \quad (\text{AV-4})$$

$$\text{where } Q_c = Q \cdot \dot{m}_c / \dot{m} \quad (\text{AV-5})$$

is the power fraction that crosses the spiral to be evacuated by the central channel.

Local temperature variations

The thermal barrier between the channels of a CICC being alternatively made of central spiral perforated and closed parts, the local thermal resistance is varying and leads to local temperature heterogeneities. While the average heat exchange coefficient allows a fast macroscopic approach, the use of a space average between spiral closed and perforated heat transfer coefficients does not reflect the real complexity of local temperatures and the maximal local temperature difference between the two channels. With mean properties, after a transition of a few Λ , the temperatures are:

$$T_A = T_{iso} + (T_A - T_C)_{asymptotic} \frac{\dot{m}_c}{\dot{m}} = T_{iso} + \Delta T_{Add} \text{ and} \quad (\text{AV-6})$$

$$T_C = T_{iso} - (T_A - T_C)_{asymptotic} \frac{\dot{m}_A}{\dot{m}} \quad (\text{AV-7})$$

The additional term of temperature increase due to thermal inhomogeneity is equal to:

$$\Delta T_{Add} = (T_A - T_C)_{asymptotic} \frac{\dot{m}_c}{\dot{m}} \quad (\text{AV-8})$$

In reality, the heat exchange coefficient H should be alternatively replaced by H_{Perfor} et H_{Closed} . Around an average value of T_A given by (AV-6), variations should be observed dues to local properties of the spiral. By definition, $(T_A - T_C)$ varies from ΔT_0 to ΔT_1 along a closed spiral section, and inversely in front of a perforation. In the closed spiral parts of length t , starting from ΔT_0 :

$$T_A - T_C = \Delta T_0 + (\Delta T_{turn} - \Delta T_0) \left(1 - e^{-\frac{x}{\Lambda_{spiral}}} \right) \quad (\text{AV-9})$$

and in the open parts of length g , starting from ΔT_1 :

$$T_A - T_C = \Delta T_{perfor} + (\Delta T_1 - \Delta T_{perfor}) e^{\frac{-x}{\Lambda_{perfor}}} \quad (\text{AV-10})$$

where the characteristic heat exchange length are calculated with local heat exchange coefficients.

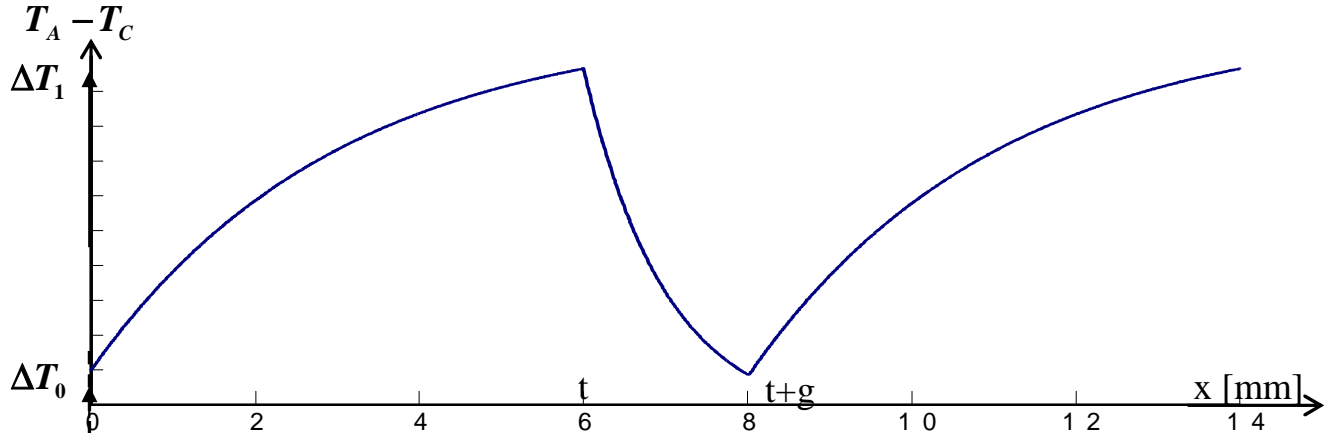


Figure A-15: Zoom in on the periodicity of T_A at the spiral perforation scale varying about the average $(T_A - T_C)_{asymptotic}$ for a constant distributed heat load

Asymptotic limits of exponential curves are defined in the open and closed parts:

$$\Delta T_{perfor} = \frac{Q \Lambda_{perfor}}{m_A C_p} \quad (\text{AV-11})$$

$$\Delta T_{spiral} = \frac{Q \Lambda_{spiral}}{m_A C_p} \quad (\text{AV-12})$$

Superconducting strand maximal temperature T_A

The closing equations at the end of each length are, with $x = t$ or $x = g$ depending on the case:

$$\left\{ \begin{array}{l} \Delta T_1 = \Delta T_0 + (\Delta T_{spiral} - \Delta T_0) \left(1 - e^{\frac{-t}{\Lambda_{spiral}}} \right) \\ \Delta T_0 = \Delta T_{perfor} + (\Delta T_1 - \Delta T_{perfor}) e^{\frac{-g}{\Lambda_{perfor}}} \end{array} \right. \quad (\text{AV-13})$$

$$\left\{ \begin{array}{l} \Delta T_1 = \Delta T_0 + (\Delta T_{spiral} - \Delta T_0) \left(1 - e^{\frac{-t}{\Lambda_{spiral}}} \right) \\ \Delta T_0 = \Delta T_{perfor} + (\Delta T_1 - \Delta T_{perfor}) e^{\frac{-g}{\Lambda_{perfor}}} \end{array} \right. \quad (\text{AV-14})$$

Hence it is possible to calculate the maximal temperature difference ΔT_1 , that shall replace $(T_A - T_C)$ to evaluate the maximal rise of superconducting strands temperature:

$$\Delta T_1 = \Delta T_0 e^{\frac{-t}{\Lambda_{spiral}}} + \Delta T_{spiral} \left(1 - e^{\frac{-t}{\Lambda_{spiral}}} \right) \quad (\text{AV-15})$$

and by replacing ΔT_0 by its expression (AV-14), comes the final answer:

$$\Delta T_1 = \frac{\Delta T_{perfor} \left(1 - e^{\frac{-g}{\Lambda_{perfor}}} \right) e^{\frac{-t}{\Lambda_{closed}}} + \Delta T_{spiral} \left(1 - e^{\frac{-t}{\Lambda_{spiral}}} \right)}{\left(1 - e^{\frac{-g-t}{\Lambda_{perfor} - \Lambda_{spiral}}} \right)} \quad (\text{AV-16})$$

similarly:

$$\Delta T_0 = \frac{\Delta T_{perfor} \left(1 - e^{\frac{-g}{\Lambda_{perfor}}} \right) + \Delta T_{spiral} \left(1 - e^{\frac{-t}{\Lambda_{spiral}}} \right) e^{\frac{-g}{\Lambda_{perfor}}}}{\left(1 - e^{\frac{-g-t}{\Lambda_{perfor} - \Lambda_{spiral}}} \right)} \quad (\text{AV-17})$$

For each $(T_A - T_c)$ corresponds a ΔT_{add} , complement of $T_{uniforme}$ to get T_A , evaluated by

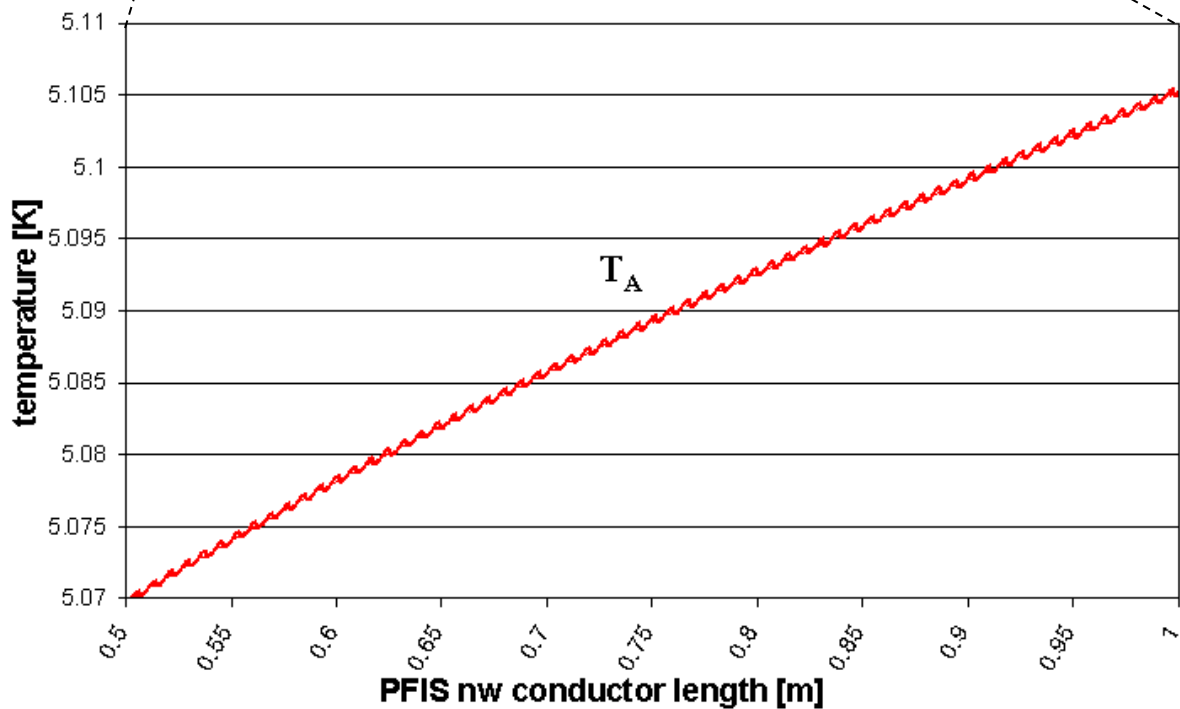
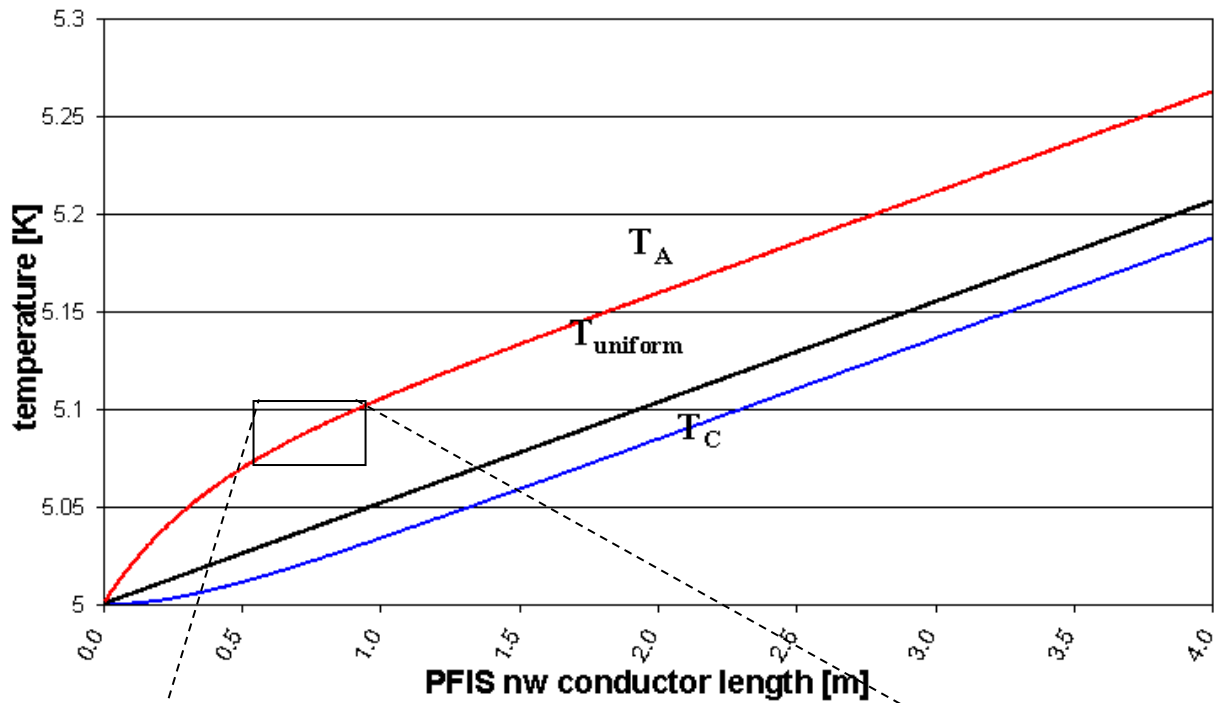
$$\Delta T_{Add} = (T_A - T_c) \dot{m}_c / \dot{m}. \quad (\text{AV-18})$$

Eventually ΔT_{add} with an average Λ is replaced by the very close $\Delta T_{1 Add}$ and the maximal temperature obtained is of:

$$T_A = T_{uniform} + \Delta T_{1 Add}$$

In fact, the mean temperature difference, calculated with the macroscopic spiral properties and leading to the annular temperature simple evaluation $T_{uniform} + \Delta T_{Add}$ is very close to the more rigorous local calculation. Spiral step scale variations are not significant for temperature varying at the space scale of Λ (see Figure A-17). The more practical ΔT_{Add} is hence retained to quantify interchannel temperature difference.

The temperature difference ΔT_{Add} is to be subtracted from the temperature margins of the superconducting strands, therefore an evaluation is crucial to the proper functioning of the magnets when carrying nominal intensity.



Appendix VI: Transient thermal resolution

Equations (3.3-1) are developed into (AVI-1) where U is the mean helium velocity in the respective channels:

$$\begin{cases} \frac{\partial T_A}{\partial t} + U_A \frac{\partial T_A}{\partial x} + \gamma_A (T_A - T_C) = Q \\ \frac{\partial T_C}{\partial t} + U_C \frac{\partial T_C}{\partial x} - \gamma_C (T_A - T_C) = 0 \end{cases} \quad (\text{AVI-1})$$

The specific heat C_p is assumed constant for each channel; so is the global heat exchange coefficient H , given the weak temperature variation. A method to solve this equation has been early proposed by A. Martinez [Mar93].

Change of reference frame and Laplace transform

We consider the initial temperature of both channels to be T_0 :

$$T_A(0, x) = T_C(0, x) = T_0 \quad \forall x \quad (\text{AVI-2})$$

The cable is fed with He at temperature T_1 at $x = 0$ starting from $t \geq 0$:

$$T_A(t, 0) = T_C(t, 0) = T_1 \quad (\text{AVI-3})$$

Reduced temperatures are used to obtain evolutions from initial conditions set at $T = 0$ at $t = 0$, to $T = 1$ at $t = \infty$, at any given x position:

$$\begin{cases} \theta_A(t) = \frac{T_A(t) - T_0}{T_1 - T_0} \\ \theta_C(t) = \frac{T_C(t) - T_0}{T_1 - T_0} \end{cases} \quad (\text{AVI-4})$$

The system of equations (AVI-1) leads to a window of interest $[U_A \cdot t ; U_C \cdot t]$ expanding and shifting in space (Figure 3-14). This space window has a length $(U_C - U_A) \cdot t$. Similarly, the time window of interest $[x/U_A ; x/U_C]$ is expanding and shifting in time (Figure 3-14 again). With unmodified time reference, the change of spatial reference

$$x' = x - U_A t \quad (\text{AVI-5})$$

allows to follow the area of interest, with static annular He in the new frame. From (AVI-1) the new system of equation is obtained with $Q = 0$, as no local heat source is present:

$$\begin{cases} \frac{\partial \theta_A}{\partial t} + \gamma_A (\theta_A - \theta_C) = 0 \\ \frac{\partial \theta_C}{\partial t} + (U_C - U_A) \frac{\partial \theta_C}{\partial x'} - \gamma_C (\theta_A - \theta_C) = 0 \end{cases} \quad (\text{AVI-6})$$

The analytical resolution is proposed for a heating (or cooling) step entering the CICC and progressively replacing the helium present in the cable at $t = 0$.

For $t < 0$, we have

$$\theta_A = \theta_C = 0 \quad (\text{AVI-7})$$

The boundary condition is

$$\theta_A(x' = 0, t > 0) = \theta_C(x' = 0, t > 0) = 1 \quad (\text{AVI-8})$$

The Laplace transform of equation (AVI-6) reduces the partial differential equations to:

$$\begin{cases} (p + \gamma_A) \Theta_A - \gamma_A \Theta_C = 0 \\ (U_C - U_A) \frac{\partial \Theta_C}{\partial x'} + (p + \gamma_C) \Theta_C - \gamma_C \Theta_A = 0 \end{cases} \quad (\text{AVI-9})$$

where Θ is the Laplace transform of θ . We now have the boundary condition:

$$\Theta_C(x' = 0) = \frac{1}{p} \quad (\text{AVI-10})$$

Transient thermal resolution

Introducing ΔU , the difference of channel He velocity, we can solve (AVI-9) in the Laplace domain:

$$\begin{cases} \Theta_A(x', p) = \gamma_A \exp\left(-\frac{x' \gamma_C}{\Delta U}\right) \exp\left(-\frac{x' p}{\Delta U}\right) \exp\left(-\frac{x' \gamma_A \gamma_C}{\Delta U(p + \gamma_A)}\right) / p(p + \gamma_A) \\ \Theta_C(x', p) = \exp\left(-\frac{x' \gamma_C}{\Delta U}\right) \exp\left(-\frac{x' p}{\Delta U}\right) \exp\left(-\frac{x' \gamma_A \gamma_C}{\Delta U(p + \gamma_A)}\right) / p \end{cases} \quad (\text{AVI-11})$$

$$\text{with } \Delta U = (U_C - U_A) \quad (\text{AVI-12})$$

The image temperatures Θ_A and Θ_C lead us back to θ_A and θ_C after some algebra, and reversing (AVI-5):

$$\begin{cases} \theta_A(x, t) = 2\alpha \cdot \exp(-\alpha) \int_0^\delta \beta \cdot \exp(-\alpha\beta^2) I_0(2\alpha\beta) d\beta \\ \theta_C(x, t) = \exp(-\alpha) \left(1 + 2\alpha \int_0^\delta \exp(-\alpha\beta^2) I_1(2\alpha\beta) d\beta \right) \end{cases} \quad \text{for } x/U_C < t < x/U_A \quad (\text{AVI-13})$$

where I_0 , I_1 , are modified Bessel functions of the first kind,

$$\alpha(x, t) = \gamma_C (x - U_A t) / \Delta U \quad (\text{AVI-14})$$

β is a non-dimensional integration variable, and

$$\delta(x, t) = \sqrt{\frac{(U_C t - x) \gamma_A}{(x - U_A t) \gamma_C}} \quad (\text{AVI-15})$$

Integrating by part expression (AVI-13) leads to:

$$(\theta_C - \theta_A)(x, t) = \exp(-\alpha - \alpha\delta^2) I_0(2\alpha\delta) \quad (\text{AVI-16})$$

$$\frac{d\theta_C}{dt}(x, t) = \frac{\exp(-\alpha - \alpha\delta^2)}{\Delta U} \cdot \left(\gamma_C U_A I_0(2\alpha\delta) + \frac{\gamma_A U_C I_1(2\alpha\delta)}{\delta} \right) \quad (\text{AVI-17})$$

Use of implicit transient solutions

Although explicit formulae of $\theta_A(x, t)$ and $\theta_C(x, t)$ solutions are not given, it is straightforward to calculate temperatures from (AVI-16) and (AVI-17), see Figures 3-14 and 3-15.

For $t < x/U_C$, the Heavyside step in temperature has not reached x:

$$\theta_A(x, t < x/U_C) = \theta_C(x, t < x/U_C) = 0 \quad (\text{AVI-18})$$

At $t = x/U_C$, $\theta_A(x, t)$ is continuous

$$\begin{cases} \theta_A(x, t = x/U_C) = 0 \\ \theta_C(x, t = x/U_C) = (\theta_C - \theta_A)(x, t) \end{cases} \quad (\text{AVI-19})$$

For $x/U_C < t < x/U_A$, the Heavyside step in temperature has reached x in the central, but not in the annular channel θ_C is integrated while θ_A is known from the difference (AVI-16)

$$\begin{cases} \theta_C(x, \frac{x}{U_C} < t < \frac{x}{U_A}) = \theta_C(x, x/U_C) + \int_{x/U_C}^t \frac{d\theta_C}{dt}(x, t) dt \\ \theta_A(x, \frac{x}{U_C} < t < \frac{x}{U_A}) = \theta_C(x, t) - (\theta_C - \theta_A)(x, t) \end{cases} \quad (\text{AVI-20})$$

For $t > x/U_A$, the Heavyside step in temperature has reached both channels at the point x considered:

$$\theta_A(x, t > x/U_A) = \theta_C(x, t > x/U_A) = 1 \quad (\text{AVI-21})$$

Another way to derive temperatures is to use the continuity of $\theta_C(x, t)$ at $t = x/U_A$, with

$$\begin{cases} \theta_c(x, t = x/U_A) = 1 \\ \theta_A(x, t = x/U_A) = 1 - (\theta_c - \theta_A)(x, t) \end{cases} \quad (\text{AVI-22})$$

Temperature difference and derivatives moving at \bar{U}

When moving at the mean velocity \bar{U} , $\alpha(x, t = x/\bar{U}) = \frac{\gamma_c}{\Delta U} x \left(1 - \frac{U_A}{\bar{U}}\right)$ and $\delta = 1$. We have:

$$(\theta_c - \theta_A)(x, t = x/\bar{U}) = \exp(-2\alpha) I_0(2\alpha) \quad (\text{AVI-23})$$

$$\begin{cases} \frac{d\theta_A}{dt}(x, t = x/\bar{U}) = \frac{\exp(-2\alpha)}{\Delta U} (\gamma_A U_C I_1(2\alpha) + \gamma_C U_A I_0(2\alpha)) \\ \frac{d\theta_c}{dt}(x, t = x/\bar{U}) = \frac{\exp(-2\alpha)}{\Delta U} (\gamma_A U_C I_0(2\alpha) + \gamma_C U_A I_1(2\alpha)) \end{cases} \quad (\text{AVI-24})$$

For large values of α (as x or $t \rightarrow \infty$), annular and central temperatures converge and the temperature slopes eventually tend to zero:

$$\frac{d\theta_A}{dt}(x, t = \frac{x}{\bar{U}}) \approx \frac{d\theta_c}{dt}(x, t = \frac{x}{\bar{U}}) \approx \frac{(\gamma_A U_C + \gamma_C U_A)^{3/2}}{2\Delta U \sqrt{\pi \gamma_A \gamma_C x}} \quad (\text{AVI-25})$$

The mean velocity \bar{U} allows to define a transition time:

$$\frac{1}{d\theta_{\bar{U}}/dt} \approx \tau(x) = \frac{2\Delta U \sqrt{\pi \gamma_A \gamma_C x}}{(\gamma_A U_C + \gamma_C U_A)^{3/2}} = \frac{2\Delta U \cdot A_C A_A}{(A_C U_C)^{3/2} + (A_A U_A)^{3/2}} \sqrt{\frac{\pi \rho C_p x}{H \cdot p}} \quad (\text{AVI-26})$$

Nomenclature and abbreviations

| | |
|---|--|
| a, c | indices relative to the CICC annular & central channel |
| s, j | indices relative to the CICC spiral & jacket |
| a [m/s] | sound velocity in the fluid |
| A_j [m^2] | jacket cross-sectional surface (stainless steel) |
| A_a, A_c [m^2] | annular or central channel helium cross-sectional surface $A_c = S$ |
| α_A (%) | proportion of annular to total CICC mass flow $\alpha_A = m_A / \dot{m}$ |
| α (rad) | angle of the spiral with the spiral axis $\alpha = \frac{\pi}{2} - \arctan\left(\frac{p}{\pi D}\right)$ and $p = \pi D \tan\left(\frac{\pi}{2} - \alpha\right)$ |
| α - | non-dimensional relative position in the transient space window $\alpha(x, t) = \gamma_c (x - U_A t) / \Delta U$ |
| β - | non-dimensional integration variable in Appendix VI |
| β_A [K/m] | rate of temperature increase, heat supported by bundle only $\beta_A = Q / m_A C$ |
| β_{iso} [K/m] | rate of temperature increase in isothermal CICC $\beta_{iso} = Q / m C$ |
| β_p [K^{-1}] | thermodynamic coefficient of isobaric volume variation $\beta_p = \frac{1}{V} \frac{\partial V}{\partial T}$ |
| C_p | [J/kgK] calorific capacity |
| C_f | - friction coefficient C_f (American) = $f/4$ (European) |
| id/od | [m] spiral inner / outer diameter $id = od - 2e$ |
| D_h | [m] spiral hydraulic diameter $D_h = 4 \frac{S}{w}$ |
| D_j | [cm ² /s] jacket diffusivity |
| δ | - calculation parameter $\delta(x, t) = \sqrt{\frac{(U_c t - x)\gamma_A}{(x - U_A t)\gamma_c}}$ |
| e | [m] spiral thickness (stainless steel) |
| e_j | [m] jacket thickness (stainless steel) |
| ϵ (-) | relative roughness of a conduit wall |
| f | - friction coefficient f (European) = $C_f * 4$ (American) |
| f_{unit} | [m] European friction factor per unit flow singularity (spiral period) $f_{unit} = f \cdot p$ it is the friction factor (per unit length) divided by the spiral spatial frequency |
| γ | thermodynamic constant $\gamma = C_p / C_v$ |
| γ_A, γ_C [s ⁻¹] | ratio of lineic heat transfer over heat capacity $\gamma_i = \frac{H \cdot p}{\rho_i \cdot A_i \cdot C_{p,i}}$ |
| g | [m] spiral gap length |
| g | [kg.m/s ²] acceleration of gravity |
| h_c | [W/m ² K] forced convection coefficient in the central spiral |
| h_a | [W/m ² K] forced convection coefficient in the annular region, near spiral or near jacket wall |
| H | [W/m ² K] annulus-center total heat exchange coefficient |
| ΔH | [J/kg] inlet/outlet superconductor cable enthalpy variation |
| $H.p$ | [W.m ⁻¹ K ⁻¹] interchannel heat exchange rate per meter CICC |
| id | [m] spiral internal diameter |
| k | [kg ⁻¹ m ⁻²] pressure drop coefficient $k = f \cdot w / (8 \rho \cdot S^3)$ |
| K | [m ²] permeability constant |
| ζ | singular friction coefficient |
| L / R | left / right |

| | | |
|-----------------------|--------------------------------------|---|
| L | [m] | length (between pressure probes, length of heated zone) |
| L _t | [m] | conductor length subject to thermosiphon |
| λ | [W.m ⁻¹ K ⁻¹] | thermal conductivity |
| λ_{ss}/e_{ss} | [W/m ² K] | intensity of conduction through the spiral closed portions (stainless steel) |
| Λ | [m] | characteristic annular-central heat exchange length $\Lambda = (m_A m_C C) / (H p m)$ |
| \dot{m} | [kg/s] | (total) mass flow rate $m = \rho v S$ |
| μ | [kg/m.s] | dynamic viscosity |
| μ_{JT} | [K/Pa] | Joule-Thomson coefficient |
| M | - | Mach number $M = \frac{v}{a}$ |
| η_{Carnot} | (%) | Carnot refrigeration efficiency |
| η_{circ} | (%) | circulating pumps efficiency |
| η_{cryo} | (%) | global cryogenic refrigerator efficiency |
| Nu | - | Nusselt number |
| NW | | absence of wrappings in a CICC sample stripped of them |
| od | [m] | spiral outer diameter |
| p | [mm] | spiral twist pitch length $p = t + g$ |
| p _{AJ} | [m] | perimeter of the bundle region |
| p | [m] | (mean) perimeter of the spiral |
| Φ | rad | angle between conductor and horizontal plane |
| ϕ | rad | attack and trailing edge angle of the spiral profile (angle effectively observed by the flow) the spiral ribbon angles assumed equal are $\arctan(\tan(\phi)/\cos(\alpha)) = \phi = \pi/2$ |
| P | [Pa] | pressure |
| ΔP | [Pa] | pressure drop |
| Perfor | (%) | spiral perforation (or porosity) $\text{Perfor} = \frac{\theta}{2\pi} = \frac{g}{p} = \left(1 - \frac{t}{p}\right)$ |
| Pr | - | Prandtl number |
| P _{circ} | [W] | additional power required by coolant circulation |
| P _{hl} | [W] | power of heat load falling on the coils in operation |
| Q | [W/m] | heat load falling on a conductor, in particular lineic heat load imposed on the CICC |
| Q _v | [m ³ /s] | volume flow rate |
| r | - | thermosiphon reverse pressure risk ratio $r = \frac{\Delta P_{\text{thermosiphon}}}{\Delta P_{\text{friction}}}$ |
| R / L | | right / left |
| ρ | [kg/m ³] | fluid average density |
| Re | | Reynolds number $Re = \frac{\rho v D_h}{\mu} = \frac{4m}{\mu \cdot w}$ |
| ρ | [kg/m ³] | fluid density |
| S _{id} | [m ²] | disc surface of the internal spiral diameter $\pi.id^2/4$ |
| S _{od} | [m ²] | disc surface of the external spiral diameter $\pi.od^2/4$ |
| S | [m ²] | canal area $S = \text{Perfor}.S_{od} + (1 - \text{Perfor}).S_{id}$ |
| St | - | Stanton number |
| τ | [s] | time constant for heat wave travel $\tau(x) = \frac{2\Delta U.A_C A_A}{(A_C U_C)^{3/2} + (A_A U_A)^{3/2}} \sqrt{\frac{\pi \rho C_p x}{H.p}}$ |
| θ | (radian) | gap bow angle in the plane orthogonal to the spiral axis |

| | | |
|-----------------------------|--|---|
| θ_A, θ_C [K] | reduced temperature | $\theta_i(t) = \frac{T_i(t) - T_0}{T_1 - T_0}$ |
| t [m] | spiral turn length | |
| T [K] | temperature | |
| T_{uniform} [K] | average cable temperature, as if channels had a uniform isothermal behaviour | |
| ΔT_{AJ} [K] | temperature difference imposed by the uniform heat load | $\Delta T_{AJ} = Q/h_{AJ}p_{AJ}$ |
| ΔT_{Add} [K] | $\Delta T_{\text{Add}} = T_A - T_{\text{uniform}}$ | |
| Θ [K] | Laplace transform of reduced temperature θ | |
| U [m/s] | He velocity | |
| \bar{U} [m/s] | mean He velocity in the CICC | $\bar{U} = \frac{U_C \gamma_A + U_A \gamma_C}{\gamma_A + \gamma_C}$ |
| ΔU [m/s] | difference of channel He velocity | $\Delta U = (U_c - U_A)$ |
| v [m/s] | superficial fluid velocity | |
| void (%) | fluid fraction in the bundle channel | |
| V [m ³] | volume of channel | |
| w [m] | canal wetted perimeter | $w = \text{Perfor}.\pi.\text{od} + (1 - \text{Perfor})\pi.\text{id} + 2e$ |
| wrap (%) | conductor petals wrappings coverage | |
| W50, W80 | wrappings coverage (50%, 80%) of a CICC | |
| Δz [m] | difference of height | |

Abbreviations:

| | |
|-----------|---|
| AC | alternative current |
| AH | annular heaters |
| CEA | Commissariat à l'Energie Atomique (F) |
| CICC | Cable-In-Conduit Conductors |
| CRPP | Centre de Recherches en Physique des Plasmas (CH) |
| DRFC | Département de Recherches sur la Fusion Contrôlée (CEA Cadarache) |
| FZK | Forschungs Zentrum Karlsruhe (D) |
| GCRY | Groupe CRYomagnétisme (STEP) |
| ITER | International Thermonuclear Experimental Reactor |
| JET | Joint European Torus (GB) |
| PFIS | Poloidal Field Insert Sample |
| PFCI-FSJS | Poloidal Field Coil Insert - Full Size Joint Sample |
| PSI | Paul Scherrer Institute (CH) |
| STEP | Service Tokamak Exploitation et Pilotage (DRFC) |
| SULTAN | SUPraLeiter Test ANlage (CH) |
| TF | Toroidal Field |
| TFMC | Toroidal Field Model Coil (or a sample of its conductor) |
| TOSKA | TORoidalSpulen Testanlage KArlsruhe (D) |
| EU-TFAS | European Toroidal Field Sample |
| W / NW | with wraps / no wraps |
| W7-X | Wendelstein Stellarator (D) |

Bibliography

- [Bal92] Balsamo E.P. et al. ‘Final tests of the SULTAN 12T facility in the split coil configuration’ 1992 17th Symp. on Fusion Tech. Proc., Rome, Italy
- [Bes92] Bessette D, Ciazynski D, Decool P, Duchateau J-L. & Kazimierzak B. B. ‘Fabrication and test results of the 40kA CEA conductors for NET/ITER’ 1992 proceedings of the 17th Symposium On Fusion Technology, Rom (Italy) 788-792
- [Bes98] Bessette D. ‘Assessment of the strand twist angle distribution in a conductor cross section’ 1998
- [Bes05] Bessette D. ‘ITER thermohydraulic modelling status with Vincenta and design issues/concerns’ presentation at the 6th ITER-CEA meeting on the cryogenic system, thermohydraulics and magnets, 2005 Grenoble
- [Bigot] Lecture notes and course reader for Network Fluid Dynamics by Dr. G. Bigot, Ecole Normale Supérieure de Cachan Civil Engineering Department, France
- [Bos95] Boscary J. ‘Transfert thermique et flux critique dans un écoulement hélicoïdal en tube chauffé asymétriquement’ 1995 Ph.D. thesis, INP Toulouse, Institut de Mécanique des fluides de Toulouse
- [Bot 98] Bottura L. ‘Modelling stability in superconducting cables’ 1998 Physica C: Superconductivity, Vol. 310, 1-4, 316-326
- [Bot00] Bottura L., Rosso C., Breschi M. ‘A general model for thermal, hydraulic and electric analysis of superconducting cables’ 2000 Cryogenics 40, 617-626
- [Bot06CHATS] Bottura L, Bruzzone P, Marinucci C. & Stepanov B. ‘Analysis of transverse heat transfer coefficient in CICCs with central cooling channel’ CHATS 2005 conf. Proc. TM5, Twente, Netherlands Cryogenics Volume 46, Issues 7-8, July-August 2006 Pages 597-605
- [Bot06LHC] Bottura L, Calvi M. & Siemko A. ‘Stability analysis of the LHC cables’ 2006 Cryogenics in press
- [Bre79] Brennan P. J. & Kroliczek E. J. ‘Heat pipe design handbook’ prepared for NASA under contract, Goddard space flight center, Greenbelt, Maryland, june 1979
- [Bru98] Bruzzone P. ‘AC losses and stability on large cable-in-conduit superconductors’ 1998 Physica C: Superconductivity, 310;1-4;240-246
- [Cha00] Chang S. W. & Su L. M. ‘Heat transfer of reciprocating helical tube fitted with full circumferential ribs’ 2000 International Journal of Engineering Science, Vol. 44, 3025-3042
- [Che01] Che X. D, Xu X. Y, Nguang S. K. & Bergles A. E. ‘Characterization of the effect of corrugated angles on hydrodynamic and heat transfer performance of four-start spiral tuber’ 2001 International Journal of Engineering Science, Vol. 123, 1149-1158
- [Cia02] Ciazynski D.: Task M50: ‘Testing Program of the PF-FSJS in SULTAN’, internal report DRFC/AIM/NTT-2002.013

-
- [Cia oral] Ciazynski D. ‘15 months of NbTi CICC results in SULTAN, thermohydraulics and calibration’ 22-24 Jan 2003 CRPP workshop on NbTi CICC, Gstaad, unpublished
- [Cia 05] Ciazynski D. ‘Dimensionnement d’un Conducteur Supraconducteur’ lecture notes, Ecole sur les Conducteurs Supraconducteurs, organised by Association Française du Froid, Archamps, oct. 2005
- [Cia06] Ciazynski D, Bruzzone P, Muzzi L, Renard B. & Zani L. ‘EFDA task TW6-TMSC-FSTEST: testing program for TFAS2 in SULTAN’ 2006, int. report AIM-NTT-2006.017
- [Col38] Colebrook, ‘Turbulent flow in pipes, with particular reference to the transition region between the smooth and rough pipe laws’, Journal of the Institution of Civil Engineers, 1938-1939, vol 11, 133-156.
- [Cos98] Costea M. & Feidt M. ‘The effect of the overall heat transfer coefficient variation on the optimal distribution of the heat transfer surface conductance or area in a Stirling engine’ 1998 Energy Conversion and Management, Vol. 39, 16-18, 1753-1761
- [Dec97] Decool P. et al. ‘Sensibilité des propriétés critiques du Nb₃Sn à la compression dans les grands câbles à refroidissement forcé’ 1997 5èmes journées de Cryogénie et de Supraconductivité, Aussois (France)
- [Dec02-1] Decool P. ‘Design and Manufacture of a Prototype NbTi FSJS for the ITER PF coils’ 2002 Proceedings of the 22nd Symposium on Fusion Technology, Helsinki, Finland 1165-1169
- [Dec02-2] Decool P. ‘Tâche CODES: Evaluation du coefficient d’échange thermique entre les canaux d’un conducteur cable-en-conduit à double canal. Proposition expérimentale’ int. report DRFC/AIM/NTT-2002.024
- [Dec03-1] Decool P. ‘Design of the HECOL test facility’ internal report DRFC/STEP/AIM/NTT-2003.008
- [Dec03-2] Decool P. ‘Starting tests on the HECOL facility’ internal report DRFC/AIM/NTT-2003.029
- [Dec03-3] Decool P. et al. ‘Task M50: PF-FSJS Conductor Characteristics’ 2003 int. report DRFC/AIM/NTT-2003.003
- [Dit30] Dittus P.W, Boelter I.m.K. ‘Heat transfer in automobile radiators of tubular type’ 1930 Univ. Calif. Pub. Eng. Vol. 2, 13, pp. 443-461
- [Duc76] Duchateau J-L, Turck B, Krempasky L. & Polak M. ‘The self-field effect in twisted superconducting composites’ 1976 Cryogenics, Vol. 16, 2, 97-102
- [Duc02] Duchateau J-L, Spadoni M, Salpietro E, Ciazynski D, Ricci M, Libeyre P. & Della Corte A. ‘Development of high-current high-field conductors in Europe for fusion application’ 2002 Superconductor Science and Technology 15 R17-R19
- [Duc04SAMFSS] Duchateau J.L. et al. ‘Proposed design and instrumentation of the SAMFSS samples in relation with program objectives’ 2004 internal report DRFC/AIM/NTT-2004.001
- [Duc04thermosiphon] Duchateau J-L. & Renard B. ‘Possible thermosiphon effect between bundle and hole regions in the ITER TF conductor along the TF inner leg’ int. report DRFC/AIM/NTT-2004.006

-
- [Duc05] Duchateau J-L, Ciazzynski D, Decool P, Renard B. & Zani L. ‘task TW2-TMST-TOSKA deliverable 4: Final report on the testing of a full size joint sample’ 2005 int. report DRFC/ AIM/NTT-2005.002 delivered to EFDA
- [Fir81] Firth R. J. ‘Investigation into the heat transfer performance of helically ribbed surfaces’ 1981 int. report CEGB Berkeley Lab. RD/B/5163N81, HTSG/N(80)38
- [Gee80] Gee D. L. & Webb R. L. ‘Forced convection heat transfer in helically rib-roughened tubes’ 1980 International Journal of Engineering Science, Vol. 23, 1127-1136
- [Gue02] Guemouri Y, Meuris C. & El Khomssi M. ‘Stability criterion and stationary states in a superconducting wire of limited length’ 2002 International Journal of Engineering Science, Vol. 40, 12, 1285-1295
- [Gni76] Gnielinski V. ‘New equations for heat and mass transfer in turbulent pipe and channel flow’ 1976 International Chemical Engineering vol. 16, 359-368
- [Fou05] Fourar M, Lenormand R. & Karimi-Fard M. ‘Inertia Effects in High-Rate Flow Through Heterogeneous Porous Media’ 2005 Transport in Porous Media 60:353–370
- [Fuc98] Fuchino S, Tamada N, Ishii I, Okano M, Higuchi N. & Hoshino T. ‘Hydraulic characteristics in superconducting power transmission line’ 1998 ICEC17 conference proceedings pp. 475-478, Bournemouth, UK
- [Han78] Han J.C., Glicksman L.R. and Rohsenow W.M. ‘An investigation of heat transfer and friction for rib-roughened surfaces’ 1978 International Journal of Heat and Mass Transfer 21 1143-1156
- [Hen91] Henrion M. & Feidt M. ‘Comportement en régime transitoire de divers types d'échangeurs de chaleur ; Modélisation et conséquences’ 1991 International Communications in Heat and Mass Transfer, Vol. 18, 5, 731-740
- [Holman] Holman J.P. ‘Heat Transfer’, ninth edition. Southern Methodist University, McGraw Higher Education, international edition
- [Hur05] Hurd F. et al. ‘Design and manufacture of a Full Size Joint Sample for the qualification of the Poloidal Field Insert Coil’ 2005 IEEE Trans. Appl. Supercond.
- [Idel'cik] Idel'cik I.E. ‘Mémento des pertes de charge, Coefficients de pertes de charge singulières et de pertes de charge par frottement’ traduit du russe par Mme M. MEURY, Eyrolles - Editeur Paris
- [ITER05] ITER Team, FDR, How J. ‘Project Integration Document’ ITER the way to fusion energy, release 2.0, sept 2005
- [Kakaç] Kakaç S, Shah R. K. & Aung W. ‘Handbook of single-phase convective heat transfer’ Wiley-Interscience publication
- [Kar39] von Kármán T. ‘The analogy between fluid friction and heat transfer’ 1939 Trans. ASME vol. 61 pp.705-710
- [Kat94] Katheder H. ‘Optimum thermohydraulic operation regime for cable in conduit superconductors (CICS)’ 1994 Cryogenics, vol. 34, pp. 595–598

-
- [Kim03] Kiml R, Magda A, Mochizuki S. & Murata A. ‘Rib-induced secondary flow effects on local circumferential heat transfer distribution inside a circular rib-roughened tube’ 2003 International Journal of Heat and Mass Transfer
- [Lew74] Lewis M. J. ‘Roughness function, the thermohydraulic performance of rough surfaces and the wall transformation. An overview’ 1974 International Journal of Heat and Mass Transfer vol. 17, 809-814
- [Lew75] Lewis M. J. ‘An Elementary Analysis for predicting the momentum and heat transfer characteristics of a hydraulically rough surface’ 1975 ASME Journal of Heat Transfer 249-254
- [Lib03] Libeyre P. ‘Minutes of meeting on the CODES task at CEA/Cadarache on 03 june 2003’ int. report DRFC/AIM/NTT 2003.023
- [Lib05-1] Libeyre P, Duchateau J-L, Gravil B, Tena E, Henry D. & Journeaux J.Y. ‘Pioneering superconducting magnets in large tokamaks: Evaluation after 16 years of operating experience in tore supra’ 2005 Fusion Engineering and Design, Vol. 75-79, 221-228
- [Lib05-2] Libeyre P. ‘The importance of being thick for a Nb₃Sn superconducting strand’ 2005 int. report DRFC/AIM/NTT 2005.008
- [Lio92] Liou T-M. & Hwang J-J. ‘Turbulent heat transfer augmentation and friction in eriodic fully developed channel flows’ 1992 ASME transactions vol. 114, 56-64
- [Liu01] Liu X. & Jensen M. K. ‘Geometry effects on turbulent flow and heat transfer in internally finned tubes’ 2001 International Journal of Heat and Mass Transfer vol. 123, 1035-1044
- [Lon95] Long A. E. ‘Transverse heat transfer in a Cable-In-Conduit-Conductor with central cooling channel’ 1995 MS thesis, MIT
- [Man95] Manglik R. M. & Bergles A. E. ‘Heat transfer and pressure drop correlations for the rectangular offset strip fin compact heat exchanger’ 1995 Experimental Thermal and Fluid Science, Vol. 10, 171-180
- [Mari04] Marinucci C, Bruzzone P, della Corte A, Savoldi Richard L, Zanino R. ‘Pressure drop of the ITER PFI Cable-In-Conduit-Conductor’ 2004 ASC04 conf. Proc. Jacksonville, USA 2LF02
- [Mar93] Martinez A, Turck B. ‘Supercritical helium cooling of a Cable-In-Conduit Conductor with an inner tube’ 1993 int. report P/EM/93.18
- [Mar02] Martinez A. ‘Conception d’une boucle à eau pressurisée pour l’évaluation du coefficient d’échange thermique entre les canaux d’un conducteur câble-en-conduit à double canal’ internal report DRFC/REF/NTT-2002.001
- [Mar03] Martinez A. ‘Measurement of the heat transfer coefficient between the two channels of a cable-in-conduit conductor’ 2003 int. report DRFC/REF/NTT-2003.003
- [Matyushov] Matyushov D. CHM 341: Elementary Physical Chemistry lecture notes, chap. 3 Arizona State University
- [Met90] Metzger D. E, Fan C. S. & Yu Y. ‘Effects of rib angle and orientation on local heat transfer in square channels with angled roughness ribs’ 1990 Compact Heat Exchangers, A Festschrift for A. L. London, Hemisphere, Washington, DC.

-
- [Meu99] Meuris C, Baudouy B, Leroy D. & Szeless B. ‘Heat transfer in electrical insulation of LHC cables cooled with superfluid helium’ 1999 Cryogenics, Vol. 39, 11, 921-931
- [Mey79] Meyer L. & Vogel L. ‘The velocity distribution and pressure loss at artificial roughnesses with sharp and rounded edges’ 1979 int. report Kernforschungszentrum Karlsruhe 2885
- [Nag86] Nag S. & Raja Rao M. ‘Forced convection heat transfer in smooth tubes roughened by helically coiled ribbons’ 1986 International Journal of Heat and Mass Transfer vol. 30, 7, 1544-1546
- [Nic00] Nicollet S, Duchateau J.L, Fillunger H, Martinez A. & Parodi S. ‘Dual channel Cable-In-Conduit thermohydraulics : influence of some design parameters’ 2000 IEEE Trans. Appl. Supercond. 10;1102-1105
- [Nic02] Nicollet S, Duchateau J-L, Fillunger H, Heller R, Maix R, Savoldi L, Zahn G. & Zanino R. ‘Hydraulic resistance of the ITER Toroidal Field Model Coil dual channel Cable-In-Conduit Conductor pancakes’ ICEC19 conference proceedings pp. 161-164, Grenoble, France 2002
- [Nic02CODES] Nicollet S. & Duchateau J-L. ‘ITER Task CODES : Cable-In-Conduit Conductor central spiral characterisation and influence of new correlation on heat transfer coefficient’ internal report DRFC/AIM/NTT-2002.009
- [Nic03] Nicollet S, Cloez H, Duchateau J-L. & Serries J-P. ‘Results of ITER type central spirals friction factor measurements in the OTHELLO facility and application for ITER Coils’ 2003 Task CODES, STEP/GAIM AIM/NTT-2003.018
- [Nic04ICEC] Nicollet S, Ciazynski D, Duchateau J-L, Lacroix B. & Renard B. ‘Evaluation of the ITER Cable-In-Conduit-Conductor heat transfer’ 2004 ICEC20 conf. Proc. Beijin, China
- [Nic04CODES] Nicollet S, Cloez H, Decool P, Duchateau J-L, Martinez A, Tena M, Renard B. & Serries J.P. ‘Task CODES: deliverable 4 Experimental investigation to determine the heat transfer coefficient between annular area and the central channel of ITER-FEAT conductors as an input to codes development’ 2004 int. report DRFC/AIM/NTT-2004.017 delivered to EFDA
- [Nij04] Nijhuis A, Ilyin Y, Abbas W, ten Haken B. & ten Kate H.H.J. ‘Change of Interstrand Contact Resistance and Coupling Loss in Various Prototype ITER NbTi Conductors with Transverse Loading in the Twente Cryogenic Cable Press up to 40,000 Cycles’ 2004 Cryogenics, Vol. 44, Issue 5, 319-339
- [Nik50] Nikuradse J. ‘Laws for flow in rough pipes’ 1950 NACA TM 1292
- [Nun56] Nunner W. ‘Heat transfer and pressure drop in rough tubes’ 1956 (German) supplement to Forschung auf dem Gebiete des Ingenieurwesens B, vol. 22, pp5-39
- [Pet58] Petukhov B. S. & Kirilov V. V. ‘The problem of heat exchange in turbulent flow of liquids in tubes’ (Russian) 1958 Teploenergetika vol. 4, 4, pp. 63-68
- [Pet63] Petukhov B. S. & Popov V. N. ‘Theoretical calculation of heat exchange in turbulent flow in tubes of an incompressible fluid with variable physical properties’ 1963 High, Temp. vol. 1 pp. 69-83
- [Pan93] Panchal C. B. & France D. M. ‘Heat Transfer and Pressure Drop in Large Pitch Spirally Indented Tubes’ 1993 Int. J. Heat Mass Transfer, vol. 36, 565-576

-
- [Par03] Park S. H. & Duchateau J-L. ‘The effect of perforation between hole and bundle in conductor’ 2003 internal report DRFC/AIM/NTT-2003.035
- [Pas04] Pasztor G, Bruzzone P, Anghel A. & Stepanov B. ‘An alternative CICC design aimed at understanding critical performance issues in Nb3Sn conductors’ 2004 IEEE Trans. Appl. Supercond. 14;1527-1530
- [Pra44] Prandtl L. ‘Führer durch die Strömungslehre’ 1944 Vieweg, Braunschweig p. 359
- [Raf03] Raff S, Schanz P, Wüchner F, Fillunger H. & Libeyre P. ‘Mechanical behaviour of the ITER toroidal field model coil (TFMC) in the single coil test’ 2003 Fusion Engineering and Design, Vol. 66-68, 995-1000
- [Ren95] Ren Y, Weinstein R, Liu J, Sawh R.P, Foster C. ‘Damage caused by magnetic pressure at high trapped field in quasi-permanent magnets composed of melt-textured Y-Ba-Cu-O superconductor’ 1995 Physica C Vol. 251 pp. 15-26
- [Ren04-1] Renard B. & Duchateau J-L. ‘Spirals friction factors in nitrogen flow with Mach number implementation and investigation of spiral geometry influence’ 2004 note DRFC AIM/NTT-2004.007
- [Ren04-2] Renard B. et al. ‘Conductionless one-dimensional model for HECOL steady state heating experiments’ 2004 int. report DRFC/AIM/NTT-2004.015
- [Ren05] Renard B. ‘Steady State Thermal Analysis In PF-FSJS Sultan Experiments’ 2005 int. report DRFC/AIM/NTT-2005.006
- [Ren06-1] Renard B, Duchateau J-L, Rousset B & Tadrist L. ‘Evaluation of Thermal Gradients and Thermosiphon in Dual Channel Cable-In-Conduit Conductors’ 2006 Cryogenics 46, 9, 629-642
- [Ren06-2] Renard B, Martinez A, Duchateau J-L. & Tadrist L. ‘Transverse heat transfer coefficients on a full size dual channel CICC ITER conductor’ 2006 Cryogenics 46, 530-540
- [Ren06-3] Renard B, Duchateau J-L. & Decool P. ‘Optimisation of central channel spiral for ITER TF CICC’ presented at the ICEC21 conference proceedings, Prague 2006
- [RenP97] Renard P. & de Marsily G. ‘Calculating equivalent permeability: a review’ 1997 Advances in water Resources vol. 20, 5-6, 253-278
- [Rou97] Rousset B, Grimaud L. & Gauthier A. ‘Stratified two-phase superfluid helium flow: I’ 1997 Cryogenics, Vol. 37, 11, 733-737
- [Rou04] Rousset B. & Girard A. ‘Preliminary analysis on Sultan\PFIS : enthalpy balance tests with main heaters, calibration and results concerning annular and local heaters’ Communication presented at testing group meeting, Villigen, dec 2004. unpublished
- [Saj95] Sajjadi S. G. & Aldridge J. N. ‘Prediction of turbulent flow over rough asymmetrical bed forms’ 1995 Appl. Math. Modelling, Vol. 19, 139-152
- [Sar01] Sarma P. K, Subramanyam T, Kishore P. S, Dharma Rao V. & Kakac S. ‘A new method to predict convective heat transfer in a tube with twisted tape inserts for turbulent flow’ 2001 Int. J. of Thermal Sciences, Vol. 41, 955-960

-
- [Sat00] Satow T. et al. ‘Results on the superconducting magnet system for the large helical device’ 2000 IEEE Trans. Appl. Supercond. 10-600
- [Siarry] Siarry & Dreyfus ‘La méthode du recuit simulé. Optimisation de systèmes complexes à n paramètres’ ESPCI ed. IDSET
- [Tad04] Tadrist L. et al. ‘About the use of fibrous materials in compact heat exchangers’ 2004 Experimental Thermal and Fluid Science, Vol. 28, 2-3, 193-199
- [Tak96] Takase K. ‘Experimental results of heat transfer coefficients and friction factors in a 2D/3D rib-roughened annulus’ 1996 Experimental Thermal and Fluid Science, Vol. 13, 142-151
- [TdI pdcA738] Les Techniques de l’Ingénieur, Machines hydrauliques et thermiques / Chaudronnerie – Tuyauterie – Robinetterie / Tuyauterie / Écoulement des fluides dans les tuyauteries / 2.2 Évaluation des pertes de charge A738
- [TdI thAF4040] Schuffenecker L, Jaubert J-N. & Solimando R. Les Techniques de l’Ingénieur, Traité sciences fondamentales - ‘Formalisme et principes de la thermodynamique’ AF4040
- [Tix95] Tixador P. ‘Les supraconducteurs’ 1995 Hermès
- [Top97] Topin F, Rahli O. & Tadrist H. ‘Temperature and pressure field visualizations in a porous medium dried in superheated steam’ 1997 Experimental Thermal and Fluid Science, Vol. 15, 4, 359-374
- [Tur93] Turck B, Bessete D, Ciazynski D. & Duchateau J-L. ‘Design methods and actual performances of conductors for the superconducting coils of Tokamaks’ 15th SOFE 1993 Hyannis, MA
- [Ulb05] Ulbricht A, Duchateau J-L, Fietz W-H, Ciazynski D, Fillunger H. et al. ‘The ITER toroidal field model coil project’ 2005 Fusion Engineering and Design 73, 189-327
- [Vic04] Vicente P. G, Garcia A. & Viedma A. ‘Experimental investigation on heat transfer and frictional characteristics of spirally corrugated tubes in turbulent flow at different Prandtl numbers’ 2004 International Journal of Heat and Mass Transfer 47, 671-681
- [Web71] Webb R. L, Eckert E.R.G. & Goldstein R.J. ‘Heat transfer and friction in tubes with repeated-rib roughness’ 1971 International Journal of Heat and Mass Transfer 14, 601-617
- [Weg02] Wegener L. et al. ‘Status of the construction of the W7-X magnet system’ 2002 IEEE Trans. Appl. Supercond. 12-653
- [Wei90] Weisend J. G. & Van Sciver S. W. ‘Pressure drop from flow of cryogens in corrugated bellows’ 1990 Cryogenics vol. 30, 935-941
- [Wilson] Wilson M. ‘Superconducting magnets’ Clarendon press, Oxford University
- [Zani04] Zani L, Ciazynski D. & J-L. Duchateau ‘Voltage–temperature characteristics in model coils using a Nb₃Sn cable-in-conduit conductor for ITER’ 2004 Physica C: Superconductivity, Vol. 401, 1-4, 15 94-98
- [Zan00] Zanino R, Santagati P, Savoldi L, Martinez A. & Nicollet S. ‘Friction factor correlation with application to the central cooling channel of cable-in-conduit super-conductors for fusion magnets’ 2000 IEEE Trans. Appl. Supercond.

[Zan03] Zanino R, Savoldi Richard L. & The TFMC Testing Group. ‘Performance evaluation of the ITER Toroidal Field Model Coil Phase I Part 1: current sharing temperature measurement’ 2003 Cryogenics, Vol. 43, 2, 79-90

[Zan04] Zanino R, Bruzzone P, Ciazynski D, Ciotti M, Gislon P, Nicollet S. & Savoldi Richard L. ‘Analysis of Thermal-Hydraulic Gravity/Buoyancy Effects in the Testing of the ITER Poloidal Field Full Size Joint Sample (PF-FSJS)’ 2004 Adv. in Cryogenic Eng. Conf. CEC 49, Am. Inst. of Phys.

[Zan05] Zanino R, Decool P. & Savoldi Richard L. ‘Status of the analysis of the HECOL transient heat transfer tests’ Jan 2005 presented at the ITER Conductor Meeting, Muerren, Switzerland

[Zan06] Zanino R. & Savoldi Richard L. ‘A review of thermal-hydraulic issues in ITER cable-in-conduit conductors’ Jul 2006 Cryogenics, Vol. 46, 7-8, 541-555

Thermohydraulisches Verhalten des Innengekühlten Zweikanalrohrsupleiterkabels für ITER

Kurzfassung

Um die Kryogen-Benutzung und -Kontrolle der Supraleitenden Großmagneten für die Kernfusion (ITER) zu optimieren, wurde der Zweikanalrohrsupleiterkabel (CICC) mit einer zentralen Spirale entworfen. Der Zentralkanal soll einen minimalen hydraulischen Widerstand und einen schnellen Heliumverkehr gewährleisten, führt jedoch zu einer schwierigeren Abkühlung des Kabels. Das qualitative und ökonomische Grundprinzip der Leiterspirale wird hier durch die Begrenzung der SupraleiterTemperatur gerechtfertigt. Der Druckabfall der zentralen Spirale wird experimentell am Stickstoff und danach am Druckwasser ausgewertet und daraus ein hydraulisches Modell vorgeschlagen. Die Temperaturen im Kabel müssen quantitativ bekannt sein, um Hitzestörungen des Supraleiters während des Betriebes der Spule zu verhindern, sowie um ausreichende Spielräume mit entsprechend niedriger Eintrittstemperatur einzustellen. Es wurden analytische eindimensionale Modelle entwickelt, um die thermische Kopplung zwischen den Kanälen des CICC im Dauer- und Übergangszustand besser zu verstehen. Die Messung der Raum- und Zeit-Konstanten liefert eine Versuchsbewertung der internen thermischen Homogenisierung. Es wird ein einfaches und ausdrückliches Modell des globalen Zwischenkanal-Wärmeaustauschkoeffizienten vorgeschlagen. Das bestehende Thermosiphonrisiko zwischen den zwei Kanälen bei vertikale Fusionsspulen verweist auf ein Kriterium. Das neue hydraulische Modell, das Wärmeaustauschmodell und das Kriterium des Thermosiphonrisikos erlauben schließlich die thermohydraulische Optimierung der Kabel-Zentralspirale.

Schlüsselwörter: Rohrsupraleiterkabel, Supraleitende Magneten, Kernfusion, gezwungen Fluß, Spirale, Wärmeübertragungskoeffizient, Wärmeaustauscher, ITER

Thermo-hydraulic behaviour of dual-channel superconducting Cable-In-Conduit Conductors for ITER

Abstract

In an effort to optimise the cryogenics of large superconducting coils for fusion applications (ITER), dual channel Cable-In-Conduit Conductors (CICC) are designed with a central channel spiral to provide low hydraulic resistance and faster helium circulation. The qualitative and economic rationale of the conductor central channel is here justified to limit the superconductor temperature increase, but brings more complexity to the conductor cooling characteristics. The pressure drop of spirals is experimentally evaluated in nitrogen and water and an explicit hydraulic friction model is proposed. Temperatures in the cable must be quantified to guarantee superconductor margin during coil operation under heat disturbance and set adequate inlet temperature. Analytical one-dimensional thermal models, in steady state and in transient, allow to better understand the thermal coupling of CICC central and annular channels. The measurement of a heat transfer characteristic space and time constants provides cross-checking experimental estimations of the internal thermal homogenisation. A simple explicit model of global interchannel heat exchange coefficient is proposed. The risk of thermosiphon between the two channels is considered since vertical portions of fusion coils are subject to gravity. The new hydraulic model, heat exchange model and gravitational risk ratio allow the thermohydraulic optimisation of a CICC central spiral.

Keywords: cable-in-conduit conductors, superconducting magnets, fusion, forced flow, spiral, heat transfer coefficient, heat exchanger, ITER

Comportement thermo-hydraulique des supraconducteurs de type câble-en-conduit à double canal pour ITER

Résumé

Afin d'optimiser le contrôle cryogénique des aimants supraconducteurs pour la fusion (ITER), les conducteurs de type câble en conduit à double canal (CICC) comprennent un canal central qui assure une résistance hydraulique minimale et une circulation d'hélium rapide. Le canal central constitué d'une spirale limite la température des supraconducteurs, mais complique singulièrement le refroidissement du câble. Les pertes de charge de la spirale centrale sont évaluées en azote puis en eau pressurisée ; un modèle de friction hydraulique est ainsi proposé. Les températures doivent être connues dans le câble, afin de garantir le fonctionnement des supraconducteurs sous charge thermique. Il est alors possible de définir les marges et de fixer la température d'entrée. Des modèles 1D analytiques en régime permanent et transitoire ont été développés afin de mieux comprendre le couplage thermique entre les canaux du CICC. La mesure des constantes caractéristiques d'espace et de temps fournit une évaluation expérimentale de l'homogénéisation thermique interne. Un modèle simple et explicite du coefficient d'échange intercanal est proposé. Le risque de thermosiphon existant entre les deux canaux pour les parties verticales des bobines de fusion est évalué grâce à un critère. Les nouveaux modèles hydrauliques, thermiques et le critère de risque de thermosiphon permettent l'optimisation thermo-hydraulique de la spirale centrale de CICC.

Mots-clefs : conducteurs de type cable-en-conduit, aimants supraconducteurs, fusion, circulation forcée, spirale, coefficient d'échange thermique, échangeur thermique, ITER